# Cryogenic Solar Absolute Radiometer

*A potential SI standard for Solar Irradiance*

Rainer Winkler

University College London

Submitted in partial fulfilment of the requirements for the degree of Doctor of Philosophy (PhD)

## Declaration

I, Rainer Winkler, confirm that the work presented in this thesis is my own. Where information has been derived from other sources, I confirm that this has been indicated in the thesis.

_____

London, 2012

*It is unwise to be too sure of one's own wisdom.*

Mahatma Gandhi

## Abstract

This thesis reports the development of an instrument which could act as a future standard for Solar Irradiance. The instrument is called Cryogenic Solar Absolute Radiometer (CSAR), and it exploits the advances made in the field of cryogenic radiometry in the last few decades. The aim is to significantly reduce the measurement uncertainty as compared to the current standard (the World Radiometric Reference) and to guarantee the long-term stability of the measurement record.

Several tests were carried out in order to verify the performance of CSAR. In a first test, CSAR was found to agree within 0.01% with the National Physical Laboratory's SI standard for radiant power.

In a second test, CSAR and the World Radiometric Reference were compared on the World Radiation Center's solar tracker in Davos/Switzerland. In this comparison, the World Radiometric Reference measured 0.309% higher than CSAR; the relative standard uncertainty of the comparison was 0.028%. This difference between the current Solar Irradiance standard and CSAR is able to explain the offset between the two space experiments VIRGO/SOHO and TIM/SORCE. The CSAR result is further confirmed by the fact that a similar offset between the World Radiometric Reference and the SI-scale has been determined through experiments independently performed at the Laboratory for Atmospheric and Space Physics (University of Colorado Boulder).

CSAR has also been designed with space flight in mind. Although no full evaluation of the space-worthiness has been carried out, thermal tests indicate that CSAR could cope with the limited

cooling power provided by readily available space coolers. The relative standard uncertainty of space-based Total Solar Irradiance measurements by CSAR is estimated to be 0.011%.

# Table of Contents

# List of Figures

# List of Tables

## Acknowledgements

I would like to express my sincere gratitude towards my teachers, colleagues, family, and friends. Their inspiration, their knowledge and their kindness made it possible for me to write this thesis. I consider myself extremely fortunate to have had the opportunity to work and be in contact with such dedicated individuals.

In particular, I would like to thank:

- My principal academic supervisor Ian Hepburn for his unwavering support and encouragement, which was especially important at the time of writing up the thesis.
- My subsidiary academic supervisor Alan Smith for introducing me to the world of space science and for his enthusiasm.
- Tom Bradshaw (external examiner) and Andrew Coates (internal examiner) for agreeing to act as examiners, for their interest in the subject matter presented in the thesis, and their constructive feedback and encouragement.
- André Fehlmann (PMOD/WRC) for help in managing the CSAR project, and his contribution to the build of CSAR, and also for writing the measurement software for CSAR, as well as for preparing the Transmission Monitor. I highly value the mutual respect and friendship that developed between us as a result of our intense collaboration.
- Nigel Fox (NPL fellow) for entrusting me with the project and for valuable feedback regarding the development of CSAR.
- David Gibbs (Group Leader, NPL) for invaluable management support.

- Peter Lovelock (Senior Design Engineer, NPL) for engineering support (design), and the production of engineering drawings, as well as mechanical finite-element-analysis of the detector stages. All 3D model images of CSAR presented in this thesis were drawn by Peter. We spent many hours going over the design again and again, and I enjoyed every minute of it.
- Eric Usadi (Principle Research Scientist, NPL) for his input and advice regarding the optical design of CSAR.
- Geoff Stammers (Head of Engineering Services, NPL), Keith Burgon (Production Manager, NPL), and Paul Stevens (Workshop Supervisor, NPL) for engineering support and management.
- NPL and METAS engineers for doing an excellent job regarding the manufacture of the CSAR parts.
- Robert Roskilly (Workshop Technician, NPL) for excellent engineering support during the build of CSAR.
- Dipak Gohil (Higher Research Scientist, NPL) for providing his expertise in Scanning Electron Microscopy.
- Peter Harris (Principle Research Scientist, NPL) for giving valuable advice regarding the uncertainty analysis.
- Andrew Deadman (Senior Research Scientist, NPL) for reflection measurements of black samples (visible and near-infrared) and window transmittance measurements (visible and near-infrared).
- Christopher Chunnilall (Senior Research Scientist, NPL) for reflection measurements of black samples (infrared) and window transmittance measurements (infrared)

- The whole PMOD team for being very helpful whenever a problem or question arose.
- Wolfgang Finsterle (Head of Solar Radiometry, PMOD/WRC) for providing generous advice regarding the World Radiometric Reference and the World Standard Group.
- Werner Schmutz (director, PMOD/WRC) for giving me the opportunity to work for a total of five months at the PMOD, and for allowing me to stay in the PMOD building during my second stay in Switzerland.
- Sonja Degli Esposti (Head administration, PMOD/WRC) for being an excellent first point of contact with the PMOD/WRC and for the organisational support.
- Malcolm White (Principle Research Scientist, NPL) and Jane Ireland (Senior Research Scientist, NPL) for helpful discussions on cryogenic radiometry.
- Peter Blattner (Head of Optics, METAS) for allowing us to use his laboratory for initial CSAR tests, and for the administrative and scientific support during our stay.
- Rolf Zwahlen (Head of Engineering, METAS) for detailed discussions on the manufacturing of the radiometer head, and the engineering team at METAS for doing a great job regarding the manufacturing the majority of the CSAR parts.
- Berend Winter (head of Mechanical and Thermal Engineering) for advice on how to approach the mechanical design of a space instrument.
- Andrew Gibson (Cryogenic Engineering Group, Astrium Stevenage) for advice regarding Astrium space coolers and the interface to CSAR.

- The Department for Business, Innovation and Skills for providing funding for the CSAR project work as well as my university fees.
- The National Physical Laboratory for giving me the freedom and flexibility to combine full-time employment with a part-time PhD.
- Sivananda Yoga Vedanta Centers in London and Reith for hosting me for a number of months during the PhD project and during some of the write-up period of the thesis. Thanks in particular to the directors Sw. Ramapriyananda (Reith) and Sw. Krishnadevananda (London) as well as all other members of staff.

But most of all, I would like to thank my parents, who have always encouraged me to follow my aspirations, and who have always been prepared to help me achieve my aims. Vielen herzlichen Dank.

I would also like to thank my sisters Renate and Andrea for being just that – my sisters and friends.

And last, but certainly not least, I would like to thank Carolin Holl for being a fabulous friend.

## Acronyms

Although I have tried to minimise the use of acronyms throughout the text, it might be useful to print or copy the list of acronyms given in Table 1.

**Table 1 List of Acronyms used in the thesis text**

| Abbreviation | Full name |
|---|---|
| ACRIM | Active Cavity Radiometer Irradiance Monitor |
| BIPM | Bureau International des Poids et Mésures |
| CGPM | Conférence Générale des Poids et Mésures (General Conference on Weights and Measures) |
| CIMO | Commission for Instruments and Methods of Observation |
| CLARREO | Climate Absolute Radiance and Refractivity Observatory |
| CNES | Centre National d'Etudes Spatiales |
| CSAR | Cryogenic Solar Absolute Radiometer |
| DSR | Direct Solar Radiation |
| ERB | Earth Radiation Budget |
| ERBS | Earth Radiation Budget Satellite |
| ESA | European Space Agency |
| ECV | Essential Climate Variable |
| FOV | Field Of View |
| GUM | Guide to the Expression of Uncertainty in Measurement |

| Abbreviation | Full name |
|---|---|
| GCOS | Global Climate Observing System |
| IAU | International Astronomical Union |
| IPC | International Pyrheliometer Comparisons |
| IRMB | Institut Royal Météorologique de Belgique |
| JCGM | Joint Committee for Guides in Metrology |
| METAS | Das Bundesamt für Metrologie |
| MISR | Multiangle Imaging SpectroRadiometer |
| MLI | Multi-Layer Insulation |
| MODIS | Moderate Resolution Imaging Spectroradiometer |
| NPL | National Physical Laboratory |
| NRC | National Radiation Centers |
| OFHC | Oxygen-Free High Conductivity |
| PICARD | The PICARD mission was named after the French astronomer Jean Picard (1620-1682). |
| PMOD/WRC | Physikalisch-Meteorologisches Observatorium Davos (World Radiation Center) |
| PREMOS | PREcision MOnitor Sensor |
| RRC | Regional Radiation Center |
| RRR | Residual Resistivity Ratio |
| SARR | Space Absolute Radiometric Reference |

| Abbreviation | Full name |
|---|---|
| SI | International System of Units |
| SMM | Solar Maximum Mission |
| SOHO | SOlar Heliospheric Observatory |
| SORCE | Solar Radiation and Climate Experiment |
| TIM | Total Irradiance Monitor |
| TM | Transmission Monitor |
| TRF | TSI Radiometer Facility |
| TRUTHS | Traceable Radiometry Underpinning Terrestrial- and Helio-Studies |
| TSI | Total Solar Irradiance |
| UARS | Upper Atmosphere Research Satellite |
| UV | Ultra violet |
| VIRGO | Variability of solar IRradiance and Gravity Oscillations |
| WMO | World Meteorological Organisation |
| WRC | World Radiation Center |
| WRR | World Radiometric Reference |
| WSG | World Standard Group |

# Chapter 1 Introduction

## 1.1 General Context

The Sun is the key driver of the Earth's climate system. In order to gain a satisfactory understanding of this system, it is important to understand the interaction between Sun and Earth.

This interaction may have many more aspects to it than the ones we are currently aware of, but one can safely say that Solar Irradiance has – at least in absolute terms - the greatest effect on climate. The most common physical quantities that allow us to determine this irradiation is the so-called 'Direct Solar Radiation' (for ground-based measurements) or 'Total Solar Irradiance' (for space-based measurements); they are measures of radiant power (originating from the Sun) per irradiated area, across the whole wavelength spectrum.

The current techniques to determine the most important climate variables are not always adequate to meet the needs of Climate Science. The recognition of this situation led to a growing awareness that measurements relevant to climate science need to conform to the rigours of traceability to the International System of Units (SI). The SI standards are maintained by the National Measurement Institutes (NMIs), which are formally represented by the Bureau International des Poids et Mesures (BIPM) and its body of representatives of eighteen NMIs – the International Committee for Weights and Measures (CIPM).

It is in this context that in 1999, the 21st General Conference on Weights and Measures (CGPM) recognised the need "to use SI units in studies of Earth resources, the environment, human well-being and related issues" (CGPM, 1999). More specifically, resolution 11 of the

23rd General Conference on Weights and Measures (CGPM) calls for "a set of SI-traceable radiometric standards and instruments to allow […] traceability to be established in terrestrial and space based measurements" (CGPM, 2007). In a significant, but only consequential step, the presidents of the WMO and the BIPM signed an International Committee for Weights and Measures Mutual Recognition Agreement (CIPM MRA) in 2010.

## 1.2 Terrestrial measurement of Solar Irradiance

In his review of the history of solar radiometry, Fröhlich points out that the main motivation for solar radiometry has – from its earliest days – been the study of the influence of the Sun on the Earth's climate (Fröhlich, 1991). Fröhlich also describes in great detail the obstacles that had to be overcome to achieve a worldwide homogeneous set of data; the establishment of the so-called 'World Radiometric Reference (WRR)' in 1977 (Fröhlich, 1977) was the decisive step towards achieving homogeneity of worldwide Solar Irradiance measurements.

The World Radiometric Reference (WRR) serves as the worldwide reference scale for Solar Irradiance measurements. The practical implementation of the World Radiometric Reference is through the World Standard Group (WSG) – originally a set of 15 electrical substitution radiometers, which differ from each other in their specific designs (Fröhlich, 1977). An example of this type of instruments is described in (Brusa and Fröhlich, 1986). This standard group is held at the Physikalisch-Meteorologisches Observatorium Davos / World Radiation Center (PMOD/WRC) in Davos (Switzerland), by appointment of the World Meteorological Organisation (WMO).

The Bundesamt fuer Metrologie (METAS) is the National Measurement Institute of Switzerland. In 2004, METAS designated the PMOD/WRC as a member of the International Committee for Weights and Measures (CIPM) Mutual Recognition Arrangement (MRA), and in July 2008, the quantity "Solar Irradiance" was formally accepted by the Consultative Committee on Photometry and Radiometry (CCPR). Therewith the World Radiometric Reference (WRR) was accepted as the reference scale for Solar Irradiance measurements within the SI system.

METAS designated the Physikalisch-Meteorologisches Institut Davos / World Radiation Center (PMOD/WRC) for maintaining the primary standard for Solar Irradiance. Currently, PMOD/WRC is the only institute with Calibration and Measurement Capability (CMC) for Solar Irradiance. Every five years, an International Pyrheliometer Comparison (IPC) is held at Davos, Switzerland[1] to disseminate the reference scale and to validate its stability by comparison to a large group of approximately fifty external instruments. Figure 1 shows several instruments mounted on a solar tracker for the purpose of such a comparison.

[1] The choice of Davos as a location is due to historical - rather than scientific - reasons.

**Figure 1 Radiometers of the World Standard Group on a solar tracker, together with other Solar Irradiance instruments (picture courtesy of PMOD/WRC, Davos)**

There is no denying the historical importance and success of the current standard for Solar Irradiance (TSI); however, various problems are now becoming apparent.

One of the most obvious problems of the World Standard Group (WSG) is that the instruments are reaching the end of their useful lifetime, and are eventually failing. The most recent example of instrument failure is the case of two of the WSG instruments failing the stability tests during the IPC-XI in 2010[2]. Originally, the WSG consisted of fifteen instruments; however, the current WSG is reduced to only five pyrheliometers (with four being founding members). Considering that the 'CIMO guide' (WMO, 2006) requires the WSG to be populated by at least three absolute cavity radiometers of different

[2] Personal communication with Wolfgang Finsterle (Head of Solar Irradiance, PMOD/WRC)

make, action is required in the near future to ensure the continuity of the WRR.

Another problem of the WSG is the possibility of a long-term deterioration that is common to all instruments of the WSG. In the absence of an absolute standard, such changes in instrument performance could go undetected, and recent experience suggests that such concerns are valid. As Finsterle et al. report, "between the year 2000 and 2005 the sensitivity of one WSG instrument (PMO2) seemingly drifted with respect to the others by roughly +0.015% per year. It was only during the 10th International Pyrheliometer Comparisons (IPC-X / 2005) when it became apparent that PMO2 agreed well with 58 national and regional standard pyrheliometers and that instead the remaining WSG instruments appeared to have suffered from an annual drift of -0.015%" (WMO, 2010).

It is necessary to secure the future of ground-based TSI measurements; Finsterle et al. (WMO, 2010) outline three possible scenarios. The first scenario is the most conservative one; the World Standard Group (WSG) would continue to provide the WRR in the future and would be re-populated with newer instruments. Currently, two radiometers loaned from a Chinese manufacturer (SIAR-2a and SIAR-2b) are undergoing long-term stability tests at the WRC. However, this first scenario of repopulating the World Standard Group has not been pursued very vigorously since no other manufacturer of Solar Irradiance radiometers was prepared to lend instruments for long-term testing and no instruments were purchased by PMOD/WRC.

The second scenario as suggested by Finsterle et al. is that the World Standard Group (WSG) provides the World Radiometric Reference (WRR) only during the five years between consecutive International Pyrheliometer Comparisons (IPCs). During the IPCs all regional and national standard pyrheliometers with a sufficiently long history of IPC participation would form an "IPC standard group".

The third scenario is to abandon the concept of an artefact-based primary standard for Solar Irradiance in favour of a new primary standard with a clear link to the rest of the International System of Units (SI), such as the instrument which is the subject of this thesis - the Cryogenic Solar Absolute Radiometer. This third scenario would be most in line with the recent development towards harmonisation of measurements in meteorology and metrology.

## 1.3 Satellite measurements of Solar Irradiance

The main focus of this thesis is on the ground-based measurement of Solar Irradiance; however, the radiometer described here was also developed for space-based measurements and some of the design features only make sense in the context of space-use. Therefore, some of the aspects related to satellite measurements are presented in the following.

In addition to the determination of Solar Irradiance at the Earth's surface, it is also necessary to make measurements at the top of the atmosphere. For example, it was only with the beginning of satellite-based measurements that the 11-yearly variations in Solar Irradiance could be detected. Before, these variations were hidden in the signal noise due to atmospheric variations. Any long-term change in solar output, which may significantly affect temperatures on Earth,

can only be detected reliably in the absence of atmospheric effects. Also, Solar Irradiance at the top of the atmosphere is one of the most important input parameters of climate models.

The current consensus view regarding the requirements for top-of-atmosphere Total Solar Irradiance is presented in a report by the National Oceanic and Atmospheric Administration, NOAA (Ohring, 2007). The requirement is to (1) either have uncertainties of <0.01% in accuracy or to (2) have uncertainties of <0.001% / year in long-term repeatability and continual, overlapping measurements.

Currently, the same technology that is used for ground-based TSI measurements is employed for satellite-based TSI measurements. However, although instrument makers quote substantially lower uncertainties for the space-based versions of their TSI instruments, it is clear from the historical data record that at least some of these quoted uncertainties significantly underestimated the true uncertainties.

Figure 2 illustrates the spread in the different satellite-based measurements that were made during the last three decades. Calculating the standard deviation of these data is not strictly meaningful, but it is an appropriate measure to gain a rough idea of the spread in the dataset; it is of the order of 0.24% (0.18%, if the less accurate ERB and ERBE data are ignored), which gives strong reasons to doubt the accuracy claims of typically 0.1% (k=1). Comparing this large spread in the data record to the requirements for climate science indicates that the data are not accurate enough.

**Figure 2 Satellite-based TSI record of the last three decades. Plot reproduced from (Kopp and Lean, 2011).**

The satellite data record of TSI is, for the above-mentioned reasons, not sufficiently accurate in absolute terms. But it is also controversial whether these data can be used to establish a 'relative' TSI record, which would not be accurate in absolute terms, but would give a precise representation of the relative changes in TSI over time. Detecting such changes is of particular interest for the study of Climate Change. To this end, the offsets between the different data sets are removed and the data are joined together to form a so-called 'TSI-composite'. Three different TSI composites have so far been produced by different teams of scientists (for a comparison of the composites, see Figure 3). The first of these composites is the 'PMOD-composite'. It was presented at the IAU General Assembly in Kyoto by Fröhlich and Lean and documented in (Fröhlich and Lean, 1998) and updated in a series of subsequent publications (Fröhlich, 2000, Fröhlich, 2003, Fröhlich, 2006). The second TSI composite that has received much attention is the 'ACRIM composite' (Willson, 1997, Willson and

Mordvinov, 2003). A third composite was added in 2004 (Dewitte et al., 2004) and is called the 'IRMB composite'.

**Figure 3 Differences between monthly mean reported and modeled irradiance variations for TIM/SORCE and three irradiance composites [PMOD, ACRIM, RMIB]. Plot reproduced from (Kopp and Lean, 2011)**

These composites vary quite considerably and give rise to significantly differing answers to the question of how much influence the Sun had on a rise in global temperatures over the last 30 years. While some researchers are of the opinion that the Sun's output has not changed significantly (Lockwood and Fröhlich, 2007, Lockwood and Fröhlich, 2008), others assert that according to the TSI record, it could have changed by 0.047% per decade (Willson and Mordvinov, 2003).

While these different results for the various TSI composites give an indication of the uncertainties involved, the scientific discussion suffers at times from a lack of uncertainty analysis. Dewitte et al. were the first to give an assessment of the associated uncertainties together with their new 'IRMB composite' (Dewitte et al., 2004). The most

careful evaluation of the problems associated with overlapping different TSI datasets was carried out by DeToma and White (DeToma and White, 2006); DeToma and White underline "the difficulty of combining observations from different instruments to create an accurate composite TSI record over several solar cycles".

## 1.4 Requirements for establishing a long-term measurement record

There is a striking resemblance between the approach to long-term records that was taken by National Measurement Institutes (NMIs) over the last century and the approach the space science community has taken in the last few decades. The NMIs started out with the understandable, but rather naïve belief that long-term stability (extending over decades and centuries) is possible without paying sufficient attention to absolute accuracy. The same notion prevailed in the space science community at least until very recently.

Over time, NMIs have learnt the lesson that absolute measurements are preferable - most markedly with the standard of voltage. This standard was based on artefacts (Weston cells) and was found to suffer from long-term drifts when a new standard based on fundamental physical principles (Josephson effect) was established (Melchert, 1978, Cohen and Taylor, 1973). NMIs therefore now seek to establish all SI base units with respect to fundamental constants, i.e. on the basis of a thorough understanding of the underlying physical principles. The kilogram is the only base unit that is still defined with respect to an artefact - with all the associated problems, see e.g. (Milton et al., 2007).

This problem has now increasingly been recognised by the space science community (although it has to be said that not all science teams subscribe to the idea that SI traceability or absolute accuracy is necessary for the establishment of a long-term record). For example, after presenting a risk analysis concerning the possible discontinuity of climate records, the NOAA report comes to the conclusion that "the risk of relying on data continuity for a climate data record expected to last centuries is high. Mitigating this risk requires a greater emphasis on absolute accuracy" (Ohring, 2007). This view can already be found in a publication by the then directors of the International Bureau of Weights and Measures (BIPM) and the PMOD/WRC more than one decade ago (Quinn and Fröhlich, 1999). In their article, Quinn and Fröhlich criticize that "although national metrology institutes now have absolute radiometers using new technology with accuracies below 0.01%, they have not been used for these important [Total Solar Irradiance] measurements" (Quinn and Fröhlich, 1999). The "new technology" Quinn and Fröhlich are referring to is cryogenic radiometry.

## 1.5 Cryogenic Radiometry

The principle of cryogenic radiometry was first suggested by Ginnings and Reilly (Ginnings and Reilly, 1972) and was first successfully implemented by Quinn and Martin (Quinn and Martin, 1985), in an attempt to evaluate the Stefan-Boltzmann constant with optical methods. The Quinn and Martin radiometer measured total radiation of black bodies from 233 K to 373 K, whereas an adapted instrument was able to measure the radiant power of a stabilised laser beam (Martin et al., 1985). In an attempt to minimise the size and weight,

Fox et al. modified the instrument for the use with a mechanical cooler (Fox et al., 1996).

Cooling electrical substitution radiometers to cryogenic temperatures led to an improvement in absolute uncertainty levels by more than a factor of fifty (Quinn and Martin, 1985) as compared to room-temperature radiometers. As Fox and Rice point out in their review (Fox and Rice, 2005), there are four main reasons for the superior performance of cryogenic radiometers.

The first major advantage of cooling to cryogenic temperatures is that it allows the use of relatively large cavities with high absorptivity; this is due to the massive reduction in the specific heat capacity of the cavity material. Secondly, the level of background radiation is severely reduced. Thirdly, the heat flow path is better defined because there is no convection (due to the vacuum) and negligible heat exchange through radiation. And lastly, superconducting materials can be used in order to avoid Joule heating in the electrical leads.

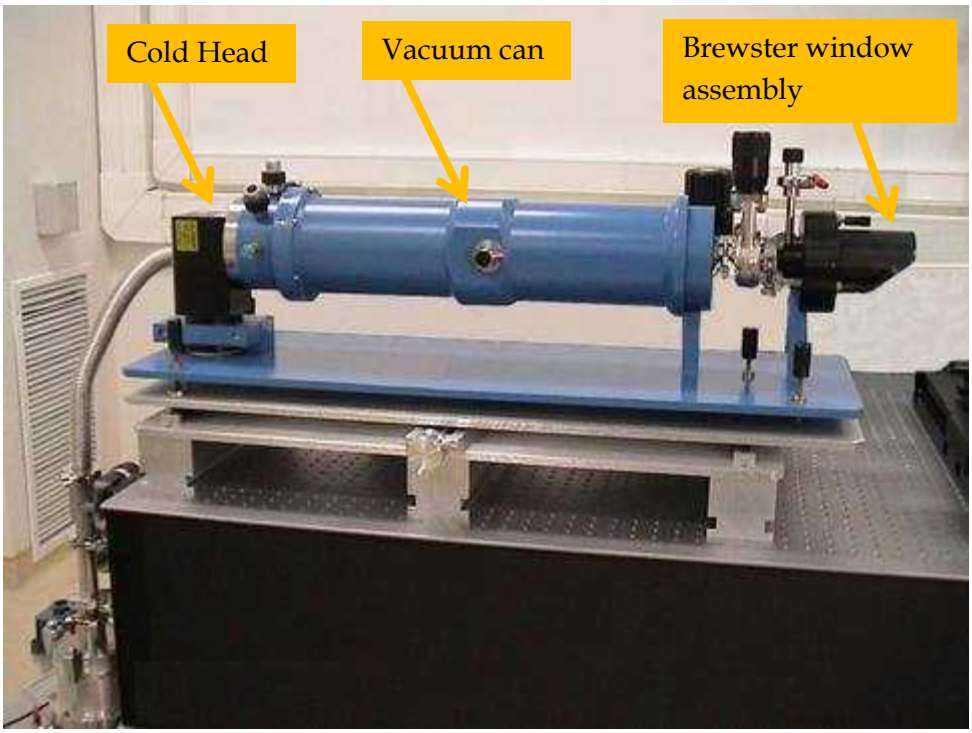


**Figure 4 NPL Cryogenic Radiometer, primary standard, mechanically cooled**

The ground-based application of cryogenic radiometry to the measurement of Solar Irradiance has so far been mainly hindered by the relatively high cost and the fact that a standard is already in existence. Now, since the weaknesses of the current standard are becoming apparent, alternatives such as a cryogenic radiometer are seriously considered.

The use of a cryogenic radiometer to measure Total Solar Irradiance (TSI) from the top of the atmosphere was suggested soon after the first cryogenic radiometer had been built and its potential advantages have been pointed out repeatedly since then (Foukal et al., 1990, Quinn and Fröhlich, 1999, Martin and Fox, 1994 , Fox et al., 2011); however, none has been built so far that fulfils the accuracy requirements or that is suitable for long-term space-flight. This was mainly due to the lack of appropriate space coolers until recently.

In order to find reasons for the systematic offsets of Solar Irradiance measurements in space, a workshop was sponsored by NASA and held at NIST (Butler et al., 2008); all current TSI teams were present. The meeting did not arrive at a conclusive answer, but two possible solutions for the problem of pre-flight calibration were recommended – both of which involved the use of cryogenic radiometry. The first recommendation is to compare the space instruments against a cryogenic TSI radiometer on a mountain-top; this is seen as the scientifically preferred, but more challenging option. The second – easier, but less ideal – solution concerns a lab-based intercomparison of the TSI instruments; a continuation and improvement of the comparison method originally conceived by NPL and PMOD/WRC was recently developed at the University of Colorado (Kopp et al., 2007); the experiment is called "Total Solar Irradiance Facility (TRF)". A discussion of the most important results of the TRF, and how these results relate to the CSAR results, is given in Chapter 5.

## 1.6 Cryogenic Solar Absolute Radiometer

The aim of this PhD project was to exploit cryogenic radiometry for making direct measurements of Solar Irradiance, and thereby firmly linking the measurement of Solar Irradiance to the rest of the International System of Units (SI). To this end, an instrument was designed, built and tested – the Cryogenic Solar Absolute Radiometer (CSAR).

Since there is an immediate and urgent need (and therefore available funding) regarding the World Radiometric Reference, the main focus of the CSAR development was on the ground-based application. However, requirements regarding space flight have also

been considered in the design. The uncertainty aim for the space application was 0.01% (one standard uncertainty), and for the ground application 0.03% (one standard uncertainty)[3]. While the uncertainty aim for the space application was purely driven by scientific requirements, the uncertainty aim for the ground application was limited by practical considerations – in particular the achievable uncertainty in the window transmission measurement.

I also recognise that during the time it took to develop CSAR, science teams have taken significant steps towards greater SI traceability of their instruments, as well as the linkage to the World Radiometric Reference. I will give an account of these efforts in Chapter 5. I was involved in some of these efforts, especially in the context of PREMOS / PICARD, which is the latest space experiment to launch Solar Irradiance radiometers.

[3] All uncertainties in this thesis are quoted at the one standard uncertainty level, unless stated otherwise.

# Chapter 2 Theory and Functional Requirements

## 2.1 Overview

The overall aim of this chapter is to translate the science goal formulated in the previous chapter into requirements at the functional level. The science goal is to exploit cryogenic radiometry for making direct measurements of Solar Irradiance, and thereby firmly linking the measurement of Solar Irradiance to the International System of Units (SI). The accuracy aim for ground-based Solar Irradiance is 0.03% (one standard uncertainty), and the accuracy aim for Total Solar Irradiance at the top of the atmosphere is 0.01% (one standard uncertainty).

Section 2.2 gives a definition of the terms that are commonly used in relation with Solar Irradiance measurements. In particular a definition of "Direct Solar Radiation (DSR)" - the ground based Solar Irradiance - is presented. The definition of Total Solar Irradiance (TSI) - the Solar Irradiance at the Top of the Atmosphere - is also given. Furthermore, the use of the term "Solar Irradiance" in this thesis is explained.

Section 2.3 gives an overview over the functional elements of a cryogenic radiometer.

Section 2.4 identifies the input quantities and gives an explicit statement of the measurement equation. Identifying the input quantities implies the identification of the major sources of uncertainty which will contribute to the overall uncertainty budget. This section further explains what methodology will be followed in this thesis to evaluate measurement uncertainty; the uncertainty analysis in this

thesis is based on the Guide to the Expression of Uncertainty in Measurement (GUM). The section closes with a discussion of how small an individual uncertainty contribution needs to be in order to be considered "negligible" (space: relative uncertainty < 0.001%, ground: relative uncertainty < 0.004%); this information is essential in the design phase.

Section 2.5 deals with the detector system. It begins with a statement of general requirements of a cryogenic radiometer – as formulated by Quinn and Martin, who developed the first highly accurate cryogenic radiometer. The section then identifies requirements that are specific to CSAR; the analysis reveals that the overall detector absorptivity needs to be > 99.997% in space and > 99.986% on the ground. The requirements regarding the spectral characteristics of the detector absorptivity are also discussed – given the spectral distribution of the Solar Irradiance. Furthermore, a requirement for a time constant < 10 sec is identified based on considerations regarding the rate of change of Solar Irradiance over a measurement day and the necessary length of the measurement period in order to reduce the measurement noise. Finally the dynamic range is determined as [800 W $m^{-2}$ (minimum value); 1100 W $m^{-2}$ (maximum value)] for the ground, and [1300 W $m^{-2}$ (minimum value); 1420 W $m^{-2}$ (maximum value)] for space. Reasons are also given for why CSAR should be able to measure radiant power < 0.01 W.

Section 2.6 discusses the requirements regarding the aperture geometry and the stray light rejection. At the beginning of the section, the official recommendations of the World Meteorological Organisation (WMO) regarding the aperture geometry are presented. However, an analysis of the currently existing radiometers shows that

almost none of the current radiometers comply with the official recommendations. There are also compelling scientific reasons for not following the official recommendations; they are therefore not considered as binding for the design of CSAR. The section finishes with the requirements regarding stray light rejection (< 0.004%).

Section 2.7 discusses the functional requirements regarding the vacuum window. Besides a high transmittance in the solar spectrum, it is also important that the window is suitable for outdoor use.

Section 2.8 discusses the cooling power restrictions when using a space cooler. The Astrium 10 K cooler serves as an example.

Section 2.9 discusses the requirements regarding the mass of the detector, the mechanical structure and the size of the detector. The majority of these requirements are dominated by the space application.

Section 2.10 gives a summary table of the functional requirements discussed in this chapter.

## 2.2 Definition of terms

Before going into the detail of the functional requirements, it is beneficial to state the definition of the physical quantity that is to be measured by the instrument. It is important to note that the name as well as the definition for the quantity is slightly different for measurements on the ground and in space. In space, the physical quantity is called “Total Solar Irradiance”, whereas on the ground it is “Direct Solar Radiation”. The difference is due to the absence or presence of the atmosphere, as will become clear from the definitions reproduced below.

Total Solar Irradiance (TSI) is defined as:

> *The amount of solar radiation received outside the Earth's atmosphere on a surface normal to the incident radiation, and at the Earth's mean distance from the Sun (IPCC, 2007).*

For the equivalent terrestrial measurand (Direct Solar Radiation), the aim is in principle also to measure the amount of solar radiation received on a surface normal to the incident radiation. However, the measurements are not corrected for the distance between the Earth and the Sun and there is a slight complication due to the optical scattering of some of the solar radiation in the atmosphere. Ideally, the measurement of Direct Solar Radiation would only include radiation that is in direct line of sight of the "solar disk", but this is not practical. For this reason, Direct Solar Radiation is defined to include sky radiation originating from a small annulus around the solar disc:

> *Direct solar radiation is measured by means of pyrheliometers, the receiving surfaces of which are arranged to be normal to the solar direction. By means of apertures, only the radiation from the sun and a narrow annulus of sky is measured, the latter radiation component is sometimes referred to as circumsolar radiation or aureole radiation (WMO, 2008).*

In this thesis, the term "Solar Irradiance" is used as a general term – not distinguishing between ground measurements and satellite-based measurements.

However, from a practical point of view, it should also be noted that the terms as defined above are not used very consistently in the published literature. For example, the term "Total Solar Irradiance" is often used in both contexts, the measurements from the top of the atmosphere as well as the measurements on the ground. Nevertheless,

for the sake of clarity, the text in this thesis will follow the definitions given above.

## 2.3 Functional elements of a cryogenic radiometer – overview

As already mentioned in the introductory chapter, the aim of the work described here is to employ the principle of cryogenic radiometry for the purpose of measuring Direct Solar Radiation and Total Solar Irradiance. Therefore, the starting point of this design is cryogenic radiometry.

Figure 5 shows the typical elements of a cryogenic radiometer. It consists of a detector system, some optical elements to define a certain solid angle or irradiated area, and a cooling mechanism with cold-shields attached to minimise radiative heat transfer between the different temperature stages. All these components are encased in a vacuum tank, which has a window in front to allow optical radiation to enter the vacuum tank.

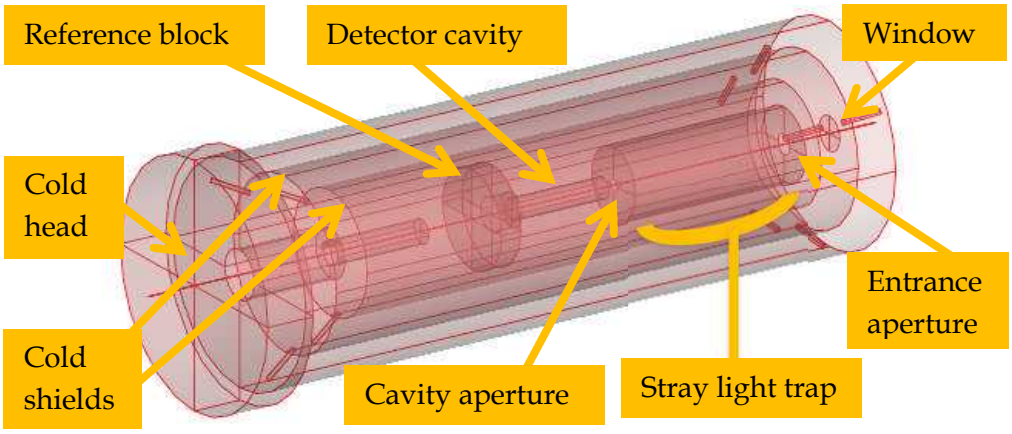


**Figure 5 Schematic of a typical cryogenic radiometer. This schematic only shows one channel, whereas the final system has several DSR/TSI channels.**

In the following, the principles of cryogenic radiometry will be described in greater detail, and the specific requirements of measuring

Direct Solar Radiation and Total Solar Irradiance will be explored in this context. The attempt is made in this chapter to establish the historical context and to indicate where the work presented here goes beyond previous work. Since the fundamentals of cryogenic radiometry have been explored quite comprehensively by Quinn and Martin, reference is made occasionally to their original work (Quinn and Martin, 1985).

## 2.4 Measurement equation and uncertainties

From a technological point of view, cryogenic radiometry is the underlying principle applied in this thesis; however, more fundamental than that is the treatment of uncertainties, especially since a low uncertainty in the measurement of Solar Irradiance is the primary aim of the CSAR development.

As far as the treatment of uncertainties is concerned, this thesis follows the recommendations given in the "Guide to the expression of uncertainty in measurement (GUM)" (JCGM, 2008). This section presents the relevant parts of the GUM and discusses them in the context of the CSAR measurement situation[4].

### 2.4.1 Modelling the measurement – general introduction

According to the GUM, "the objective of a measurement is to determine the value of the measurand, that is, the value of the particular quantity to be measured. In addition, the GUM observes that "in most cases, a measurand $Y$ (the output quantity) is not measured directly, but is determined from $N$ other input quantities $X_1$, $X_2$, …, $X_N$ through a functional relationship $f$:

$$Y = f\left(X_1, X_2, ..., X_N\right) \qquad (2.1)"$$

[4] All quotations in this section are from the GUM, if no other reference is made.

This functional relationship between the measurand and the input quantities can sometimes also be referred to as the "measurement equation".

The GUM implicitly assumes that in many measurement situations, the exact values of the input quantities $X_1$, $X_2$, …, $X_N$ cannot be known, and therefore the exact value of the measurand can also not be known. However, the GUM states that "an estimate of the measurand $Y$, denoted by $y$, is obtained from [Equation (2.1)] using *input estimates* $x_1$, $x_2$, …, $x_N$ for the values of the N quantities $X_1$, $X_2$, …, $X_N$. Thus the *output estimate* $y$, which is the result of the measurement, is given by

$$y = f\left(x_1, x_2, ..., x_N\right) \tag{2.2}$$

According to the GUM, these estimates are only complete when accompanied with a statement of the associated uncertainties of these estimates. Therefore, each of the input estimates as well as the output estimate have uncertainty values associated with them. The GUM distinguishes between the uncertainty associated with input quantities and the uncertainty associated with the output quantity and gives the following definitions: "the estimated standard deviation associated with the output estimate or measurement result $y$, termed *combined standard uncertainty* and denoted by $u_c(y)$, is determined from the estimated standard deviation associated with each input estimate $x_i$, termed *standard uncertainty* and denoted by $u(x_i)$."

The term *standard uncertainty* can be further differentiated into

(1) *Type A standard uncertainty,* and

(2) *Type B standard uncertainty*.

This differentiation is made according to the way the standard uncertainty is derived: "a Type A standard uncertainty is obtained from a probability density function derived from an observed frequency distribution, while a Type B standard uncertainty is obtained from an assumed probability density function based on the degree of belief that an event will occur [often called 'subjective probability']."

### 2.4.2 Type A evaluation of standard uncertainty

The GUM states: "In most cases, the best available estimate of the expectation or expected value $\mu_q$ of a quantity $q$ that varies randomly […], and for which $n$ independent observations $q_k$ have been obtained under the same conditions of measurement […], is the arithmetic mean or average of the $n$ observations:

$$\overline{q} = \frac{1}{n}\sum_{k=1}^{n} q_k \qquad (2.3)$$

Thus, for an input quantity $X_i$ estimated from n independent repeated observations $X_{i,k}$, the arithmetic mean $\overline{X}_i$ obtained from [Equation (2.3)] is used as the input estimate $x_i$ in [Equation (2.2)] to determine the measurement result $y$; that is, $x_i = \overline{X}_i$. […]

The individual observations $q_k$ differ in value $\overline{q}$ because of random variations in the influence quantities, of random effects […]. The experimental variance of the observations, which estimates the variance $\sigma^2$ of the probability distribution of $q$, is given by

$$s^2(q_k) = \frac{1}{n-1}\sum_{j=1}^{n}\left(q_j - \overline{q}\right)^2 \qquad (2.4)$$

This estimate of variance and its positive square root $s(q_k)$, termed the experimental standard deviation […], characterize the variability of the observed values $q_k$, or more specifically, their dispersion about their mean $\bar{q}$.

The best estimate of $\sigma^2(\bar{q}) = \sigma^2 / n$, the variance of the mean, is given by

$$s^2(\bar{q}) = \frac{s^2(q_k)}{n} \tag{2.5}$$

The experimental variance of the mean $s^2(\bar{q})$ and the experimental standard deviation of the mean $s(\bar{q})$ […], equal to the positive square root of $s^2(\bar{q})$, quantify how well $\bar{q}$ estimates the expectation $\mu_q$ of $q$, and either may be used as a measure of the uncertainty of $\bar{q}$.

Thus, for an input quantity $X_i$ determined from n independent repeated observations $X_{i,k}$, the standard uncertainty $u(x_i)$ of its estimate $x_i = \bar{X}_i$ is $u(x_i) = s(\bar{X}_i)$, with $s^2(\bar{X}_i)$ calculated according to Equation (2.5). For convenience, $u^2(x_i) = s^2(\bar{X}_i)$ and $u(x_i) = s(\bar{X}_i)$ are sometimes called a *Type A variance* and a *Type A standard uncertainty*, respectively"(JCGM, 2008).

Figure 6a shows an ideal random distribution with the expected value $\mu$ and standard deviation $\sigma$. Figure 6b shows a possible experimental result with the estimate $\bar{t}$, the experimental standard deviation $s(t_k)$, and the experimental standard deviation of the mean $s(\bar{t})$.

**Figure 6 Graphical illustration of evaluating the standard uncertainty of an input quantity from repeated observations[5].**

### 2.4.3 Type B evaluation of standard uncertainty

"For an estimate $x_i$ of an input quantity $X_i$ that has not been obtained from repeated observations, the associated estimated variance $u^2(x_i)$ or the standard uncertainty $u(x_i)$ is evaluated by scientific judgement based on all of the available information on the possible variability of $X_i$. The pool of information may include

[5] The graph is reproduced from the GUM.

- Previous measurement data;
- Experience with or general knowledge of the behaviour and properties of relevant materials and instruments;
- Manufacturer's specifications;
- Data provided in calibration and other certificates;
- Uncertainties assigned to reference data taken from handbooks.

For convenience, $u^2(x_i)$ and $u(x_i)$ evaluated in this way are sometimes called a *Type B variance* or a *Type B standard uncertainty*, respectively" (JCGM, 2008).

Figure 7 illustrates an example of assigning an a priori probability density distribution. In this case, the assumption is made that all measurement values are limited to the interval $[\mu - a, \mu + a]$, and that all values within this interval are equally likely to occur. Such a probability distribution is also referred to as a 'rectangular probability distribution'. The standard uncertainty of the estimate $\mu$ is

$$u(\mu) = \frac{a}{\sqrt{3}} \tag{2.6}$$

**Figure 7 Graphical illustration of evaluating the standard uncertainty of an input quantity from an *a priori* distribution[6].**

### 2.4.4 Combined standard uncertainty

After the evaluation of the standard uncertainties of the input quantities, these uncertainties need to be combined in an appropriate manner in order to arrive at the standard uncertainty of the output quantity $y$. Furthermore, according to the GUM, in the case where all input quantities are independent (i.e. uncorrelated), the combined standard uncertainty $u_c(y)$ is the positive square root of the combined variance $u_c^2(y)$, which is given by

$$u_c^2(y) = \sum_{i=1}^{N} \left( \frac{\partial f}{\partial x_i} \right)^2 u^2(x_i) \qquad (2.7)$$

where $y$ is the estimate of measurand $Y$, and $x_1, x_2, ..., x_N$ are the input estimates.

In the case of uncorrelated input quantities, the combined standard uncertainty $u_c(y)$ is therefore

[6] Reproduced from the GUM

$$u_c(y) = \sqrt{\sum_{i=1}^{N} \left( \frac{\partial f}{\partial x_i} \right)^2 u^2(x_i)} \tag{2.8}$$

In the case of correlated input quantities, the combined standard uncertainty is evaluated in the following manner:

$$u_c(y) = \sqrt{\sum_{i=1}^{N} \left( \frac{\partial f}{\partial x_i} \right)^2 u^2(x_i) + 2\sum_{i=1}^{N-1} \sum_{j=i+1}^{N} \frac{\partial f}{\partial x_i} \frac{\partial f}{\partial x_j} u(x_i) u(x_j) r(x_i, x_j)} \tag{2.9}$$

where the correlation coefficient $r(x_i, x_j)$ characterizes the degree of correlation between the input quantities $x_i$ and $x_j$.

### 2.4.5 CSAR measurement equation

Irrespective of whether the measurement is performed on the ground or in space, the physical quantity that is to be determined is irradiance $I$, or power $P$ per area $A$:

$$I = \frac{P}{A} \tag{2.10}$$

In our case, $P$ is the solar spectral power integrated over all wavelengths and $A$ is the area on which this power is incident. Equation (2.10) is also the simplest statement of the measurement equation possible, if $I = I_{SI}$ (where $I_{SI}$ stands for Solar Irradiance). This simple relation assumes a perfect radiometer. If, however, the detector is not perfect, the measurement equation must reflect the potential short-comings of the instrument. These short-comings are due to practical limitations, which in turn arise from the use of imperfect functional elements.

A more complete mathematical model for the determination of Solar Irradiance $I_{SI}$ is given by the following set of two equations:

$$P_{measured} = A\int_0^\infty \tau(\lambda) F_{diff}(\lambda) \alpha(\lambda) I_{SSI}(\lambda) d\lambda \qquad (2.11)$$

$$I_{SI} = \int_0^\infty I_{SSI}(\lambda) d\lambda \qquad (2.12)$$

where

$P_{measured}$ is the optical power measured by the detector.

$F_{diff}(\lambda)$ is the spectral correction for diffraction at the first aperture,

$A$ is the detector area irradiated by the solar radiation,

$\tau(\lambda)$ is the spectral window transmittance,

$\alpha(\lambda)$ is the spectral cavity absorptivity

$I_{SSI}(\lambda)$ is the Solar Spectral Irradiance, and

$I_{SI}$ is the measurand, Solar Irradiance.

Note that Equation (2.11) is an implicit statement with respect to the solar spectral irradiance $I_{SSI}(\lambda)$, which – in theory – needs to be determined before determining the measurand $I_{SI}$. Equation (2.11) can in principle be solved numerically for $I_{SSI}(\lambda)$, with $\lambda \in [0, \infty]$ - provided that further information about the spectral distribution of $I_{SSI}(\lambda)$ is available. Equation (2.11) also suggests that knowledge of the spectral distributions of the transmittance, the diffraction effect

and the cavity absorptivity is required. However, an explicit statement of the measurement equation can be developed, which does – at least conceptually – not require knowledge of spectral distributions of the input quantities.

Equation (2.11) can be expanded by using Equation (2.12):

$$P_{measured} = A \cdot \left( \int_0^\infty \tau(\lambda) F_{diff}(\lambda) \alpha(\lambda) I_{SSI}(\lambda) d\lambda \right) \cdot \frac{I_{SI}}{\int_0^\infty I_{SSI}(\lambda) d\lambda}$$

(2.13)

Equation (2.13) can be further expanded:

$$P_{measured} = A \cdot \frac{\int_0^\infty \tau(\lambda) F_{diff}(\lambda) \alpha(\lambda) I_{SSI}(\lambda) d\lambda}{\int_0^\infty F_{diff}(\lambda) \alpha(\lambda) I_{SSI}(\lambda) d\lambda} \cdot \frac{\int_0^\infty F_{diff}(\lambda) \alpha(\lambda) I_{SSI}(\lambda) d\lambda}{\int_0^\infty \alpha(\lambda) I_{SSI}(\lambda) d\lambda} \cdot \frac{\int_0^\infty \alpha(\lambda) I_{SSI}(\lambda) d\lambda}{\int_0^\infty I_{SSI}(\lambda) d\lambda} \cdot I_{SI}$$

(2.14)

For the purpose of illustration, Equation (2.14) is slightly re-ordered:

$$\frac{P_{measured}}{A} = \frac{\int_0^\infty \tau(\lambda) F_{diff}(\lambda) \alpha(\lambda) I_{SSI}(\lambda) d\lambda}{\int_0^\infty F_{diff}(\lambda) \alpha(\lambda) I_{SSI}(\lambda) d\lambda} \cdot \frac{\int_0^\infty F_{diff}(\lambda) \alpha(\lambda) I_{SSI}(\lambda) d\lambda}{\int_0^\infty \alpha(\lambda) I_{SSI}(\lambda) d\lambda} \cdot \frac{\int_0^\infty \alpha(\lambda) I_{SSI}(\lambda) d\lambda}{\int_0^\infty I_{SSI}(\lambda) d\lambda} \cdot I_{SI}$$

(2.15)

The first three terms on the right-hand side of Equation (2.15) represent the three spectrally dependent components of the radiometer: (1) the window transmittance, (2) the diffraction effect, and (3) the cavity absorptivity. The significance of Equation (2.15) is that it is in principle conceivable to make a series of ratio

measurements involving the spectrally integrated Spectral Solar Irradiance in order to evaluate all spectrally dependent input parameters (window transmittance, diffraction effect, and cavity absorptivity), without necessarily having to have knowledge about the spectral distribution of these input quantities. In how far it is practical to evaluate these ratios by experiment is discussed in Sections 3.4.6 (diffraction effect), 3.5.3.7 (cavity absorptivity), and 3.6.3 (window transmittance).

If the first three fractions on the right-hand side of Equation (2.15) are termed *integrated window transmittance* $\tau$ *, integrated diffraction effect* $F_{diff}$ *, and integrated cavity absorptivity* $\alpha$ *, respectively*, Equation (2.15) can be written as

$$\frac{P_{measured}}{A} = \tau \cdot F_{diff} \cdot \alpha \cdot I_{SI} \tag{2.16}$$

Rearranging Equation (2.16) leads to an explicit statement of the measurement equation:

$$I_{SI} = \frac{1}{\tau F_{diff} \alpha} \frac{P_{measured}}{A} \tag{2.17}$$

where

$P_{measured}$ is the optical power measured by the detector,

$F_{diff}$ is the integrated diffraction effect at the first aperture,

$A$ is the detector area irradiated by the solar radiation,

$\tau$ is the integrated window transmittance,

$\alpha$ is the integrated cavity absorptivity, and

$I_{SI}$ is the measurand, Solar Irradiance

For the purposes of the further discussion in the present chapter, it may be noted that for the measurement of Direct Solar Radiation (DSR), there are five major input quantities of which knowledge needs to be acquired before the sought-after measurand can be estimated. These quantities are: (1) the aperture area[7] $A$, (2) the measured optical power[8] $P_{measured}$ which is determined by substituting the incoming optical power with electrical power, (3) the integrated window transmittance $\tau$, (4) the integrated cavity absorptivity $\alpha$, and (5) the integrated diffraction correction $F_{diff}$.

For the measurement of Total Solar Irradiance ($I_{TSI}$), the same set of equations apply, except that $\tau(\lambda) = \tau = 1$ for all wavelengths. The transmittance is equal to unity in the case of satellite-based TSI measurements because no window is needed in space, whereas a window is needed for the ground-based measurement of DSR in order to admit solar radiation into the vacuum-chamber that is surrounding the detector.

It is also worth noting that the calculation of the combined uncertainty is particularly straightforward in the case of CSAR (assuming that all input quantities are uncorrelated). It can be shown that if Equation (2.8) is applied in order to evaluate the combined uncertainty of the estimate for Solar Irradiance (see Equation (2.17)), the expression for the combined standard uncertainty can be simplified in the following manner:

[7] For further detail, see Section 2.6 and Section 3.4.
[8] For further detail, see Section 3.5.6 and Section 3.5.8.

$$u_c\left(i_{DSR}\right)=\sqrt{\sum_{i=1}^{N}\left(\frac{\partial i_{DSR}}{\partial x_i}\right)^2 u^2\left(x_i\right)}=i_{DSR}\sqrt{\sum_{i=1}^{N}\left(\frac{u\left(x_i\right)}{x_i}\right)^2} \tag{2.18}$$

which means that the relative combined standard uncertainty $u_c\left(i_{DSR}\right)/i_{DSR}$ can be determined by a straightforward combination of individual relative uncertainty components:

$$\frac{u_c\left(i_{DSR}\right)}{i_{DSR}}=\sqrt{\sum_{i=1}^{N}\left(\frac{u\left(x_i\right)}{x_i}\right)^2} \tag{2.19}$$

### 2.4.6 Uncertainties of CSAR input quantities

In order to define the functional requirements, it is necessary to know how large the uncertainties of the individual estimates of the input quantities can become, without violating the overall uncertainty aim.

If no further assumptions shall be made at the outset of the design considerations, it appears reasonable that all uncertainty contributions of the various input quantities should be allowed to be of equal size. The aim for the combined relative uncertainty of the TSI measurements is

$$\frac{u_c\left(i_{TSI}\right)}{i_{TSI}}\le 0.01\% \tag{2.20}$$

In combination with Equation (2.19), and the assumptions mentioned above, this means that the relative uncertainties of the major four input quantities of the TSI measurement should be smaller than or equal to 0.005%:

$$\frac{u\left(x_i\right)}{x_i}\le 0.005\%, \tag{2.21}$$

for $x_i \in \left\{ P_{measured}, A, \alpha, F_{diff} \right\}$.

The aim for the combined relative uncertainty of the DSR measurements is

$$\frac{u_c\left(i_{DSR}\right)}{i_{DSR}} \leq 0.03\% \tag{2.22}$$

This means that the overall uncertainty aim of the DSR measurements would be met if the uncertainties of the major five input quantities of the DSR measurement were smaller than or equal to 0.013%:

$$\frac{u\left(x_i\right)}{x_i} \leq 0.013\% \tag{2.23}$$

for $x_i \in \left\{ P_{measured}, A, \alpha, F_{diff}, \tau \right\}$.

Table 2 summarises the above mentioned targets for the individual uncertainty components. Of course, these targets do not constitute a strict requirement, but they give a good starting point as to the order of magnitude the design should be aiming for. It is also expected that some of the uncertainty components will need to be restricted further due to additional information not considered here, and that this will allow some other uncertainty components to exceed the values given in Table 2.

**Table 2 Projected uncertainty targets (standard uncertainties) for the major input quantities.**

| Input quantity | Uncertainty target DSR (ground) | Uncertainty target TSI (top of the atmosphere) | Additional permissible uncertainty component for DSR (when compared to TSI) |
|---|---|---|---|
| Optical power | ≤0.013% | ≤0.005% | ≤0.012% |
| Aperture area | ≤0.013% | ≤0.005% | ≤0.012% |
| Cavity reflectivity | ≤0.013% | ≤0.005% | ≤0.012% |
| Diffraction | ≤0.013% | ≤0.005% | ≤0.012% |
| Window transmittance | ≤0.013% | n/a | ≤0.013% |

### 2.4.7 The uncertainty level which can be considered "negligible" in the context of CSAR measurements

Another point to note is that beside these major contributors to the uncertainty budget, there will be a number of additional "minor" sources of uncertainty. For a meaningful discussion of uncertainties at the design stage, it is necessary to know how small an individual uncertainty contribution needs to be in order that it may be regarded as negligible.

With an instrument of CSAR's complexity, it is reasonable to assume that the number of these minor uncertainty contributions will be not significantly more than ten. Ideally, the impact of all of these on the overall uncertainty budget should be negligible. Please note that the calculations regarding the combined standard uncertainty in this section are based on Equation (2.19).

Figure 8 gives an idea of how the term "negligible" could be quantified in the context of Direct Solar Radiation. The graph shows the impact of ten minor uncertainty contributions on the overall uncertainty budget, when the combined standard uncertainty of the major uncertainty components is 0.03%. For example, the effect of adding ten individual uncertainty contributions, each of which is as large as 0.004%, increases an uncertainty budget of 0.03% by less than 0.003%. Since this constitutes an increase of less than 10% in the overall uncertainty budget, this increase could be considered "negligible".

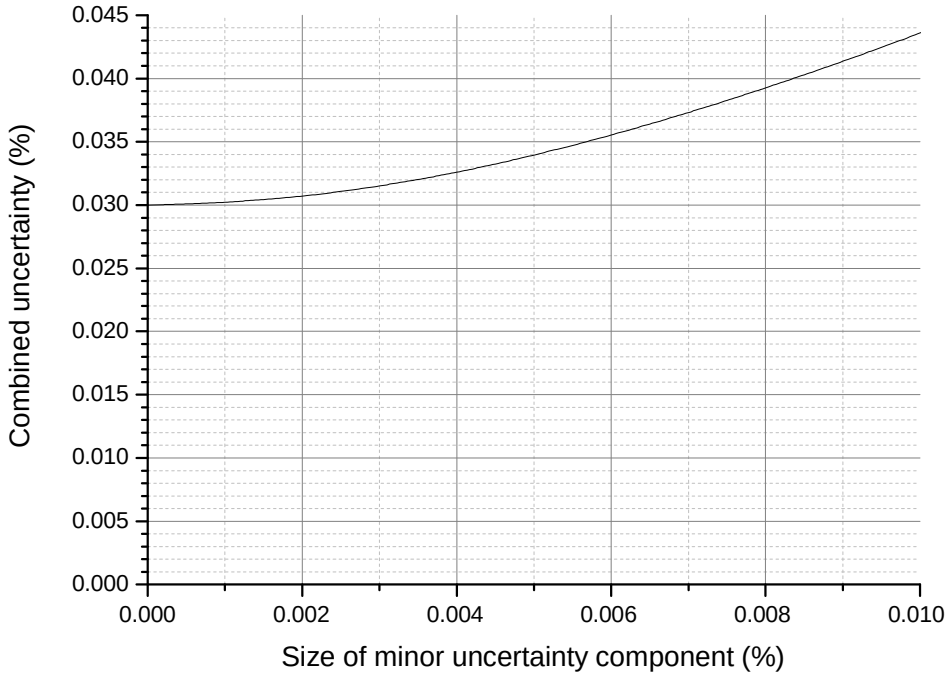


**Figure 8 Overall uncertainty, assuming a combined standard uncertainty of the major uncertainty contributors of 0.03% plus ten minor uncertainty components.**

Figure 9 shows the combined standard uncertainty, given an overall uncertainty of 0.03% of the major uncertainty contributions, and depending on the size of the individual minor uncertainty contributions (0.001% - 0.005%) and the number of minor contributions

(0 – 100). It shows that even for an unrealistically high number of 100 minor contributions of 0.004% each, the combined uncertainty would only increase to 0.05%, which is still significantly smaller than the uncertainty of the current standard – the World Radiometric Reference.

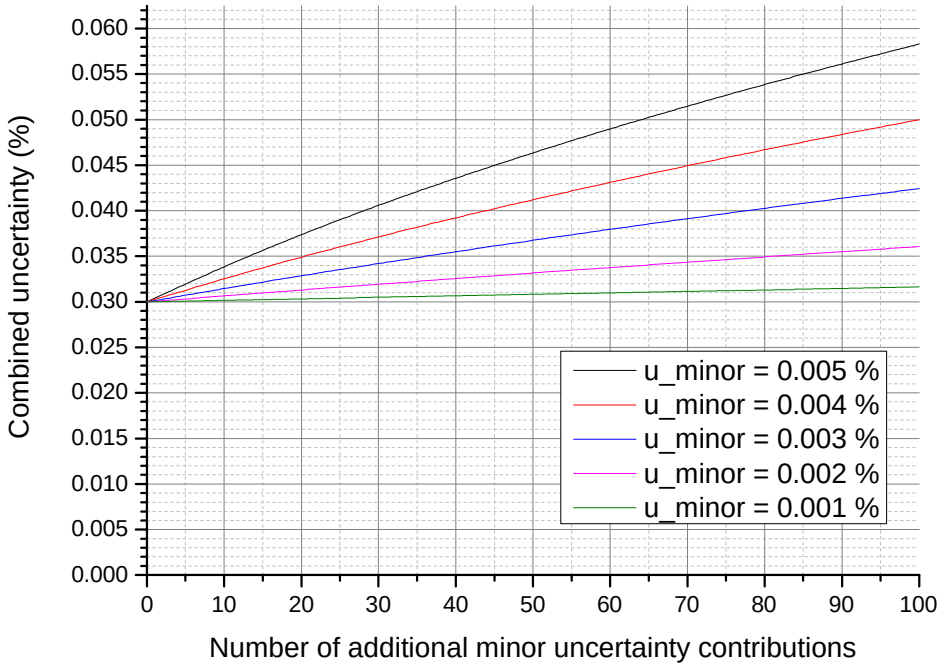


**Figure 9 Overall uncertainty, assuming a combined uncertainty of the major uncertainty contributors of 0.03% plus a variable number of minor uncertainty components.**

Figure 10 and Figure 11 show the equivalent graph for the TSI application. In a space context, ten additional contributions of 0.001% increase an existing uncertainty budget from 0.010% to less than 0.011% (see Figure 10).

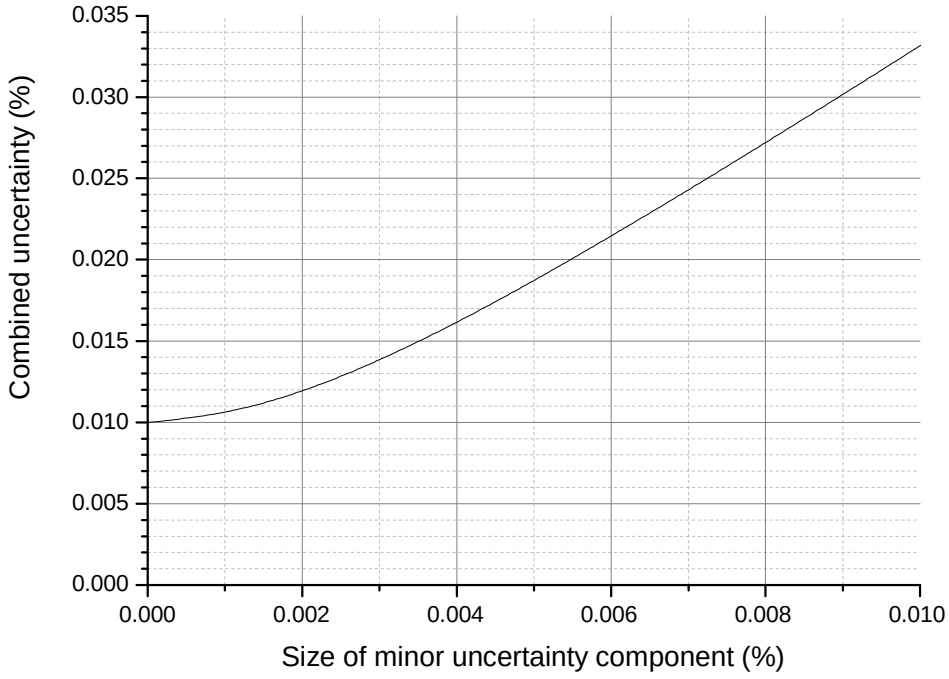


**Figure 10 Overall uncertainty, assuming a combined uncertainty of the major uncertainty contributors of 0.01% plus ten minor uncertainty components**

Figure 11 shows the combined uncertainty, given an overall uncertainty of 0.01% of the major uncertainty contributions, and depending on the size of the individual minor uncertainty contributions (0.001% - 0.005%) and the number of minor contributions (0 – 100). It shows that even for an unrealistically high number of 100 minor contributions of 0.001% each, the combined uncertainty would be < 0.015%, which is significantly lower than the uncertainty of any other TSI space radiometer.

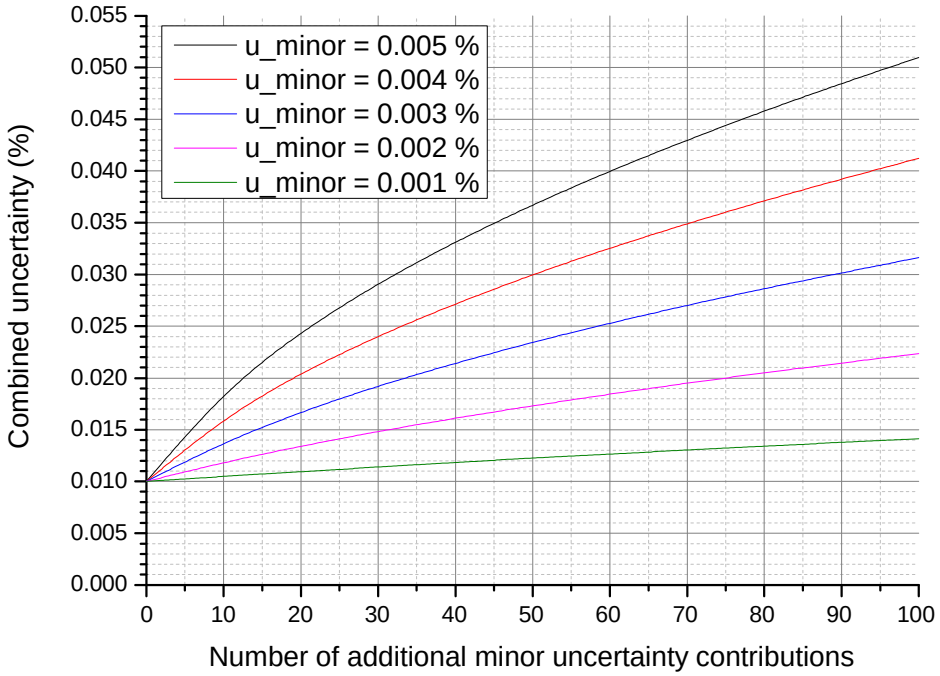


**Figure 11 Overall uncertainty, assuming a combined uncertainty of the major uncertainty contributors of 0.01% plus a variable number of minor uncertainty components.**

In summary, individual uncertainty contributions ≤ 0.004% will in this thesis be considered "negligible" in the context of Direct Solar Radiation measurements (i.e. ground-based measurements). In the context of Total Solar Irradiance (space-based), an individual uncertainty component will be considered "negligible" if it does not exceed 0.001%.

This definition of terms is only seen as a useful tool for the design process, where it is necessary to quantify the impact of individual sources of uncertainty without already having an overview over all other sources of uncertainty. Of course, all uncertainty contributions must be included in the final uncertainty budget at the

end of the test phase – either listed separately, or as part of one of the "major" uncertainty components[9].

## 2.5 Functional requirements for the CSAR detector system

In the previous sections, the main sub-systems of CSAR and the resulting main components of the overall uncertainty budget have been discussed. The following sections explore the functional requirements for these sub-systems.

The detector system includes all subcomponents that are vital for the measurement of optical power, such as the detector cavity, the heat link, the reference block system (see Figure 12) and the electronics.

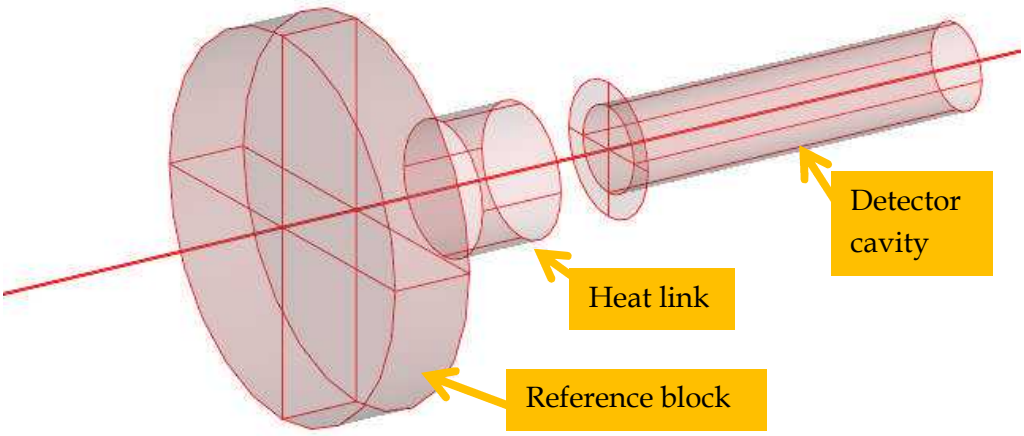


**Figure 12 Schematic of the detector assembly. Components from left to right: reference block, heat link, cavity. Thermometers, heaters, and electronics are not shown in this figure.**

For the purpose of this thesis, a cryogenic radiometer can be defined as an Electrical Substitution Radiometer which is cooled down to cryogenic temperatures. Figure 13 illustrates the operating principle of Electrical Substitution Radiometers. A cavity that is connected to a heat sink via a weak heat link is first heated up by incoming radiation

[9] The overall uncertainty budget of CSAR is given in Section 3.8.

(Figure 13, left hand side); subsequently, the radiation is blocked and the cavity is electrically heated to the same temperature (Figure 13, right hand side). This procedure allows the determination of radiant power through the measurement of electrical power. The reasons for cooling to cryogenic temperatures have been described by Quinn and Martin (Quinn and Martin, 1985) and these reasons will also become evident in this chapter and the following chapter of this thesis.

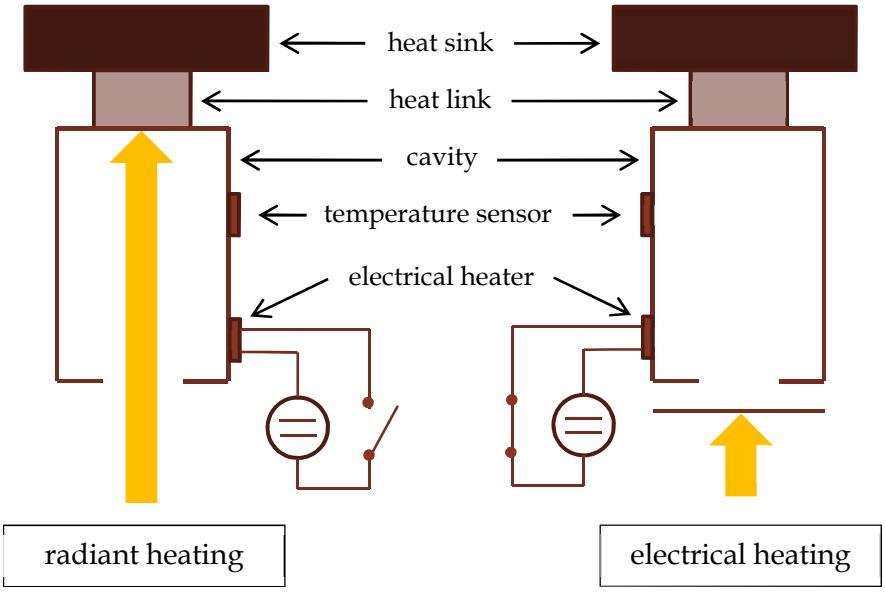


**Figure 13 Operating principle of Electrical Substitution Radiometers**

### 2.5.1 General Requirements for the detector system of a cryogenic radiometer

Quinn and Martin have identified a number of conditions that need to be satisfied, in order that the thermometer responds equally to equivalent radiant and electrical power. These conditions are listed in the following:

1) "The radiometer detector (cavity) should have a high absorptivity to ensure that all the incident radiant flux is absorbed and contributes to the rise in the detector temperature.
2) All the electrical power supplied should be dissipated as heat in the detector, and negligible power should be dissipated in, or conducted down, the connecting leads.
3) The heat flow path from the detector to the reference temperature heat sink should be identical for electrical and radiant heating, and should not be influenced by any difference in temperature gradients in the detector created by the two separate heating modes.
4) The thermometer which monitors the temperature rise of the detector should have a small thermal capacity and be in thermal equilibrium with the detector; it should also have appropriate resolution and sensitivity.
5) The temperature of the reference heat sink should remain constant during the period of measurement.
6) The detector should be shielded from other sources of thermal radiation, and its field of view restricted to reduce any scattered radiation falling on the detector surface" (Quinn and Martin, 1985).

Only the first of the above formulated requirements regarding the detector absorptivity – overall absorptivity, as well as spectral response characteristics - will be explored further in the present chapter. All other points listed by Quinn and Martin are more a matter of practical implementation (material choice, component choice, etc.) than theory, and will be dealt with accordingly in the following chapter.

Beside the six requirements mentioned above, further requirements that are specific to the CSAR application are also explored below. These are dealing with limitations regarding the natural time constant of the detector system, the instrument noise, and the dynamic range.

### 2.5.2 Overall detector absorptivity – Requirements

The requirement with respect to the detector absorptivity is one of the most important factors in the instrument design, since it heavily influences the design of the detector cavity itself, and the detector's time constant, and hence it also has a significant influence on the measurement procedure (for further detail see Section 2.5.4).

In order to determine the absorptivity of a detector, the spectral characteristics of the detector reflectivity as well as the spectral characteristics of the light source need to be taken into account. The overall reflectivity $\rho$ (weighted for the spectral randiance characteristics of the source) can be defined according to the following relation

$$\rho = \frac{\int_0^\infty \rho(\lambda) J(\lambda) d\lambda}{\int_0^\infty J(\lambda) d\lambda} \tag{2.24}$$

where $\rho(\lambda)$ is the spectral reflectivity of the cavity and $J(\lambda)$ is the spectral distribution of the source radiance; see also (Quinn and Martin, 1985), where a very similar definition is given.

The overall reflectivity leads naturally to the overall absorptivity $\alpha$ of the detector (assuming zero transmittance through the cavity wall):

$$\alpha = 1 - \rho \tag{2.25}$$

The reflectivity $\rho_{cavity}(\lambda)$ of the detector cavity at a specific wavelength $\lambda$ can be considered to be dependent on two factors. Firstly, the absorptivity is dependent on the geometry of the cavity. For a cylindrical cavity with an inclined back plate these geometrical parameters are (1) the length of the cavity $l$, (2) the radius of the entrance aperture $r$, and (3) the inclination angle of the back plate $\theta$ with respect to normal incidence of the incoming radiation. Secondly, the cavity absorptivity is also dependent on the reflectivity of the internal cavity surfaces $\rho_{surface}(\lambda)$. This is illustrated by the relation

$$\rho_{cavity}(\lambda) = \rho_{surface}(\lambda)\frac{r^2}{r^2 + l^2}\cos\theta \tag{2.26}$$

which assumes diffuse reflection of the incoming beam only (Quinn, 1983). Much more complicated relations have been derived, either analytically (see for example (Quinn and Martin, 1985)) or via computer models, e.g. in (Grobner, 2008); however, for the purpose of the work described here, the simple relation given above proved to be sufficiently in accordance with experimental findings (see Section 3.5.3.6).

The absorptivity $\alpha_{cavity}(\lambda)$ of the cavity at a specific wavelength $\lambda$ is given by

$$\alpha_{cavity}(\lambda) = 1 - \rho_{cavity}(\lambda) \tag{2.27}$$

From Equations (2.26) and (2.27) follows the relation for the cavity absorptivity $\alpha_{cavity}(\lambda)$:

$$\alpha_{cavity}(\lambda) = 1 - \rho_{cavity}(\lambda) = 1 - \rho_{surface}(\lambda)\frac{r^2}{r^2 + l^2}\cos\theta \tag{2.28}$$

Equation (2.28) reveals that there are two categories of parameters which influence the cavity reflectivity – (1) the surface reflectivity[10] $\rho_{surface}(\lambda)$, and (2) the geometrical parameters (i.e. the radius of the cavity entrance aperture $r$, the cavity length $l$, and the inclination angle of the cavity back plate $\theta$). Any changes in the reflectivity of internal surfaces or in the cavity geometry would change the cavity absorptivity.

It is unlikely that the geometry will change in any significant way over the lifetime of the instrument. The internal surface coating can, however, be much more susceptible to deterioration due to prolonged solar irradiation. This effect is also referred to as the "solar aging" of black coatings.

The sensitivity of the cavity absorptivity $\alpha_{cavity}(\lambda)$ with respect to changes in the surface reflectivity of the cavity is given by partial differentiation of Equation (2.28) with respect to the surface reflectivity $\rho_{surface}(\lambda)$:

$$\frac{\partial\left(\alpha_{cavity}(\lambda)\right)}{\partial\left(\rho_{surface}(\lambda)\right)} = -\frac{r^2}{r^2 + l^2}\cos\theta \tag{2.29}$$

The impact of the solar aging of the black surface coating on the cavity absorptivity therefore depends on how much the cavity design

[10] Only the diffuse reflectivity of the cavity surface is considered here, whereas the specular component is not considered. In this sense, the following evaluation of the surface deterioration can be regarded as a worst-case approximation of the deterioration of the diffuse surface reflectivity. This approach has been chosen for reasons that will become evident later in the thesis; CSAR's cavity can be made large enough so that the specular reflection component becomes negligible, which only leaves the diffuse component to be considered.

relies on the low reflectivity of the black coating and how much it relies on the geometry of the cavity. It is clear from Equation (2.28) that the same high cavity absorptivity can be achieved by (1) either using a surface coating with a low reflectivity, or (2) by using a favourable geometry. However, the sensitivity of the cavity absorptivity $\alpha_{cavity}(\lambda)$ with respect to absolute changes in the surface reflectivity $\rho_{surface}$ is very different in the two scenarios. In the following, two illustrative examples are discussed; in both cases, the cavity absorptivity is 99.99%.

In the first example, it is assumed that the cavity is coated with Nickel-Phosphor (NiP) black. NiP black is the black with the lowest reflectivity ever reported in the visible part of the wavelength spectrum; the lowest reported value for hemispherical diffuse reflectivity is 0.1% in the visible part of the spectrum (Kodama et al., 1990). A cavity geometry with length $l = 14\ mm$, radius $r = 5\ mm$, and inclination angle $\theta = 30^\circ$ leads to a cavity absorptivity of 99.99%. For this case, Equation (2.29) yields a sensitivity of the cavity absorptivity with respect to the surface reflectivity of -0.1. This means that an increase in surface reflectivity from 0.1% to 1.1% would lead to a decrease in the cavity absorptivity from 99.99% to 99.89%.

In the second example, no special effort is made in the selection of the surface coating. Many blacks have a diffuse hemispherical reflectivity of the order of 10% (or less). It is assumed that such a black is chosen in this second example. If all other geometrical parameters are the same as in the first example (radius $r = 5\ mm$, and inclination angle $\theta = 30^\circ$), then the length needs to be $l = 150\ mm$ in order to achieve a cavity absorptivity of 99.99%. For this case, Equation (2.29) yields a sensitivity of the cavity absorptivity with respect to the surface

reflectivity of -0.001. This means that an increase in surface reflectivity from 10% to 11% would lead to a decrease in the cavity absorptivity from 99.990% to 99.989%. The sensitivity of the cavity absorptivity is by approximately two orders of magnitudes smaller than in the first example, whereas the length (and therefore the cavity mass) has only increased by approximately one order of magnitude.

These two examples show that – while the choice of a low surface reflectivity always allows one to choose the most compact cavity design – it is not necessarily advantageous to rely too heavily on the low surface reflectivity, since the sensitivity of the cavity absorptivity with respect to the deterioration of the surface reflectivity is only a function of the cavity geometry and is independent from the choice of surface coating. In conclusion, it can be said that there is a compromise to be found between reducing the degradation of the cavity absorptivity over time and the mass of the cavity - which has a direct impact on the natural time constant of the detector system.

When it comes to the deterioration of black coatings, a clear distinction must be made between ground and space applications. In order to underline this distinction, the experimental experience with a black coating called "Aeroglaze Z302" is reviewed. Aeroglaze Z302 (formerly Chemglaze Z302) is the black coating with the longest history of use in ground–based as well as space-based measurements of Solar Irradiance. It is the coating of choice for all solar radiometers produced by PMOD/WRC. It was also applied to numerous cavities of cryogenically cooled detectors – it was used for the first cryogenic radiometers developed by NPL, before being replaced with Nickel-Phosphor in 1990.

Brusa et al. report that the absorptivity of the PMO6-cavities, which are coated with Aeroglaze Z302, decreases (on the ground) by approximately 200 ppm in the first year after being freshly painted and that the absorptivity does not decrease significantly after the first year (Brusa and Fröhlich, 1986). Using a rearranged version of Equation (2.29), together with the geometrical parameters of the PMO6 cavity, it can be shown that the 200 ppm decrease in cavity absorptivity is equivalent to a 0.48% increase in surface reflectivity (for clarification: what is meant here is an increase in absolute terms, not in relative terms, i.e. not 0.48% of the reflectivity).

The situation is very different if the PMO6 radiometer is used on a satellite. Figure 14 shows the change in responsivity of the VIRGO – PMO6 radiometer that is used to measure TSI on a daily basis. After an initial increase in responsivity within the first 100 days, which is attributed to other effects, the responsivity declines steadily due to the deterioration of the cavity reflectivity. This deterioration of the cavity reflectivity takes place at a rate of 0.11% per year and does not show any significant signs of slowing down after one year. The deterioration of the VIRGO PMO6 cavity reflectivity is equivalent to an increase of the surface reflectivity of the Aeroglaze Z302 coating of 2.2% per year.

The reasons for the deterioration of the black coatings are not well understood; however, the increased deterioration at the top of the atmosphere is probably due to the presence of atomic oxygen and increased levels of ultraviolet radiation. The energetic particle radiation environment in space may also play a role.

**Figure 14 Deterioration of the PMO6 radiometer response on VIRGO. Graph reproduced from (Fröhlich et al., 1997)**

The Total Irradiance Monitor (TIM) cavities have been shown to deteriorate much less than the PMO6 cavities. This is mostly due to the greater aspect ratio of the TIM cavity – and therefore a lower sensitivity of the cavity absorptivity with respect to a change in surface reflectivity - and partly due to a lower rate of change of the surface reflectivity of the Nickel-Phosphor cavity coating when compared to Aeroglaze Z302.

Figure 15 shows that the deterioration of the cavity reflectivity of the primary cavity on TIM is of the order of 0.005% per year. Given the cavity geometry of TIM, this overall deterioration is equivalent to an increase of the surface reflectivity of 1.1% per year.

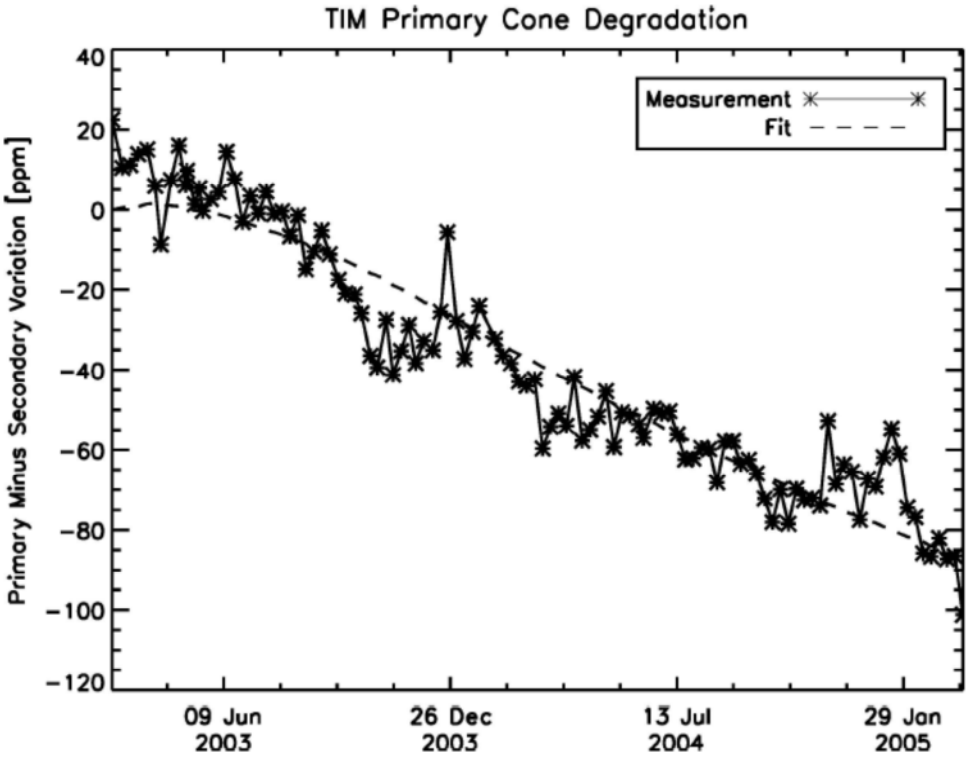


**Figure 15 Deterioration of the primary TIM cavity. Graph reproduced from (Kopp et al., 2005)**

It would be ideal if the initial overall cavity reflectivity was so small by design that the uncertainty due to it not being measured was negligible, i.e. smaller than 0.001% (space) or 0.004% (ground). Applying the GUM rule for evaluating Type B uncertainties for which only the upper and lower bounds can be estimated, the afore mentioned uncertainty requirements lead to the following acceptable ranges for the initial cavity absorptivity: 99.997% - 100.000% (space) and 99.986% - 100.000% (ground). Table 3 shows that none of the current state-of-the-art Solar Irradiance radiometers meets these requirements; however, the NPL cryogenic radiometer is fitted with a cavity that has an absorptivity of 99.998% at a wavelength of 647 nm.

**Table 3 Cavity Absorptivity of various radiometers.**

| Radiometer | Cavity Absorptivity | Measurand | Source |
|---|---|---|---|
| VIRGO / SOHO | 99.970% - 99.977% (Solar weighted) | TSI (satellite) | (Brusa and Fröhlich, 1986) |
| TIM / SORCE | 99.964% - 99.983% (Solar weighted) | TSI (satellite) | (Kopp et al., 2005) |
| PREMOS / PICARD | 99.980 % @ 632 nm | TSI (satellite) | (Schmutz et al., 2009) |
| | | | |
| NPL cryogenic radiometer | 99.998% @ 647 nm | Radiant power | (Fox et al., 1996) |

In addition to the uncertainty associated with the cavity absorptivity at the beginning of the instrument's lifetime, the uncertainty due to the deterioration of the cavity absorptivity over the course of the lifetime of the radiometer also needs to be considered. While it is currently common practice to monitor the cavity deterioration with the help of redundant cavities which are very infrequently exposed to solar radiation, it would be even better to dispose of any requirement for an experimental evaluation of the cavity deterioration. Instead, it would be ideal to control the end-of-lifetime uncertainty already at the design stage. Therefore, the cavity should be designed such that the uncertainty arising from the initial deviation from perfect absorptivity (discussed in the previous paragraph) in combination with the uncertainty arising from the

deterioration over the lifetime of the instrument is smaller than the target uncertainty for the cavity reflectivity stated in Table 2.

This means that the overall uncertainty for the end-of-lifetime uncertainty of the cavity absorptivity should be ≤ 0.013% for the ground-based application, and ≤ 0.005% for the top-of-the-atmosphere case. With an assumed uncertainty of 0.004% (ground) and 0.001% (top-of-the-atmosphere) associated with the initial cavity absorptivity, the application of the rules for combining uncertainties (discussed in Section 2.4.4) leads to an uncertainty target of ≤ 0.0124% (ground) and ≤ 0.0049% (top-of-the-atmosphere) for the deterioration over the lifetime of the instrument. This implies that the cavity absorptivity can deteriorate by up to 0.0428% (ground) and 0.0170% (top-of-the-atmosphere) if the rules for the treatment of Type B uncertainties with a rectangular probability distribution are applied (see Section 2.4.3). Assuming a lifetime of 10 years for the ground-application and 5 years for the space-application, this leads to a maximum tolerable deterioration of 0.0043% per year (ground) and 0.0034% per year (top-of-the-atmosphere).

### 2.5.3 Spectral response characteristics of the detector – Requirements

In Section 2.5.2, the requirement for the overall cavity absorptivity was formulated. However, it is also important to note that the cavity absorptivity of any real cavity will have some variation across the solar spectrum. The aim of this section is to explore how these spectral variations of the cavity absorptivity may look like – these theoretical considerations will be used in Section 3.5.3.3 to evaluate the suitability of the cavity design.

In Section 2.5.2, the relation between (1) overall detector absorptivity, (2) spectral characteristics of the detector reflectivity and (3) spectral characteristics of the light source was already discussed (see Equation (2.24)). Since the goal for the overall absorptivity is known and the spectral characteristics of the solar radiation is also known, it is possible to deduce which spectral distributions of the detector reflectivity would satisfy Equation (2.24).

As already discussed in Section 2.5.3, the aim for the overall cavity reflectivity is $\rho < 30$ ppm. For the purpose of this consideration, the spectral radiance distribution $J(\lambda)$ of the Sun can be approximated through a Planck-distribution with an effective Temperature of 5777 K (see Figure 16). There is any number of spectral reflectivity distributions $\rho(\lambda)$, which would satisfy Equation (2.24) under these circumstances. Mathematically, the most trivial case would be a constant reflectivity $\rho(\lambda) = \rho$ for all wavelengths; however it seems very unreasonable to demand that the reflectivity of the detector should be wavelength-independent. This is especially true since – as shown by Figure 16 - the solar output is heavily concentrated in the visible and near-infrared region, whereas the contribution in the infrared is very weak (although still significant for our purpose).

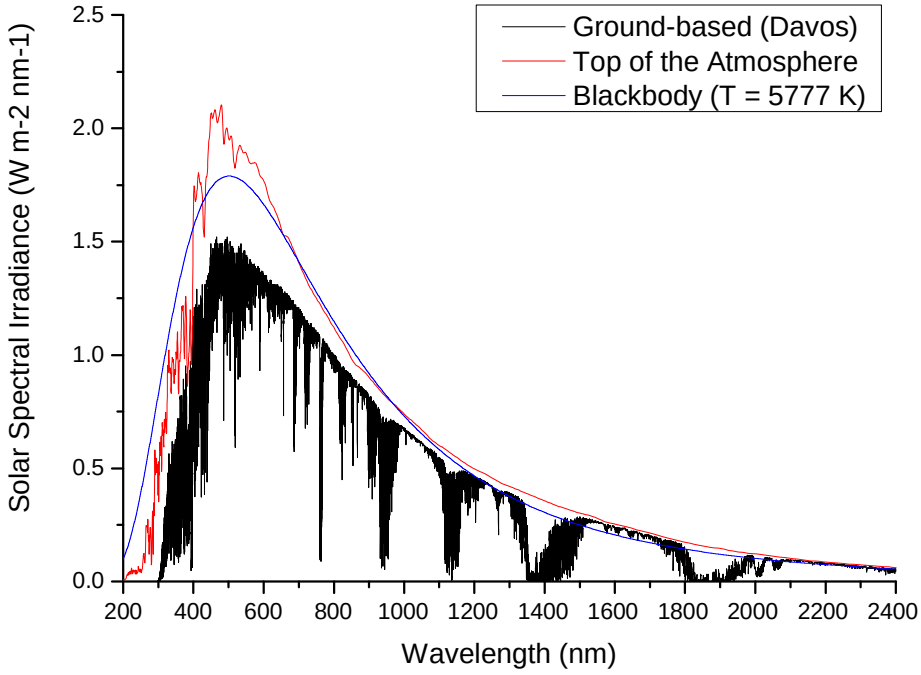


**Figure 16 Solar Spectral Irradiance. (1) The data for "Ground-based (Davos)" is derived from a MODTRAN model assuming a Solar Zenith Angle of 20° (data courtesy of André Fehlmann, PMOD/WRC). The integrated Solar Irradiance of this particular model is 965 W m$^{-2}$, which is a typical value for good measurement days in Davos. (2) The "Top of the Atmosphere" data are from the SORCE mission[11]. (3) The "Blackbody" curve is based on the Planck-radiation of a blackbody with a temperature of 5777 K (which is the effective temperature of the Sun) and a solid angle of 6.79×10$^{-5}$ sr (assuming mean values for the diameters of the Sun and the Earth and the mean distance between Sun and Earth)[12].**

Because the distribution of the spectral solar radiation is so uneven across the relevant wavelength range, it would be reasonable to relax the requirements in the infrared, particularly in light of the fact that the reflectivity of many commonly used black coatings is higher in the infrared region than in the visible or near-infrared region; see, for example (Dury et al., 2006).

[11] Online: http://lasp.colorado.edu/sorce/data/tsi_data.htm [Accessed 5 October 2012]
[12] More detail about the idealised Spectral Solar Irradiance, the effective temperature of the sun, and the solid angle can be found in Appendix A.

Instead of demanding a constant spectral reflectivity across all wavelengths, one could also consider a reflectivity distribution which is inversely proportional to the solar spectral irradiance. In this case, the cavity would absorb equal amounts of solar radiation in all segments of the solar spectrum. However, real blacks are even more unlikely to have such a spectral reflectivity distribution as they may be assumed to have constant reflectivity across all wavelengths; the spectral reflectivity distribution of real black coatings lies somewhere between these two extremes.

Therefore, the assumption is made that $\rho(\lambda)$ is proportional to $\left[J(\lambda)\right]^a$, where $a \in [-1, 0]$. This leads to the following relation[13]

$$\rho(\lambda) = \frac{\int_0^\infty J(\lambda)\,d\lambda}{\int_0^\infty \left[J(\lambda)\right]^a J(\lambda)\,d\lambda} \left[J(\lambda)\right]^a \rho \qquad (2.30)$$

which is illustrated in Figure 17 for values of *a* ranging from - 0.5 to 0. Figure 17 was produced assuming blackbody radiation (T = 5777 K) and assuming that there is no significant solar radiation below 200 nm or above 20 μm). The trivial case is a = 0, where the reflectivity is not spectrally dependent at all; however, for all curves, the overall reflectivity is 30 ppm. It can be seen very clearly that a slightly lower reflectivity in the VIS/NIR is able to compensate a relatively large reflectivity in the infrared region of the spectrum. The practical relevance of Figure 17 is that a reflectivity distribution of the detector is acceptable if the spectral values are consistently below the values of any of the shown curves.

[13] The derivation of Equation (2.30) is given in Appendix B.

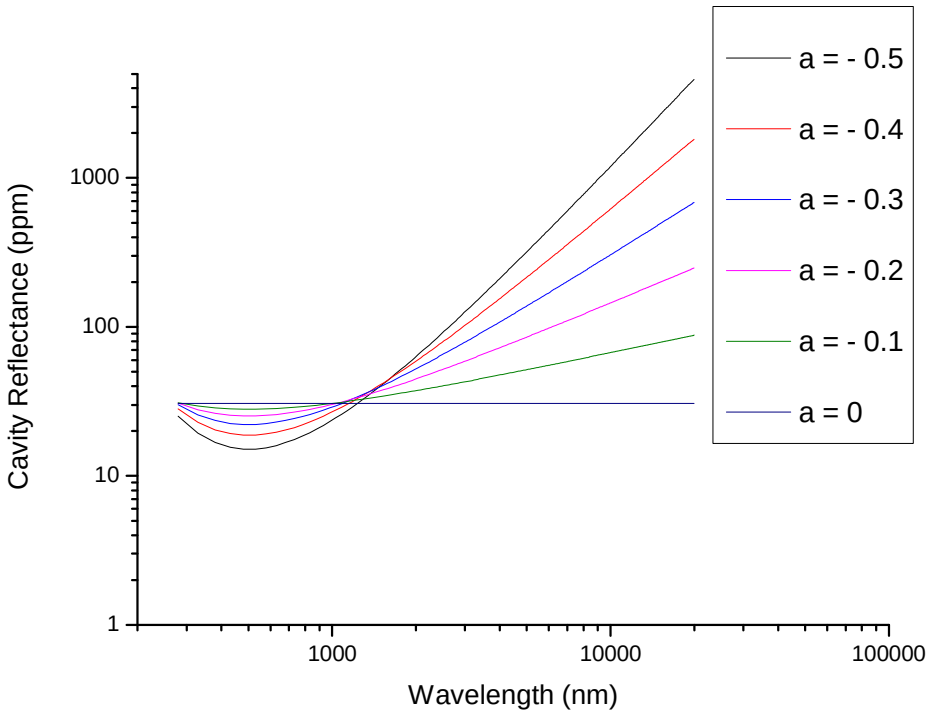


**Figure 17 Various spectral reflectivity characteristics of the detector, that all result in the same overall cavity reflectivity of 30 ppm – if exposed to the radiation of a 5577 K – blackbody (which approximates the solar spectral radiation distribution)**

The above consideration regarding the spectral characteristics is, strictly speaking, only valid for systems without window (i.e. the space application). On the ground, a window must be used, which will have non-ideal transmittance characteristics. The performance of the detector cavity becomes less critical in the spectral regions where the window blocks significant parts of the incoming radiation.

### 2.5.4 Natural time constant of the CSAR detector system – requirements

The natural time constant is one of the most crucial design parameters of the detector system; this section will explore the requirements regarding this important parameter in the context of Solar Irradiance measurements.

Very often, cryogenic radiometers operate under ideal laboratory conditions, with almost complete control over the various components of the experimental setup. The list of requirements by Quinn and Martin reproduced at the beginning of this chapter, assumes such ideal conditions. However, while the general requirements formulated in this list also hold for CSAR, some additional requirements need to be taken into consideration due to the specific circumstances under which CSAR is operated.

One of these additional requirements is associated with the radiation source, which – in the laboratory – can normally be kept at a constant output level. In contrast to that, when measuring the solar radiation on the ground, the detector must be able to accommodate changes in the irradiation level. The change in Direct Solar Radiation over the course of a day could introduce a systematic error if the detector was too slow. The aim of this section is to explore which response times of the detector system is adequate for this application. Figure 18 shows the Direct Solar Radiation (DSR) values on a good measurement day as taken by PMO2, one of the World Standard Group (WSG) instruments.

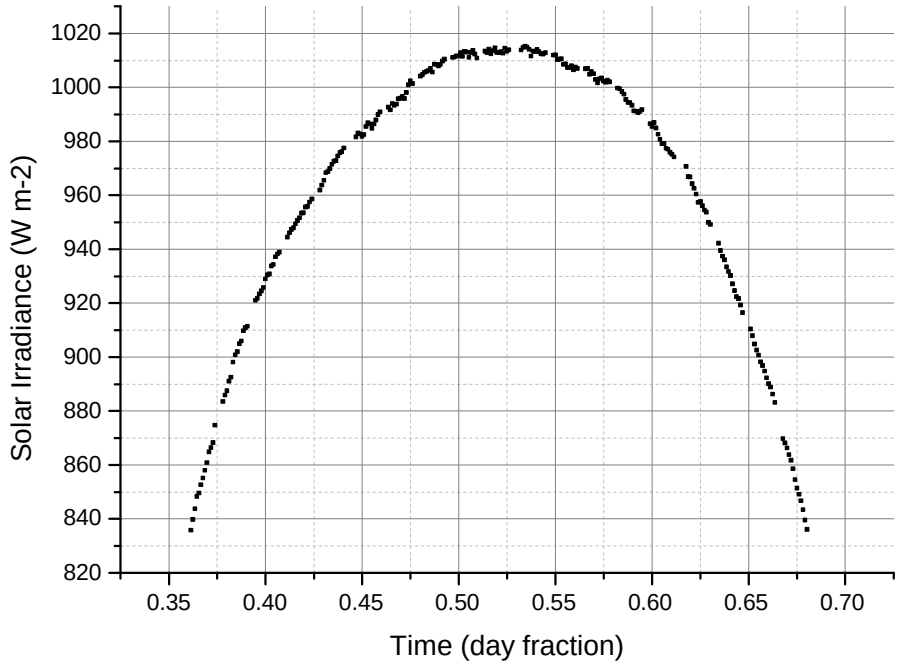


**Figure 18 Direct Solar Radiation measurements on a very good measurement day (8 March 2011). Data recorded by PMO2, one of the World Standard Group instruments.**

Figure 19 shows the rate of change in the signal over the course of a measurement day (the same data were used as in Figure 18). The changes in DSR are particularly small around midday. In the morning, the signal rises by slightly more than 0.2% per minute and in the late evening, the signal decreases at a rate of 0.2% per minute. However, around the time of solar maximum (day fraction 0.53), the change is of the order of only ± 0.02% per minute.

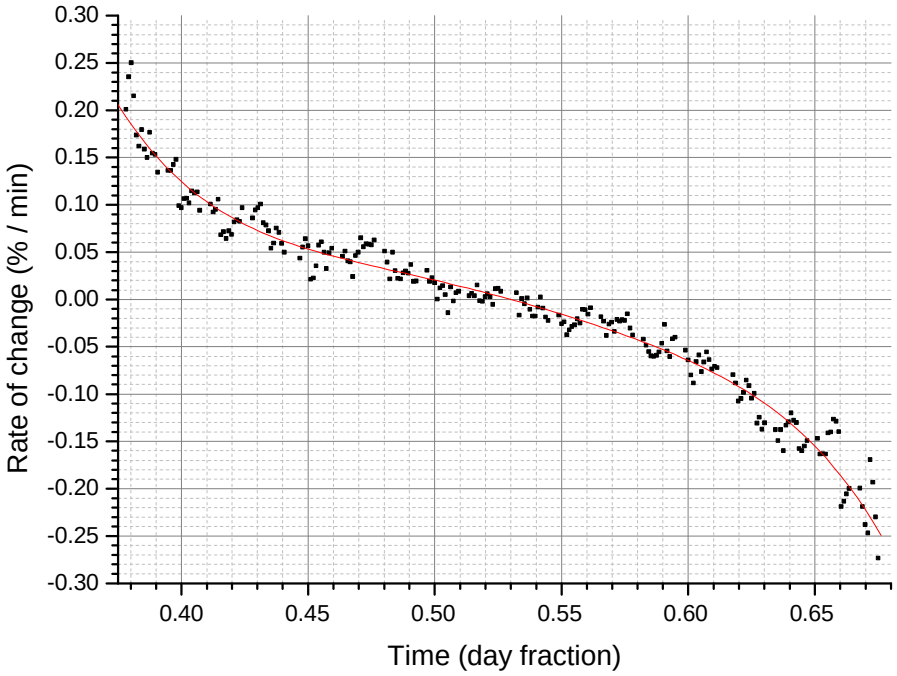


**Figure 19 Rate of change in signal over the course of a very good measurement day (8 March 2011). The data are based on a recording of Solar Irradiance by PMO2 – one of the WSG instruments. The red curve is based on a polynomial data fit.**

A simplified thermal model of the detector was set up in order to evaluate how the rate of change of the Sun's irradiance affects the uncertainty of the measurement. The model is graphically represented in Figure 20. It consists of a heat link element and a thermal mass (the "cavity"), which is attached to the heat link. The thermal properties of the heat link element and the cavity element are those of nylon and copper, respectively. The temperature of the heat link element is kept fixed at 20 K at the bottom surface. The cavity element is irradiated from above with a heat flux that is equivalent to an irradiance of 850 W $m^{-2}$ if a 5 mm diameter aperture is used (the reason for choosing a 5 mm diameter aperture will become clear later on in the thesis, see

Section 3.4.1). Figure 21 shows the step response to this stationary irradiation.

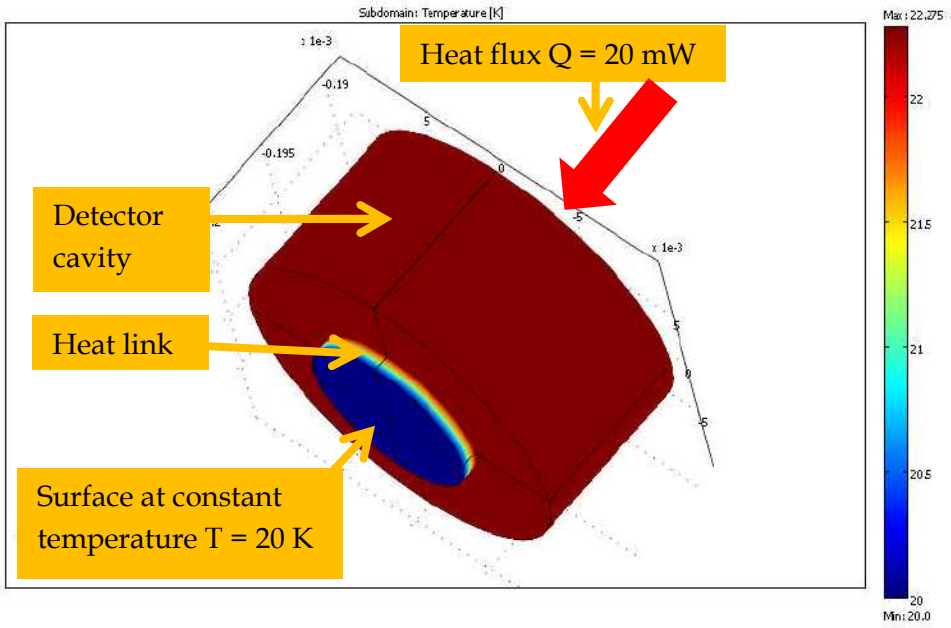


**Figure 20 Simple thermal FEA model of the detector system**

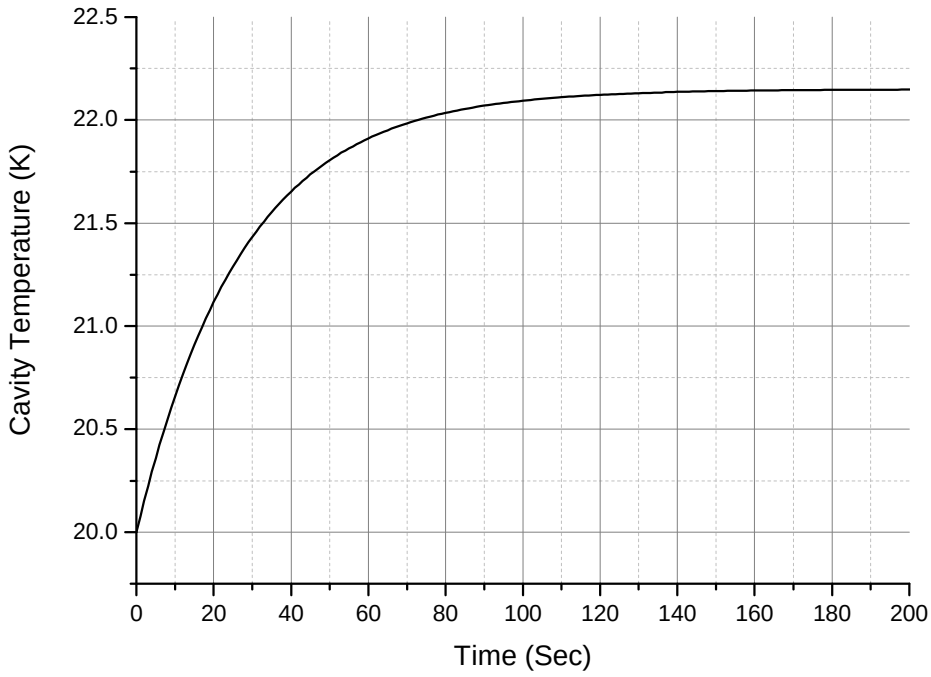


**Figure 21 Response of the model cavity temperature to a step change in irradiance.**

The stationary solution was calculated for different incoming power levels, assuming that the thermal properties of the materials are independent of temperature. By using linear interpolation, it is therefore possible to deduce the incoming power from the cavity temperature. For example, if the cavity temperature is measured to be 22 K, then the incoming power should be 0.0155 W. The power level that is arrived at in this way (i.e. via the temperature) will in the following be referred to as "measured power", as opposed to the "true power" which is the power level applied to the model.

The "measured power" and the "true power" are exactly equal only as long as the "true power" is not changing over time and as long as the cavity temperature is allowed to stabilise for an infinite amount of time. If the incoming power is constantly changing over time, then

there will be a measurement error even if the settling time is infinite, because the detector response (and therefore the cavity temperature) is constantly lagging behind the true signal. In order to evaluate the difference between the measured power level and the true power level under the conditions of a changing true power level, the power level applied to the model is increased linearly with elapsed time, starting with a value that is equivalent to 850 W m-2 (assuming a 5mm diameter aperture), which is the irradiance level in the morning of a typical measurement day. Figure 22 shows the step response of the simple detector model to an irradiance level, which starts at 850 W m-2, and which increases linearly at a rate of 0.2% per minute. Using the relationship between the cavity temperature and the incoming power level, one can deduce the "measured power".

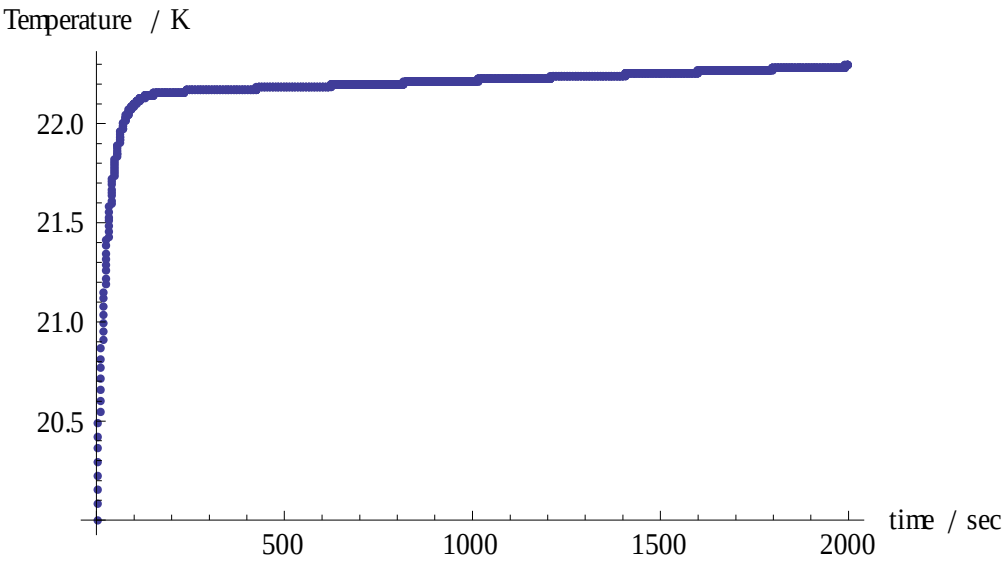


**Figure 22 Detector response to irradiance level, which starts at 850 W m-2, and which increases linearly at a rate of 0.2% per minute.**

The relative difference between the "true power level" that was applied to the model, and this "measured power level" is shown in Figure 23. After the initial obvious reduction in measurement offset

there remains a residual error, which does not diminish significantly within a practical timeframe.

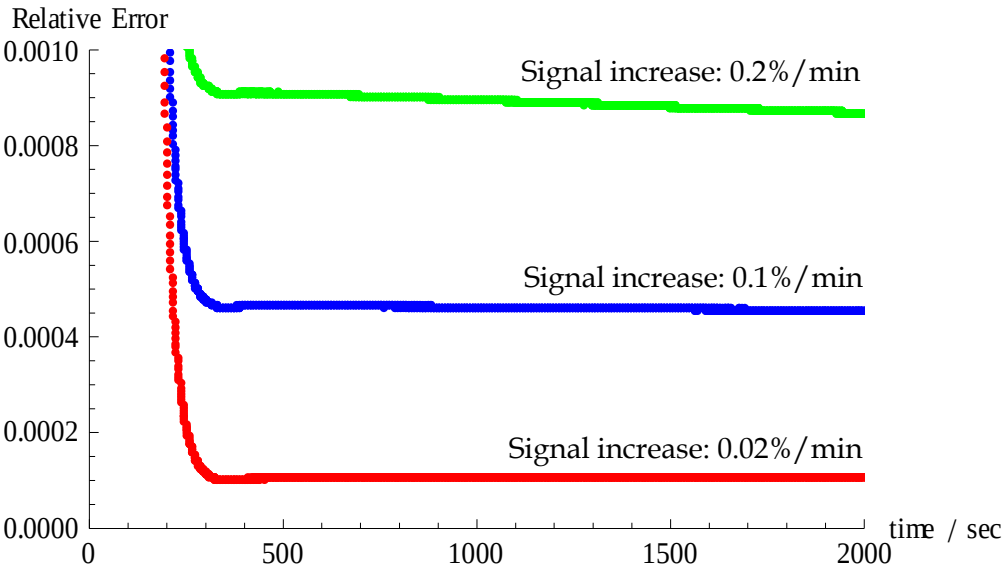


**Figure 23 Error due to time lag of measurement response to linearly increasing signal. This is for a time constant of 30 sec. Shown on the y-axis is the relative error (true power – measured power)/true power.**

Figure 23 shows the errors due to the time lag of the detector for a cavity with a natural time constant of 30 seconds. The three curves show the residual errors for a light source whose irradiance is increasing linearly by 0.2% per minute, by 0.1% and by 0.02%, after an initial step change in the power level from shutter closed to shutter open. Considered in combination with Figure 19, Figure 23 shows that (for a detector with a natural time constant of 30 seconds) in the morning, when irradiance changes are largest, the residual measurement error is approximately 0.09%, approximately 0.01% around the time of the solar maximum, and approximately -0.09% in the evening. These results illustrate that the requirements regarding the time constant of the detector vary considerably over the course of one measurement day.

Table 4 shows in greater detail the relation between the natural time constant of the detector, the rate of change of the Sun, and the relative offset error due to the detector's time lag.

**Table 4 Relative error due to rate of change for various time constants**

| Time constant / sec | Relative error for a rate of change of | | | | | |
|---|---|---|---|---|---|---|
| | 0.02% /min | 0.03% /min | 0.04% /min | 0.05% /min | 0.1% /min | 0.2% /min |
| 1 | 0.0010% | 0.0030% | 0.0050% | 0.0070% | 0.0120% | 0.0250% |
| 2 | 0.0013% | 0.0033% | 0.0053% | 0.0073% | 0.0130% | 0.0267% |
| 3 | 0.0017% | 0.0037% | 0.0057% | 0.0077% | 0.0140% | 0.0283% |
| 4 | 0.0020% | 0.0040% | 0.0060% | 0.0080% | 0.0150% | 0.0300% |
| 5 | 0.0023% | 0.0043% | 0.0063% | 0.0083% | 0.0160% | 0.0317% |
| 6 | 0.0027% | 0.0047% | 0.0067% | 0.0087% | 0.0170% | 0.0333% |
| 7 | 0.0030% | 0.0050% | 0.0070% | 0.0090% | 0.0180% | 0.0350% |
| 8 | 0.0033% | 0.0053% | 0.0073% | 0.0093% | 0.0190% | 0.0367% |
| 9 | 0.0037% | 0.0057% | 0.0077% | 0.0097% | 0.0200% | 0.0383% |
| 10 | 0.0040% | 0.0060% | 0.0080% | 0.0100% | 0.0210% | 0.0400% |
| 15 | 0.0045% | 0.0070% | 0.0095% | 0.0120% | 0.0230% | 0.0450% |
| 20 | 0.0050% | 0.0090% | 0.0130% | 0.0170% | 0.0330% | 0.0650% |
| 25 | 0.0075% | 0.0115% | 0.0155% | 0.0195% | 0.0390% | 0.0775% |
| 30 | 0.0100% | 0.0140% | 0.0180% | 0.0220% | 0.0450% | 0.0900% |

The values shown in Table 4 are offset errors rather than standard uncertainties. The values in Table 4 can be seen as maximum boundaries *a*; the values can lie in the interval [-a, a]. Assuming a rectangular probability density distribution, these values correspond to the standard uncertainties given in Table 5. These standard

uncertainties were calculated using Equation (2.6) in Section 2.4.3. The standard uncertainties which can be considered "negligible" are shown in bold font. For example, a rate of change in the solar output of 0.04%/min gives rise to a standard uncertainty of 0.004% for a detector cavity with a natural time constant of 7 seconds.

**Table 5 Standard uncertainties of the Solar Irradiance measurements arising from various time constants and various rates of change of the Sun. The uncertainties which can be considered "negligible" are in bold font.**

| Time constant / sec | Relative uncertainty for a rate of change of | | | | | |
|---|---|---|---|---|---|---|
| | 0.02% per min | 0.03% per min | 0.04% per min | 0.05% per min | 0.10% per min | 0.20% per min |
| 1 | **0.0006%** | **0.0017%** | **0.0029%** | **0.0040%** | 0.0069% | 0.0144% |
| 2 | **0.0008%** | **0.0019%** | **0.0031%** | 0.0042% | 0.0075% | 0.0154% |
| 3 | **0.0010%** | **0.0021%** | **0.0033%** | 0.0044% | 0.0081% | 0.0164% |
| 4 | **0.0012%** | **0.0023%** | **0.0035%** | 0.0046% | 0.0087% | 0.0173% |
| 5 | **0.0013%** | **0.0025%** | **0.0037%** | 0.0048% | 0.0092% | 0.0183% |
| 6 | **0.0015%** | **0.0027%** | **0.0038%** | 0.0050% | 0.0098% | 0.0192% |
| 7 | **0.0017%** | **0.0029%** | **0.0040%** | 0.0052% | 0.0104% | 0.0202% |
| 8 | **0.0019%** | **0.0031%** | 0.0042% | 0.0054% | 0.0110% | 0.0212% |
| 9 | **0.0021%** | **0.0033%** | 0.0044% | 0.0056% | 0.0115% | 0.0221% |
| 10 | **0.0023%** | **0.0035%** | 0.0046% | 0.0058% | 0.0121% | 0.0231% |
| 15 | **0.0026%** | **0.0040%** | 0.0055% | 0.0069% | 0.0133% | 0.0260% |
| 20 | **0.0029%** | 0.0052% | 0.0075% | 0.0098% | 0.0191% | 0.0375% |
| 25 | 0.0043% | 0.0066% | 0.0089% | 0.0113% | 0.0225% | 0.0447% |
| 30 | 0.0058% | 0.0081% | 0.0104% | 0.0127% | 0.0260% | 0.0520% |

### 2.5.5 Instrument noise – Requirements

In the previous section, the standard uncertainty due to the response time of the detector and the change in Solar Irradiance was discussed. This discussion did not include the error due to the noise in the measurement. The aim of this section is to establish an upper limit for the instrument noise of the detector, or - in case this proves impossible - to develop an understanding of the relationship of the instrument noise with other important instrument characteristics such as the response time.

Some additional information not mentioned so far is necessary for analysing the impact of the detector noise on the measurement uncertainty. It is not sufficient for CSAR to make accurate measurements at the desired uncertainty level. More importantly, it should be possible to compare existing radiometers (especially the World Standard Group) with CSAR at the level of the desired accuracy. This implies that a certain noise floor is part of the comparison uncertainty, which is solely given by the instrument noise of that other radiometer, and which cannot be reduced further by reducing the instrument noise of CSAR. This "noise floor" can only be decreased by increasing the number of measurement points.

The standard deviation of the measurements of the PMO2 radiometer (which is normally used for comparisons to the World Standard Group) is of the order of 0.1%. In order to establish a minimum number of measurement points and a lower limit for the time necessary to compare CSAR with the WRR, the assumption is made that CSAR does not contribute any significant noise to the comparison. In this case, a minimum of 70 measurements would be required to reduce the noise of the comparison measurement to the

level of 0.012%[14], which takes a total of 105 minutes in the case of the fastest World Standard Group instrument (the PMO2 radiometer). The PMO2 radiometer takes readings[15] in intervals of 90 seconds.

In order to establish a maximum number of measurement points and an upper limit for the measurement time necessary to compare CSAR with the WRR, it is assumed that CSAR has the same instrument noise as PMO2. In this case it would take a minimum of 139 readings (or 209 minutes) to reach the 0.012% noise level for the comparison.

In summary, it can be said that the minimum number of required PMO2 readings will be between 70 and 139 (if CSAR's measurement cycle is as fast as or faster than the 90 seconds of the PMO2). This is not an unreasonable amount of measurements to aim for, since one of the requirements for a successful International Pyrheliometer Comparison is "that the minimum number of acceptable data points be 150 for the PMO2 taken over a minimum of three days during the comparison period" (Finsterle, 2011).

However, while the data selection criteria for the final evaluation of an International Pyrheliometer Comparison do not discriminate data on the basis of what time of day the data were gathered, it is suggested here to limit the measurement period to a symmetrical time window around the time of the Solar Irradiance maximum. If it is assumed that 140 PMO2 data points are gathered over the course of three days, at the rate of ~47 measurements per day,

[14] This is the size of the additional allowable uncertainty component for the ground application (see Table 2 in Section 2.4.6)

[15] One reading is the result of a measurement cycle, where the shutter is open for 45 seconds, and subsequently closed for another 45 seconds. The signal is averaged over the last 10 seconds of the shutter-open and shutter-closed states, respectively. The Solar Irradiance value is derived from these two average values.

and that all these data points are collected around midday, then the ideal time window for the measurements would be from day fraction 0.505 to day fraction 0.555. From Figure 19 it can be seen that the rate of change of the Solar Irradiance is within ±0.02% for this time interval. And from Table 5 it can be deduced that the uncertainty arising from the rate of change of the Solar Irradiance is negligible if the natural time constant of the CSAR detector is 20 seconds or smaller.

The limitation of having to have three good measurement days where the data from a very specific time period is useful is potentially quite demanding, since a cirrus cloud during that time around midday can render the whole day useless as a measurement day. Therefore it would be desirable to be able to take measurements for a more extended time period. If one applies the same reasoning process as in the previous paragraph, the requirement for taking the 140 data points in two days leads to a measurement interval of day fraction 0.493 to 0.57 and a requirement for a time constant of ≤ 15 sec. And similarly, the requirement for taking the 140 data points in one day leads to a measurement interval of day fraction 0.457 to 0.603 and a requirement for a time constant of < 1 sec.

In order to arrive at a single value for the requirement regarding the natural time constant of the CSAR detector, the average of the results of the previous three scenarios (20 sec, 15 sec, and 1 sec) is calculated. Following these considerations, a natural time constant of 12 seconds (or smaller) can be considered desirable.

### 2.5.6 Irradiance levels and Dynamic range of the detector – Requirements

In Davos (where the primary standard for Direct Solar Radiation is currently situated), Direct Solar Radiation levels vary between ~ 800 W $m^{-2}$ in the morning and up to ~ 1100 W $m^{-2}$ at midday. In order to make the instrument also useful for top-of-the-atmosphere (TOA) measurements, it is required to measure irradiance values between ~ 1300 W $m^{-2}$ at aphelion and ~ 1420 W $m^{-2}$ at perihelion (Howell et al., 2010).

In addition to the measurements on the solar tracker, CSAR also needs to perform measurements in the lab at the National Physical Laboratory (NPL). CSAR should be compared against NPL's primary standard for radiant power, in order to check the consistency with the International System of Units (SI). Typically, a power-stabilised laser is employed for this comparison. The laser used at NPL can deliver several hundred milliwatts in a beam (at a wavelength of 647 nm), but after stabilising and after spatially filtering the beam in order to reduce the stray light around the main beam to an insignificant level, only about a maximum of 10 to 15 mW are left; however, producing a "clean" beam with a power level of this order takes considerable effort. Producing a clean beam with 5 mW of power, on the other hand, is relatively easy. For the sake of this comparison of CSAR against the SI, it would therefore be very convenient, if the detector system offered sufficient resolution at the 5 mW power level.

## 2.6 The aperture geometry – requirements and recommendations

The aperture system is part of the optical system of CSAR. The optical elements (for each DSR/TSI channel) are: a detector cavity that

absorbs the incoming optical power, a precision aperture that defines the irradiated area, a radiation trap to reduce internal stray light, a field-of-view limiting aperture, and a window for operation on the ground; Figure 24 illustrates these components.

This section is concerned with the apertures, the arrangement of these apertures and the radiation trap between the apertures. The importance of accurately defining the detector area becomes immediately obvious from the measurement equation derived in Section 2.4.5.

Apart from the defining aperture, a second aperture is used in order to limit the field-of-view. For the ground-application, this additional aperture prevents the largest part of the sky radiation from entering the detector (all but the "circumsolar radiation"), and for the space application, it blocks external light emitted or reflected from other parts of the payload or spacecraft.

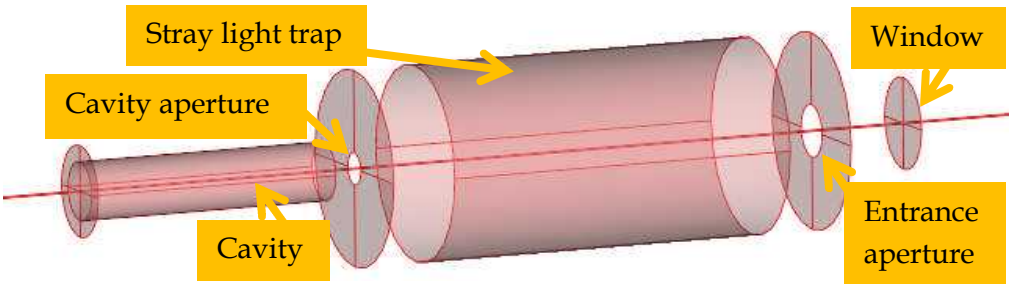


**Figure 24 Schematic of the optical system for DSR/TSI.**

### 2.6.1 Aperture system - Recommendations by the World Meteorological Organisation (WMO)

Especially for the ground-based application, it would be ideal to match the field-of-view of the radiometer such that only direct sunlight is

collected, and no indirect light that is scattered by the atmosphere. However, this is not practical for a detector with an extended cavity aperture area (i.e. no point detector), mainly for two reasons. Firstly, an arrangement of apertures as shown in Figure 24 produces a 'shadow-annulus', i.e., from a certain source area the light is only partly collected (as discussed in, e.g., (Edwards, 2004)). Secondly, as the field-of-view approaches the 'ideal' geometry, the detector becomes more and more sensitive to the alignment of both apertures with the Sun. This is not only due to potential clipping of the beam of direct solar radiation, but also due to increased sensitivity of the diffraction effect to the size and position of the apertures (for further detail, see Section 3.4.1.5).

Since it is not possible to select an ideal geometry, the World Meteorological Organisation (WMO) makes recommendations for an aperture arrangement that is common to all DSR radiometers, in order to simplify the comparison between radiometers and the calibration of radiometers against the primary standard. If the WMO recommendations were fully implemented, it would still not be directly resolvable how much circumsolar radiation contributes to the measurement signal, but at least all the radiometers would measure nominally the same amount of circumsolar radiation.

The WMO recommends an optical setup as shown in Figure 25. The WMO guideline assumes that the cavity aperture is smaller than the entrance aperture. In addition to that, it states: "As to the view-limiting geometry, it is recommended that the opening half-angle be 2.5° ($5*10^{-3}$ sr) and the slope angle 1° for all new designs of direct solar radiation instruments" (WMO, 2008).

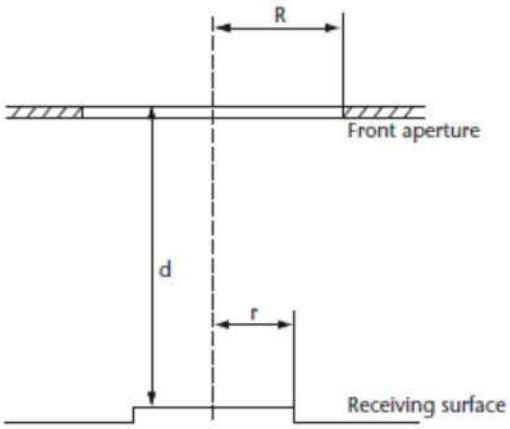


**Figure 25 Recommended optical geometry for pyrheliometers. The opening half-angle is Arctan[R/d]; the slope angle is Arctan[(R-r)/d]. Reproduced from (WMO, 2008).**

### 2.6.2 Aperture system - Review of existing radiometers

The recommendations of the WMO have only been introduced in recent years, and therefore – to the author's knowledge - only PMOD/WRC's current commercially available radiometer (the PMO-6) is fully compliant with the CIMO guide. Table 6 shows that none of the World Standard Group (WSG) instruments that were operational at the International Pyrheliometer Comparison in 2005 fulfils the requirements of the CIMO guide.

The optical geometries of current satellite instruments are shown in Table 7. Not surprisingly, the space radiometers vary even more in their aperture geometry than the ground-based radiometers, since the reduction of diffuse sky radiation was not a primary concern during their design.

**Table 6 Aperture geometries of WSG instruments operational at the IPC X in 2005 (Finsterle, 2011). Data courtesy of André Fehlmann (Fehlmann, 2011).**

| Radiometer | Front aperture / mm | Cavity aperture / mm | Aperture distance / mm | Slope angle / ° | Half opening angle / ° | Limit angle / ° |
|---|---|---|---|---|---|---|
| PMO2 | 3.60 | 2.50 | 75.00 | 0.84 | 2.75 | 4.65 |
| CROM2L | 6.29 | 5.00 | 144.05 | 0.51 | 2.50 | 4.48 |
| MK67814 | 8.20 | 5.65 | 187.60 | 0.78 | 2.50 | 4.22 |
| HF18748 | 5.81 | 3.99 | 134.70 | 0.77 | 2.47 | 4.16 |
| PAC3 | 8.18 | 5.64 | 190.50 | 0.76 | 2.46 | 4.15 |
| PMO5 | 3.70 | 2.50 | 95.40 | 0.72 | 2.22 | 3.72 |

**Table 7 Optical geometries of current satellite-based TSI radiometers**

| Radiometer | Front aperture / mm | Cavity aperture / mm | Aperture distance / mm | Slope angle / ° | Half opening angle / ° |
|---|---|---|---|---|---|
| VIRGO | 4.25 | 2.50 | 95.40 | 1.05 | 2.55 |
| SOVIM | 4.80 | 2.50 | 98.50 | 1.34 | 2.79 |
| DIARAD | 6.52 | 4.00 | 144.00 | 1.00 | 2.59 |
| ERBE | 12.09 | 4.04 | 100.80 | 4.57 | 6.84 |
| ACRIM | 6.65 | 3.99 | 150.47 | 1.02 | 2.53 |
| TIM | 3.99 | 7.62 | 101.60 | -2.05 | 2.25 |
| PREMOS | 4.25 | 2.50 | 95.40 | 1.05 | 2.55 |

Since the current WMO guidelines with respect to the optical geometry are not well established, they were not considered as strictly

binding for the design of CSAR. It was considered more beneficial to aim to implement the best possible optical design, rather than to follow guidelines. This design philosophy was in accordance with the colleagues at the WRC, who are largely responsible for the WMO guidelines.

### 2.6.3 Stray light rejection – Requirements

The requirements regarding the stray light rejection are determined by the desired instrument accuracy and the ratio between Direct Solar Radiation and sky radiation. On a good measurement day, the total sky radiation is equivalent to less than 10% of the direct solar radiation[16]. Bearing in mind the overall accuracy goal of 0.03% for the ground-based application, it would be desirable to keep the uncertainty caused by the sky radiation below 0.004%. This means that the stray light rejection of the diffuse sky radiation must be of the order of 0.04%, while the stray light rejection of any unwanted direct solar radiation should be of the order of 0.004%.

Since the requirements regarding the stray light rejection of direct solar radiation are much more stringent than the rejection of diffuse sky radiation, the main attention of the design should ideally focus on preventing any unwanted direct radiation from entering the system. If the unwanted direct sunlight does not enter the system, then there is no need to deal with this light within the system. This fact provides a strong argument for placing the "defining aperture" in front of the field-of-view limiting aperture, i.e., to place the smaller aperture in front of the larger aperture. This is a deviation from the WMO guidelines (WMO, 2008) and is discussed in more detail in Section 3.4.

[16] Personal communication with André Fehlmann, PMOD/WRC

## 2.7 Window – requirements

On the ground, the use of a window is necessary in order to provide a vacuum environment for the cryogenic detector. This section focusses on the requirements with respect to this vacuum window.

Atmospheric modelling shows that significant portions of terrestrial solar radiation are found in the wavelength range extending from 0.29 µm up to 15 µm (see Appendix C). The window material should ideally have a high transmittance in this wavelength range, but there are other considerations that are of similar importance. The optical properties of the window must be stable in outdoor conditions (including repeated cleaning); it is therefore preferable not to use coatings or soft window materials, which may be subject to change under these conditions. Since the outdoor humidity is not controllable, it is also important that the window material be not hygroscopic.

## 2.8 Cooling power – restrictions

While the previous sections are dealing with the components of CSAR that are directly related to the measurement process itself, this current section and the following section focus on aspects of the instruments that provide the correct operational conditions for these measurements, but that are not directly related to the measurement process.

A cryogenic radiometer requires cooling, and it is essential for the design process that the available cooling power be known. The available cooling power is a crucial parameter in the design process, because it largely determines the operating temperature of the detector. The operating temperature has a great influence on the detector characteristics, such as its time constant or the materials that

can be used for superconducting wires. The available cooling power also determines which thermal design features need to be introduced in order to allow the radiometer to be operated at sufficiently low temperatures. This section outlines the available cooling power that is assumed during the design of CSAR.

The thermal load requirements are almost exclusively driven by the space application, and more specifically, by the limited cooling power provided by space coolers. In contrast to space coolers, ground coolers offer abundant cooling power at not significantly higher cost.

In terms of thermal performance, the design aim is to match the performance characteristics of an Astrium 10K cooler. This machine provides cooling power at two stages. The second stage (cold tip) provides 400 mW of cooling power at 19 K, while a 500 mK load is applied at the first stage (@ 120 K)[17]. Ideally, the system should be designed to work with just one of these Astrium 10 K coolers, in order to minimise weight and cost of the space instrument.

The restricted cooling power has an impact on the structural support of the detector system, as well as on the size of the entrance aperture that admits a certain amount of solar radiation, and also on the design of the radiation shields.

## 2.9 Mass, mechanical structure and size – requirements

### 2.9.1 Mass

For the ground application, the overall mass and the mass distribution of the instrument are important, because otherwise the solar tracker,

[17] This information regarding the performance characteristics of the cooler were made available by Andrew Gibson (Cryogenic Engineering Group, Astrium Stevenage).

on which CSAR is to be mounted, may be overloaded and may not be able to track the sun properly.

PMOD/WRC engineers estimated the requirements for the instrument mass and mass distribution on the basis of the performance characteristics of their solar tracker. It was determined that the instrument (including the vacuum can and cold head) should have a mass of less than 100 kg and that the centre of mass should be as close as possible to the mounting plane.

For the space application, the design goal was to keep the mass of the radiometer head below 10 kg.

### 2.9.2 Mechanical structure and materials

The structural elements and the choice of materials is very important regarding the mechanical as well as the thermal performance of the radiometer. This section briefly outlines the limitations regarding the mechanical structure and the materials.

For the space-application, the radiometer head needs to be able to withstand typical vibration tests. The instrument design aimed for the instrument to survive uniform accelerations of 100g, and for all component groups to have a natural Eigenfrequency in excess of 100 Hz.

Another requirement is that all the materials and components of the radiometer head should be either space-qualified or space-qualifiable or easily replaceable by space-qualified components. This requirement is naturally given by the space application, but the ground application under vacuum also limits the choice of materials and components.

Furthermore, it is important that differences in the coefficient of thermal expansion of different materials do not lead to significant misalignment of the optical components when cooling the radiometer from room temperature to operating temperatures.

### 2.9.3 Size restrictions

The design aim for the radiometer head was to restrict the volume of the radiometer head to a volume of 250 mm X 300 mm X 300 mm, where the length should not be greater than 250 mm. This restriction is primarily due to the space application.

For the ground-based applications, the size restriction regarding the vacuum chamber was not to take up more than one quarter of the space on the mounting surface of the solar tracker. The basic support structure of the tracker table is shown in Figure 26 and Figure 27.

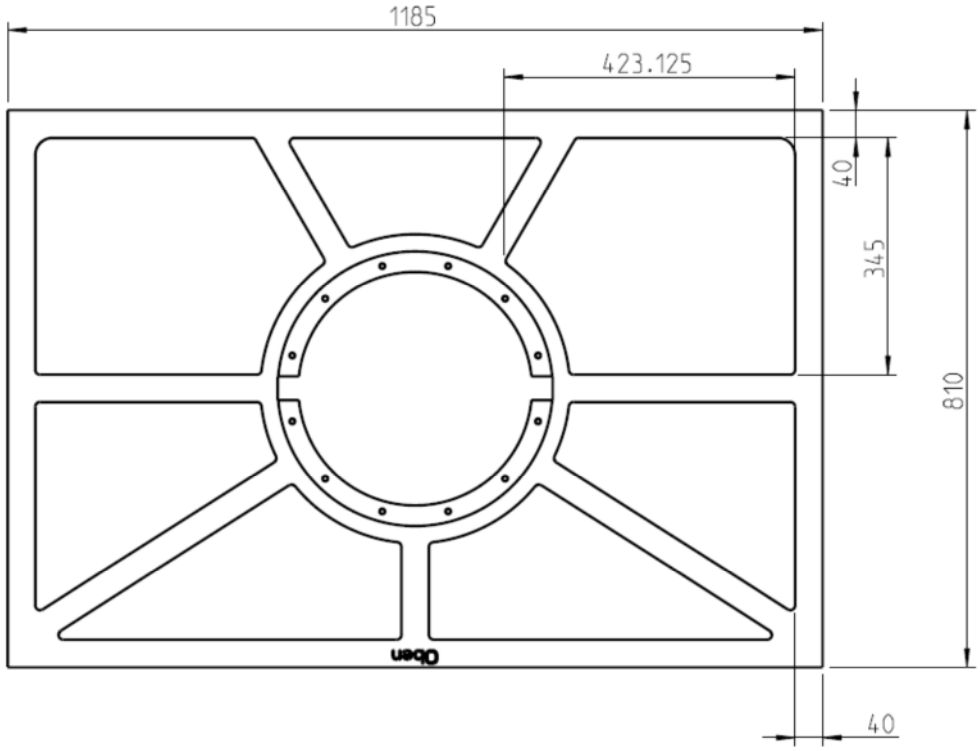


**Figure 26 Basic support structure of the solar tracker table at the World Radiation Center (2D-drawing and measurements)**

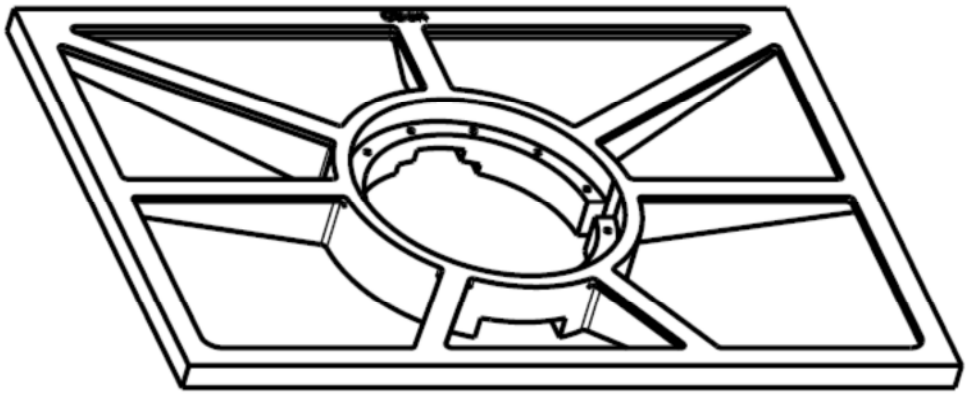

**Figure 27 Basic support structure of the solar tracker table at the World Radiation Center (3D-drawing)**

## 2.10 Summary of functional requirements

The above-mentioned requirements set the limits for the design. They are of a relatively general nature, or in other words, they are not component-specific. In most cases, they have an impact on various

component groups. The following chapter, which deals with the instrument design, will refer back to these requirements. Table 8 summarises the baseline performance requirements.

**Table 8 Summary of technical requirements**

| | Ground (primary application) | Space (secondary objective), additional requirements |
|---|---|---|
| **Natural time constant τ** | $\tau < 12$ sec | |
| **Irradiance level I** | 800 W $m^{-2}$ < I < 1100 W $m^{-2}$ | 1300W $m^{-2}$ < I < 1420 W $m^{-2}$ |
| **Cavity absorptivity α** | $\alpha > 99.986\%$, deterioration < 0.0043% per year | $\alpha > 99.997\%$, deterioration < 0.0034% per year |
| **Spectral range** | 280 nm < λ < 15 µm | 200 nm < λ < 20 µm |
| **Stray light level** | Diffuse sky: < 0.04% of signal<br>Direct radiation: < 0.004% | |
| **Thermal load** | First stage: < 30 W (@ T = 48 K)<br>Second stage: < 5 W (@ T = 20 K) | First stage: < 500 mW (@ T = 110 K)<br>Second stage: < 400 mW (@ T = 20 K) |
| **Mechanical structure** | • Mass < 100 kg (radiometer head & vacuum can & cold head)<br>• Centre of mass close to mounting plane | • Mass < 10 kg (radiometer head)<br>• Survive static accelerations (x,y,z) < 100g<br>• Eigenfrequency > 100 Hz |
| **Size** | Less than one quarter of the surface area of the solar tracker in Davos | The radiometer head should be smaller than 250 mm x 300 mm x 300 mm (l x w x h) |

Some of the requirements are competing and consequently must be weighed up against each other. For example, the requirements regarding the natural time constant and regarding the cavity absorptivity are opposing each other. Also, a compromise must be found to satisfy thermal load requirements and mechanical structure requirements at the same time. These trade-offs between competing requirements are described in more detail in the next chapter, which describes the thought process during the design of the instrument.

# Chapter 3 Design and Practical Implementation

The aim of this chapter is to show how the functional requirements (established in Chapter 2) were translated onto the design level.

## 3.1 Overview

Section 3.2 gives a first impression of the instrument by showing a number of drawings and photographs, thereby giving an overview over the radiometer head as well as the complete radiometer as it is operated on the ground.

Section 3.3 describes the thermal management of the heat load on the cooler. It describes a theoretical, as well as an experimental evaluation of the heat load, which suggests that CSAR may - after some minor modifications - be operated with a single Astrium 10 K cooler.

Section 3.4 is concerned with the design of the aperture system. It explains why the aperture configuration of CSAR is reversed when compared with conventional pyrheliometers. It also gives reasons for choosing a 5 mm diameter for the defining aperture, and discusses the shape of the defining aperture in detail. Furthermore, measures to reduce stray light are presented. The section concludes with a discussion of the uncertainty associated with the alignment of the two apertures and a discussion of the effect of the spectral distribution of the Solar Irradiance on the diffraction effect of CSAR.

Section 3.5 describes the CSAR detector system. After a description of the thermal design and a discussion of the thermal material properties of copper at cryogenic temperatures, the design choices regarding the cavity are presented. Test results indicate that the solar-weighted absorptivity of the CSAR cavity is 99.998%.

Further, measures to increase the equivalence of optical and electrical heating are discussed (among them are the use of superconducting wires). The section concludes with test results regarding the basic performance of the detector system. The natural time constant of the detector was measured to be nine seconds, and the detector response was shown to be very linear for Solar Irradiance levels from 650 W $m^{-2}$ to 1100 W $m^{-2}$.

Section 3.6 deals with the window transmittance. It describes the use of a separate transmittance monitor and describes various tests that support the validity of the transmittance value derived from the measurements of the transmittance monitor.

Section 3.8 presents an uncertainty budget for CSAR. The overall standard uncertainty for ground-based measurements is estimated to be 0.032% with sapphire window and 0.039% with fused silica window[18]. For satellite-based measurements, where no window is required, the estimated standard uncertainty is 0.011%.

## 3.2 CSAR – overview over the complete design

Figure 28 shows a 3D-model of the CSAR radiometer head.

[18] These uncertainties are associated with the measurement result of one measurement day.

**Figure 28 CSAR radiometer head, 3D model**

Figure 29 shows how the CSAR radiometer head could be used in space. It could be connected to space coolers via flexible braids (one of them would be redundant), and a two-axis sun sensor for positioning to the sun.

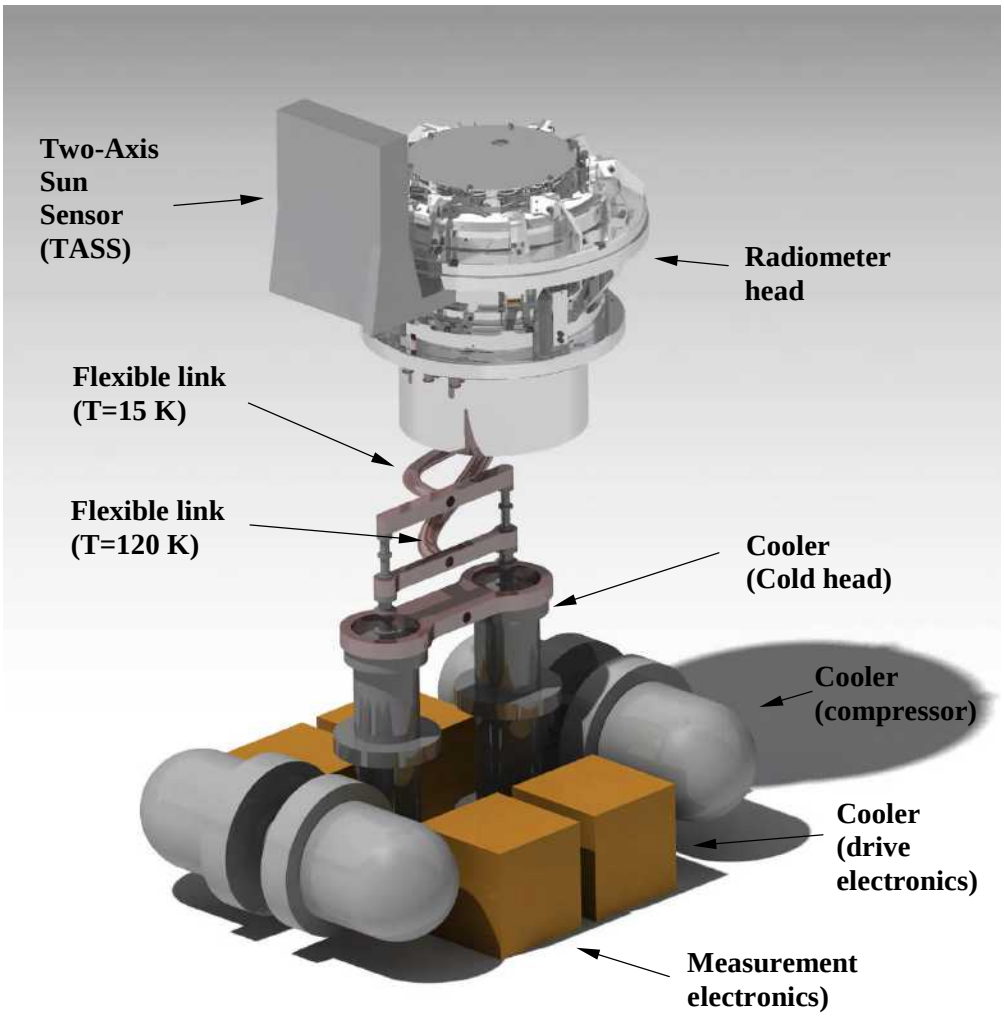


**Figure 29 CSAR radiometer head connected to space-cooler via flexible braids – 3D model of the most important elements. A cryostat will be required in addition to various cooled shields to protect the instrument and the cooler.**

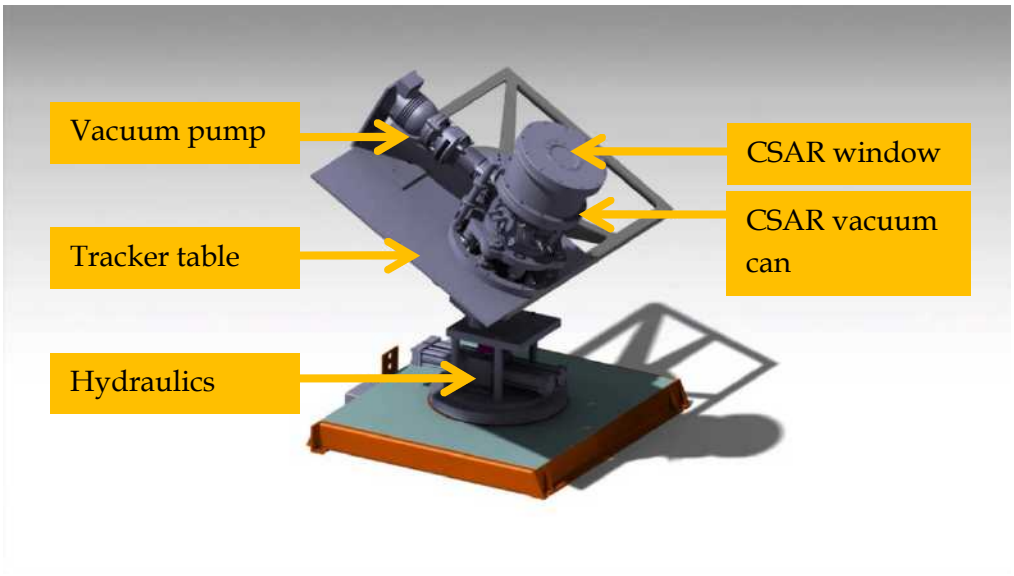


**Figure 30 CSAR mounted on solar tracker - 3D model**

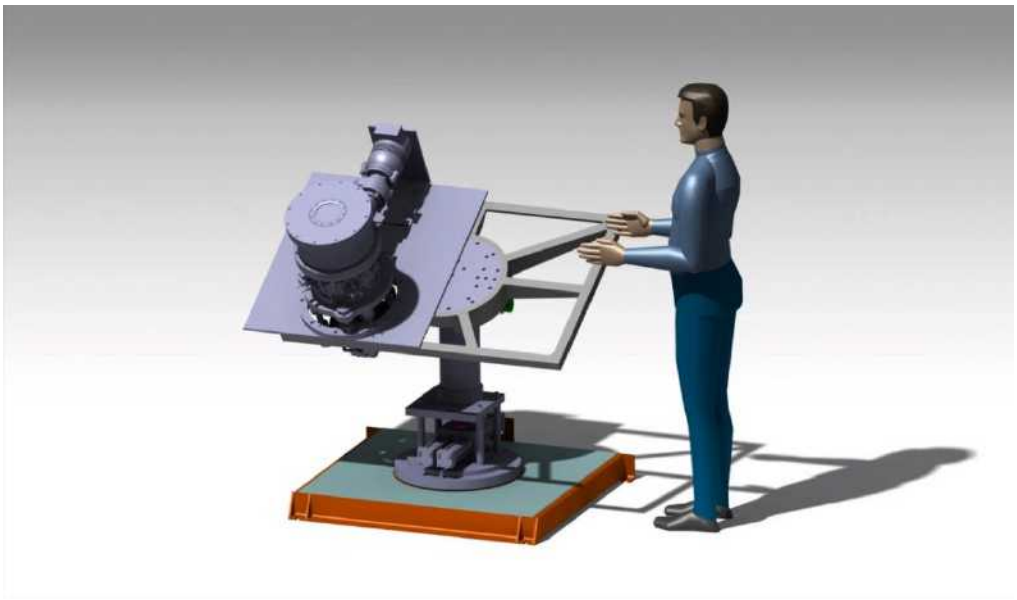

**Figure 31 CSAR on solar tracker, with size reference - 3D model**

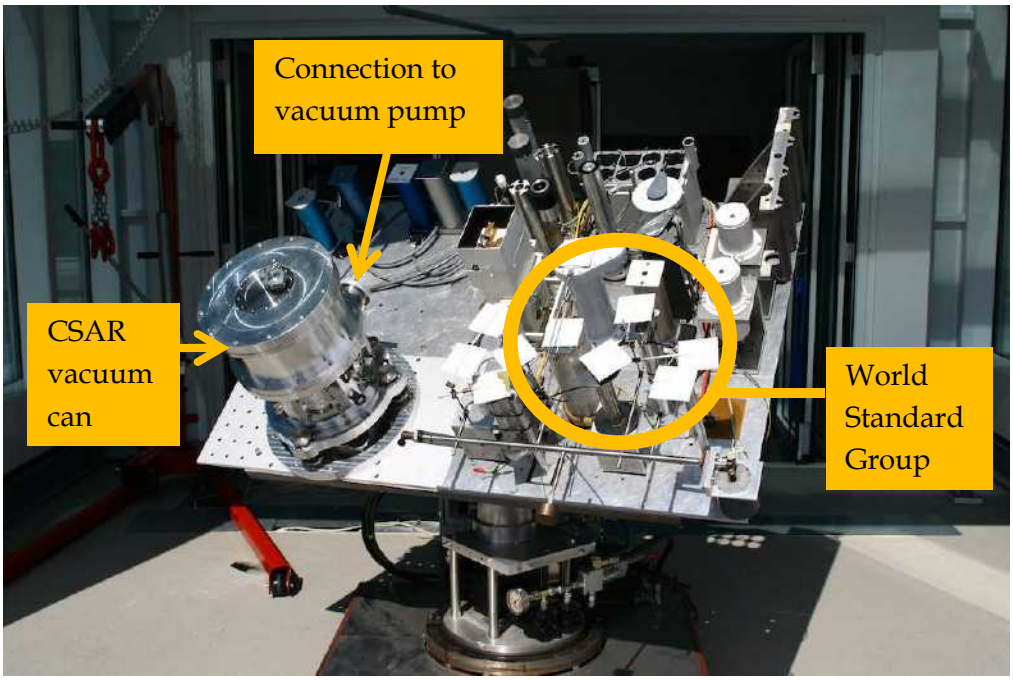


**Figure 32 Vacuum can of CSAR mounted on solar tracker in Davos (vacuum pump not connected and window replaced by steel plate)**

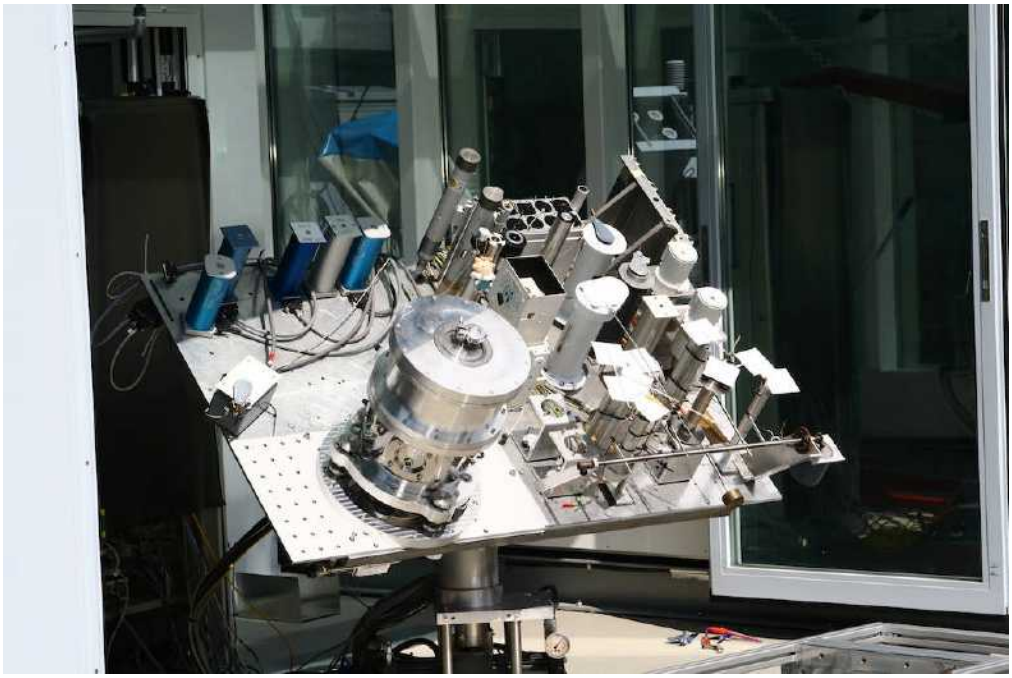

**Figure 33 Vacuum can of CSAR mounted on solar tracker in Davos (vacuum pump not connected and window replaced by steel plate)**

Figure 30 illustrates the integration of CSAR on the solar tracker in Davos, and Figure 31 gives an idea of the size of the instrument. Figure 32 and Figure 33 show a photograph of the vacuum chamber of CSAR mounted on the solar tracker in Davos (without vacuum pump and without front window).

For ground use, the radiometer head sits in a vacuum chamber (see Figure 34, Figure 35, and Figure 36) and is cooled using a closed-cycle refrigerator system with helium acting as the process gas. Figure 35 and Figure 36 also show the window, through which the light is admitted into the vacuum chamber.

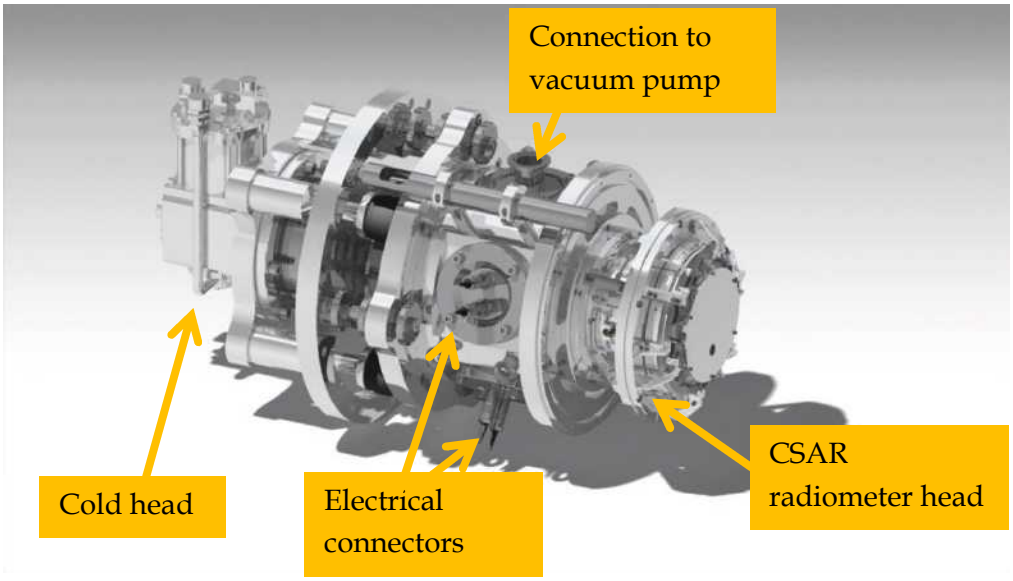


**Figure 34 CSAR radiometer head mounted in vacuum chamber, 3D model**

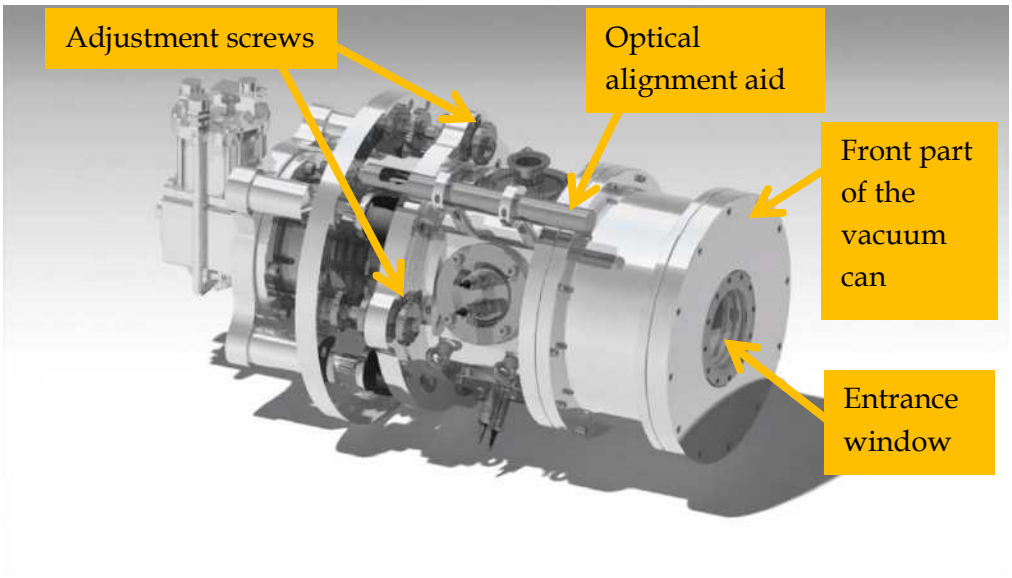


Figure 35 CSAR, vacuum chamber closed - 3D model

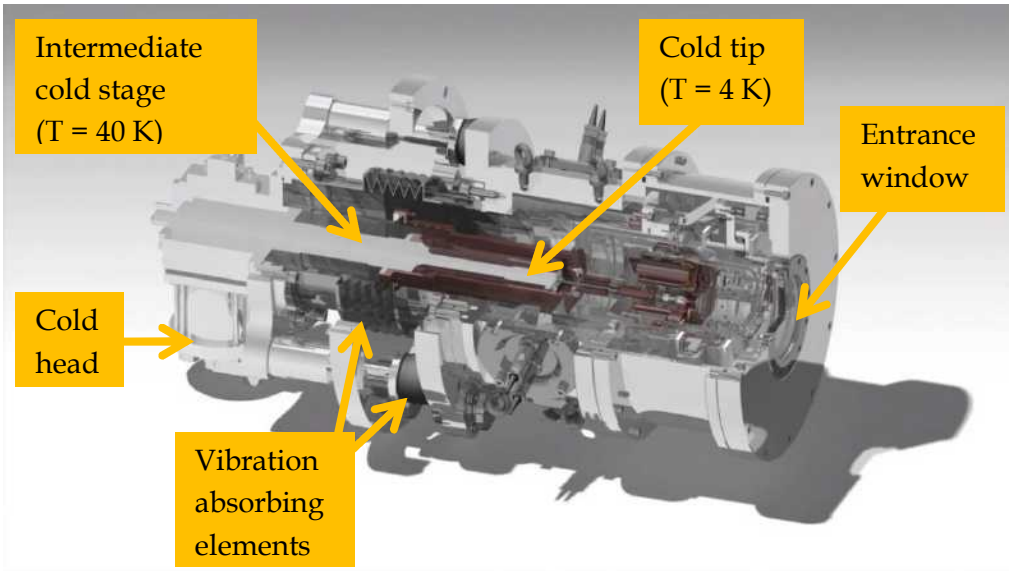


Figure 36 CSAR, radiometer head in vacuum chamber, cross-section; 3D model.

## 3.3 The radiometer head: thermal management

Figure 37 shows a cross-section of the radiometer head in the assembled state and Figure 38 gives an impression of all the main components of the radiometer head. The detector stage contains six "pockets", in each of which a cavity can be mounted. Four of these pockets are reserved for Solar Irradiance cavities; this is in order to

provide redundancy for space use. The other two places can carry high-sensitivity cavities to measure the absolute power of on-board calibration sources. However, for the purpose of the tests reported in this paper, only one Solar Irradiance cavity was installed. The detector stage (including the cavity) is almost completely surrounded by three thermal shields, which reduce radiative heat transfer from the higher to the lower temperature stages.

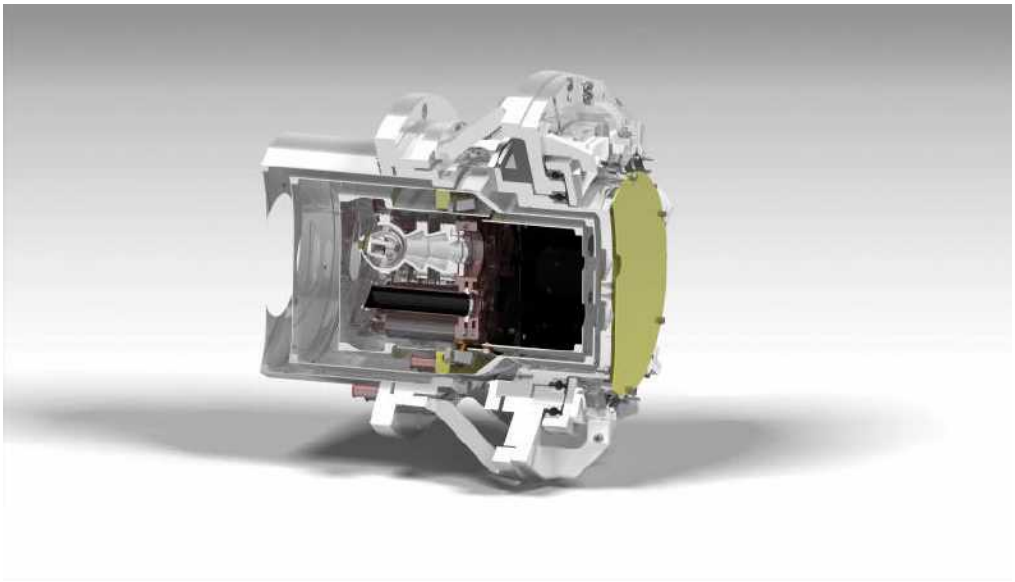

**Figure 37 CSAR radiometer head – 3D model, cross section**

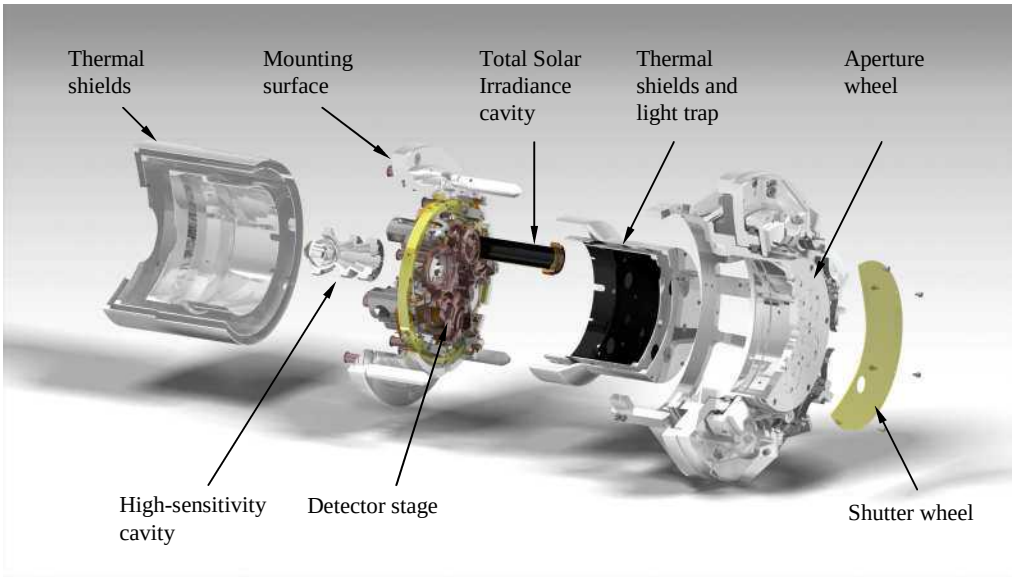


**Figure 38 Exploded view of CSAR radiometer head**

### 3.3.1 Thermal management of the heat load: design overview

This section gives an overview over the design elements that have major influence on the thermal conditions inside the radiometer head. The three different temperature levels and the two-stage cooler that creates these temperature levels are presented. Various measures to minimise the heat flow between the different stages are also introduced.

#### *3.3.1.1 Three temperature levels - overview*

There are three different temperature levels in the radiometer head (see Figure 39). The room temperature stage surrounds the intermediate temperature stage. This intermediate stage in turn encloses the detector stage which operates at the lowest temperature. The temperatures that are achievable at these stages are a function of the cooling power provided by the cooler and the heat transfer processes between the stages.

The cold stages do not carry any moving parts or critical optical elements apart from the cavities and the field-of-view apertures (on

the detector stage). All mechanisms and the precision apertures sit on the room temperature stage. This is in order to avoid unnecessary complexity of the mechanical system due to the cryogenic operation.

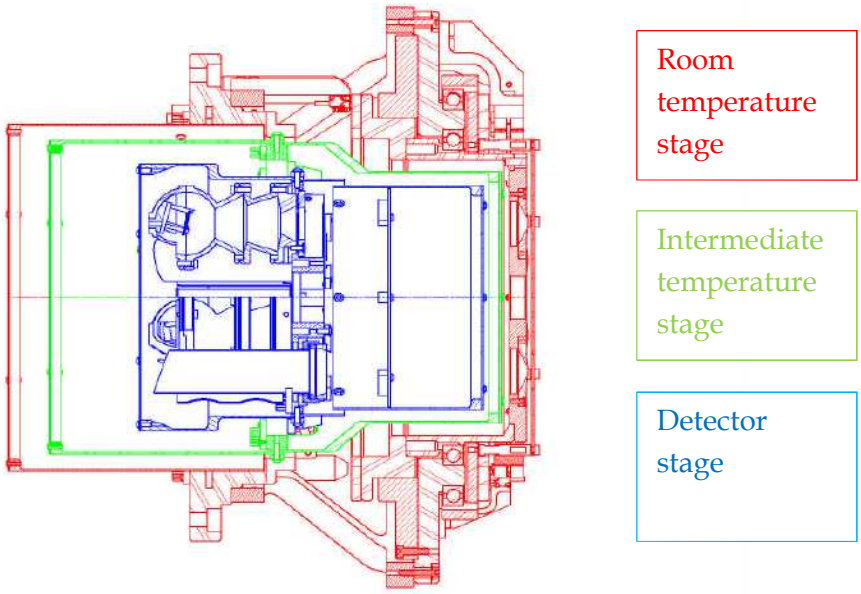


**Figure 39 Three temperature levels of the radiometer.**

Figure 39 also show the "shells" of each temperature stage. These enclosures minimise the radiative heat transfer between the different stages; this effect will be discussed further in Section 3.3.2.

### *3.3.1.2 Reference block and support structure*

The design sought to keep the cold stages as low mass as possible, in order to increase the Eigenfrequency while reducing the thermal heat transfer between the stages to a minimum. Sets of three Torlon® dumbell links (3 mm and 4 mm in diameter) mechanically connect one stage to the next stage (see Figure 40 and Figure 41)[19]. These Torlon® links are at a slight angle in order to increase the natural Eigenfrequency of the structure to 120 Hz – this was verified by finite-

[19] Torlon® was chosen due to its low thermal conductivity, its high mechanical strength, and the fact that it is a material which is commonly used in space applications.

element-analysis (FEA)[20]. FEA-modelling also indicates that the structure withstands static accelerations of 100g in any direction (see Figure 42); the maximum stress in the material is 63.9 MPa, while the tensile strength of Torlon 4203® is 124 MPa, and the compressive strength 165 MPa[21]. These design features make the radiometer in all likelihood suitable for spaceflight.

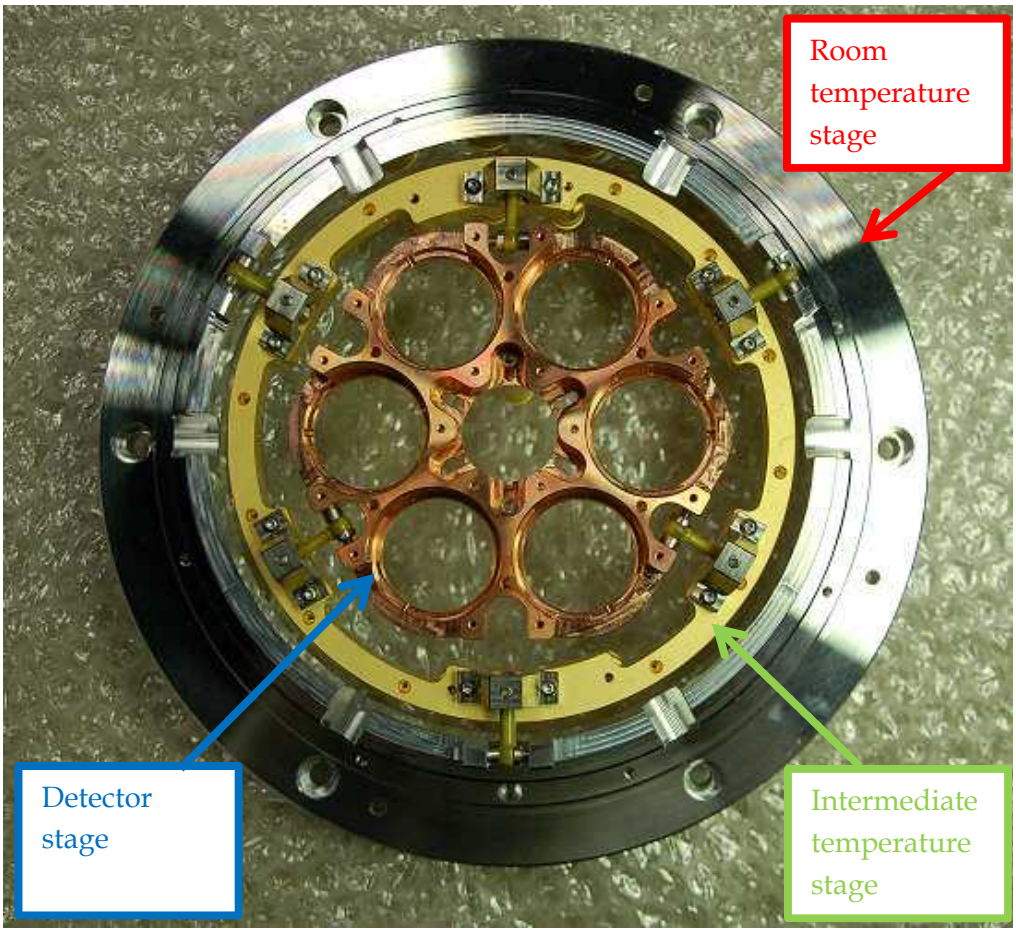


**Figure 40 Structural elements of the three temperature stages (top view)**

[20] The finite-element-analysis was performed by my colleague Peter Lovelock (NPL, Senior Design Engineer).
[21] See, for example, http://www.polytechindustrial.com/products/plastic-stock-shapes/torlon-4203 [Accessed 5 October 2012]

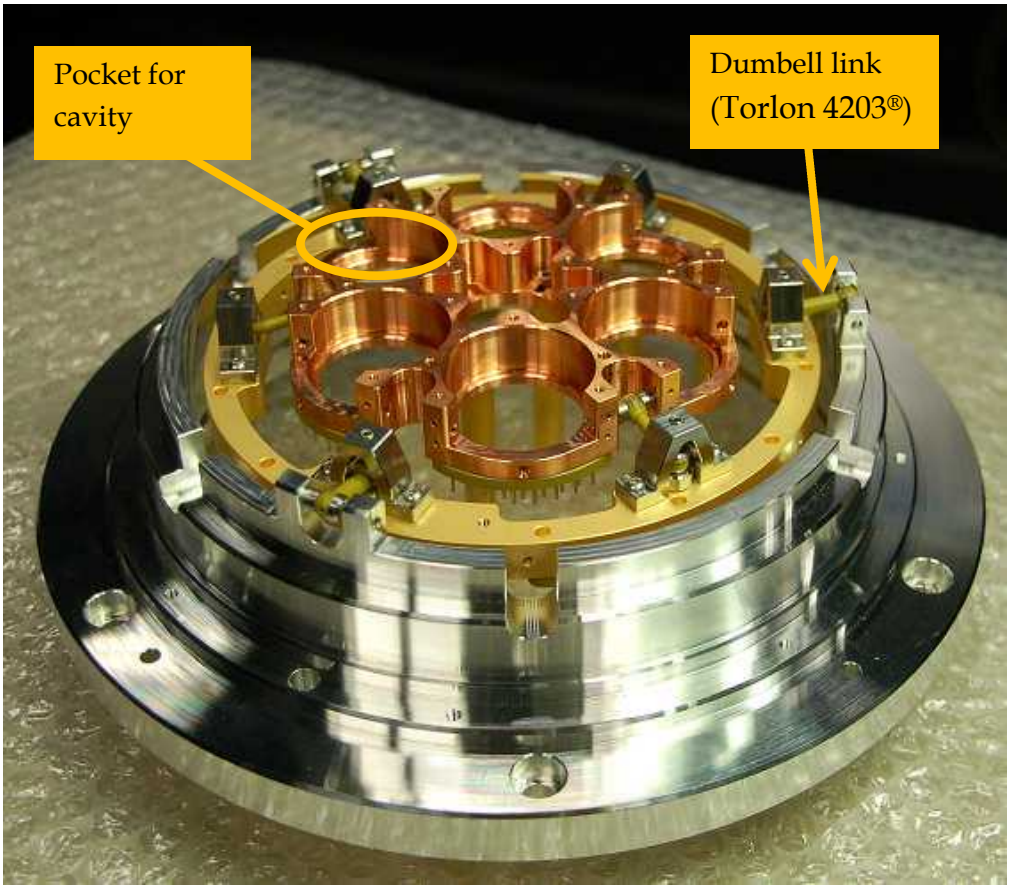


**Figure 41 Structural elements of the three temperature stages (side view)**

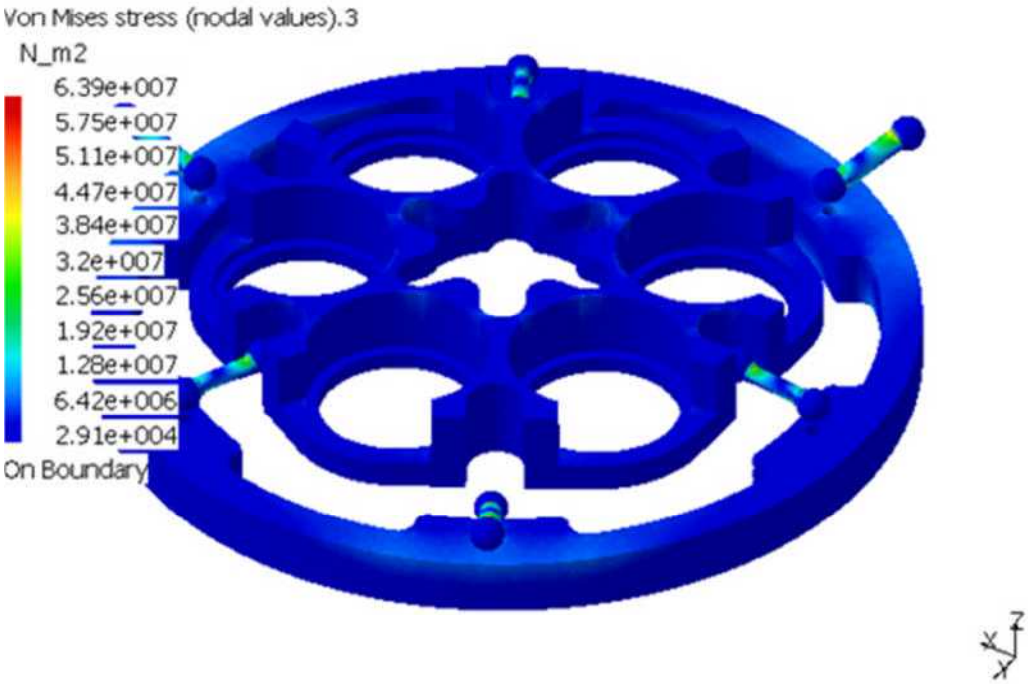


**Figure 42 Von Mises stresses due to static acceleration of 100g**

### *3.3.1.3 The mechanical cooler for ground application*

The two cold stages of the radiometer head (the intermediate stage and the detector stage) need to be connected to a mechanical cooler. The cooler that was selected for CSAR is described briefly in the following.

Figure 43 shows the cold head, which provides two cold stages, and Figure 44 shows CSAR in its lab- and transport frame; in this picture, it can be seen how the cold head of the Sumitomo cold head is integrated into the CSAR vacuum can.

Figure 45 shows the air-cooled compressor, which is connected to the cold head via flexible, metal-clad supply lines. It was necessary to select an air-cooled compressor, rather than a water-cooled compressor, since PMOD/WRC could not ensure a suitable water

supply – apart from an open-cycle water supply, which is not justifiable from an environmental point of view.

**Figure 43 Sumitomo cold head[22]**

[22]picture by Sumitomo Heavy Industries / Cryogenics Group, (online: http://www.shicryogenics.com/index.php?option=com_content&task=blogcategory&id=22&Itemid=169&lang=en) [Accessed 5 October 2012]

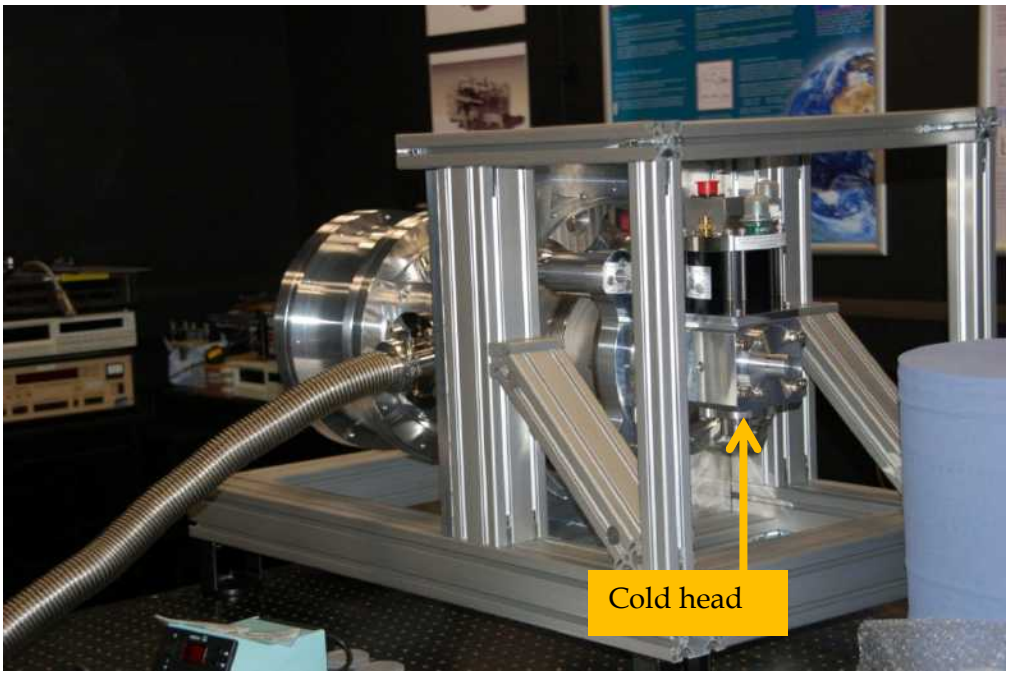


**Figure 44 CSAR in lab- and transport-frame, with cold head attached.**


**Figure 45 Air-cooled compressor[23]**

[23] Picture by Sumitomo Heavy Industries / Cryogenics group (online: http://www.shicryogenics.com/index.php?option=com_content&view=category&layout=blog&id=33&Itemid=249&lang=en) [Accessed 5 October 2012]

The performance characteristic of the Sumitomo cooler that was selected for operation on the solar tracker is shown in Figure 46. For example, it provides cooling power of 0.4 W at a cold tip temperature of 4.15 K (second stage), with a load of 15 W and a temperature of 36 K at the first cooler stage.

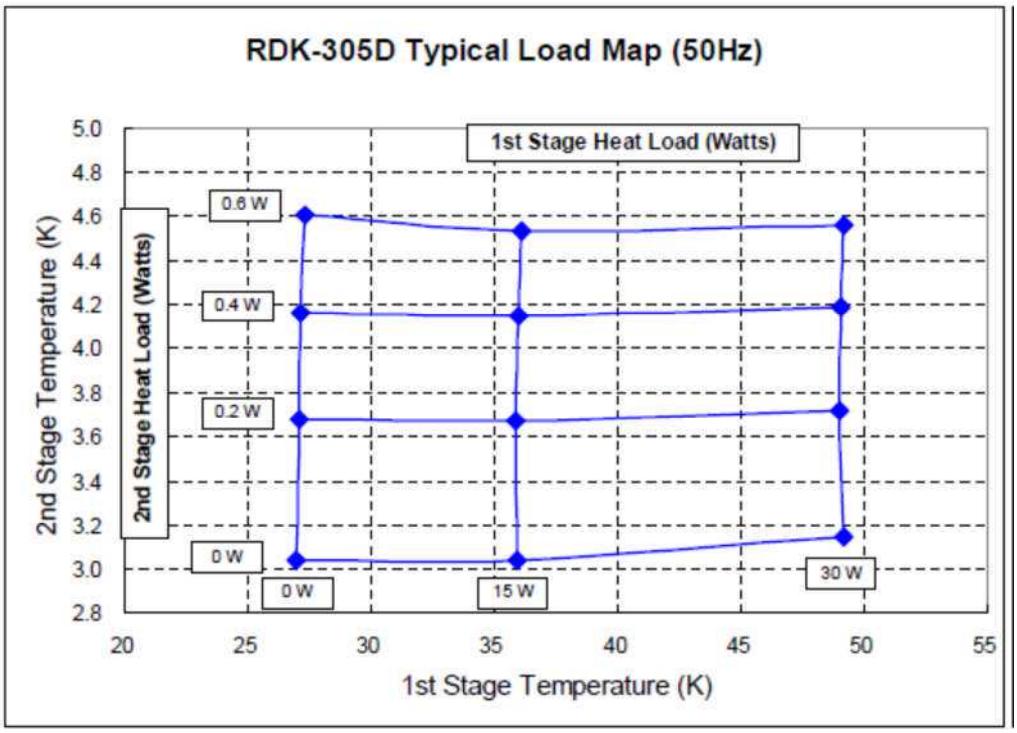


**Figure 46 Load map of SUMITOMO Gifford-McMahon Cryocooler (SRDK-305D series)[24]**

### *3.3.1.4 Connection of the cooler to the detector stage*

Flexible copper braids connect the two cold stages of the mechanical cooler (see Figure 47) to the cold stages of the radiometer head. Figure 48 shows the connection of the second stage of the cold head with the detector stage of CSAR, and Figure 49 shows the connection of the first stage of the cold head with the intermediate temperature stage of CSAR.

[24] Figure courtesy of Brian Pugsley, Sumitomo (SHI) Cryogenics of Europe Limited.

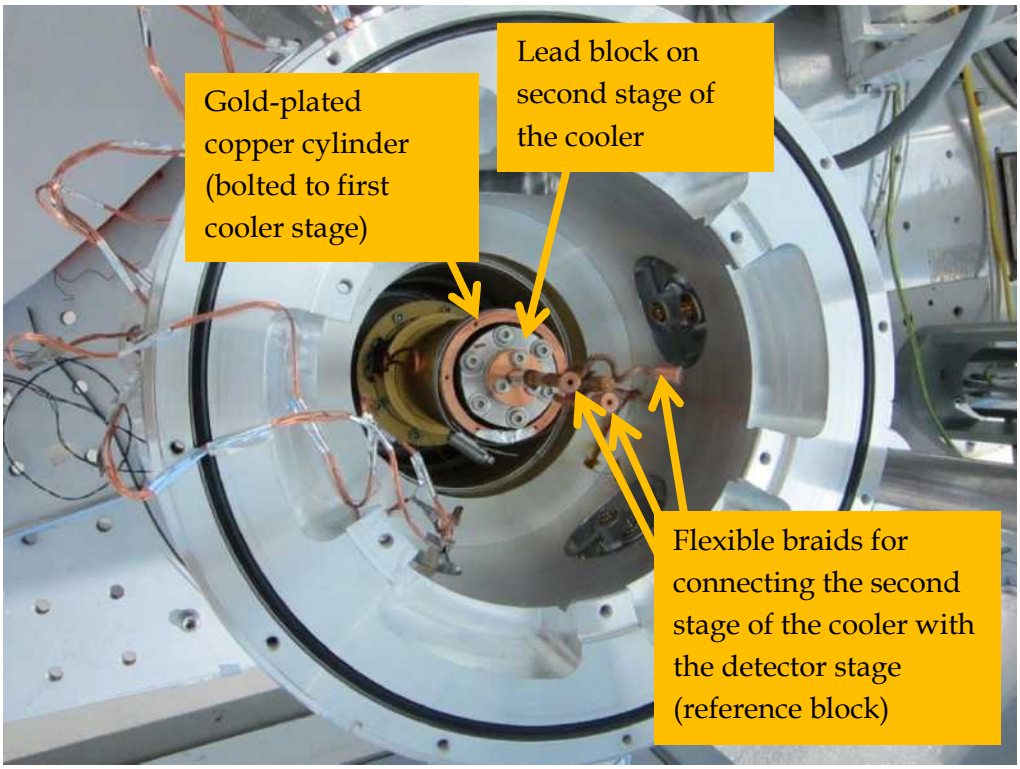


**Figure 47 Cryogenic cooler in vacuum chamber, with additional components attached (cold shield, Pb-block and flexible braids)**

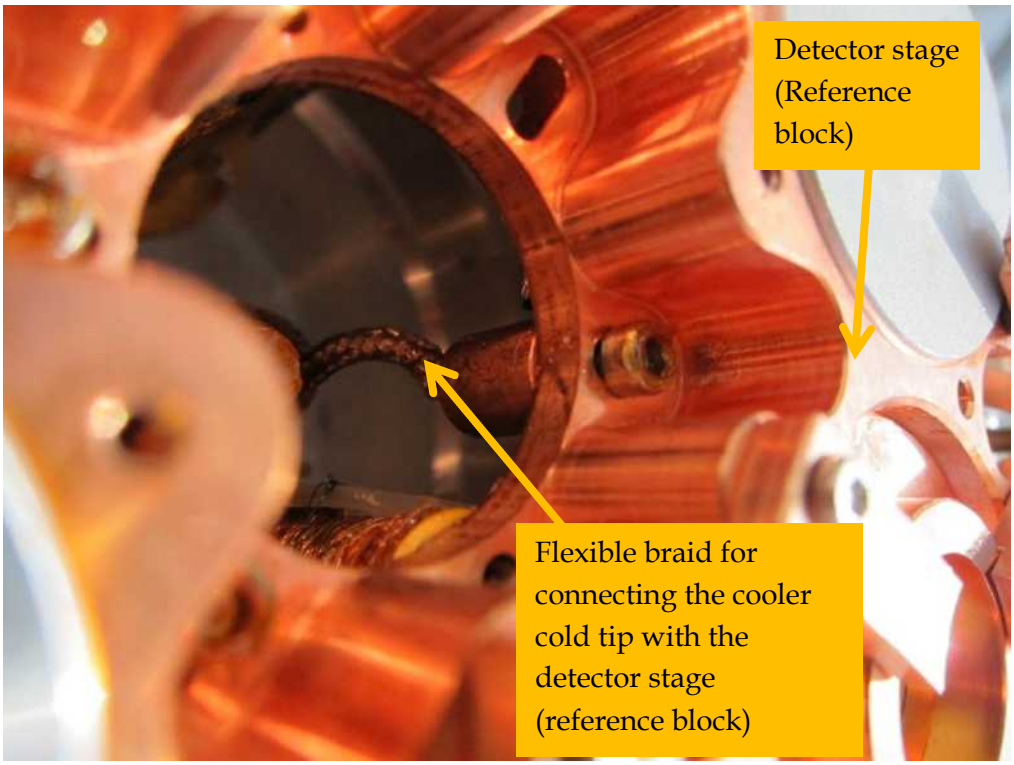


**Figure 48 Attachment of flexible braids to the reference block (the detector stage).**

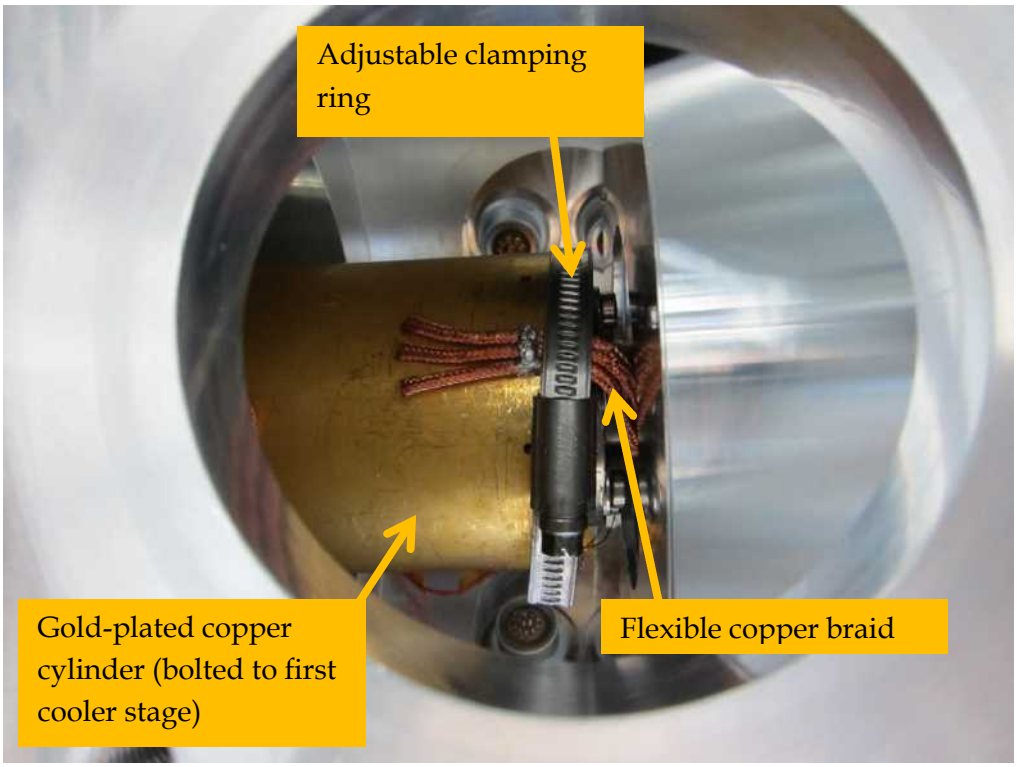


**Figure 49 Copper braids connecting the intermediate temperature stage of CSAR with the first stage of the cooler.**

### 3.3.2 Different routes of heat flow into the cold stages

The previous section gave an overview of the major design elements that determine the thermal conditions inside the radiometer head. However, in order to quantify the heat flow into the cold stages, a more detailed analysis is required; the theoretical concepts and the detailed practical implementation are presented in this current section.

Figure 50 is a schematic representation of the various paths of heat flow into the cold stages. The main paths of heat flow from the warmer to the colder stages are: (1) conduction through the support structure, (2) conduction through the electrical wires, and (3) direct radiative heat transfer between the cold shields, and (4) radiative heat transfer through openings in the cold shields. The theory underlying these four effects is considered in the current section.

Figure 50 also shows two sources of heat flow into the detector stage which do not have their origin in the other two temperature stages. These external sources of heat are (1) the electrical heating of the detector stage for the purpose of controlling its temperature, and (2) the solar radiation entering the detector. The amount of solar radiation entering the detector is a function of the size of the entrance aperture; these considerations are discussed in Section 3.4.1.

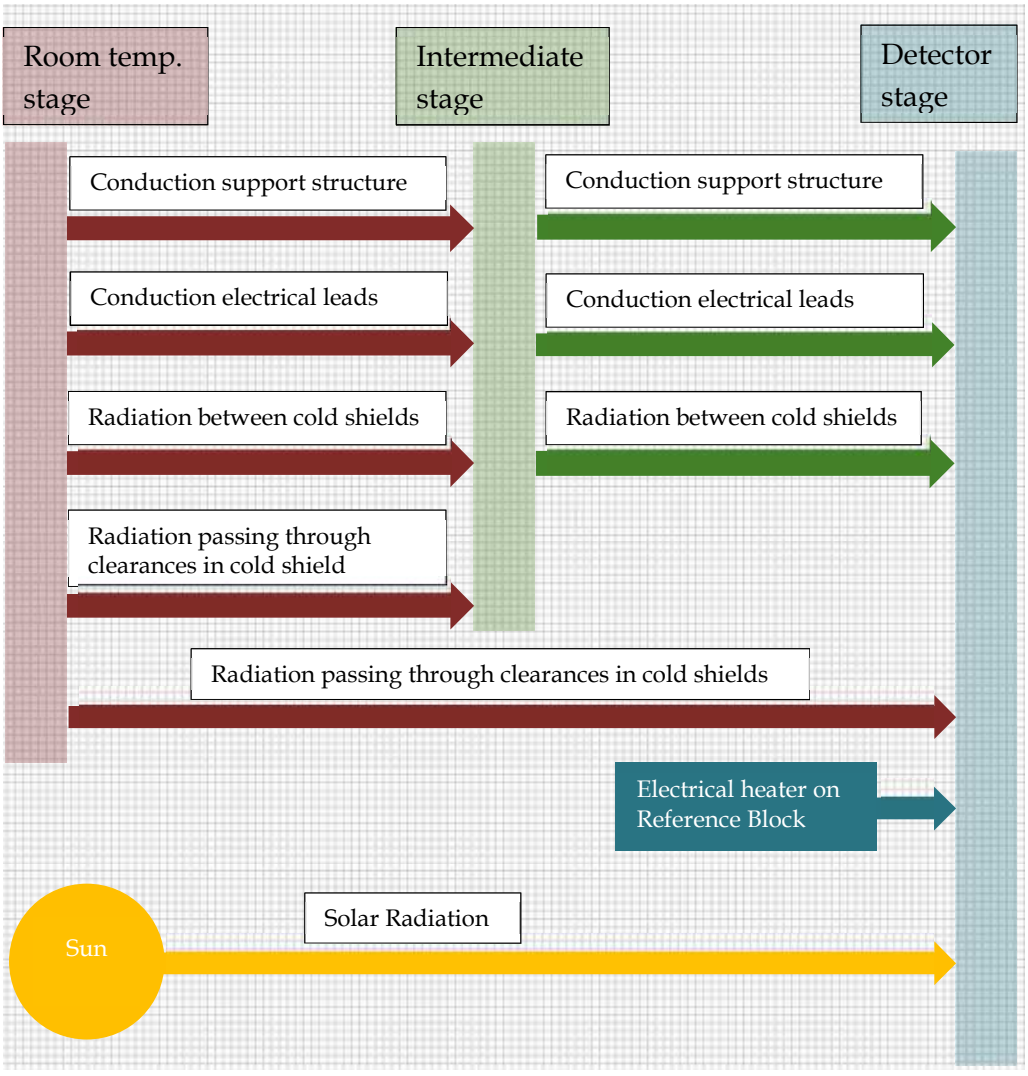


**Figure 50 Schematic illustration of various sources of heat flux into the cold stages.**

### 3.3.2.1 *Conduction of heat through the support structure*

As already mentioned in Section 3.3.1.2, the structural connection between the three temperature stages consists of two sets of three dumbbell links. Figure 51 gives a close-up view of one of the Torlon® dumbbell link connections. Here, the heat flow by conduction through the dumbbell links is explored in general terms. Calculation results are presented in the Section 3.3.3.

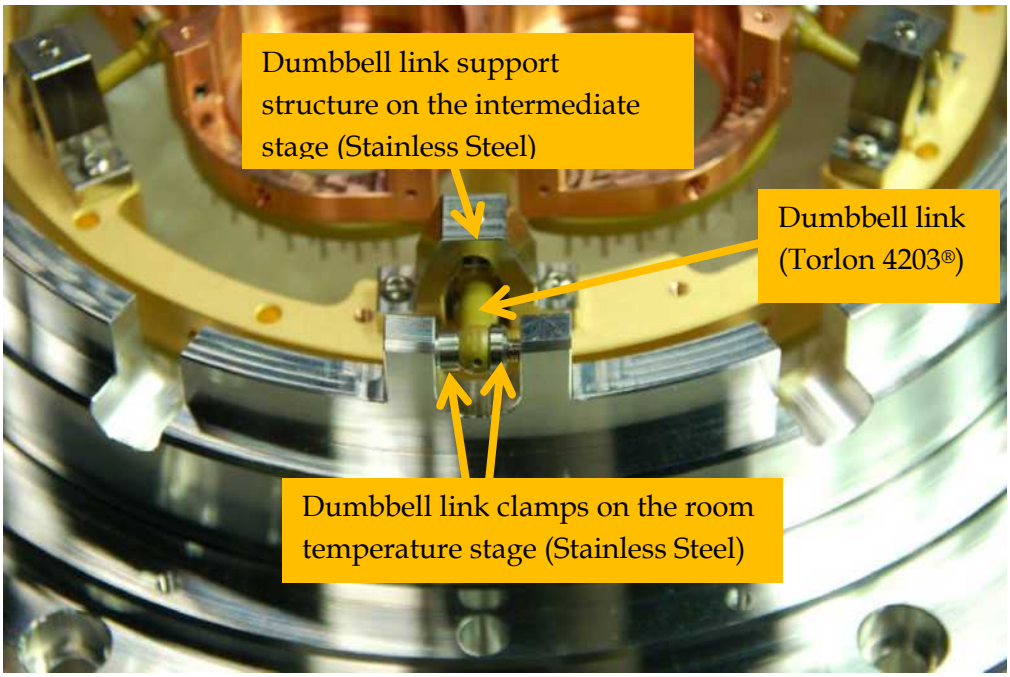


**Figure 51 Torlon® link between cold stages (detail)**

For a conductor of cross-sectional area A and length L, the steady-state heat flow $\dot{Q}$ across an element of length dl is

$$\dot{Q} = \kappa(T) A \frac{dT}{dl}, \tag{3.1}$$

so that

$$\dot{Q} \int_0^L dl = A \int_{T_1}^{T_2} \kappa(T)\, dT, \tag{3.2}$$

where $T_1$ and $T_2$ are the temperatures at $l_1$=0 and $l_2$=L, respectively.

The heat flow is therefore

$$\dot{Q} = \frac{A}{L}\int_{T_1}^{T_2} \kappa(T)\,dT \qquad (3.3)$$

Equation (3.3) shows that the heat flow through the connection is determined by the aspect ratio of the link and the thermal conductivity of the material. Since the aspect ratio also has an impact on the mechanical strength of the connection, the design called for a trade-off between mechanical and thermal requirements. The connections were designed such that the mechanical requirements for space flight can be met while at the same time not allowing too much heat flow between the temperature stages. Figure 52 shows the thermal conductivity of Torlon 4203® at temperatures between 4 K and 300 K.

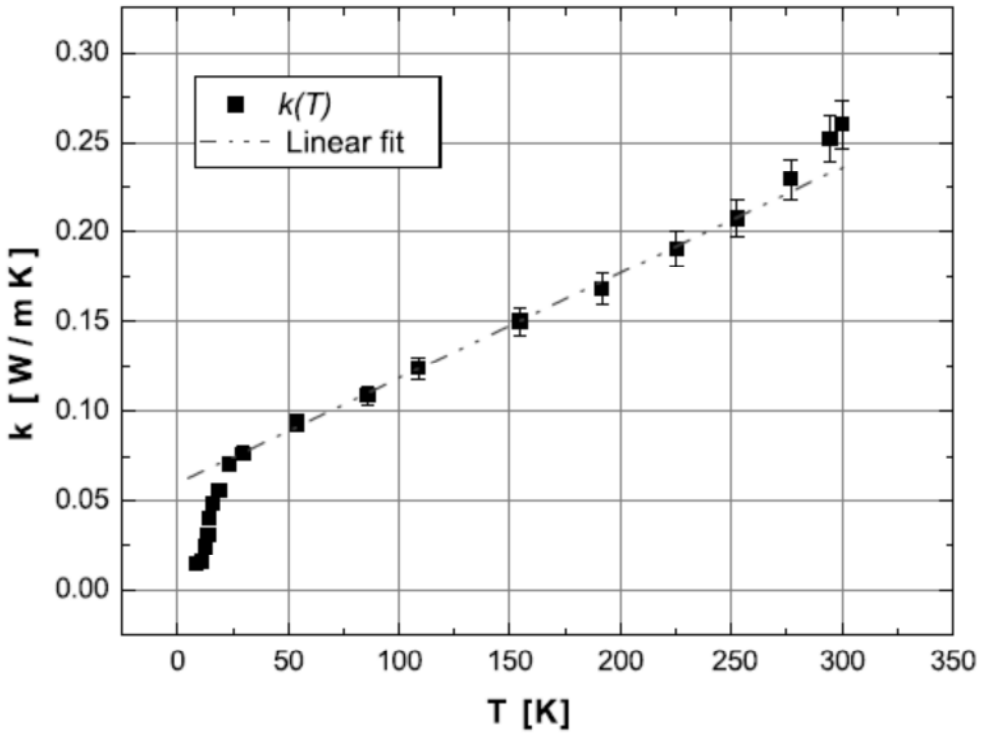


**Figure 52 Thermal conductivity of Torlon 4203® in the temperature range 4.2 K – 300 K. Graph reproduced from (Barucci et al., 2005).**

### *3.3.2.2 Conduction through electrical leads*

The temperature sensors on all six cavities plus the thermometer and heating elements on the reference block require 68 wires connecting the room temperature stage to the intermediate stage, and 64 wires connecting the intermediate stage to the detector stage[25]. For the calculation of the heat flow by conduction through these leads, the same formalism applies as in the case of the dumbbell links (see Equation (3.3)).

There are several different materials that could have been used for the electrical wires; however, constantan was preferred due to its low thermal conductivity and due to the fact that it is comparatively

[25] The calculations presented here assume the use of one thermometer on the intermediate stage and of eight thermometers as well as eight heaters on the detector stage.

easy to work with (e.g. good solderability and good ductility – compared to other cryogenic wires).

The diameter of the constantan wires is 61 μm, and the length of the wires was optimised with regard to the wires that carry the highest current. There is an optimum length of the wire where the sum total of thermally conducted heat and electrically dissipated heat in the wire is at a minimum. Buyanov et al. (Buyanov et al., 1975) give relations for materials whose electrical resistivity does not change significantly over the applied temperature range. Given this assumption, which is sufficiently valid for constantan, the minimum amount of heat transfer is

$$\dot{Q}_{\min} = I\sqrt{2\rho\int_{T_{cold}}^{T_{hot}}\kappa(T)\,dT}\,, \tag{3.4}$$

where I is the electrical current flowing through the wire and ρ is the electrical resistivity of the wire material.

This minimum heat transfer calculated in Equation (3.4) is observed if the ratio of wire length L and cross-section A is at an optimum (again, see (Buyanov et al., 1975)):

$$\left(\frac{L}{A}\right)_{opt} = \frac{1}{I}\sqrt{\frac{2}{\rho}\int_{T_{cold}}^{T_{hot}}\kappa(T)\,dT} \tag{3.5}$$

The current *I* is very different for the different electrical wires used in CSAR. While the voltage sensing wires do not carry any significant current, some wires carry a current of 0.2 mA – energizing the thermometers. The highest current that is necessary is for the

electrical heating of the Total Solar Irradiance cavities[26] – and these are the wires the optimisation has been carried out for in the following.

An irradiance of 1365 W/m$^2$ at the top of the atmosphere and a defining aperture with diameter 5 mm leads to an optical power of 26.8 mW entering the cavity. In order to substitute this optical power with electrical power, a current of 5.2 mA must be applied to a 1000 Ω heating element.

Using the manufacturer data for the electrical resistivity of the constantan wires (ICEOxford) and conductivity data from (White and Meeson, 2002), and a wire cross-section with diameter 61 µm, Equation (3.5) leads to an optimum wire length of 46 mm and a heat transfer of 8 mW between the intermediate stage and the detector stage. For the wires between the room temperature stage and the intermediate stage, an optimum length of 74 mm and a heat flow of 13 mW was calculated; these numbers assume temperatures of 20 K at the detector stage and 120 K at the intermediate stage, which are the temperature levels expected to be achievable with a space cooler. The design sought to implement these optimum wire lengths according to these calculations.

Figure 53 shows the electrical leads connecting the different stages. The wires are heat sunk at every stage by wrapping them around heat sink bobbins. Note that Figure 53 only shows the electrical wiring necessary for the operation of one cavity. This was the configuration used in the comparison of CSAR with the SI and with

[26] The requirements for measuring Total Solar Irradiance at the top of the atmosphere was chosen as the baseline for the wire optimisation calculations because the most stringent restrictions regarding heat transfer between the stages originates from the low cooling power of space coolers.

the World Radiometric Reference, which are experiments reported later on in this document (see Chapter 4).

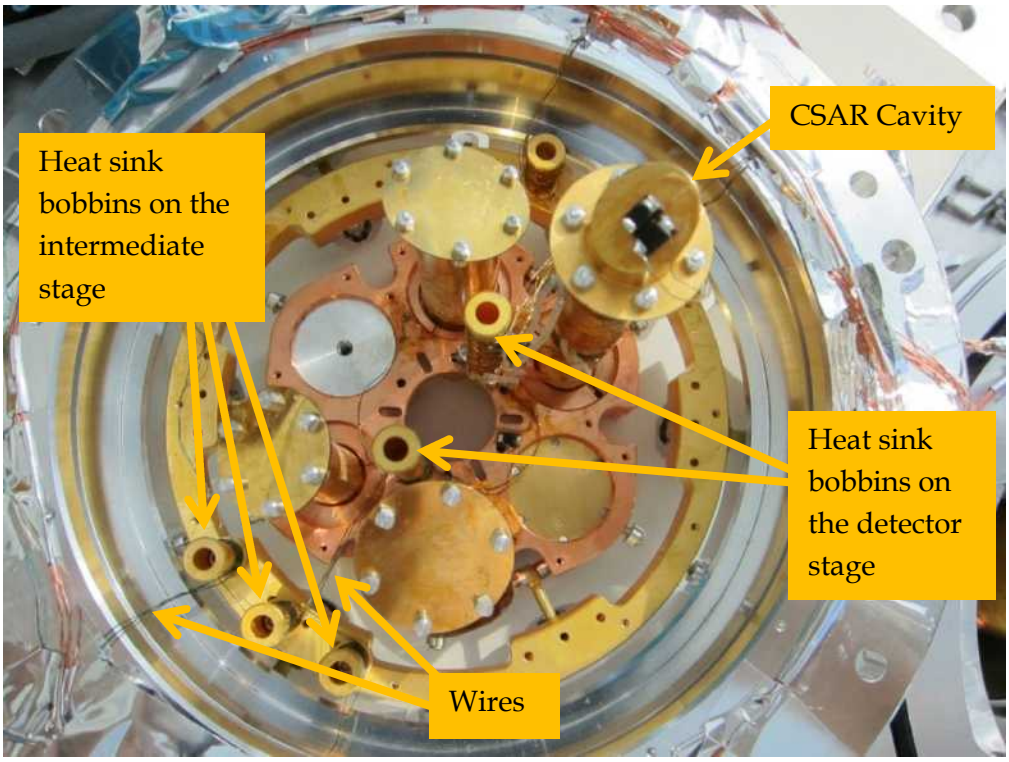


**Figure 53 Heat sinking of electrical wires**

### *3.3.2.3 Radiative heat transfer between cold shields*

The management of the thermal load also includes the design of the radiation shields and their mechanical support. The function of these radiation shields is (a) to minimise the heat load on the cooler and (b) to improve the measurements by reducing the radiative transfer of heat into the detector assembly.

Figure 54 shows a simplified schematic representation of the three cold shields; the geometry of the cold shields[27] has been simplified for the purpose of the following analytical treatment of the problem. This simplification of the geometry is justified (1) since the

[27] For a cross section of the real CSAR geometry, see Figure 39 in Section 3.3.1.1

overall uncertainty of the calculation of the radiative heat transfer will be dominated by the uncertainties in the optical surface properties of the cold shields, and also (2) since the uncertainty aim for these calculations is not particularly ambitious; an uncertainty of the order of 10% to 20% would be sufficient to evaluate the suitability of the thermal design of CSAR. The uncertainty due to the geometrical deviation from reality will be estimated by varying the geometrical parameters of the simplified geometry.

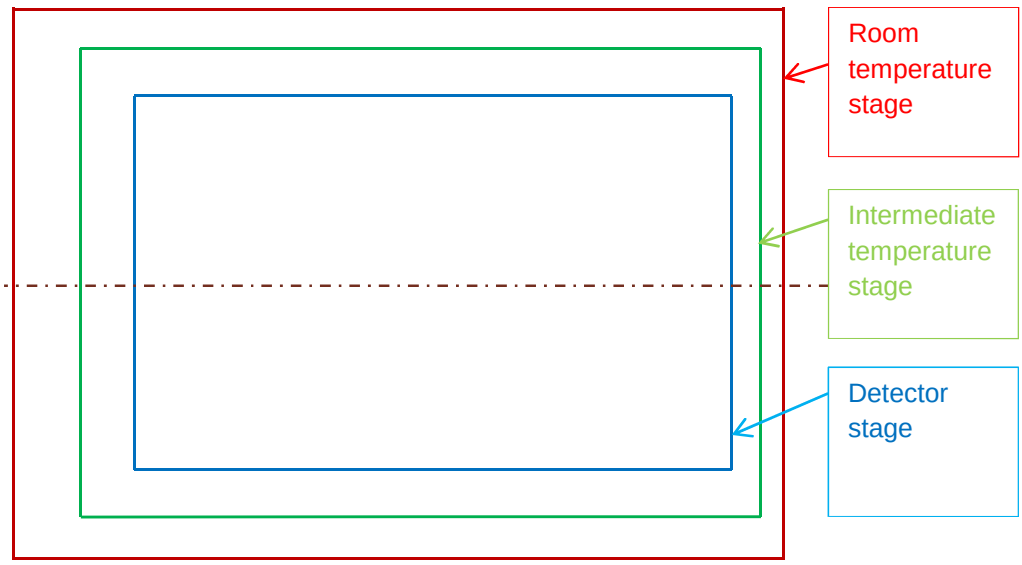


**Figure 54 Simplified schematic representation of the radiation shields surrounding the three temperature stages. The dotted line is the rotational axis of the shields.**

In order to estimate the heat transfer by radiation $\dot{Q}$, the following well-known relation is often used (see, for example (White and Meeson, 2002)):

$$\dot{Q} = \sigma A \left( T_1^4 - T_2^4 \right) \frac{\varepsilon_1 \varepsilon_2}{\varepsilon_1 + \varepsilon_2 - \varepsilon_1 \varepsilon_2}, \qquad (3.6)$$

where

A is the surface area of each of the two surfaces,

$T_1$ is the temperature of Surface 1,

$T_2$ is the temperature of Surface 2,

$\varepsilon_1$ is the hemispherical surface emissivity of Surface 1, and

$\varepsilon_2$ is the hemispherical surface emissivity of Surface 2.

Equation (3.6) only applies if the surface emissivities (and absorptivities) are wavelength-independent; however, this is not the case for Aluminium and Aluminium alloys as used for the CSAR cold shields. In a more general form, the net radiative heat transfer between two cold shields can be expressed as

$$\dot{Q}_{Rad} = \int_0^\infty A \frac{\varepsilon_1(\lambda,T_1)\,\varepsilon_2(\lambda,T_2)}{\varepsilon_1(\lambda,T_1)+\varepsilon_2(\lambda,T_2)-\varepsilon_1(\lambda,T_1)\,\varepsilon_2(\lambda,T_2)}\left[E_{BB}(\lambda,T_1)-E_{BB}(\lambda,T_2)\right]d\lambda \tag{3.7}$$

where

$E_{BB}(\lambda,T_1)$ is the blackbody hemispherical emissive power of Surface 1, and

$E_{BB}(\lambda,T_2)$ is the blackbody hemispherical emissive power of Surface 2.

The spectral distribution of the blackbody hemispherical emissive power is given by [(Howell et al., 2010), page 17]

$$E_{BB}(\lambda,T) = \frac{2\pi h c_0^2}{n^2\lambda^5\left[\exp\left(\frac{hc_0}{nk_B\lambda T}\right)-1\right]} \tag{3.8}$$

where

$c_0$ is the speed of light in vacuum,

$h$ is Planck's constant,

$k_B$ is Boltzmann's constant, and

$n$ is the refractive index.

In order to estimate the spectral hemispherical emissivities of the cold shield surfaces, $\varepsilon_H(\lambda,T)$, the model presented by Tsujimoto et al. [(Tsujimoto et al., 1982), Equations(1)-(4)] is used to first calculate the wavelength- and temperature-dependent complex refractive index of the surface. Then, the temperature dependence of the complex refractive index is estimated using measured values of the temperature dependence of the electrical resistivity of the material. The complex refractive index is then used to determine $\varepsilon_H(\lambda,T)$. Further detail regarding these calculations can be found in Appendix D.

Figure 55 shows the calculated spectral hemispherical emissivity of Al6082 for the three temperature levels that are relevant for the space application of CSAR. The plot shows that the emissivity tends to become smaller with increasing wavelengths.

The plot also shows the spectral hemispherical emissive power distributions of blackbodies at these three temperatures. It is clear from this plot that the total (i.e., spectrally integrated) hemispherical emissivity must also become smaller with decreasing temperature, since the black body emissions are shifted towards the longer wavelengths with decreasing temperatures, and since (as already

mentioned) the emissivity decrease with longer wavelengths. The total hemispherical emissivity $\varepsilon_{H,T}(T)$ is defined as:

$$\varepsilon_{H,T}(T) = \frac{\int_0^\infty \varepsilon_H(\lambda,T) E_{BB}(\lambda,T) d\lambda}{\int_0^\infty E_{BB}(\lambda,T) d\lambda} = \frac{\int_0^\infty \varepsilon_H(\lambda,T) E_{BB}(\lambda,T) d\lambda}{\sigma T^4} \tag{3.9}$$

where $\sigma$ is the Stefan-Boltzmann constant.

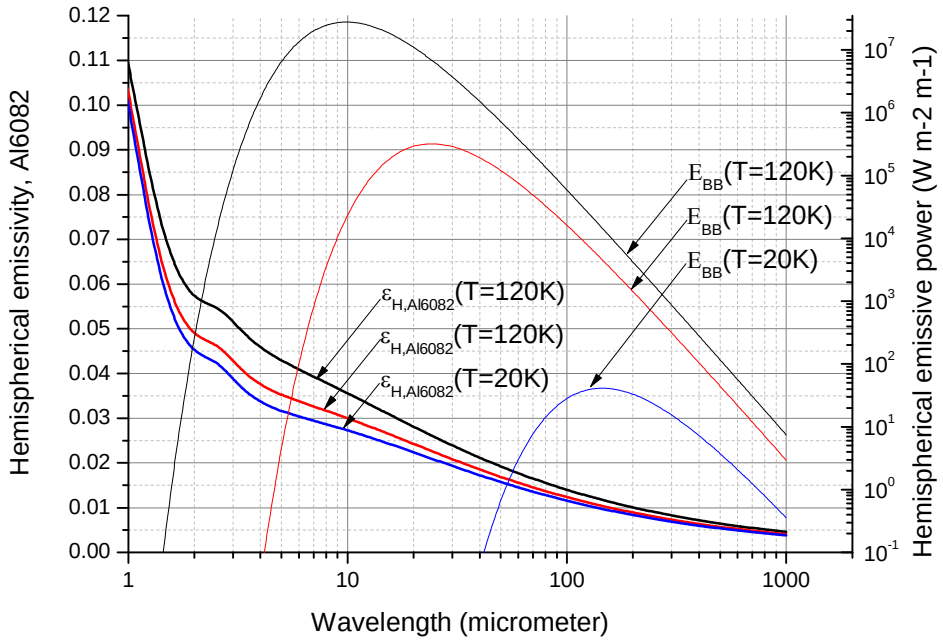


**Figure 55 Spectral hemispherical emissivity of Al6082 with respect to wavelength and temperature**

### *3.3.2.4 Radiative heat transfer through openings in the cold shields*

Purely from the perspective of thermal management, it would be ideal if the cold shields were completely closed shells. However, this would be impractical since the admittance of optical radiation into the detector requires the cold shields to have openings at the front. Figure 56 shows the six openings at the front of the intermediate stage cold

shield. The four openings for the Solar Irradiance channels are of diameter 14.8 mm, and the two clearances for the high sensitivity channels have a diameter of 8 mm each.

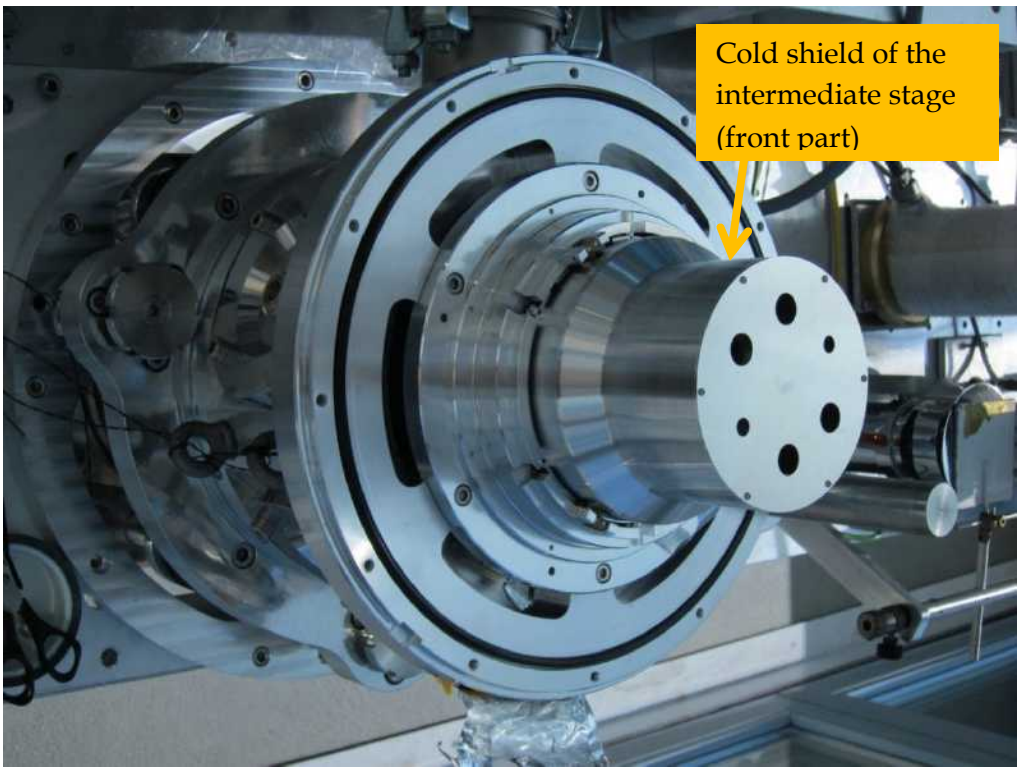


**Figure 56 Intermediate-stage cold shield (front part)**

Figure 57 shows a schematic of the three temperature stages with openings in the two cold stages. From this figure, it is clear that each temperature stage sends out thermal radiation to the two other temperature stages. These heat transfer processes are explored in the following.

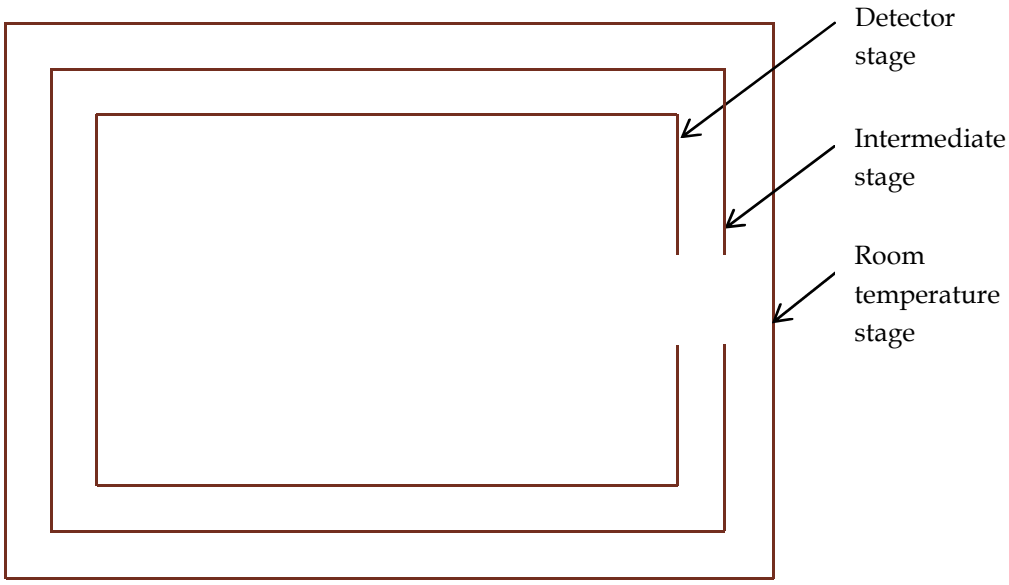


**Figure 57 Schematic of the three temperature stages with clearances in the cold shields. This schematic is for illustration purposes only; it does not give a one-to-one representation of the CSAR design.**

Figure 58 illustrates the direct radiative heat transfer from the room temperature stage to the detector stage. This part of the heat transfer can be modelled as a radiative transfer between a hollow enclosure with a circular entrance aperture of diameter $d_{\text{int}}$ (or radius $r_{\text{int}}$) and another hollow enclosure with a circular entrance aperture of diameter $d_{\text{det}}$ (or radius $r_{det}$). The enclosure with entrance diameter $d_{\text{det}}$ (the enclosure on the left hand side in the simplified schematic of Figure 58) is largely identical with the radiation trap of the detector stage – its emissivity can therefore be assumed to be unity for the purpose of this calculation. Its temperature is that of the detector stage.

The emissivity and the blackbody temperature of the enclosure on the right-hand side, however, are very difficult to determine. This is due to the complicated geometry, the combination of several different materials and the fact that not all surfaces are at the same temperature

– some surfaces are at room temperature and some are at the temperature of the intermediate stage.

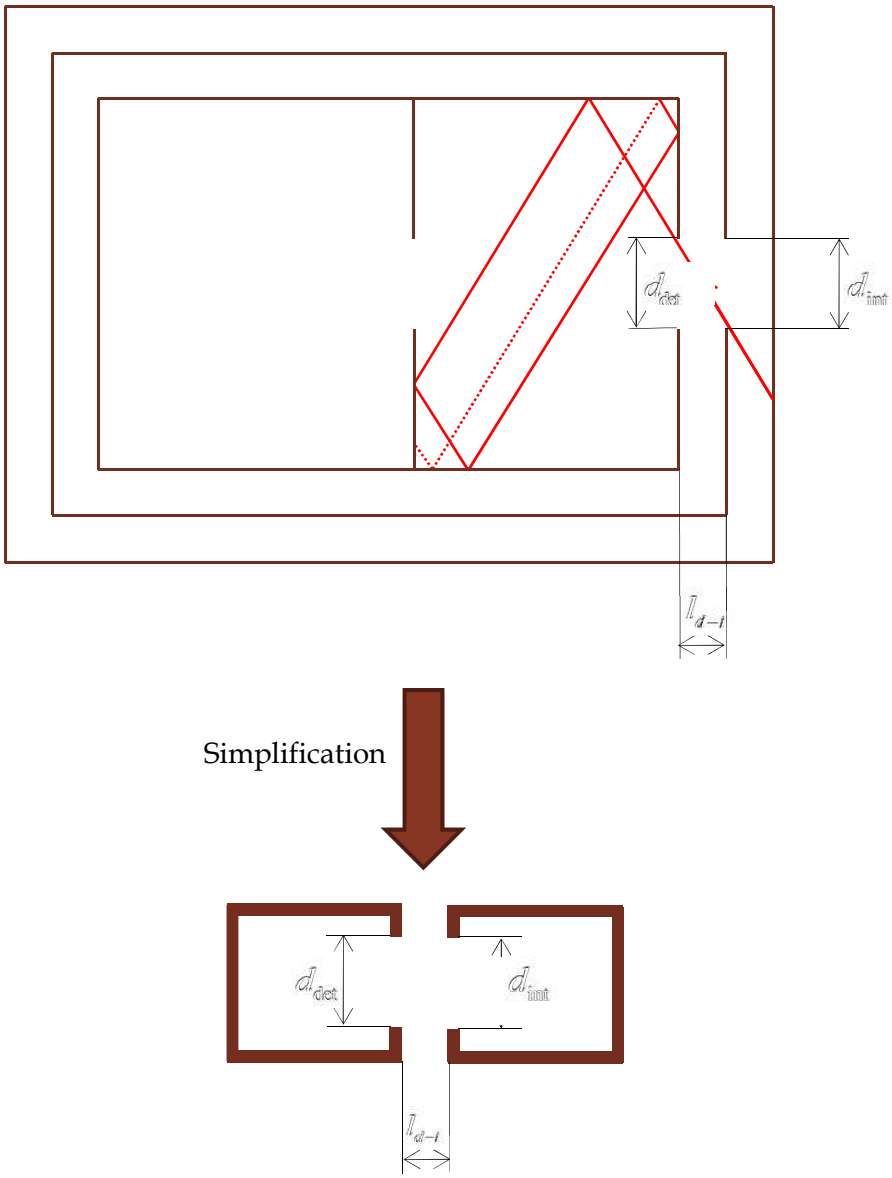


**Figure 58 Illustration of direct radiation transfer between the room temperature stage and the detector stage.**

The fact that it is not straightforward to determine the emissivity and the effective blackbody temperature of the enclosure on the right-hand side makes it difficult to calculate the exact value of the

radiative heat transfer between the two enclosures; however, it is possible to assume upper estimates for the emissivity and the temperature and therefore to calculate an upper estimate for the heat transfer. The emissivity cannot be larger than unity, and the temperature cannot be higher than room temperature $T_{rt}$. The upper estimate for the radiative heat transfer due to this effect can therefore be expressed by the following relation:

$$Q_{rt->\det,direct} = F_{rt->\det} A_{\text{int}} \sigma \left( T_{rt}^4 - T_{\det}^4 \right) \tag{3.10}$$

with a view factor of

$$F_{rt->\det} = \frac{r_{\text{int}}^2}{r_{\text{int}}^2 + r_{\det}^2 + l_{d-i}^2 + \sqrt{\left( r_{\text{int}}^2 + r_{\det}^2 + l_{d-i}^2 \right)^2 - 4 r_{\text{int}}^2 r_{\det}^2}} \tag{3.11}$$

and an entrance aperture area of

$$A_{\text{int}} = \pi r_{\text{int}}^2 \tag{3.12}$$

The minimum value for the heat transfer is zero. The standard uncertainty of this estimate for the radiative heat transfer was therefore estimated as $Q_{rt->\det,direct} / \left( 2\sqrt{3} \right)$ (as discussed in Section 2.4.3).

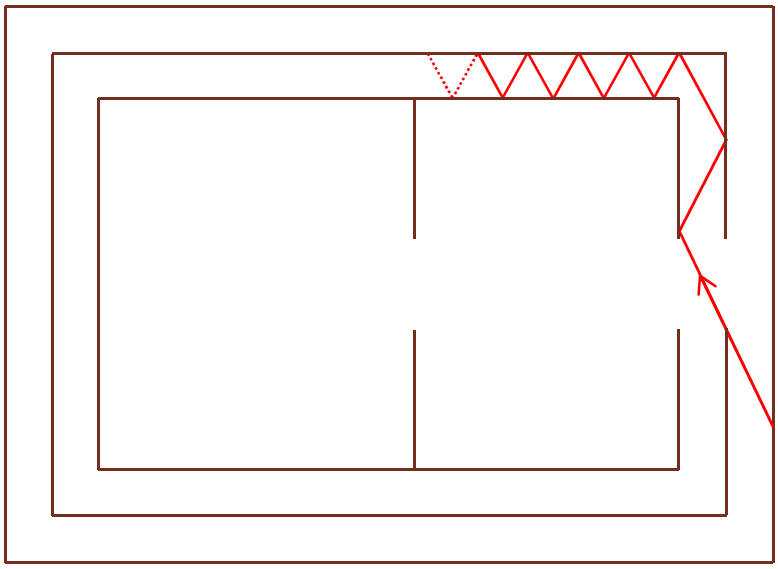

**Figure 59 Illustration of radiative heat transfer from the room temperature stage to the outside surface of the detector stage shield and the inside surface of the intermediate stage.**

Apart from the direct radiative heat transfer from the temperature stage to the inside surface of the detector stage as described above, there is also radiation emitted by the room temperature stage which is transferred to the outside surface of the detector stage shield (with an emissivity $\varepsilon_{\mathrm{det},outside}$) and the inside surface of the intermediate stage shield (with an emissivity $\varepsilon_{\mathrm{int},inside}$); this process is illustrated in Figure 59. In order to estimate this effect, it is assumed that the radiation is subsequently reflected between the two surfaces. The radiative heat flux from the room temperature stage to the outside surface of the detector shield $\dot{Q}_{rt->\mathrm{det},out}$ can be expressed in the following manner[28]:

[28] This relation is derived in Appendix E.

$$\dot{Q}_{rt->\det,out} = \int_0^\infty (1-F) A_{\text{int}} \varepsilon_{rt}(\lambda,T_{rt})\, r(\lambda,T_{rt},T_{\text{int}},T_{\det}) \left[ E_{BB}(\lambda,T_{rt}) - E_{BB}(\lambda,T_{\det}) \right] d\lambda$$

$$r(\lambda,T_{rt},T_{\text{int}},T_{\det}) = \frac{\varepsilon_{\det,out}(\lambda,T_{\det})}{\varepsilon_{\text{int},in}(\lambda,T_{\text{int}}) + \varepsilon_{\det,out}(\lambda,T_{\det}) - \varepsilon_{\text{int},in}(\lambda,T_{\text{int}})\,\varepsilon_{\det,out}(\lambda,T_{\det})} \quad (3.13)$$

Similarly, the radiative heat flux from the room temperature stage to the inside of the intermediate stage temperature, $\dot{Q}_{rt->\text{int},in}$, can be described as[29]:

$$\dot{Q}_{rt->\text{int},inside} = \int_0^\infty (1-F) A_{\text{int}} \varepsilon_{rt}(\lambda,T_{rt}) \left(1 - r(\lambda,T_{rt},T_{\text{int}},T_{\det})\right) \left[ E_{BB}(\lambda,T_{rt}) - E_{BB}(\lambda,T_{\text{int}}) \right] d\lambda$$

$$r(\lambda,T_{rt},T_{\text{int}},T_{\det}) = \frac{\varepsilon_{\det,out}(\lambda,T_{\det})}{\varepsilon_{\text{int},in}(\lambda,T_{\text{int}}) + \varepsilon_{\det,out}(\lambda,T_{\det}) - \varepsilon_{\text{int},in}(\lambda,T_{\text{int}})\,\varepsilon_{\det,out}(\lambda,T_{\det})} \quad (3.14)$$

Apart from the six openings at the front plate of the cold shields, there are also four slits in the rear half of each cold shield to allow the passage of the electrical wires. The theory is the same for these openings in the rear as for the openings at the front of the cold shields. The only thing that is different for the calculation of the radiative heat transfer through the slits is the view factor. Details on how the view factor was evaluated can be found in Appendix F.

### 3.3.3 Summary of heat loads on cooler stages

The previous section presented the theoretical concepts regarding the various heat transfer processes between the different temperature stages. These theoretical concepts are now used to estimate the heat flow into the cold stages with respect to the chosen design parameters.

The space application is the main driver for a careful consideration of the heat loads on the cooler stages. Therefore, in the

[29] This relation is derived in Appendix E

following, the focus is on the thermal regime that would apply with a readily available space cooler such as a two-stage Astrium 10K cooler, which can provide a cooling power of 0.4 W at 19 K (second stage) and 0.5 W at 120 K (first stage).

Section 3.3.3.1 describes experimental tests of the heat loads that CSAR places on the cooler stages when the detector stage operates at 20 K and the intermediate stage at 120 K. The outcome of these tests is that CSAR would – in the current configuration - need to be operated with two Astrium 10K space coolers.

Section 3.3.3.2 presents a theoretical estimate of the heat loads on the cooler stages, based on the theory given in Section 3.3.2. The theoretical estimate agrees with the experimental test results within the respective uncertainties.

These experimental tests and theoretical calculations were carried out using the current heat-shield configuration of CSAR; however, this configuration can be improved; these improvements and their impact on the heat load on the cooler are discussed in Section 3.3.3.3. Here, it is shown that it is plausible to reduce the heat load such that CSAR can be operated with a single Astrium 10K space cooler.

Finally, in Section 3.3.3.4, the thermal performance of the ground-based CSAR system operating at 20 K (detector stage) and 50 K (intermediate stage) is briefly discussed.

#### *3.3.3.1 Experimental test of the heat load with the intermediate stage at 120 K and the detector stage at 20 K*

For the experimental tests of the thermal load, the CSAR radiometer head was installed in the vacuum can. The detector stage and the

intermediate stage were thermally connected to the cold tip (2nd stage) and the intermediate stage (1st stage) of the ground cooler, respectively. The copper braid connecting the first cooler stage with the intermediate stage of CSAR was chosen such that the intermediate stage temperature stabilised at 120 K, while the detector stage was operated at a temperature of slightly less than 20 K. For the measurements presented here, the radiometer head was fully assembled apart from the support structure for the precision apertures, which was not assembled[30]. The detector assembly was as depicted in Figure 60. No multilayer insulation was used on the cold shields, no external heating was applied to the detector cavity, and the reference block was also not controlled (therefore, the heater on the detector stage was not energised)[31].

For these tests, a total of 70 electrical wires were put in place, connecting the room-temperature stage to the intermediate stage, and 60 wires connecting the intermediate stage with the detector stage. Although only the components needed for the temperature control of the detector stage and one cavity were fully wired up, the additional wires were installed in order to simulate the heat conduction through the electrical wires in the fully assembled state.

[30] At the time when these tests were carried out, the aperture support structure had not been manufactured yet.

[31] These components are added during the operation of CSAR when it is measuring. Solar radiation impinging on the detector adds up to approximately 0.03 W heat load to the detector stage. And in order to control the reference block, the reference block heater needs to be energised with approximately 0.05 W; this also adds to the heat load on the detector stage.

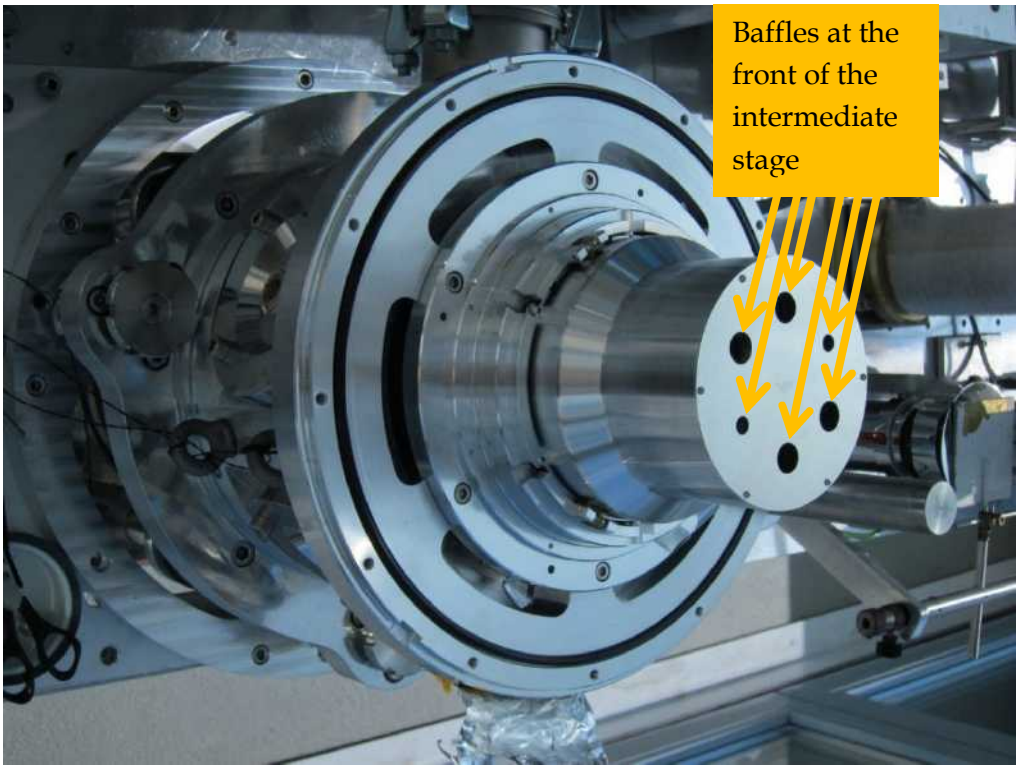


*Figure 60 Detector assembly (without support structure for precision apertures and shutter)*

In order to determine the overall heat flow into the detector stage, the temperature of the cooler tip was measured. Knowledge of this temperature allows the deduction of the heat flow into the 4 K-cold tip of the cooler (via the load map provided by the manufacturer), and thereby also the heat flow into the detector stage. The temperature measured on the cold-tip of the ground cooler was 4.11 K, which – according to the load map in Figure 46 - corresponds to a heat flow of approximately 0.37 W (standard uncertainty: 0.05 W).

While the manufacturer data for the 4 K cold tip of the cold tip (2nd cooler stage) are sufficiently detailed for an estimation of the heat flow based on one temperature measurement alone, the data for the 1st stage are not detailed enough. Therefore, the evaluation of the heat

load on the 1st cooler stage (which is connected to the intermediate detector stage) was performed in two separate steps.

In a first step, the cooler was operated without being thermally connected to the radiometer head (i.e., the copper braids were not attached to the CSAR radiometer head). The temperature of the 1st cooler stage was measured in this regime; it was 28.29 K.

In a second step, both stages of the radiometer head were connected to the respective cooler stages. This increased the temperature of the 1st cooler stage from 28.29 K (in the unconnected state) to 28.80 K. This temperature difference can be used to estimate an equivalent difference in the power input - by using the load map in order to determine the sensitivity of the 1st cooler stage temperature with respect to changes in input power. The sensitivity is estimated to be 1.7 W/K. Therefore, the observed temperature difference of 0.51 K is equivalent to a heat load difference of 0.87 W (standard uncertainty: 0.2 W).

#### 3.3.3.2 *Theoretical estimate of the heat load for CSAR with the intermediate stage at 120 K and the detector stage at 20 K*

Apart from the experimental tests, the heat load was also estimated applying the theoretical concepts of the previous section to the specific configuration of CSAR as employed for these tests. The theoretical results are shown in Table 9. One of the most important outcomes is that the sum of all theoretically calculated contributions adds up to net results that agree with the experimental results within the respective uncertainties; this is true for both cooler stages.

Another important result is that in this configuration, CSAR would require the cooling power of two Astrium 10 K coolers (one

cooler: 0.4 W @ 19 K, 0.5 W @ 120 K) or two LB2ST: Double-stage Stirling Coolers from Sumitomo (one cooler: 0.2 W @ 20 K, 1W @ 100 K). This required number of coolers is greater than what was originally desired. Ideally, CSAR should be able to operate with just one space cooler. In order to gauge the feasibility of this ideal scenario, the results need to be analysed further.

**Table 9 Heat flux into the cold stages of the radiometer head and associated standard uncertainties; result of theoretical calculations. The intermediate stage is assumed to operate at a temperature of 120 K, and the detector stage at 20 K.**

| Process | $\dot{Q}_{293\,K\,->120\,K}$ / W | $u_{293\,K\,->120\,K}$ / W | $\dot{Q}_{120\,K\,->20\,K}$ / W | $u_{120\,K\,->20\,K}$ / W |
|---|---|---|---|---|
| Conduction support structure | 0.101 | 0.010 | 0.019 | 0.002 |
| Conduction electrical leads | 0.013 | 0.001 | 0.008 | 0.001 |
| Radiation between cold shields | 0.736 | 0.074 | 0.006 | 0.001 |
| Radiation through clearances in front shield | 0.070 | 0.040 | 0.099[32] | 0.057 |
| Radiation through clearances in rear shield | 0.113 | 0.065 | 0.152[33] | 0.087 |
| SUM TOTAL | **1.033** | **0.107** | **0.284** | **0.104** |

### 3.3.3.3 *Exploring the potential for improving the thermal performance of CSAR*

The advantage of the theoretical determination is that it allows a breakdown of the total heat flux into smaller components according to

[32] This is the direct heat transfer through the clearances in the front shields from the room temperature stage (@ 293 K) to the detector stage (@ 20 K)
[33] This is the direct heat transfer through the clearances in the rear shields from the room temperature stage (@ 293 K) to the detector stage (@ 20 K)

the various heat transfer mechanisms, which would be hard to distinguish experimentally. Table 9 suggests that the radiation between the cold shields is the dominating heat transfer mechanism with regard to the intermediate stage (@120 K), contributing over 70% of the total heat flux. Similarly, the heat load on the detector stage (@20 K) is dominated by the radiation through the clearances in the front- and rear- shield. This implies that a reduction in these two heat transfer processes has the greatest potential for reducing the number of required space coolers.

The radiative heat transfer between the cold shields is mainly dependent on two factors: the surface area and the surface emissivity. There may be some scope for reducing the surface area further, but since the surface area has already been kept to a minimum during the design process, minimising the surface emissivity holds the greatest promise for further improvement. The surface emissivity could be reduced significantly through the application of a gold coating (purity > 99.99%). The use of Multilayer Insulation could be a last resort for cutting the radiative heat transfer; however, its use should be kept to a minimum in order to avoid too much outgassing in the vicinity of the detector cavity.

The cold shields are made from aluminium alloy (Al6082) and they are currently not coated with another material. The emissivity of the cold shields could be reduced by applying a gold coating; this scenario is evaluated theoretically, using the same theoretical model that was used to estimate the surface emissivity of the aluminium alloy. The model leads to a total hemispherical surface emissivity of gold of 2.0% at 293 K (as opposed to 3.7% for the aluminium alloy), which is a value that can be achieved by specialist gold plating

companies[34]. At 120 K, the total hemispherical surface emissivity is estimated to be 1.5% (as opposed to 1.8% for the aluminium alloy). Figure 61 shows the theoretical spectral hemispherical emissivity of gold, which was used for the heat flow estimates. Assuming a gold coating on the room-temperature shield and on the outside of the intermediate-stage shield leads to an expected reduction in the radiative heat transfer between these two cold shields from 0.745 W to 0.221 W when compared to the uncoated aluminium alloy shields.

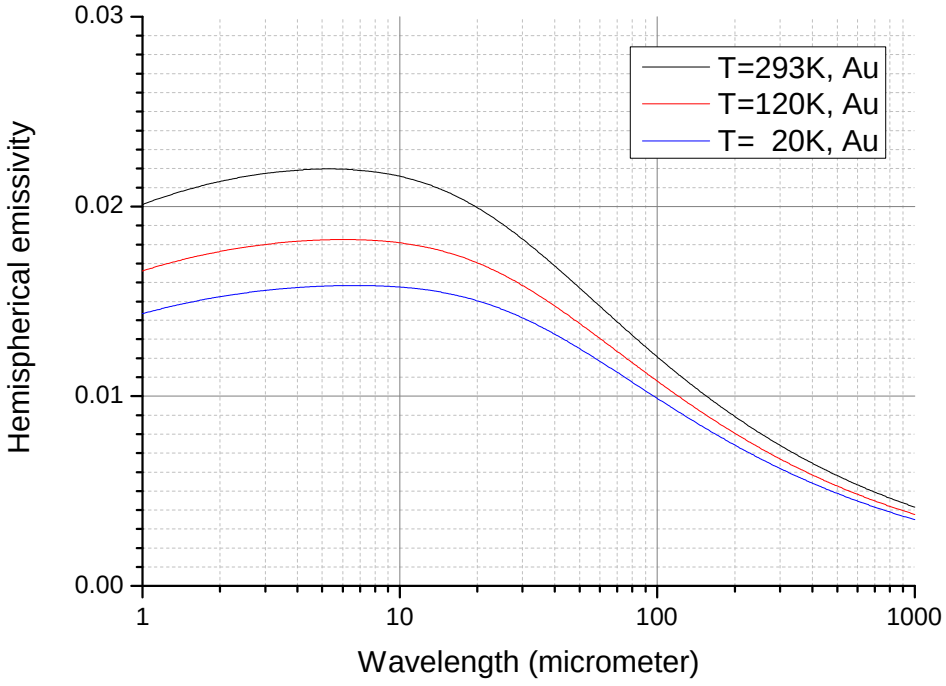


**Figure 61 Spectral hemispherical emissivity of Gold (theoretical estimate, Tsujimoto model)**

The reduction in radiative heat transfer through the application of gold plating to the room-temperature and intermediate cold shields might already be sufficient in order to allow the operation of CSAR

[34] EPNER Technology Inc. report a comparison of gold plated aluminium and aluminium alloy samples by three different plating companies. The room-temperature hemispherical emissivities of the samples were in the range from 1.7% to 3.6% (see www.lasergold.com/laser_emissivity.ssi).

with just one cooler, but given the uncertainties in the calculations and experimental tests, it would not be a very certain prospect. However, the heat loads on the cooler stages can be reduced further by reducing the heat transfer though the clearances in the cold shields. This can be achieved by reducing the size of the clearances. The clearances in the rear shields can be reduced drastically; currently, there are four slits, each of which is 6 mm wide and several centimetres long; this is not necessary for passing 70 wires with individual diameters of less than 100 µm, which is equivalent to a total surface area of only approximately 0.5 $mm^2$. The slits were made so large for the current CSAR model in order to enable the experimenter to assemble and disassemble the system easily without having to worry about damaging the electrical leads; however, for a flight model, the reduction in heat load on the cooler would justify a more elaborate assembly process. Minimising the slit area in the rear shield would reduce the relevant heat load component of 0.154 W on the detector stage and 0.110 W on the intermediate stage (see Table 9) to negligible levels.

Unfortunately, the area of the clearances in the front shields cannot be reduced significantly because such a reduction would interfere with the optical path of the incoming solar radiation.

Table 10 summarises the predicted heat loads on the cooler stages after the implementation of the suggested improvements. After the gold plating of the room-temperature- and the intermediate- cold shields, and the minimisation of the clearances in the rear shield, the heat load on the first cooler stage (120K) reduces to 0.403 W (standard uncertainty: 0.046 W). Therefore, the load on the 1st cooler stage is predicted to be 0.403 W ± 0.092 W at the 95% confidence level, which

makes it very likely that the true value will be lower than the 0.5 W that can be provided by the first stage of a single Astrium 10K cooler.

Similarly, the improvements are projected to lead to a significantly reduced heat load on the 2nd cooler stage. The predicted heat load on the 2nd cooler stage is 0.210 W ± 0.061 W at the 95% confidence level; this includes the previously not considered power input needed for stabilising the reference block and the incoming solar radiation.

In conclusion, it can be said that in the current configuration, CSAR would require two units of the Astrium 10 K cooler system; however, it is very likely that a slight modification of the thermal design can reduce the current heat load such that CSAR can be operated with a single Astrium 10 K cooler. This result is likely to be achievable without the need to resort to the use of Multilayer Insulation.

**Table 10 Heat flux into the cold stages of the radiometer head and associated standard uncertainties; result of theoretical calculations. The intermediate stage is assumed to operate at a temperature of 120 K, and the detector stage at 20 K. Results are based on possible improvements in the CSAR design.**

| Process | $\dot{Q}_{293\,K\,->120\,K}$ / W | $u_{293\,K\,->120\,K}$ / W | $\dot{Q}_{120\,K\,->20\,K}$ / W | $u_{120\,K\,->20\,K}$ / W |
|---|---|---|---|---|
| Conduction support structure | 0.101 | 0.010 | 0.019 | 0.002 |
| Conduction electrical leads | 0.013 | 0.001 | 0.008 | 0.001 |
| Radiation between cold shields | 0.221 | 0.022 | 0.006 | 0.001 |
| Radiation through clearances in front shield | 0.068 | 0.039 | 0.101[35] | 0.058 |
| Radiation through clearances in rear shield | 0.000 | 0.000 | 0.000 | 0.000 |
| Electrical Power for stage control | N/A | N/A | 0.050 | 0.020 |
| Solar Irradiation | N/A | N/A | 0.026 | 0.001 |
| SUM TOTAL | **0.403** | **0.046** | **0.210** | **0.061** |

#### *3.3.3.4 Ground-based operation: summary of heat loads on cold stages*

For the ground-based operation, CSAR's detector stage is operated at a temperature of 20 K and the intermediate stage is at 50 K. This regime constitutes a compromise between the temperatures allowed by the limited cooling power of a space cooler (see Section 2.8) and the far superior cooling power of the ground cooler (see Section 3.3.1.3).

The detector temperature of 20 K was chosen in order to demonstrate the feasibility of operating the CSAR cavities at

[35] This is the direct heat transfer through the clearances in the front shields from the room temperature stage (@ 293 K) to the detector stage (@ 20 K)

temperatures above the transition edge of conventional superconducting wires, and to demonstrate that the detector system as a whole works at temperatures dictated by a space cooler.

The intermediate temperature of 50 K (as opposed to 120 K allowable by a space cooler) was chosen in order to minimise the heat transfer from the intermediate stage to the detector stage, and in particular in order to reduce the heat flow through the electrical wires, and thereby minimising the potential parasitic heat flux that may end up flowing into the detector stage.

Table 11 shows the theoretically expected heat load on the cooler stages when the intermediate temperature stage of CSAR is operated at 50 K (assuming otherwise the same configuration as during the experimental tests reported in Section 3.3.3.1). The overall heat load is very similar to the case when the intermediate stage is operated at 120 K.

**Table 11 Heat flux into the cold stages of the radiometer head; result of theoretical calculations. Intermediate stage temperature: 50 K. Detector stage temperature: 20 K.**

| Process | $\dot{Q}_{293\,K\,->\,50\,K}$ / W | $u\left(\dot{Q}_{293\,K\,->\,50\,K}\right)$ / W | $\dot{Q}_{50\,K\,->\,20\,K}$ / W | $u\left(\dot{Q}_{50\,K\,->\,20\,K}\right)$ / W |
|---|---|---|---|---|
| Conduction support structure | 0.126 | 0.012 | 0.004 | 0.0005 |
| Conduction electrical leads | 0.014 | 0.0015 | 0.003 | 0.0005 |
| Radiation between cold shields | 0.718 | 0.072 | 0.0001 | 0.0001 |
| Radiation through clearances in front shield | 0.070 | 0.040 | 0.102 | 0.059 |
| Radiation through clearances in rear shield | 0.109 | 0.063 | 0.152 | 0.088 |
| Electrical Power for stage control | N/A | N/A | 0.050 | 0.02 |
| Solar Irradiation | N/A | N/A | 0.026 | 0.001 |
| SUM TOTAL | **1.037** | **0.104** | **0.337** | **0.108** |

The overall heat flows into either of the two cooler stages (first stage: 1.037 W, detector stage: 0.337 W) are relatively small compared to the cooling capacity of the ground cooler (see load map in Figure 46). This leads to a conveniently short cool-down time of approximately 13 hours. The cool-down of the two cold stages from room temperature to operating temperatures is shown in Figure 62. A cool-down time of 13 hours means that CSAR can be switched on in

the evening and left to cool down overnight in order to be ready to take measurements in the morning.

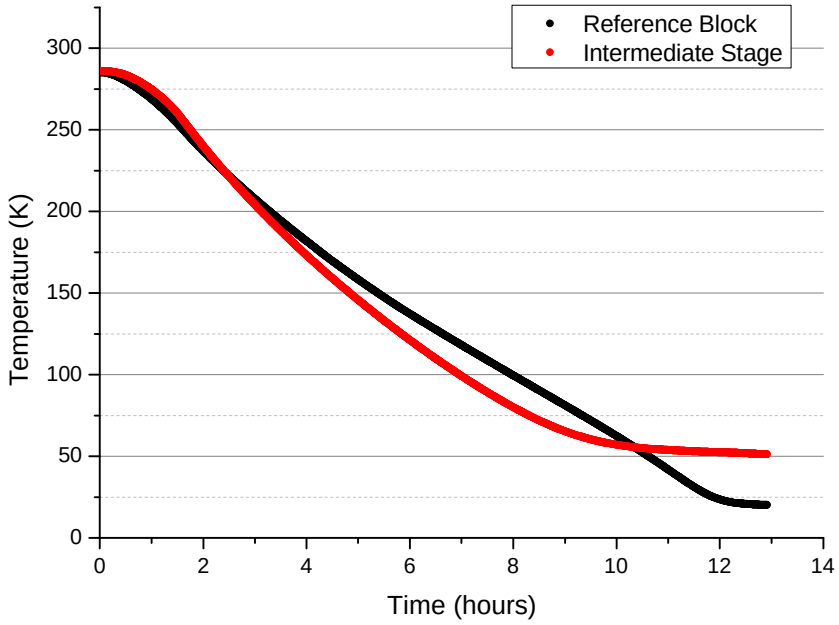


**Figure 62 Cool-down of the detector stage (black) and the intermediate stage (red), starting from room-temperature**

## 3.4 DSR/TSI aperture system – design

While Section 3.3.1 was exclusively concerned with the heat load on the cold stages, this section deals with another important aspect of the instrument design: the aperture system. The choice of the aperture system does not only influence the optical performance characteristics of the radiometer, but it also has a potentially large influence on the cooling power requirements – this will be shown at the beginning of this section. After discussing the thermal implications, the optical characteristics (such as diffraction effect and stray light rejection) will be the main focus of this section.

### 3.4.1 DSR/TSI aperture size – limiting factors

There are various limiting factors for the size of the entrance aperture and for the size of the precision aperture. These factors will be explored in this section. The "entrance aperture" is the aperture that defines the total amount of solar radiation which is admitted into the cooled part of the system. The entrance aperture is at the front of the radiometer head. The "precision aperture" can be located close to the detecting cavity, but it can also be identical with the entrance aperture, which is further away from the cavity.

#### *3.4.1.1 Cooling power and upper limit of the entrance aperture size*

The Solar Irradiance in space, together with the cooling power at the detector stage, leads to an upper limit for the size of the entrance aperture. As already shown in Section 3.3.3.1, the various heat transfer processes between the cold stages of the radiometer head lead to an experimentally determined heat flow of approximately 0.37 W for the current configuration of CSAR. This leaves only about 0.03 W of cooling reserve for the incoming solar flux – if the detector stage is to be operated at approximately 20 K. Assuming a Total Solar Irradiance of 1420 W $m^{-2}$, an upper limit of 0.03 W for the solar flux leads to an upper limit of approximately 5 mm for the diameter of the entrance aperture[36].

#### *3.4.1.2 Lower limit for the size of the precision aperture and effective aperture area*

The lower limit of the aperture size is determined by the requirements for the TSI measurement accuracy. In order to fulfil the demands

[36] This is not a hard and fast limit. If the heat flow to the detector stage can be reduced – as projected in Section 3.3.3.3, then the aperture diameter might be allowed to be larger than 5 mm. However, other restrictions might become dominant. For example, increasing the precision aperture would also lead to a larger cavity entrance aperture, and therefore to a larger cavity diameter, which would result in a longer time constant of the detector.

regarding the overall uncertainty of ground-based and space-based measurements, the effective optical area of the defining aperture should be known to an accuracy of approximately 0.013% (ground-based) or 0.005% (space-based).

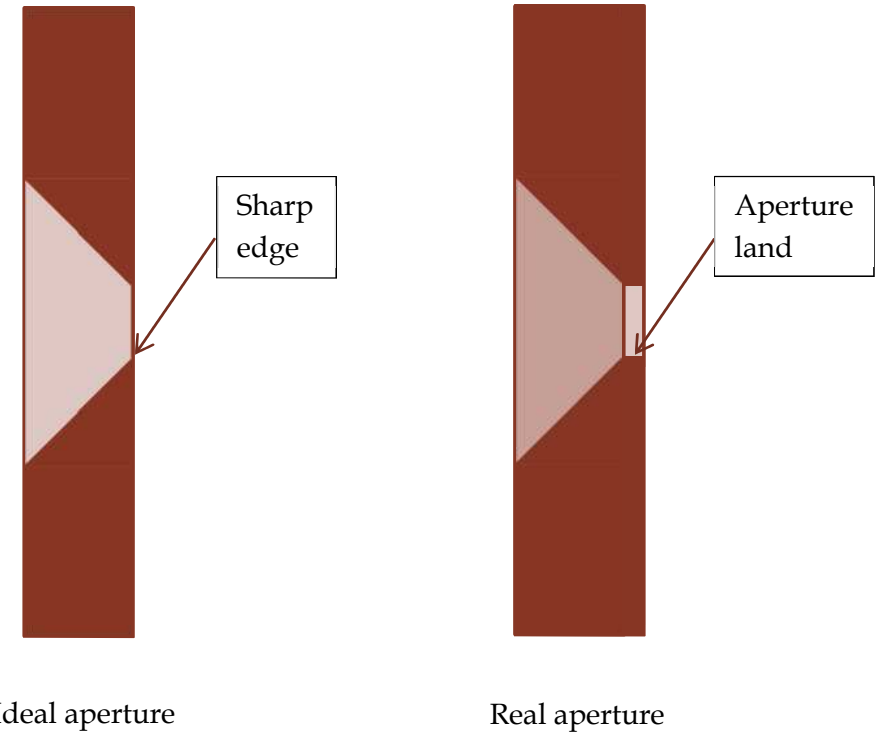


**Figure 63 Schematic of an ideal aperture versus an imperfect aperture edge ("aperture land")**

The term "effective optical area" (Hartmann, 2007) refers to the fact that no physical aperture is perfect – or, in other words - real apertures have non-ideal edges. The ideal aperture edge would have zero extension, whereas real apertures always have a land of finite length (for an illustration, see Figure 63). This extended land leads to the optical system effectively not having one single aperture, but having apertures all along the length of the aperture land. This makes the optical situation less defined than if there was only one aperture of zero extension.

The size of the effect caused by the extended aperture land mainly depends on two factors: the angle of incidence of the incoming light and the reflectivity of the aperture edge. The geometrical considerations are dealt with first. Figure 64 illustrates a collimated beam of light that hits the aperture area plane at an angle $\gamma$. The radius of the aperture is $r$, and the aperture land is described by $h$.

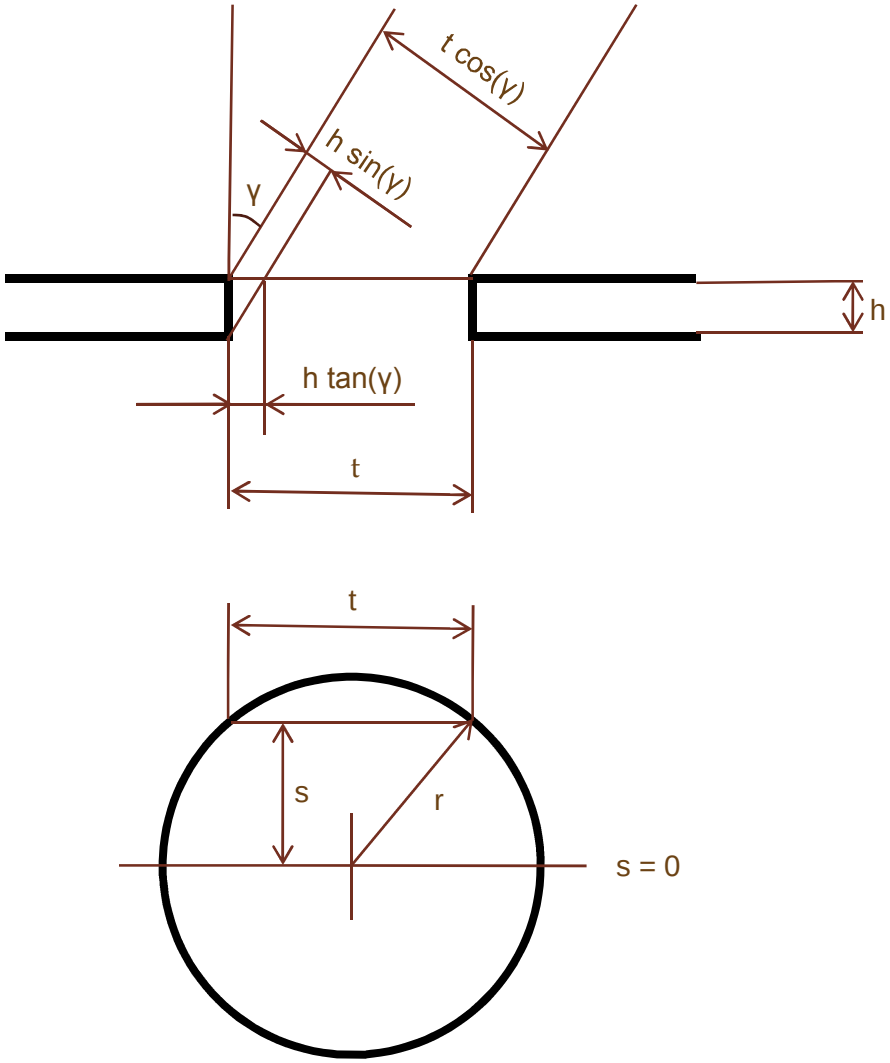


**Figure 64 Apparent aperture area for a beam impinging at an angle γ from normal. Geometrical considerations.**

In the presence of a finite aperture land $h$, the apparent or projected area $A_p(\gamma,h)$ of an aperture that is seen under an angle $\gamma$ is given by the relation

$$A_p(r,\gamma,h) = 2\int_0^{s_{max}} \left(2\cdot\sqrt{r^2-s^2}\cdot Cos(\gamma) - h\cdot Sin(\gamma)\right) ds$$

(3.15)

where

$$s_{max} = \sqrt{r^2 - \left(\frac{h\cdot Tan(\gamma)}{2}\right)^2}\,. \qquad (3.16)$$

For $h=0$, Equation (3.15) reduces to the well-known equation for the projected (elliptical) area of an ideal aperture:

$$A_p(r,\gamma,h=0) = \pi r^2 Cos(\gamma)\,. \qquad (3.17)$$

The ratio between the projected area with a positive value for $h$ and the projected area of an ideal aperture ($h=0$) is given by

$$\frac{A_p(r,\gamma,h)}{A_p(r,\gamma,h=0)} = \frac{2\int_0^{s_{max}} \left(2\cdot\sqrt{r^2-s^2}\cdot Cos(\gamma) - h\cdot Sin(\gamma)\right) ds}{\pi r^2 Cos(\gamma)}$$

(3.18)[37]

The pointing error of the solar tracker in Davos is less than ±0.25°[38]. Under these circumstances, $Cos(\gamma) > 0.99999$, and therefore the difference between the ideal area (i.e. with $\gamma=0$ and $h=0$) and the projection of this ideal area (with $h=0$) is less than 0.001% and therefore negligible. In order to evaluate the maximum offset due to

[37] The derivation of this Equation was in essence carried out by my colleague, Eric Usadi.
[38] Personal communication with André Fehlmann, 12 July 2012.

the extended aperture land, the ratio given in Equation (3.18) was evaluated and displayed for land thicknesses ranging from $h = 10\ \mu m$ up to $h = 100\ \mu m$, and for aperture diameters between 1 mm and 10 mm (see Figure 65). All these calculations were carried out assuming a pointing error of 0.25˚.

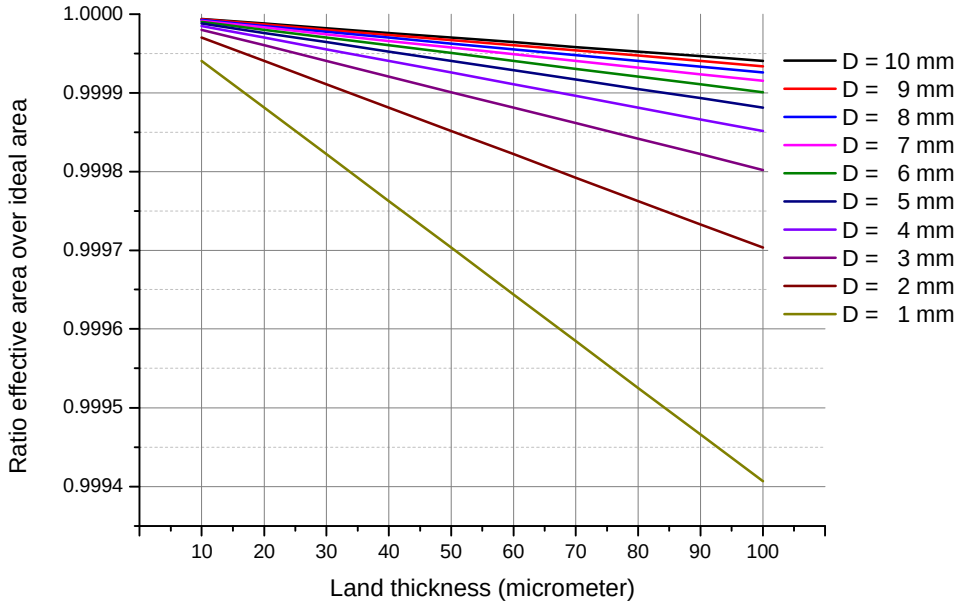


**Figure 65 Ratio of effective optical area over ideal area for incoming light at 0.25 degrees from normal, assuming that the aperture land is perfectly black. The x-axis shows the land thickness and different graphs represent different aperture diameters (from 1 mm to 10 mm).**

This evaluation of the aperture land effect is not necessarily based on a perfect representation of the physical reality since it assumes that the aperture land absorbs all radiation, whereas in reality it will reflect a large part of the radiation. However, this assumption leads to a very practical advantage; it is not necessary to have any knowledge about the (angularly dependent and wavelength-dependent) reflectivity properties of the aperture material.

If one adopts this design philosophy, one can say that for an aperture of diameter 5 mm and land thickness 100 µm, the offset error due to the land effect is smaller than 0.012% (see Figure 65); in this case, the standard uncertainty due to this effect is smaller than 0.004%[39], which makes it negligible for the ground application, but not negligible regarding the space application.

If otherwise everything else remains the same (i.e. the aperture diameter remains at 5 mm), but if the land is less than 30 µm, then the potential offset error reduces to less than 0.004%, which makes the standard uncertainty smaller than 0.001%, and therefore negligible with respect to the space application as well as the ground application[40].

#### *3.4.1.3 Aperture land and measurement uncertainty*

Apart from the above considerations, the aperture land also has an impact on the accuracy of the aperture area measurement. In the following, this point will be discussed in the context of NPL's calibration capability only; these considerations are therefore not necessarily of universal validity, but they are of great practical relevance in the context of this PhD project.

At NPL, the preferred way of measuring aperture areas is by using so-called "contact-methods", i.e. a stylus is physically touching the aperture edge – as opposed to optical methods which are preferred by other National Measurement Institutes (e.g. NIST in the USA). The primary (i.e. the most accurate) calibration facility at the NPL can

[39] A rectangular probability distribution is assumed with a lower limit of 0 and an upper limit of 0.012%. The standard uncertainty is calculated according to Equation (2.6) in Section 2.4.3.

[40] The standard uncertainty is also approximately 0.001% if the aperture land is 18 µm (see Section 3.4.1.4) and the pointing error ±0.53° (see Section 3.4.5.3), as was the case in the CSAR measurements in Davos reported in this thesis.

typically only tolerate land thicknesses greater than 100 µm. The secondary calibration facility is less accurate, but applies a much smaller measurement force (approximately reduced by a factor of 60), and can therefore measure land thicknesses of the order of 10 µm without damaging the aperture[41].

Typical measurement uncertainties of the primary and secondary NPL calibration facilities for determining the aperture area of circular apertures are shown in Figure 66. This graph shows that for an aperture of 5 mm diameter, the typical standard uncertainties are ~ 20 ppm (or 0.002%) for the primary method and slightly more than 50 ppm (or 0.005%) for the secondary method.

[41] NIST's non-contact geometric aperture calibration facility operates at similar uncertainty levels as NPL's primary contact method; however, the NIST method has the advantage that it can measure apertures with arbitrarily small land thicknesses. Nevertheless, for the purpose of the work presented in this thesis, NPL's in-house capability was considered most relevant.

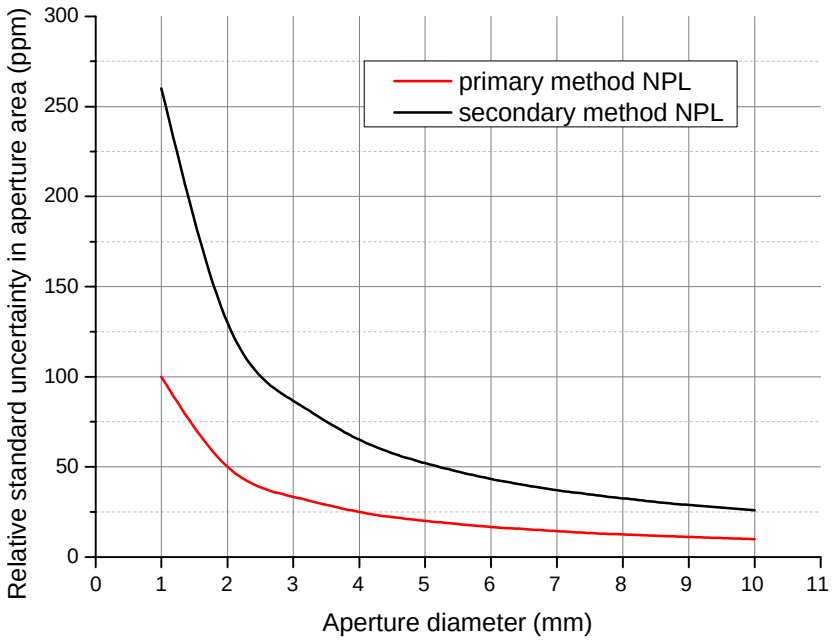


**Figure 66 Relative uncertainties of aperture area calibrations with NPL's primary and secondary calibration facilities, depending on the aperture diameter (typical values).**

In summary, one can say that the standard uncertainty due to the measurement of the aperture area is smaller for the primary calibration method, but since the primary method requires an aperture land of at least 100 µm, the standard uncertainty due to the aperture land is much higher than for significantly smaller lands. When it comes to choosing between the two calibration methods, these two effects tend to oppose each other. For example, for an aperture with 5 mm diameter (measured with primary method, standard uncertainty = 0.002%) and 100 µm land (standard uncertainty due to aperture land effect = 0.004%), the combined uncertainty is approximately 0.005%. And similarly, for an aperture with 5 mm diameter (measured with secondary method, standard uncertainty = 0.005%) and 30 µm land (standard uncertainty = 0.001%), the combined uncertainty is also

approximately 0.005%. Both apertures fulfil the uncertainty requirement with respect to the aperture area for the space- as well as the ground-application[42].

Since there is no significant advantage of using the primary calibration method, the aperture land was made as small as possible because this way the aperture is closest to an ideal aperture. The NPL Engineering Workshop approached several diamond turners; the smallest aperture land that could be produced by these diamond turners was of the order of 20 µm.

#### *3.4.1.4 CSAR precision apertures – measurement results*

Table 12 shows the land thicknesses, the roundness and the area measurement uncertainty of the precision apertures that were produced for CSAR. Measurements were made at temperatures in the range 19.9˚C to 20.1˚C. All apertures had a nominal diameter of 5 mm and were made from Aluminium. The maximum deviation from this nominal diameter is 33 µm. The land thickness ranges from 18 µm to 30 µm for the different apertures. The roundness is less than 0.4 µm for 6 apertures; only aperture number seven has an exceptionally large roundness of 1.164 µm. This larger roundness value also leads to a slightly increased value for the uncertainty in the aperture area of 0.0078% for aperture number 7. All other aperture areas were determined with an uncertainty of 0.0052%.

[42] See Table 2 in Section 2.4.6.

**Table 12 Measurement results for the CSAR precision apertures**

| Aperture # | Diameter / mm | Land thickness / µm | Roundness / mm | Relative Standard Uncertainty in area |
|---|---|---|---|---|
| 1 | 4.96811 | 30 | 0.000378 | 0.0052% |
| 2 | 4.96709 | 27 | 0.000396 | 0.0052% |
| 3 | 4.96784 | 28 | 0.000352 | 0.0052% |
| 4 | 4.97004 | 25 | 0.000327 | 0.0052% |
| 5 | 4.96762 | 22 | 0.000151 | 0.0052% |
| 6 | 4.96726 | 18 | 0.000348 | 0.0052% |
| 7 | 4.96780 | 18 | 0.001164 | 0.0078% |

Figure 67 shows electron microscope images of the aperture edges of the precision apertures that were produced for CSAR. These images show that the edges are very "clean", i.e. free from any major irregularities.

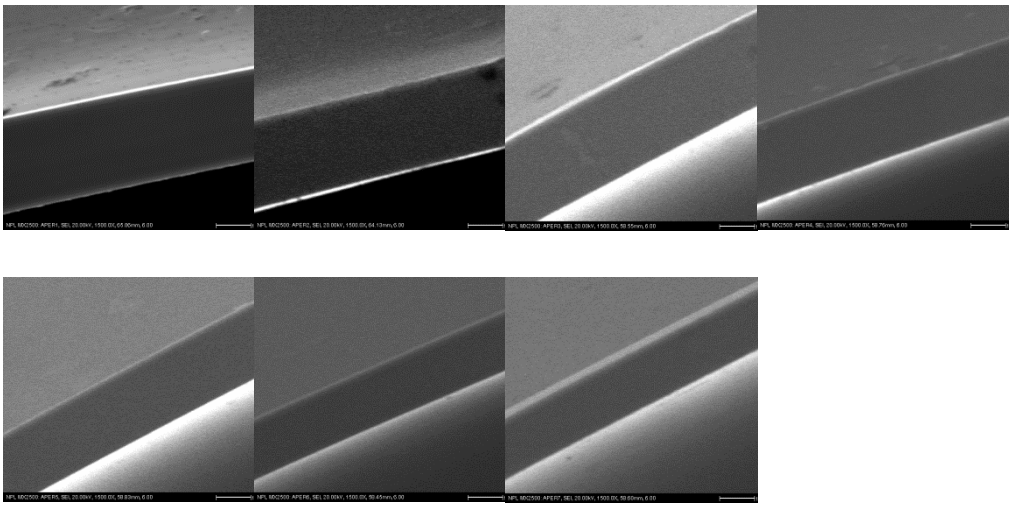

**Figure 67 Electron microscope images of the seven CSAR precision apertures. The picture on the top left shows the aperture edge of aperture number 1 and the image on the bottom right shows the edge of aperture number 7.**

### *3.4.1.5 Diffraction*

One of the optical effects that need to be considered is diffraction of light at the entrance aperture. Depending on the specific geometrical arrangement of the source, the aperture, and the detector, light is lost or gained through diffraction at the entrance aperture.

Figure 68 gives an idea of the diffraction situation. It shows the result of a calculation which assumes an entrance aperture of diameter 5 mm and a distance of 100 mm between the apertures. The diffraction effect changes with varying size of the cavity aperture. If the diffraction effect is smaller than unity, then less light enters the cavity than predicted by geometrical optics; this is the case for cavity apertures that are larger than the entrance limiting aperture.

If, on the other hand, the cavity aperture is smaller than the entrance aperture, then the diffraction effect is larger than one, which means that more light enters the cavity than predicted by geometrical optics. For example, for a cavity aperture of diameter 3 mm, the cavity

would receive a surplus of approximately 0.4% due to diffraction at the entrance aperture, and for a cavity with aperture diameter 10 mm, the cavity aperture would receive approximately 0.1% less sunlight than estimated by geometrical optics.

All the diffraction calculations presented in this thesis were performed with code developed for NPL by Edwards (Edwards, 2004). The code considers the radiative transfer from a circular source to a circular detector, with an additional circular aperture between source and detector. The code returns the ratio of (1) the radiative transfer with diffraction effect at the intermediate aperture to (2) the radiative transfer according to geometrical optics (i.e. without taking the diffraction effect into account).

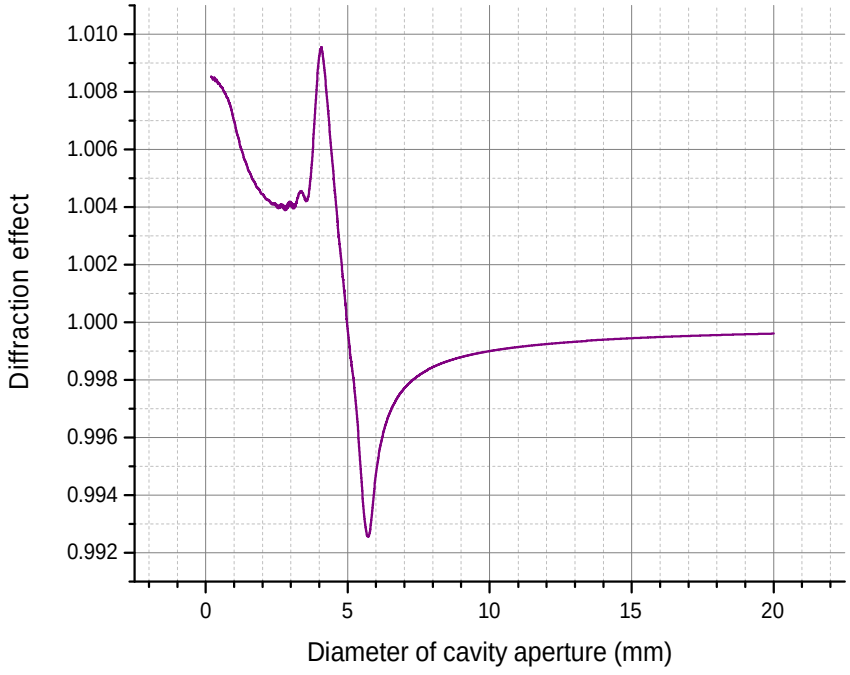


**Figure 68 Diffraction effect when viewing the Sun. The calculation assumes a diameter of 5 mm for the field-of-view-limiting aperture, and a distance of 100 mm between the apertures.**

Figure 68 gives a good idea of the diffraction effect that needs to be considered in the design of CSAR. The graph illustrates very clearly that the sensitivity of the diffraction effect depends very much on the optical geometry. It would, for example, be rather daring to make the cavity aperture the same size as the entrance aperture. The advantage would be that there is no diffraction correction necessary; however, the sensitivity of the diffraction effect to the geometry of the optical setup is highest in this configuration.

While Figure 68 gives a good idea of the local sensitivity of the diffraction effect to variations in the size of the cavity aperture, it does not represent the absolute levels of diffraction completely correctly, since the distance between the apertures was assumed to stay the same for all the different geometries. This is, however, not a very realistic representation.

Rather than keeping the distance constant, it is more meaningful to keep the cut-off angle constant, which determines how much circumsolar radiation the instrument is collecting. In Figure 69, the entrance aperture is still held constant at diameter 5 mm, but this time the cut-off angle is kept constant at 4.13˚, while the distance between the apertures varies. This allows a comparison of the absolute levels of diffraction correction that need to be applied.

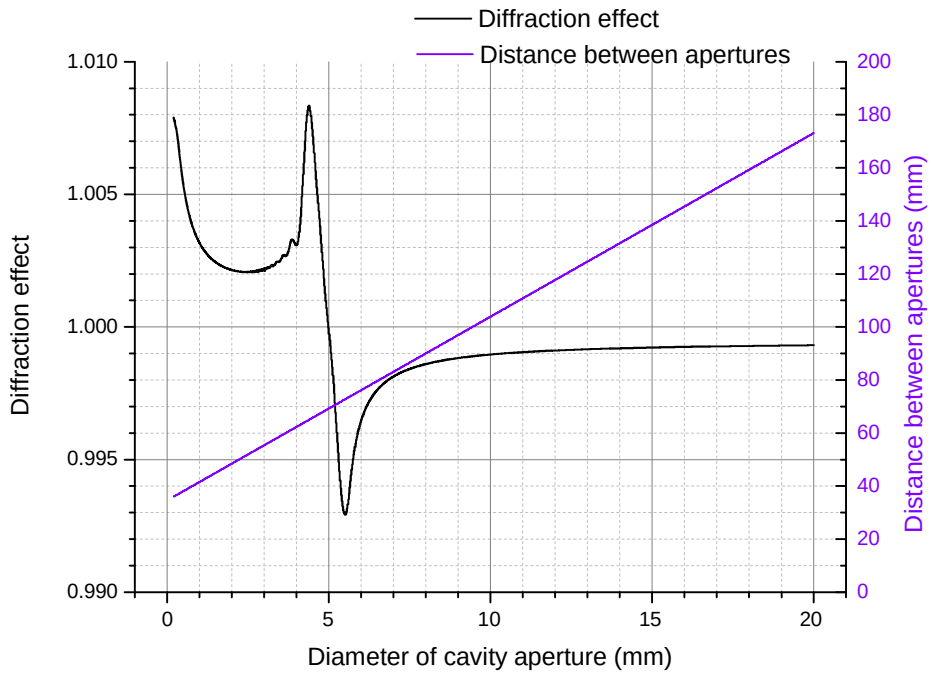


**Figure 69 Diffraction effect when viewing the Sun. The calculation assumes a diameter of 5 mm for the entrance aperture, and a cut-off angle of 4.13°. The distance between the apertures varies linearly (see the second y-axis on the right-hand side).**

Figure 69 shows that there are two regions where the diffraction effect is not very sensitive to changes in the optical geometry. The first region is between approximately 2 mm and 3 mm (diameter of cavity aperture), and the second region is where the diameter of the cavity aperture is approximately greater than 8 mm. Figure 69 also shows that, in the case of the cavity aperture being smaller than the entrance aperture, the diffraction effect is in no case smaller than 1.002 (apart from the region of highest sensitivity). In the case of the cavity aperture being larger than the entrance aperture, however, the diffraction effect can theoretically be made to be very close to unity, while the sensitivity is very small at the same time. What prevents the diffraction effect from becoming arbitrarily close to unity in this latter case are the size restrictions regarding the detector length (which

limits the distance between the apertures) and size restrictions regarding the cavity (which limits the size of the cavity aperture). A cavity diameter of 10 mm was chosen as a compromise considering the influence on all these various parameters.

#### *3.4.1.6 Thermal expansion of the aperture*

The thermal expansion of the aperture material has a direct influence on the aperture area. Figure 70 shows the thermal expansion of aluminium in the temperature range 4 K to 300 K (the data are taken from the NIST Cryogenic Materials Database (NIST, 2000)), and Figure 71 shows the resulting dependence of the aperture area on temperature.

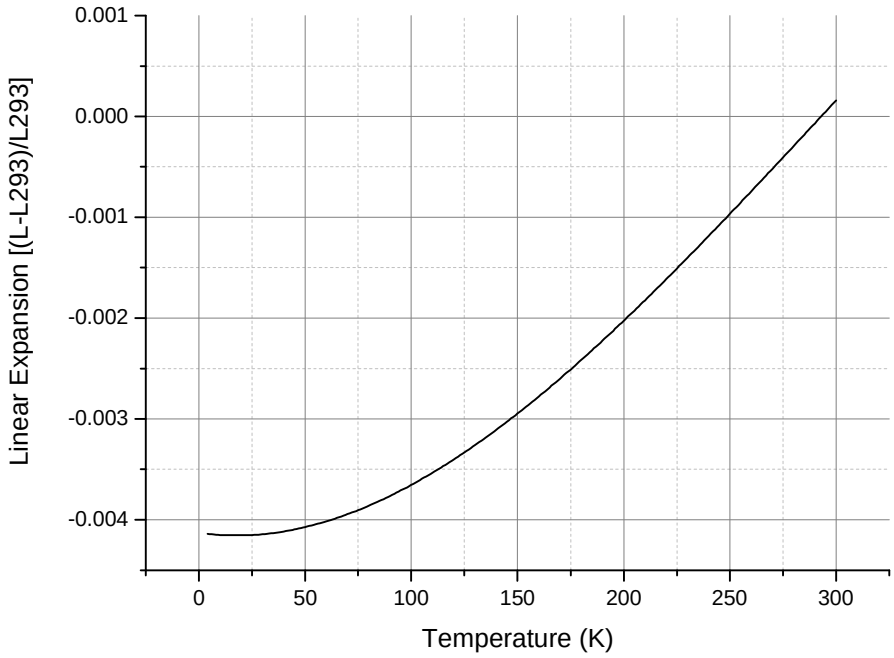


**Figure 70 Thermal expansion of Aluminium 6061-T6.**

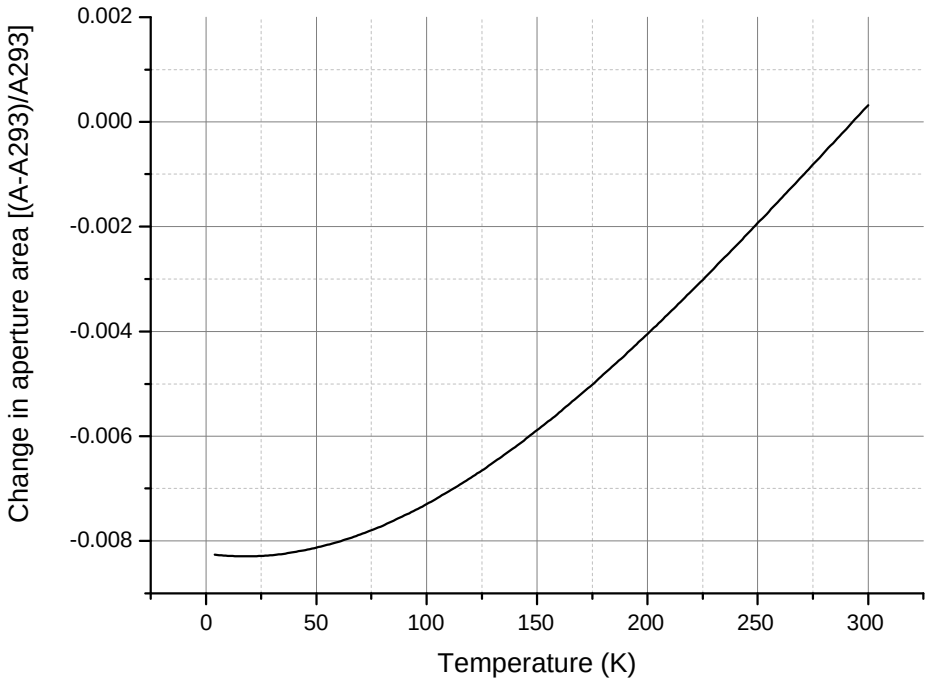


**Figure 71 Temperature dependence of the aperture area for an aperture made of Aluminium 6061-T6. The reference size is the aperture size at room temperature (T = 293 K).**

Figure 71 gives another reason why the cavity aperture was not chosen as the precision aperture. Such a choice would require a correction of approximately 0.83% due to thermal expansion – if the aperture is measured at room temperature and used at 20 K. This would require an accurate measurement of the thermal expansion of the aperture material at cryogenic temperatures. It would also be doubtful if the aperture would retain its original shape after repeated temperature cycling.

But even if the precision aperture is operated at "room temperature", there is still a need for a correction due to thermal expansion of the aperture area, due to the fact that CSAR is not operated in a temperature-controlled laboratory. Figure 71 shows that the aperture area changes by approximately 0.0045% per Kelvin. The

temperature of CSAR's vacuum chamber, which is in direct thermal contact with the "room-temperature stage" was measured and found to agree very well with data of the nearest weather station in Davos[43]. The temperature during the measurements (when comparing CSAR against the WRR) was on average 5 °C, which leads to a correction of 0.068% due to the thermal contraction of the aperture area. If one assumes that the environmental temperature correctly represents the aperture temperature to within ± 5 °C, this leads to a standard uncertainty of 0.013% for the ground-based application. This uncertainty could be reduced significantly by making a more direct measurement of the aperture temperature: a maximum error in the determination of aperture temperature of ± 1 °C would lead to an associated standard uncertainty of 0.0026%. This uncertainty level should be achievable for future ground-based measurements as well as a space-version of CSAR.

#### *3.4.1.7 Concluding remarks regarding the DSR/TSI aperture size*

In this section, a summary is given of the chosen optical configuration. First, the entrance aperture was chosen to be the defining aperture (or precision aperture, with nominal diameter 5 mm), and was placed closer to the light source (the Sun), while the field-of-view-limiting aperture (nominal diameter 10 mm) was placed directly in front of the detector cavity. For reasons given above, this is believed to be the optically superior arrangement – as compared to the reversed arrangement of the apertures, which is a feature of conventional TSI/DSR-radiometers. The reason for this choice in conventional instruments is that the cavity diameter needs to be kept as small as

[43] Online: http://weather.uk.msn.com/daily_averages.aspx?wealocations=wc:8692&q=Davos%2c+CHE+forecast:averagesd&weai=2 [Accessed 5 October 2012]

possible, and that placing the larger field-of-view-limiting aperture directly in front of the cavity would lead to too large a cavity and the time constant would become too big. The operation at cryogenic temperature, on the other hand, relaxes the constraints regarding the cavity size, which allows the choice of the optically superior arrangement.

The chosen aperture configuration is similar to that used for the Total Irradiance Monitor, TIM [4]; however, in contrast to TIM, CSAR was specifically built for ground use. This ensures that CSAR does not measure significantly different amounts of circumsolar radiation than the existing radiometers. From model calculations, we expect a difference due to circumsolar radiation of ~ 50 ppm between CSAR and the PMO2 radiometer, provided an Aerosol Optical Depth of less than 0.4 and a Solar Zenith Angle smaller than 70˚ (Fehlmann, 2011); both conditions were fulfilled during the tests reported in Chapter 4 of this thesis. The PMO2 radiometer is the WSG instrument, which is preferably used to compare radiometers against the WSG.[44]

The CSAR precision aperture is diamond-turned from aluminium and has an edge thickness of 18 µm (see aperture Nr. 7 in Table 12, Section 3.4.1.4). The front face of the precision aperture is "volcano" – shaped, so that inter-reflections between the aperture and the window cannot make their way into the detector cavity. A nominally identical aperture was also used for the window transmittance measurement.

[44] This is due to the fact that the PMO2 is the fastest of the currently operating WSG instruments; it takes measurements in intervals of 90 seconds, whereas other WSG instruments have measurement cycles of the order of 180 seconds.

The cavity aperture is made from a 200 µm thick copper sheath and is 10 mm in diameter. It is placed directly in front of the cavity, and at a distance of 104 mm from the precision aperture.

Figure 72 shows a cross section of one of the four DSR/TSI channels of the radiometer head. The first element is a shutter, which can either admit radiation into the detector channel or prevent radiation from entering. A 5 mm diameter precision aperture is located directly behind the shutter. The precision aperture is at room temperature. Then follows a heat shield that is connected to the first cooler stage (120K in the case of the space cooler, and 50 K in the case of the ground application) and after that, the heat shield of the cold stage that is connected to the second stage of the cooler (20 K). This 20K heat shield also serves as a radiation trap for the reduction of stray light; it contains two baffles and all its internal surfaces carry a diffuse black coating (3M Nextel Black Velvet). After the two stray-light baffles, the incoming radiation passes a field-of-view limiting aperture (diameter 10 mm), which sits directly in front of the detector cavity. The detector cavity is not shown in its entire length; Figure 72 only shows the front part of the cavity.

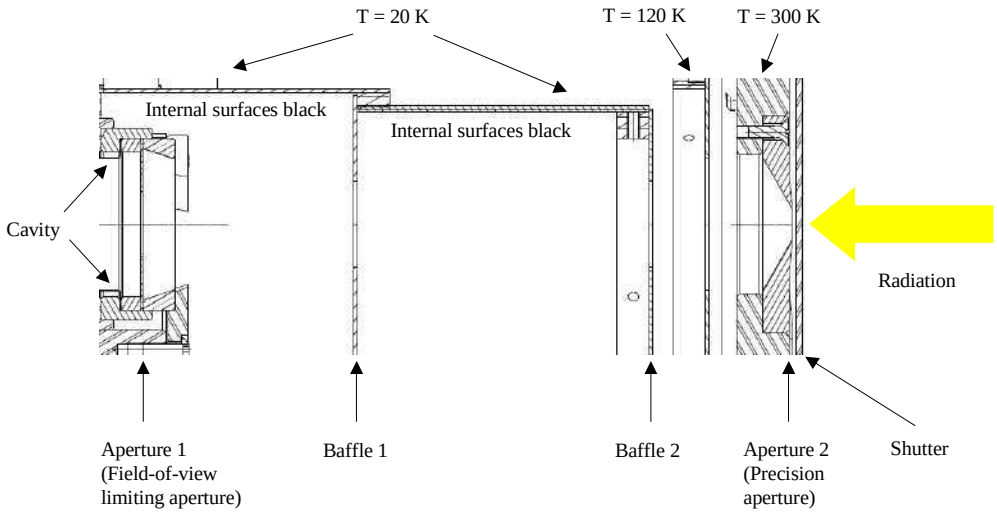


**Figure 72 Arrangement of optical components in front of the TSI cavity[45]. In the case of the ground application, a window is placed between the aperture and the shutter.**

### *3.4.1.8 Uncertainty budget regarding the aperture size*

The previous sections pointed out various sources of uncertainty in relation to the size of the precision aperture. Table 13 gives a summary of these individual uncertainty components for CSAR as it was used in Davos during the measurements reported in this thesis; the combined standard uncertainty associated with the effective optical size of the precision aperture is estimated to be 0.0152%.

The uncertainty estimates in Table 14 are valid for an improved version of the ground-based CSAR as well as a space-based version. The combined uncertainty is estimated to be 0.0059%.

[45] Design drawing by Peter Lovelock, NPL.

**Table 13 Uncertainty budget regarding the size of the precision aperture. Ground-based measurements in Davos.**

| Uncertainty component | Standard uncertainty | Discussed in Section |
|---|---|---|
| Aperture land effect | 0.0010% | 3.4.1.2 |
| Area measurement | 0.0078% | 3.4.1.3 & 3.4.1.4 |
| Thermal expansion | 0.0130% | 3.4.1.6 |
| | | |
| Combined | **0.0152%** | |

**Table 14 Uncertainty budget regarding the size of the precision aperture. Space-based measurements**

| Uncertainty component | Standard uncertainty | Discussed in Section |
|---|---|---|
| Aperture land effect | 0.001% | 3.4.1.2 |
| Area measurement | 0.0052% | 3.4.1.3 & 3.4.1.4 |
| Thermal expansion | 0.0026% | 3.4.1.6 |
| | | |
| Combined | **0.0059%** | |

### 3.4.2 Stray light rejection

#### *3.4.2.1 Radiation trap and other measures to reduce stray light*

The ground-based measurement of Total Solar Irradiance requires much greater attention to stray light than the TSI measurement in space or the measurement of radiant power. This is due to the presence of scattered light from the sky, which is of the order of 10% of the direct solar radiation[46]. The issue of stray light is exacerbated by

[46] This is according to André Fehlmann and Wolfgang Finsterle of PMOD.

the use of a window, which can give rise to inter-reflections with other optical elements.

Figure 73 illustrates the solid angle of light that should be measured by CSAR. Light originating from outside of the envelope of this solid angle is considered as "stray light", which needs to be prevented from entering the cavity.

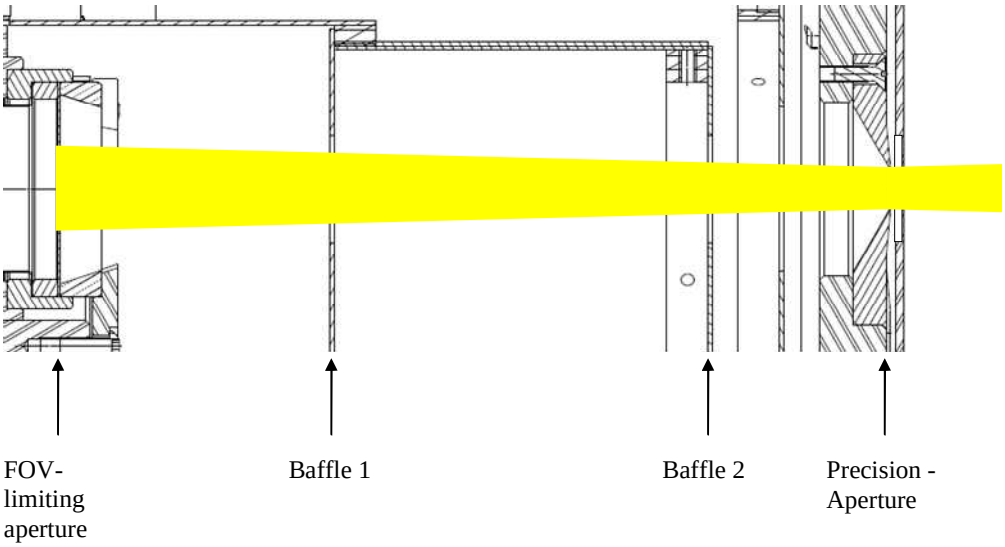


**Figure 73 Direct Sunlight (plus circumsolar light) that should be measured by the detector[47]**

Figure 74 illustrates that the baffles of the light trap are placed in such a way that it is not possible for the TSI cavity to receive light that is directly reflected from the wall of the 20 K baffle. This is true for both specularly reflected light as well as diffusely reflected light. The light therefore undergoes at least two reflections at the diffusely reflecting interior coating of the light trap. The hemispherical diffuse reflectivity of the coating is 3%. Therefore, less than 0.09% (= 3% × 3%) of the sky radiation reaches the detector. Since the sky radiation is approximately 10% of the direct solar radiation, the relative stray light

[47] Design drawing by Peter Lovelock, NPL.

effect is smaller than 0.009%. Since the largest part of the sky radiation will undergo more than two reflections inside the light trap, the contribution of the stray light to the measurement signal is expected to be negligible.

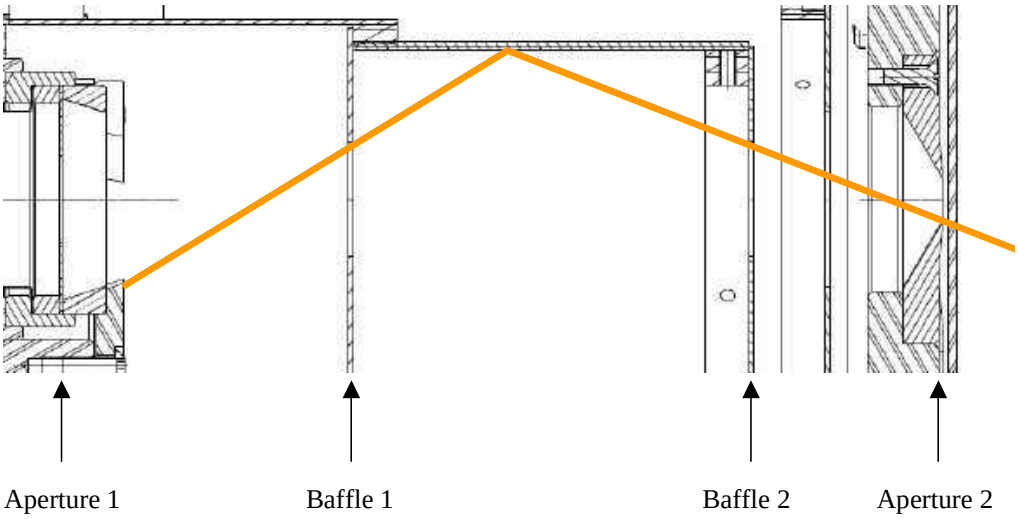


**Figure 74 Reduction of reflections from the internal surface of the 20 K heat shield[48]**

By its very nature, the light trap can only reduce stray light that enters the radiometer at an angle greater than the cut-off angle (=4.13˚, in the case of CSAR), i.e. it does not reduce stray light that originates from direct or circumsolar radiation. It is however possible that direct solar radiation or circumsolar radiation impinging on the Sun-facing surface of the precision aperture at smaller angles could inter-reflect between the aperture and the window, and could therefore make its way into the detector. In order to prevent this radiation from contributing to the main signal, the front surface of the precision apertures is inclined by an angle of 5˚ - resulting in a "volcano"-shape (see also Figure 75, or Figure 77).

[48] Design drawing by Peter Lovelock, NPL.

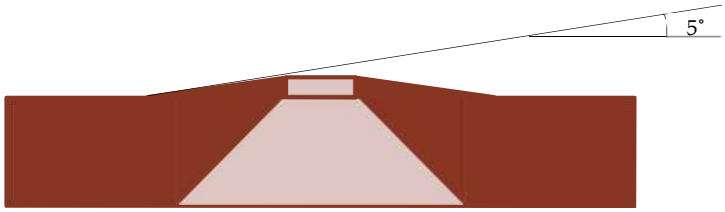


**Figure 75 Schematic of the precision aperture. The front surface is inclined ('volcano' – shaped) in order to prevent inter-reflections between the aperture and the window, which could directly enter the cavity.**

#### *3.4.2.2 Test to evaluate stray light*

In order to evaluate the contribution of the indirect sky radiation to the measured signal, the radiometer was exposed to sky radiation only (no direct sunlight), immediately after sunset, when the sky radiation level was still comparable to the radiation level during the day. Alternatingly opening and closing the shutter did not yield a significant difference in the measurement signal at the 0.003% - uncertainty level. Although this measurement also captures the sky radiation which enters directly into the system, the contribution of this component is negligible – therefore, this experiment truly evaluates the level of unwanted signal due to sky radiation.

### 3.4.3 Aperture and shutter wheel

The design of CSAR includes an aperture and shutter wheel at the front of the radiometer, which can be operated independently from each other. The aperture wheel would allow any of its apertures to be moved in front of any of the six cavities, and thus allowing a high degree of redundancy and independent verification of instrument stability on board of a satellite. Figure 76 shows the basic mechanical structure of the aperture and shutter wheel.

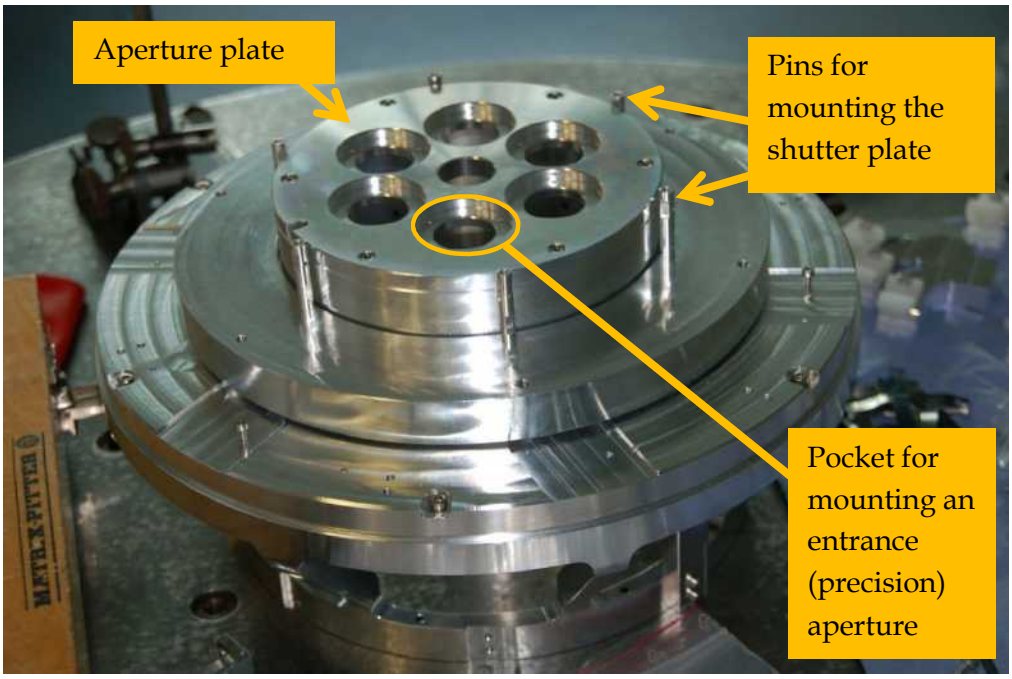


**Figure 76 Aperture and Shutter wheel – basic mechanical structure**

### 3.4.4 Static aperture support

However, the aperture and shutter wheel mechanisms were not yet operational at the time of performing the tests reported in this thesis. The aperture wheel was therefore replaced by a static aperture support (see Figure 77). The shutter wheel was replaced by a commercially available optical shutter, which was mounted in front of the vacuum window.

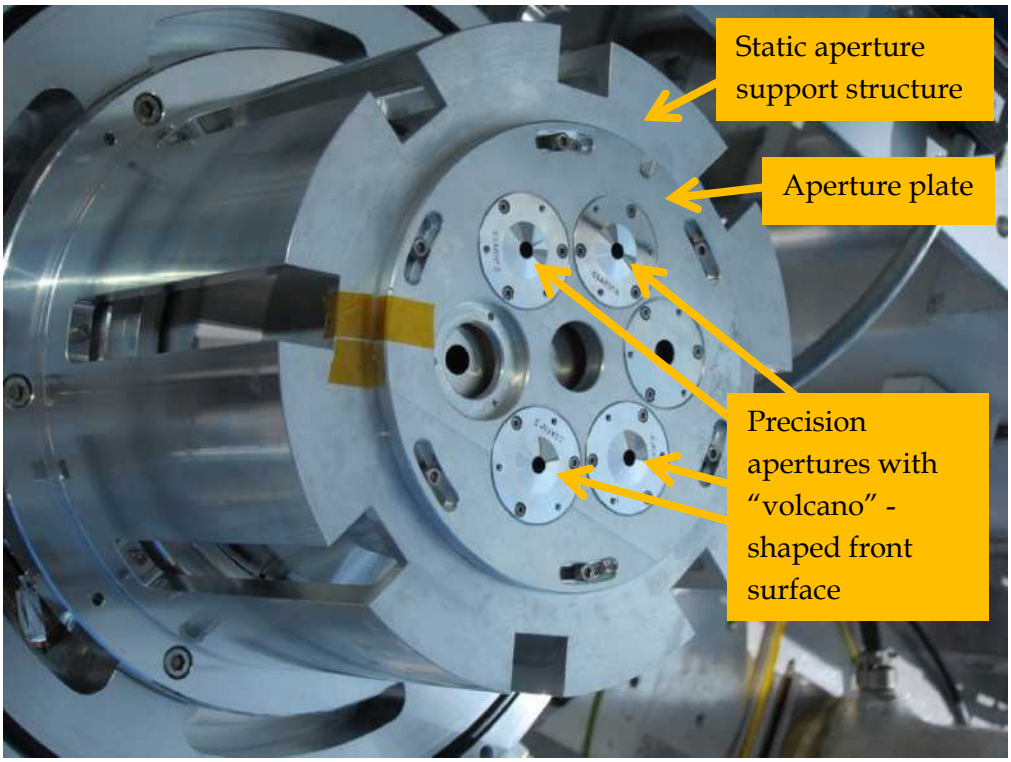


**Figure 77 Static aperture support**

### 3.4.5 Optical alignment of CSAR apertures

#### *3.4.5.1 Alignment of apertures – theoretical considerations*

The diffraction calculations assume a perfect alignment of the two apertures to the source, i.e. that the geometrical centres of the apertures and of the Sun all lie on one line. However, it is not possible to align the optical components perfectly. This unavoidable misalignment will lead to an error in the diffraction calculation.

One requirement is that the cavity aperture and the precision aperture are in line. Figure 78 shows the result of a diffraction calculation[49] which takes the sideways offset of the detector aperture (relative to the precision aperture) into account. In order for the standard uncertainty due to this offset to be negligible in the context of

[49] For this calculation the software code of Edwards was used (EDWARDS, P. J. 2004. *Diffraction Theory and Radiometry.* PhD, Imperial College.)

the ground application, it needs to be smaller than 0.004% (or < 40 ppm)[50]. This is the case if the error in the diffraction calculation due to the misalignment is within the interval [0, -130 ppm][51]; according to Figure 78 the error is within this interval as long as the offset of the apertures is ≤ 1000 μm.

In the context of the space application, the standard uncertainty due to the sideways offset needs to be smaller than 0.001% (or < 10 ppm)[52] in order to be considered negligible. This is the case if the error in the diffraction calculation due to the misalignment is within the interval [0, -34 ppm][53]; according to Figure 78 the error is within this interval as long as the offset of the apertures is ≤ 530 μm. Given the CSAR aperture geometry, this is equivalent to an angular misalignment (or pointing error) of ±0.29˚.

[50] See Section 2.4.7.
[51] See Section 2.4.3. The interval [0,-130 ppm] is a valid equivalent of a standard uncertainty of 40 ppm only after a correction of the diffraction correction factor of the ideally aligned case by -75 ppm.
[52] See Section 2.4.7.
[53] See Section 2.4.3. The interval [0,-34 ppm] is a valid equivalent of a standard uncertainty of 10 ppm only after a correction of the diffraction correction factor of the ideally aligned case by -17 ppm.

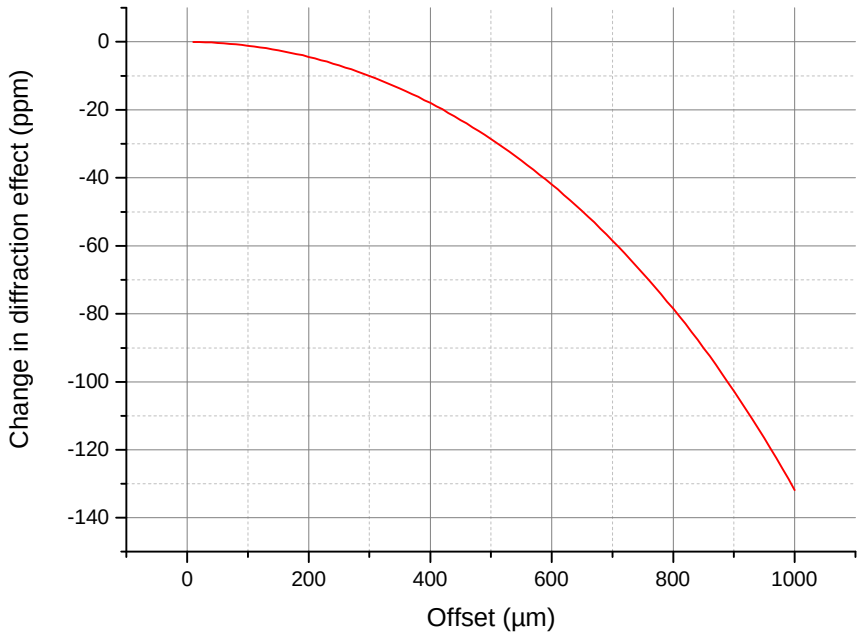


**Figure 78 Change in diffraction effect for CSAR geometry – depending on the sideways offset of the two apertures.**

### *3.4.5.2 Alignment of apertures – internal alignment*

This section explains how the apertures are aligned to each other during assembly, and Section 3.4.5.3 shows how they are aligned to the Sun during operation on the solar tracker so that the target uncertainties are not exceeded[54].

An alignment aid was employed during the assembly in order to ensure the pockets which receive the apertures are aligned to each other. A drawing of this alignment aid is shown in Figure 79; it consists mainly of a massive bottom piece, a central shaft and an extra-central shaft.

[54] see Section 3.4.5.1 for a discussion of the acceptable limits regarding the misalignment of the apertures.

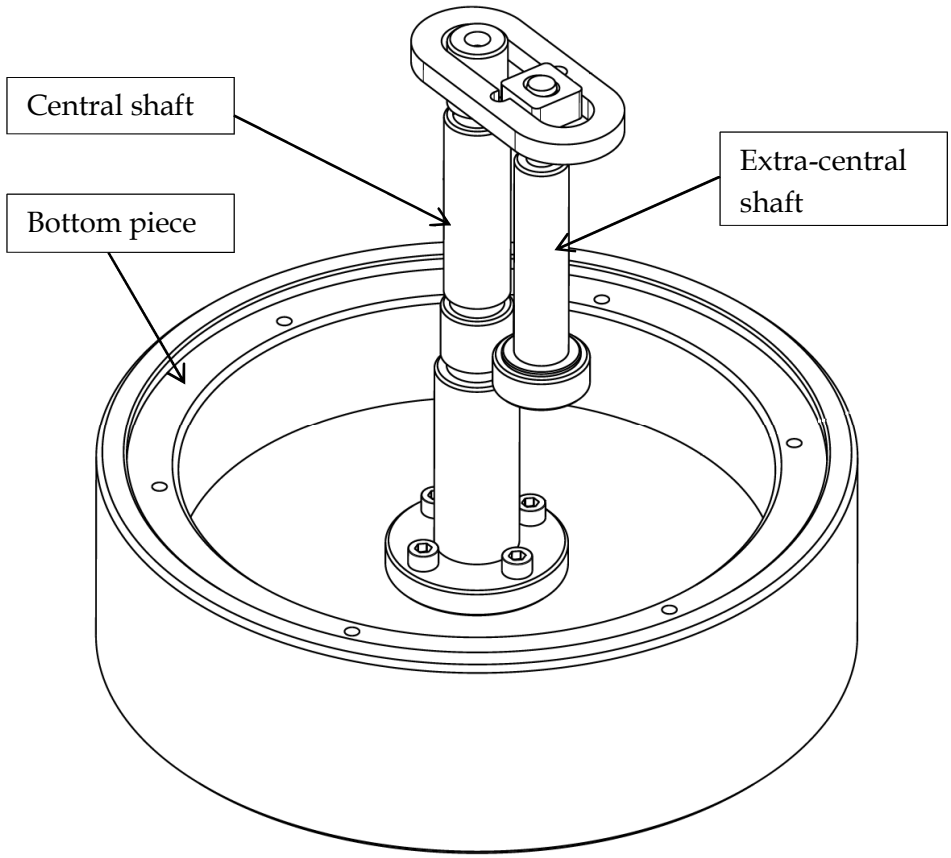


**Figure 79 Alignment aid - design drawing**[55]

Figure 80 illustrates how this alignment aid is used during assembly. The bottom piece can take up the room-temperature stage of CSAR in a location diameter. The central shaft ensures that the geometrical centre of the detector stage is aligned with the geometrical centre of the room-temperature stage. And the extra-central shaft is there to rotationally align the pockets which take up the precision apertures with the pockets that take up the cavity apertures.

[55] Drawing by Peter Lovelock (NPL)

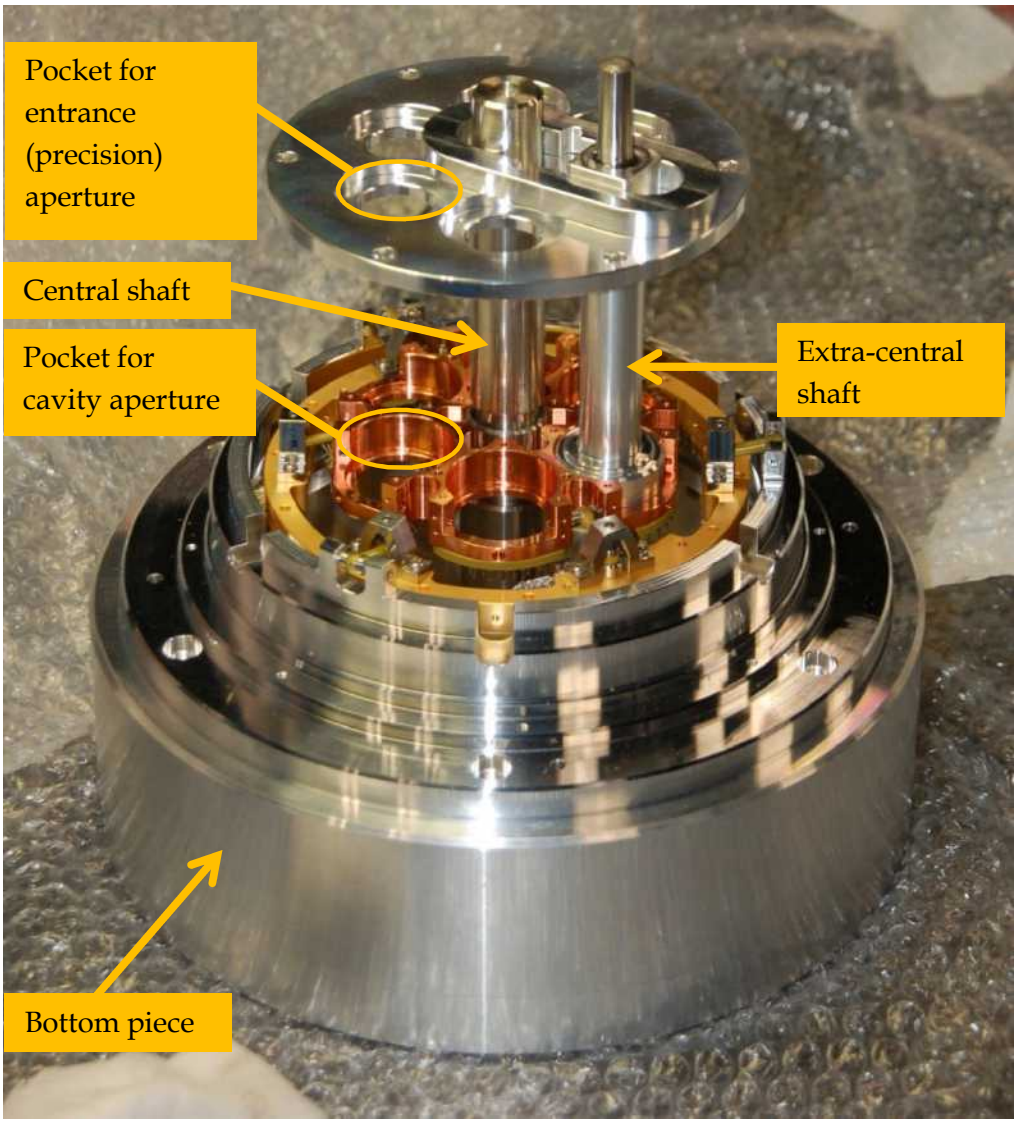


**Figure 80 Alignment aid during assembly**

In Figure 80, the alignment aid and parts of CSAR are shown, but the aperture support structure is not shown. Otherwise, it would be difficult to imagine how the alignment aid works since the most crucial component would be hidden from view. However, during the assembly, the aperture support plate is not floating in mid-air, but is connected to the support structure, as shown in Figure 81. The aperture support structure sits on a location diameter on the CSAR room-temperature stage, and the rotation is fixed with the help of a

dowel pin. This allows the aperture support structure to be removed and replaced reproducibly, without the need for using the alignment aid each time the front parts of CSAR are removed.

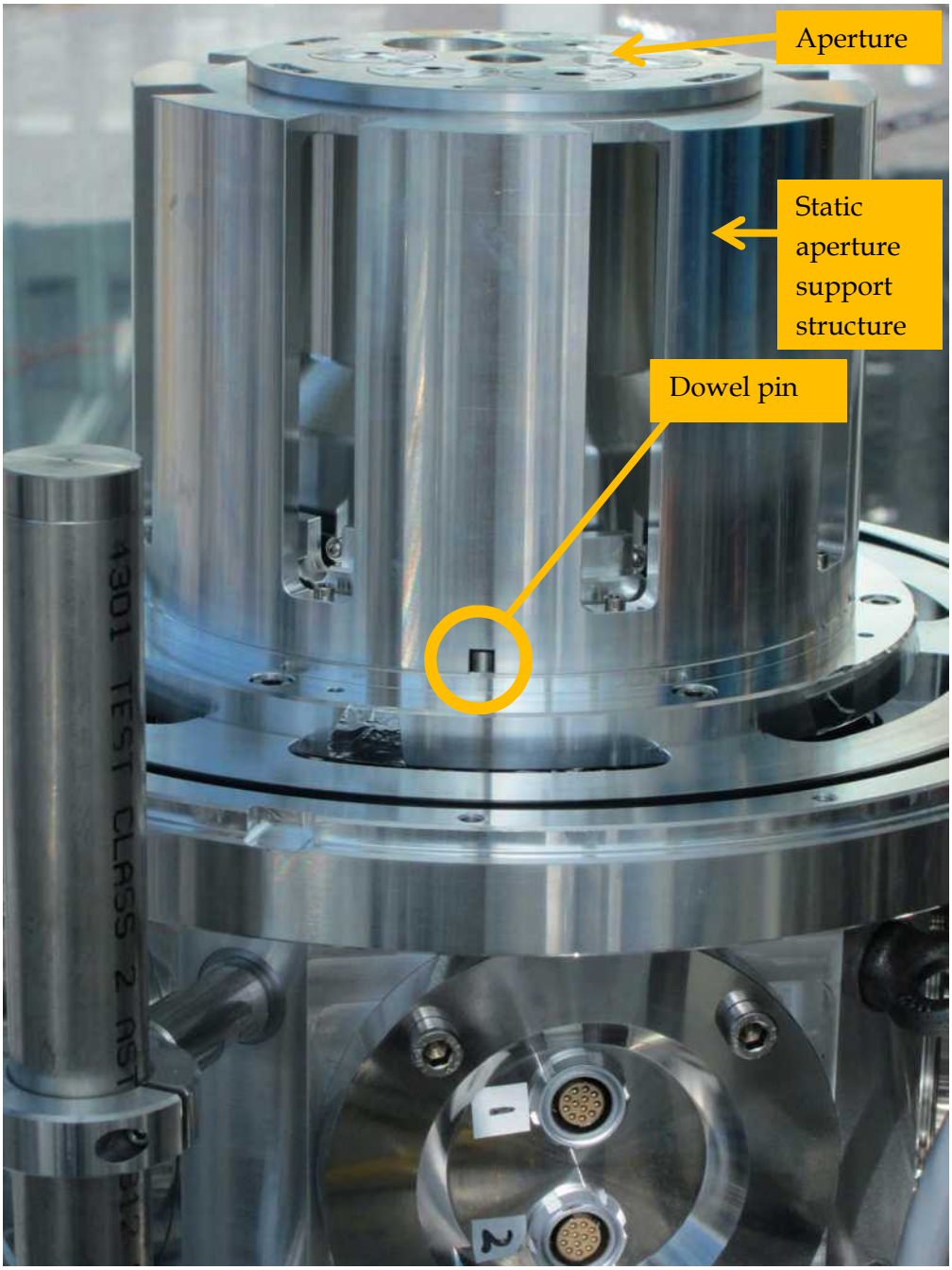


**Figure 81 Dowel pin to place static aperture support structure reproducibly**

Generally speaking, it is not very challenging to ensure an alignment of the two apertures to within ± 1000 μm or even ± 530 μm, since standard machining precision is much better than that. The most likely sources of misalignment are the dumbbell link connections between the different temperature stages of the detector.

In order to verify the alignment of the detector stages, the eccentricity of the 20K detector stage was measured relative to the outer support ring of the radiometer. The equipment used was a Taylor/Hobson Talyrond 295 (see Figure 82). First, the trace of the outer support ring was taken and fed into the machine software as a reference datum ("datum position"). Then, a trace of the central core of the 20K detector stage was taken relative to this reference datum. The result is shown in Figure 83. It shows that the eccentricity of the two stages is approximately 48 μm, and therefore well within the required tolerance[56].

[56] I am grateful to my colleague David Flack from the Dimensional Measurement Team at the NPL, who carried out these measurements.


**Figure 82 Measurement of alignment of detector stage to outer support structure**

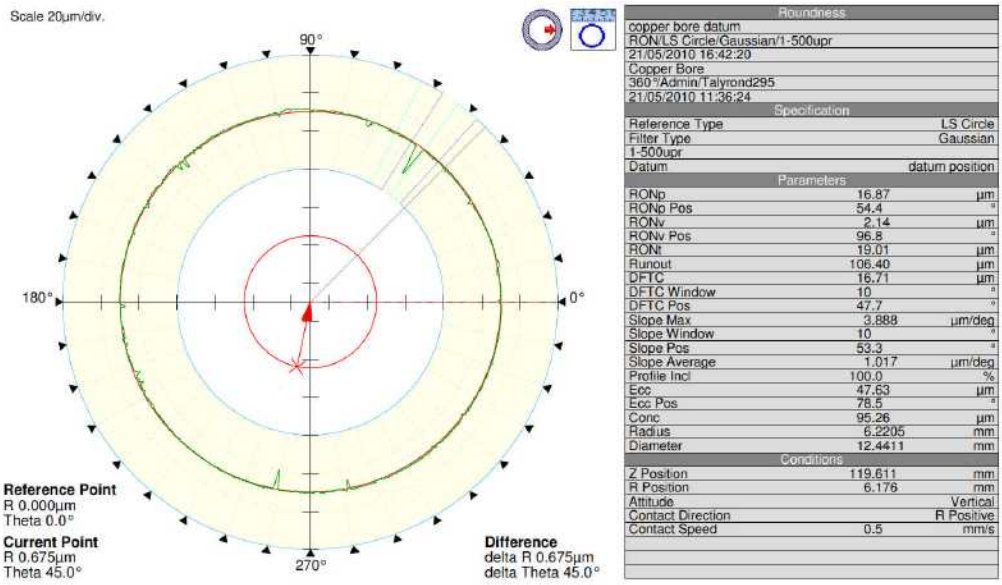


**Figure 83 Eccentricity of the detector stage**

Another effect that needs to be taken into account when it comes to the alignment of precision apertures and cavity apertures is the radial offset of the cavity apertures due to the contraction of the detector stage when cooling down to operating temperatures. The radial offset of the cavity apertures due to the contraction of the detector stage was taken into account in the design and manufacture of the instrument. The calculated radial offset on cool-down is 110 µm. As a consequence, the aperture pockets on the room temperature stage (see, e.g., Figure 88) are manufactured to sit on a virtual radius of 34.89 mm, whereas the cavity pockets on the 20 K detector stage (see Figure 82) are centred on a nominal 35 mm radius.

### *3.4.5.3 Alignment of CSAR to the Sun*

While Section 3.4.5.2 shows how the apertures are aligned to each other during assembly, this section explains how the CSAR apertures

are aligned to the Sun during operation on the solar tracker so that the target uncertainties are not exceeded[57].

The alignment of CSAR is performed in two steps. In a first step, the projection of Sunlight falling through a 8 mm diameter entrance aperture (see Figure 84) is made concentric to a 5 mm diameter target on the detector stage (see Figure 85) by adjusting the tilt of the vacuum can with respect to the tracker table (the adjustment screws can be seen in Figure 86 and Figure 88). This alignment is done while CSAR is at operating temperatures and the solar tracker is pointing to the Sun. The concentricity is judged by eye, using a beam splitter (see Figure 87). This method is adequate because the annulus of an 8 mm diameter patch of light on a 5 mm black target is only 1.5 mm wide; under these circumstances one can certainly distinguish between perfect concentricity and an offset of ±0.5 mm.

An offset of the apertures of ±0.5 mm due to the initial alignment of the instrument to the sun is equivalent to an angular misalignment of ±0.28˚. Together with a pointing error of the solar tracker of ±0.25˚, the angular misalignment of the instrument with respect to the sun can therefore be expected to lie within the range of ±0.53˚. This is equivalent to an offset of the second CSAR aperture of 0.96 mm, which leads to a standard uncertainty in the diffraction effect due to the offset of the second aperture of less than 0.004% (see Section 3.4.5.1).

The pointing error can be reduced significantly for the space application, if the solar alignment sensor is directly attached to CSAR. From the evidence presented in the previous section regarding the

[57] See Section 3.4.5.1 for a discussion of the acceptable limits regarding the misalignment of the apertures.

internal alignment of CSAR, it should be possible to achieve an overall pointing error of less than ±0.29˚, which is equivalent to an offset of the second CSAR aperture of less than 0.53 mm, and which would therefore lead to an uncertainty in the diffraction effect of less than 0.001% (see Section 3.4.5.1).

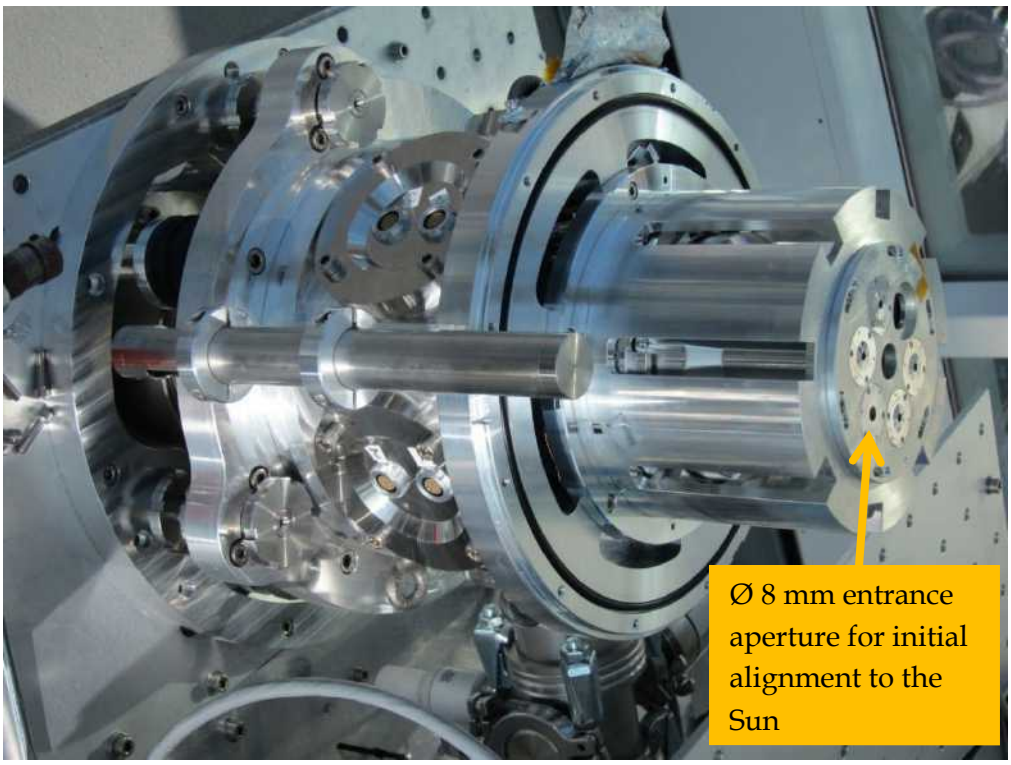


**Figure 84 CSAR with Ø 8 mm entrance aperture for initial alignment to the Sun.**

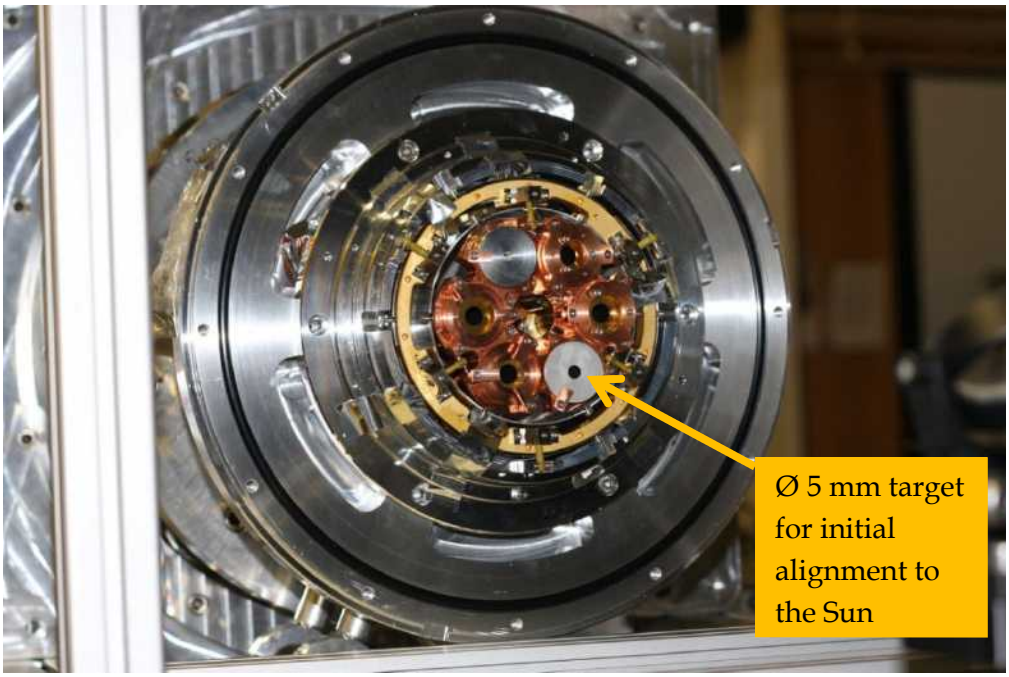


**Figure 85 Sand-blasted Aluminium target for initial alignment to the Sun.**

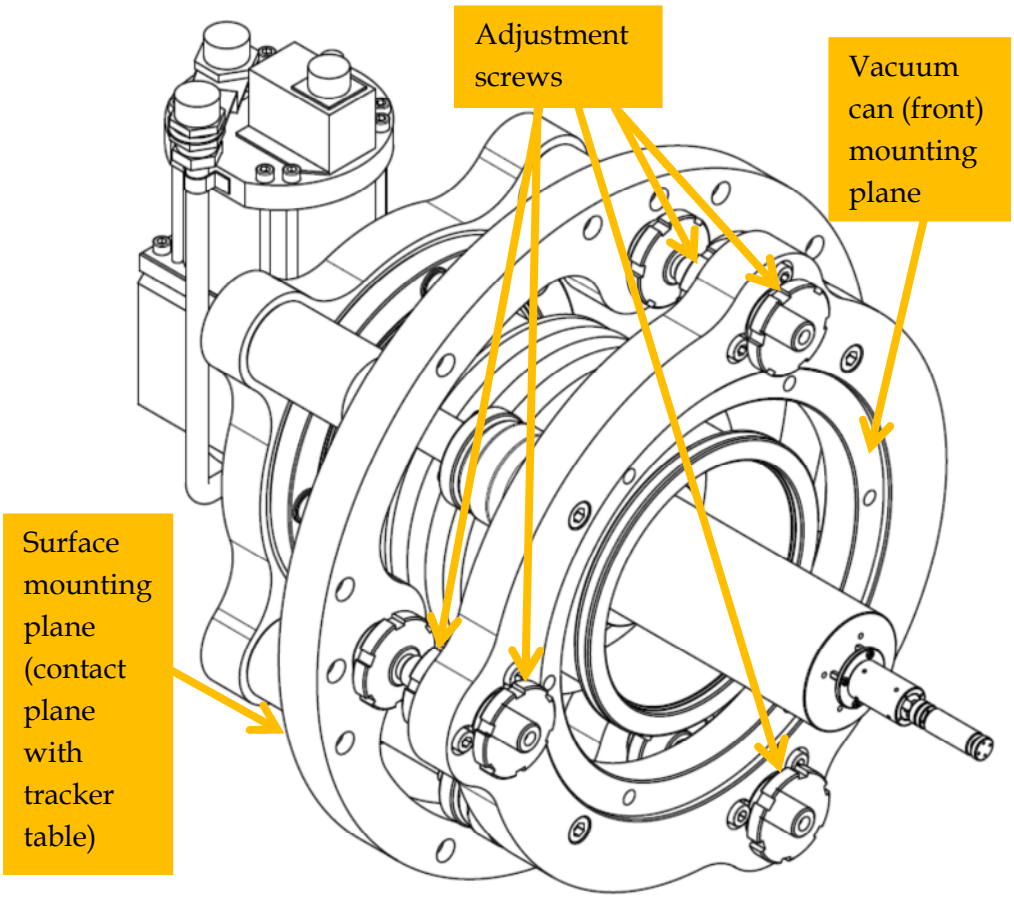


**Figure 86 Design drawing showing the three sets of adjustment screws which allow the CSAR vacuum can to be tilted with respect to the solar tracker.**

**Figure 87 Initial alignment of CSAR to the Sun. The picture shows the author with a beam splitter, and André Fehlmann (PMOD/WRC) adjusting the tilt of CSAR.**

The above described procedure for the initial alignment of CSAR to the Sun means that the operator needs to stand in front of the tracker table, casting a shadow over other instruments, and the operator needs to make physical contact with the instrument, and therefore indirectly with the tracker table. This is acceptable for a one-off alignment, but it would not be acceptable for a routine checking of the CSAR alignment during an official comparison of radiometers, e.g. an International Pyrheliometer Comparison, because it would unduly influence the other instruments' readings.

Therefore, after the initial alignment of CSAR to the Sun, another alignment tool is used to be able to check the alignment very easily at any point during the operation, and without needing to touch the radiometer or to stand upright directly in front of the solar tracker table. Figure 88 shows the alignment tool that is used for this purpose;

it is a simple tube with an entrance aperture of 1 mm diameter at the front. The sunlight that passes through this entrance aperture is projected onto an adjustable target on the back wall of the tube, and this target can be seen through two viewing ports on the side of the tube.

After the initial alignment of CSAR to the Sun, the target at the end of this external alignment aid is adjusted to be concentric with the 1 mm diameter patch of light; afterwards, this alignment aid can be used to check whether the alignment of CSAR to the Sun has changed.

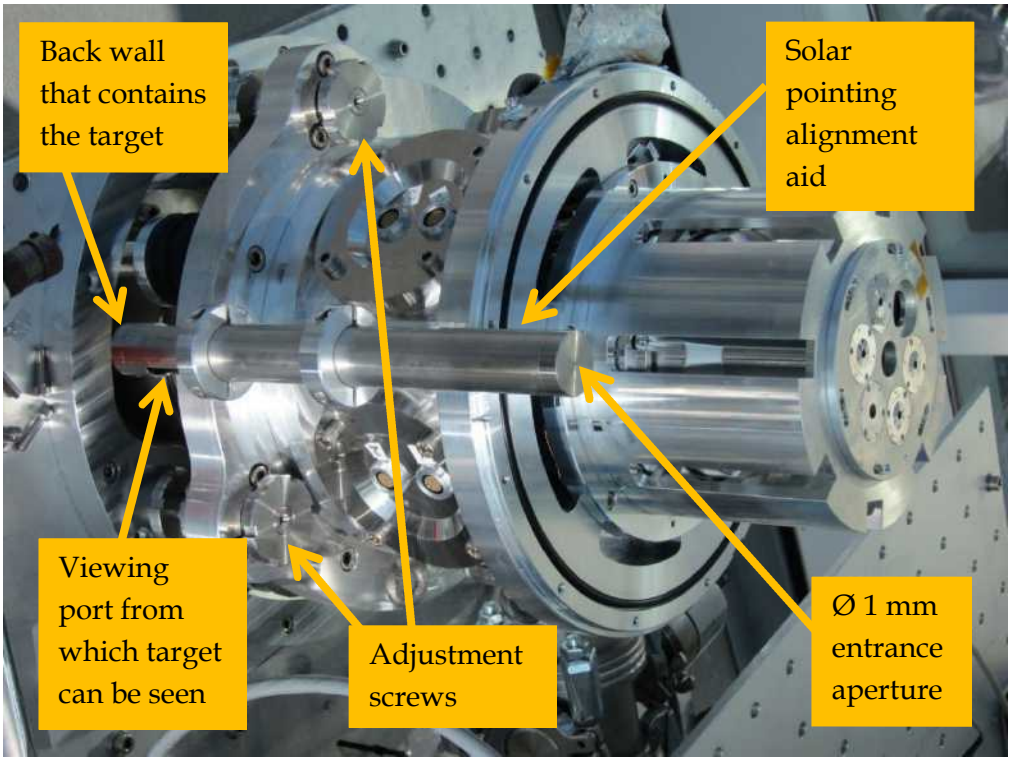


**Figure 88 CSAR on solar tracker (vacuum chamber open) with alignment aid and adjustment screws.**

### 3.4.6 Diffraction effect and spectral distribution of Solar Irradiance

The diffraction effect is not only dependent on the alignment of the apertures (as discussed in Section 3.4.5), but it is also dependent on the spectral distribution of the solar radiation and the spectral distribution

of the detector absorptivity. In order to arrive at a more convenient measurement equation, the diffraction effect was defined as follows in Section 2.4.5:

$$F_{diff} = \frac{\int_0^\infty F_{diff}(\lambda)\alpha(\lambda)I_{SSI}(\lambda)d\lambda}{\int_0^\infty \alpha(\lambda)I_{SSI}(\lambda)d\lambda} \qquad (3.19)$$

In theory, Equation (3.19) implies that a detailed knowledge about the spectral dependence of the various parameters is not necessary. $F_{diff}$ could conceptually be determined experimentally by making a ratio measurement of two radiometers that are both exposed to the same Solar Irradiance as CSAR; the first radiometer would have to have the same optical geometry as CSAR and the same cavity absorptivity as CSAR, and the second radiometer should have the same cavity absorptivity as CSAR and should not suffer from any diffraction effect at all. This implies that the second radiometer would not have a field-of-view limiting aperture, which is not realistic for the ground application due to the significant amount of sky radiation.

Since a direct experimental determination of the diffraction effect is extremely challenging in the case of the ground application, $F_{diff}$ is determined using theoretical calculations of the spectral distribution of Solar Irradiance. The uncertainty due to these calculations is estimated by trying to establish the most extreme cases of these calculations and to assume the resulting $F_{diff}$ as minimum and maximum values.

Figure 89 shows model results for the spectral distribution of Solar Irradiance in Davos. In particular it shows the two extreme cases

of a Solar Zenith Angle of 0˚ and a Solar Zenith Angle of 80˚; these two spectral distributions are significantly different with the peak value being different by a factor of three and the peak wavelength shifted by 250 nm.

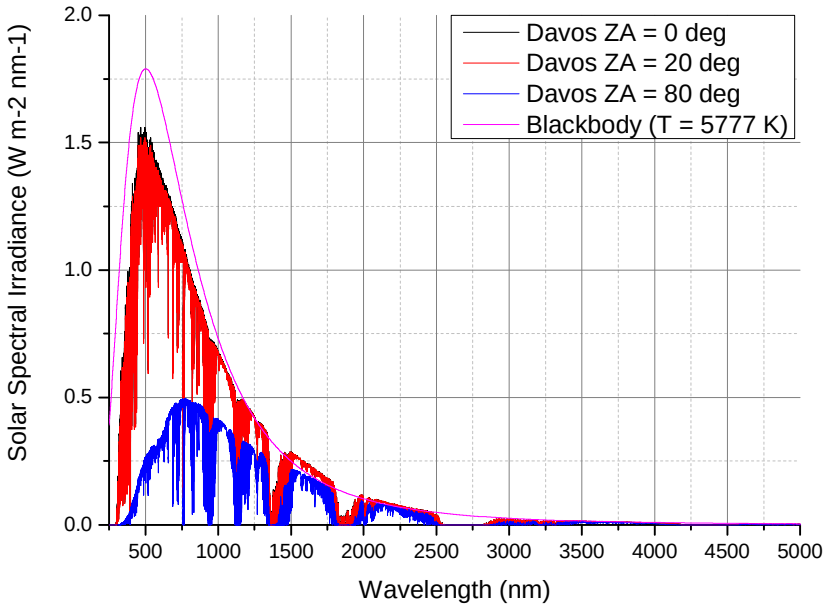


**Figure 89 Solar Spectral Irradiance in Davos for various Solar Zenith Angles (ZA), as estimated with Modtran[58]**

Table 15 shows the integrated diffraction effect $F_{diff}$ for the Solar Spectral Irradiances corresponding to the extreme Solar Zenith Angles. The values were obtained using Equation (3.19); the calculation was using absorptivity values for the CSAR cavity corresponding to the reflectivity values shown in Figure 100 (Aeroglaze Z302) in Section 3.5.3.3. The spectral diffraction effect $F_{diff}(\lambda)$ was evaluated using Mathematica code developed by

[58] Data courtesy of André Fehlmann (PMOD/WRC). The pink line shows the blackbody curve of the effective Temperature of the Sun (T = 5777 K) at the top of the atmosphere.

Edwards (Edwards, 2004)[59] and using average values for the solar radius and the distance Sun-Earth.

**Table 15 Integrated diffraction effect for the CSAR aperture geometry for various spectral distributions of Solar Irradiance**

| | $F_{diff}$ | $1 - F_{diff}$ |
|---|---|---|
| **Solar Zenith Angle = 0°** | 0.998929 | 0.001071 |
| **Solar Zenith Angle = 80°** | 0.998732 | 0.001268 |
| **Black Body Radiation ($T_{Sun}$ = 5777 K)** | 0.998883 | 0.001117 |

Table 15 shows that the maximum relative difference in the diffraction effect is 0.000197 (or 0.0197%, or 197 ppm). Using Equation (2.6) in Section 2.4.3, the standard uncertainty due to the spectral dependence of the diffraction effect can be estimated as 0.0057% (or 57 ppm).

## 3.5 The CSAR detector system

### 3.5.1 Thermal design of the detector system

One of the main advantages of operation at cryogenic temperatures is the significant reduction in heat capacity of typical cavity materials, when compared to room temperature. This allows the use of a larger cavity, which enables a much higher absorptivity, while maintaining a small time constant. The following sections will explain how these various parameters are interlinked, and what solution was implemented for CSAR.

[59] The function is called "DiffractionLossFocke".

An overview over the functionality of a cryogenic detector was already given at the beginning of Section 2.5. In the following, the fundamental operating principles are explored further.

#### 3.5.1.1 *The detector system – general observations*

Consider a constant radiant power $\dot{Q}$ absorbed in a cavity at temperature $T_c$ and connected by a heat link of thermal resistance $R$ to a heat sink at temperature $T_s$. For a small temperature difference $dT = T_s - T_c$ and an incremental time period $dt$, the heat flow equation can be written as (Smith et al., 1968)

$$\dot{Q}\,dt - (dT / R)\,dt = C\,dT \tag{3.20}$$

which can be solved to give the following equation

$$dT = R\dot{Q}\left(1 - e^{-\frac{t}{RC}}\right) \tag{3.21}$$

where C is the thermal capacity of the cavity and is equal to the mass of the cavity $m$ times its specific heat $c$. Thus the temperature of the receiver will rise exponentially with a natural time constant of

$$\tau = RC = Rmc \tag{3.22}$$

to a value of

$$\Delta T = R\dot{Q} \tag{3.23}$$

for $t \to \infty$.

$\Delta T$ will in further discussions be referred to as the 'temperature rise'. It is the maximum temperature difference between the heat sink and

the cavity detector, and it occurs when the maximum radiant power is incident on the detector cavity.

How well the cavity temperature can be resolved depends on the sensitivity of the cavity thermometer $S_{c,th}$, its resistance $R_{c,th}$ and the ability of the electrical system to resolve changes in the resistance, $dR_{c,th}/R_{c,th}$:

$$dT_c = \frac{dT_{c,th}}{dR_{c,th}} \frac{dR_{c,th}}{R_{c,th}} R_{c,th} = \frac{1}{S_{c,th}} \frac{dR_{c,th}}{R_{c,th}} R_{c,th} \qquad (3.24)$$

#### 3.5.1.2 *The thermometer, the heat link, and power resolution*

The thermometers chosen for this instrument are bare chip RhFe sensors with silica substrates and gold coatings on the contact surface (see Figure 90 for a photograph). According to the manufacturer, they are suitable for use in space, due to their robustness and high resistance to ionizing radiation. Apart from that, they have a highly linear temperature response in the relevant temperature range and a very low thermal capacity (the thermal time constant is of the order of a few milliseconds, according to the manufacturer). Over the last 20 years, they have been used for almost all new cryogenic radiometer developments at NPL.

A thin-film rhodium-iron thermometer typically has a sensitivity of approximately $0.2\,\Omega\,K^{-1}$ at temperatures of approximately 20 K (Bedford et al., 1997). In order to determine the resistance of the thermometer, a Tinsley SENATOR automatic resistance thermometer bridge, Type 5840 is used. In the 10Ω-range, the resolution of the resistance measurement is 1 part in $10^7$. The selected temperature sensors (bare chip, Lakeshore) have a resistance

of approximately 12 Ω at this temperature. This leads to a temperature resolution of approximately 6 μK.

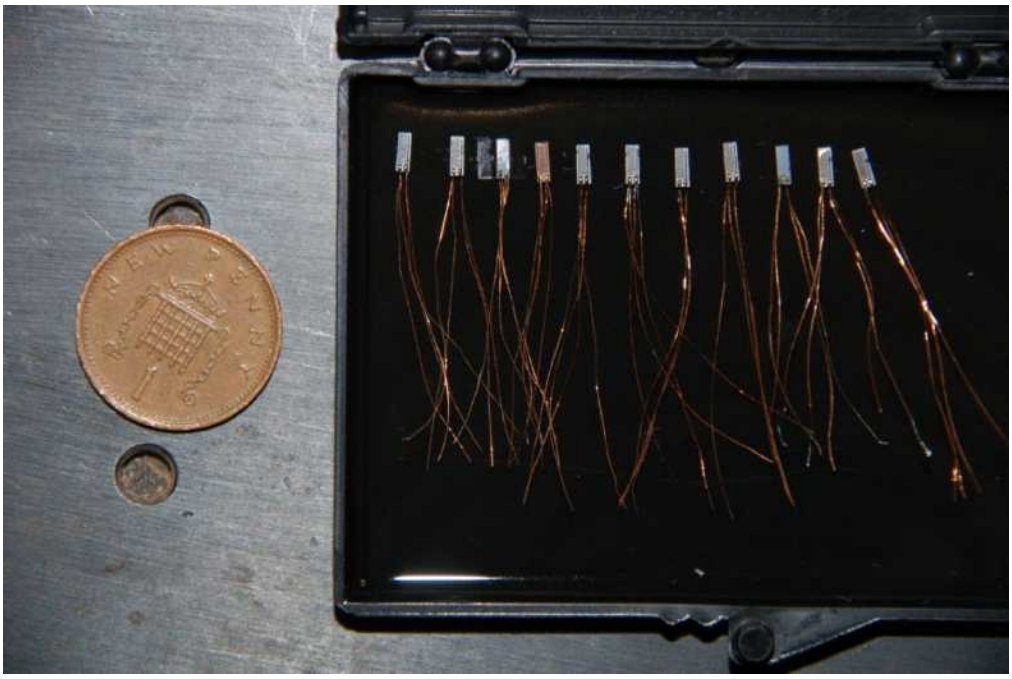

**Figure 90 RhFe temperature sensors, Lakeshore, bare chip.**

The temperature rise of the cavity is approximately 0.4 K when the cavity is exposed to maximum levels of Direct Solar Radiation (assuming a 5 mm diameter defining aperture), i.e. ~18 mW. A temperature resolution of 6 μK is therefore approximately equivalent to a power resolution of 0.3 μW, or equivalent to a relative power resolution of the order of 0.0015%. For a measurement in the lab, where the power in the laser beam may only be 5 mW, a power resolution of 0.3 μW is equivalent to a relative power resolution of 0.006%.

This simple calculation, which assumes a linear detector response, is justified because the thermal conductivity of copper (which was used as the heat-link material) is practically constant at temperatures around 20 K. Figure 91 shows the heat link, which

consists of 100 windings of bare copper wire (diameter 100 µm, no insulation) around the cavity and the heat-sink bobbin of the reference block.

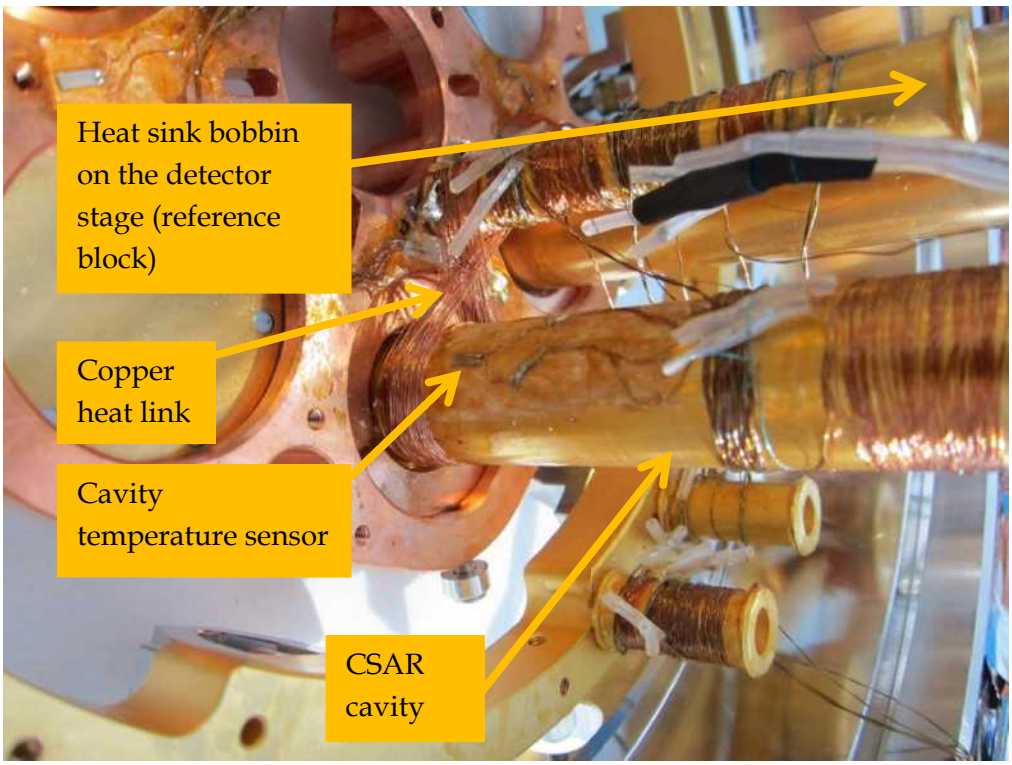


**Figure 91 CSAR cavity and heat link to the reference block**

### 3.5.2 Thermal material properties of copper at cryogenic temperatures

This sub-section is dedicated to the thermal material properties of copper at cryogenic temperatures, since the main thermal and structural elements of the detector system are made out of oxygen-free high conductivity copper (OFHC copper); this includes the reference block, the heat link, as well as the cavity. All the data presented in this sub-section were retrieved from the NIST Cryogenic Materials Properties Database (Marquardt et al., 2000).

### 3.5.2.1 *Specific heat capacity of OFHC copper*

Figure 92 shows that the specific heat capacity of OFHC copper decreases significantly at cryogenic temperatures. The value at 20 K is by a factor of fifty lower than the room temperature value. According to Equation (3.22), this means that the thermal time constant of a detector system will be reduced by the same factor of fifty when changing the operating temperature from room temperature to 20 K. Or, in other words, the mass of a cavity operated at 20 K can be fifty times higher than that of a room-temperature cavity, and both systems will still have the same time constant. This allows the construction of a much larger cavity with a much larger absorptivity in the case of a cryogenic radiometer.

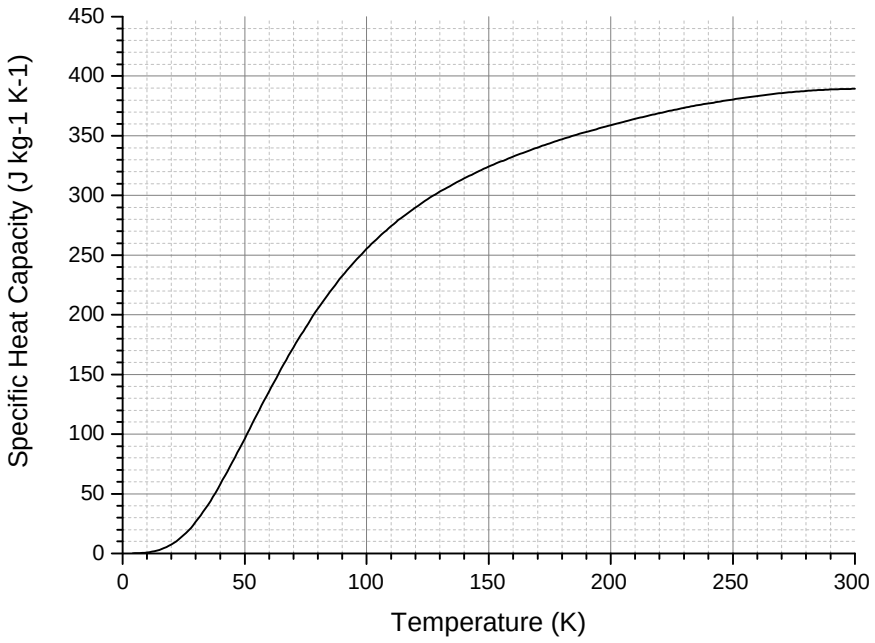


**Figure 92 Specific heat capacity of copper (OFHC) in the temperature range 4 K – 300 K**

### 3.5.2.2 *Thermal conductivity of OFHC copper*

The thermal conductivity of copper increases significantly below 100 K and reaches a maximum at around 20 K, and decreases again for even lower temperatures. This is shown in Figure 93.

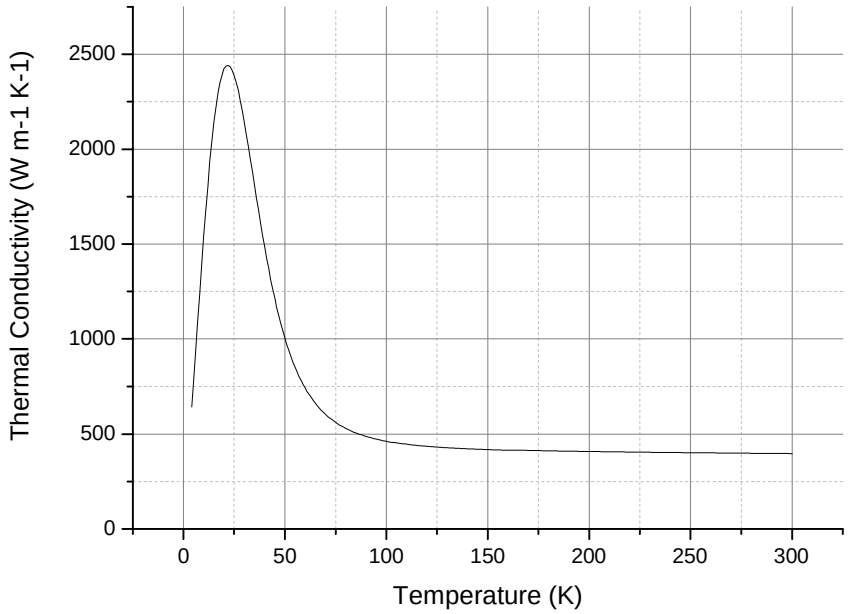


**Figure 93 Thermal conductivity of OFHC copper.**

The increased thermal conductivity increases the thermal diffusivity, which will be discussed in the next sub-section (Section 3.5.2.3). But the temperature-dependence of the heat-link material (OFHC copper) also has a direct influence on the linearity of the temperature response of the detector system; the temperature-response will only be linear if the thermal conductivity of the heat-link material is constant over the temperature range that corresponds to the dynamic range of the detector. Figure 94 shows that the thermal conductivity of OFHC copper plateaus in the region from 21 K to 22 K.

The CSAR detector system is therefore expected to be most linear in this temperature range.

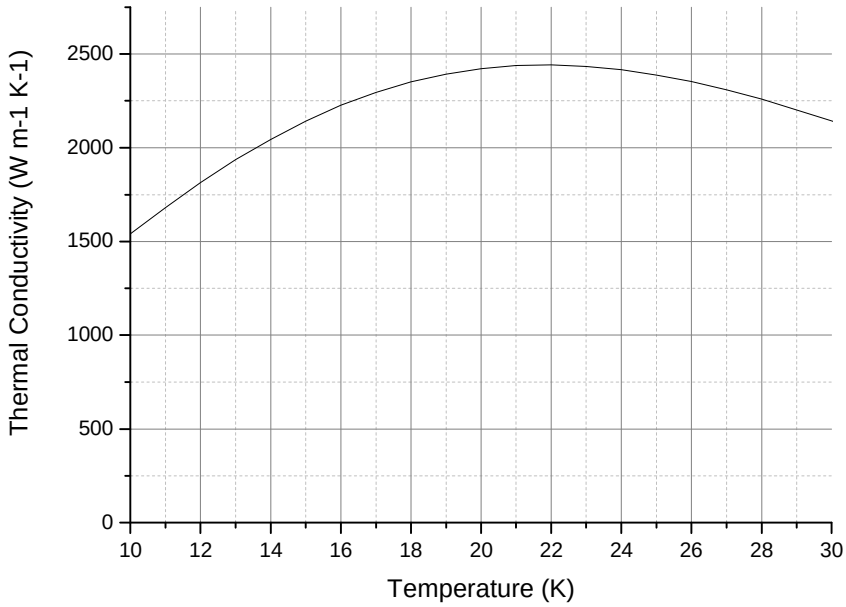


**Figure 94 Thermal conductivity of OFHC copper in the temperature range 10 K – 30 K. This plot is based on the same data as Figure 93.**

### *3.5.2.3 Thermal diffusivity of OFHC copper*

This sub-section combines the information of the previous two sections, by focussing on the thermal diffusivity of OFHC copper at cryogenic temperatures. Thermal diffusivity $D$ is a measure of thermal inertia of a material; the higher the thermal diffusivity, the faster the propagation of heat into the medium. It is defined as

$$D = \frac{k}{\rho c_p} \tag{3.25}$$

where

$k$ is the thermal conductivity,

$\rho$ is the density, and

$c_p$ is the specific heat capacity of the material.

This definition and interpretation of thermal diffusivity can be found in standard textbooks such as (Venkanna, 2010) .

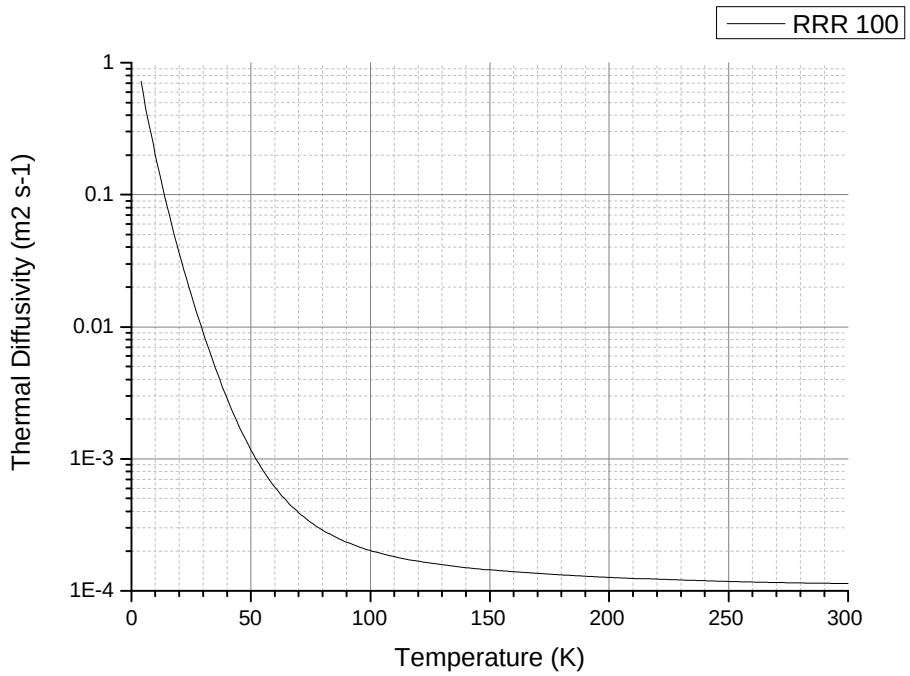


**Figure 95 Thermal diffusivity of OFHC copper**

Figure 95 shows that the thermal diffusivity increases by approximately two orders of magnitude – when comparing an operating temperature of 20 K with room temperature. This means that – after a change in input power, the various components of a cryogenic detector system will reach a thermodynamic equilibrium in a fraction of the time that it takes a room-temperature radiometer.

### 3.5.3 The cavity

The cavity is one of the most vital elements of the radiometer. Its function is to absorb the incoming radiation. Figure 96 shows

schematically how the cavities are integrated into the radiometer head. However, although there are six pockets for cavities in the reference block, only one cavity was installed and wired up completely for the purpose of the measurements reported in this thesis.

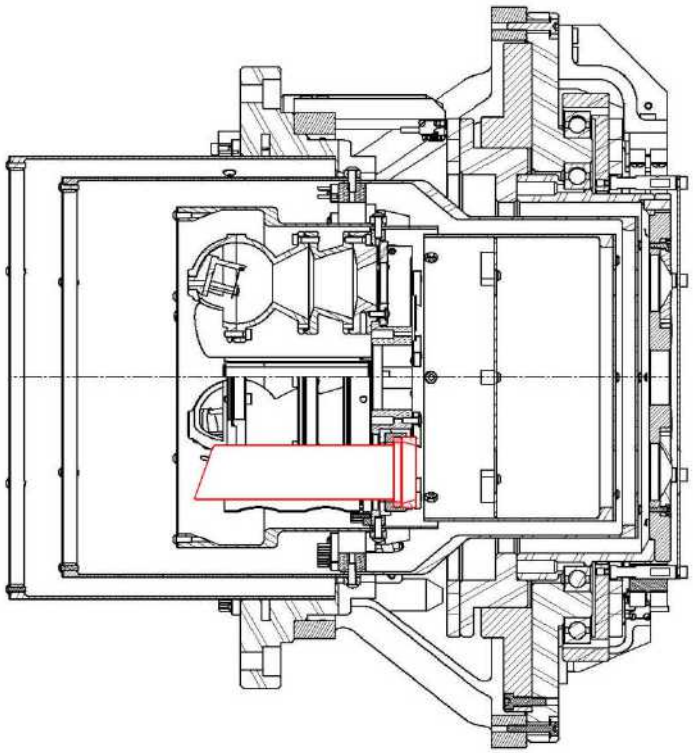

**Figure 96 The cavity mounted on the detector stage. The cavity is mechanically fixed at the front flange, with two nylon rings thermally isolating it from the reference block. A copper heat link is added at the front of the cavity (this heat link is not shown in this picture). A 10 mm aperture is mounted at the cavity entrance.**

### *3.5.3.1 Cavity geometry*

Figure 97 shows a drawing of the cavity that was used. The cavity is made of electroformed copper and has a diameter of 15 mm and a length of 110 mm. The front entrance is closed off with a 10 mm diameter aperture. The wall thickness of the cavity and of the entrance aperture is 0.2 mm; the walls are coated on the inside with Aeroglaze Z302 and are gold-plated on the outside. The main body of

the cavity consists of two parts, which are bolted together in the assembled state; the cavity is split into two parts in order to be able to guarantee a good black coating at the back plate, where the optical beam impinges first. The back plate is inclined by an angle of 32˚. The front part of the cavity consists of a 100 mm long cylinder. The total mass of the cavity is 10 g.

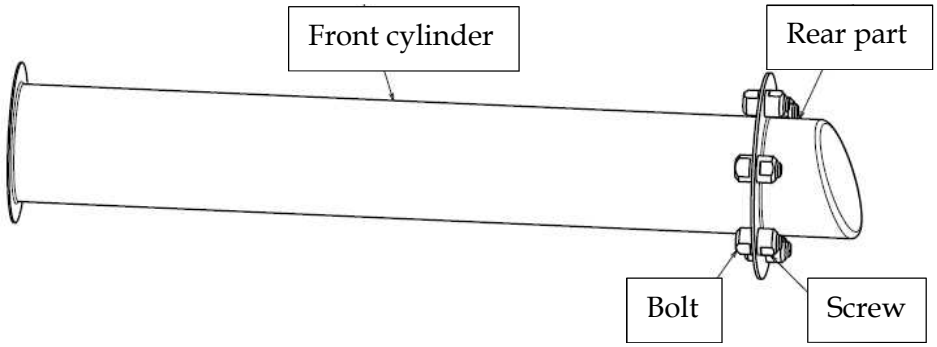


**Figure 97 CSAR cavity**

After impinging on the back plate, the sunbeam undergoes at least ten specular reflections inside the cavity, before reaching the entrance aperture of the cavity (the field of view limiting aperture); this reduces the specular component to an insignificant level, assuming a specular reflection of <10.5% for the wavelength range from 0.3 to 40 µm (Datla et al., 1992). Figure 98 illustrates the beam path of specularly reflected light at the rear end of the cavity.

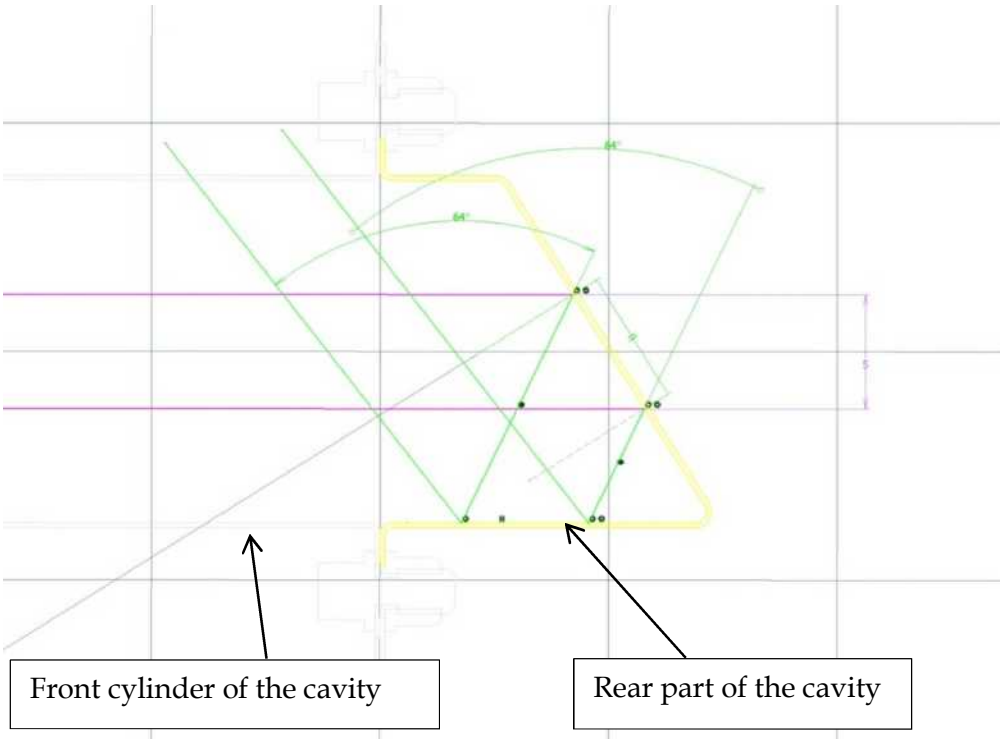


**Figure 98 Illustration of the geometrical beam path at the rear part of the cavity. The incoming beam (diameter 5 mm) is shown in pink. The reflected beam is shown in green[60].**

### *3.5.3.2 Cavity surface coatings - candidates*

As already explained in Section 2.5.2, the cavity reflectivity is directly proportional to the diffuse reflectivity of the internal surface coating of the cavity. For this research project, two different black coatings were evaluated – Nickel Phosphorus (NiP) and Aeroglaze Z302. While Aeroglaze Z302 has a significant track record on TSI space radiometers, NiP has so far only been used once - in the Total Irradiance Monitor (TIM). However, the performance of NiP on TIM seems to be very satisfactory, which is why it was also considered for the CSAR design.

Figure 99 shows the spectral diffuse reflectivity of two different Nickel-Phosphorus (NiP) black samples and of Aeroglaze Z302, as

[60] Drawing by Peter Lovelock (NPL)

measured at NPL. The first type of Nickel-Phosphorus black was produced at NPL and measured by Martin Dury (Dury et al., 2006). The second type of NiP-black was produced by NEC Toshiba Satellite Systems in Japan, and the reflectivity measurements were performed by Eric Usadi (NPL)[61]. The Aeroglaze Z302 measurements were performed on a sample that was coated using the same procedure as for the coating of the CSAR detector cavity[62]; the measurements were performed by my NPL-colleagues Andrew Deadman and Chris Chunnilall.

In the visible region of the wavelength spectrum and the infrared region up to 2400 nm, the diffuse hemispherical reflectivity of Aeroglaze Z302 was measured directly; however, in the infrared beyond 2400 nm, the diffuse hemispherical reflectivity was estimated from measurements of the total hemispherical reflectivity in combination with the assumption that the ratio between diffuse and total reflectivity stays approximately constant in the whole infrared region of the spectrum. This approximation was necessary due to the fact that the NPL calibration facility for measuring diffuse hemispherical reflectivity was out of commission in the final one and a half years leading up to the submission of this thesis.

[61] More detailed information about this NiP black can be found in Appendix G.
[62] The coating of the CSAR cavity, as well as the samples, with Aeroglaze Z302 was carried out by colleagues at the World Radiation Center (Davos).

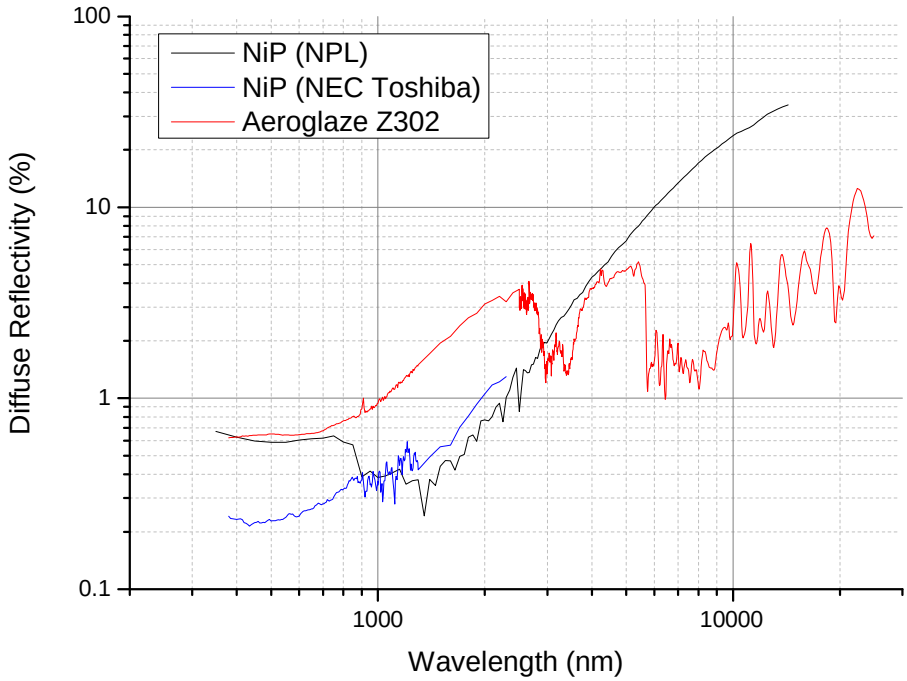


**Figure 99 Spectral diffuse hemispherical reflectivity of two different Nickel-Phosphorus (NiP) – blacks and of Aeroglaze Z302.**

### *3.5.3.3 Cavity Reflectivity*

As already discussed in Section 2.5.2, the cavity reflectivity can be derived from the diffuse reflectivity of the surface coating and the geometry of the cavity. Using the reflectivity measurements shown in Figure 99, and the cavity geometry as described in Section 3.5.3.1 leads to the spectral cavity reflectivity presented in Figure 100.

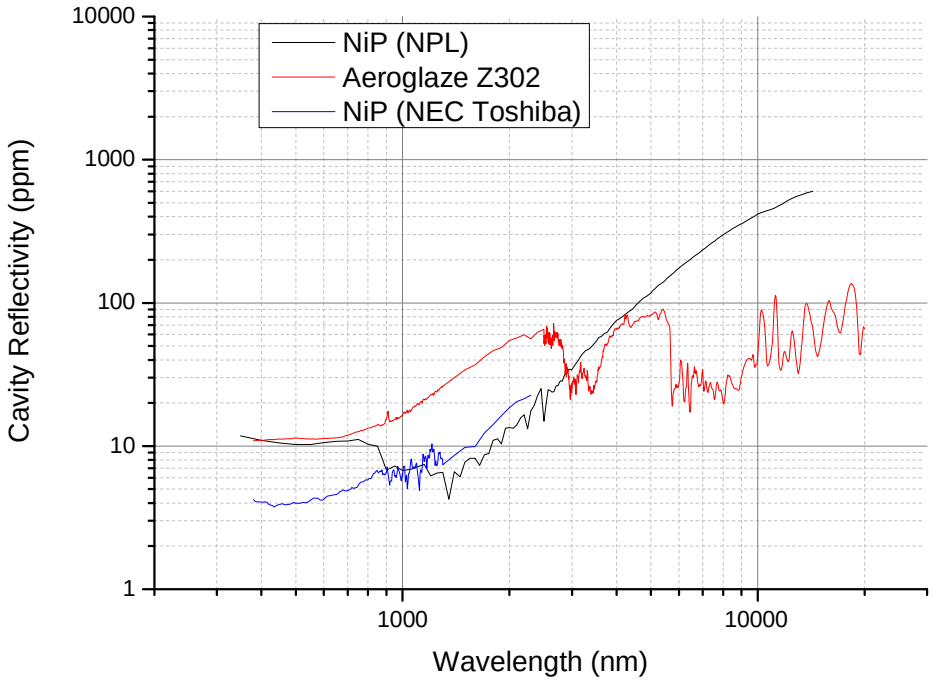


**Figure 100 Calculated spectral cavity reflectivity for the CSAR cavity geometry, assuming (a) Nickel-Phosphorus (NiP) – black or (b) Aeroglaze Z302 as surface coatings.**

The cavity reflectivity values of all three coatings are below the desired 30 ppm[63] in the visible range of the spectrum; however, in the infrared the reflectivity is significantly higher than 30 ppm. In the previous chapter, acceptable spectral distributions of the cavity reflectivity have been discussed (see Figure 17 in Section 2.5.3). Figure 101 shows the spectral cavity reflectivities in the context of these theoretically derived acceptable distributions; this graph illustrates that the solar-weighted cavity reflectivity is below 30 ppm (for both NiP-blacks as well as Aeroglaze), since the reflectivity stays below at least one of the theoretical curves for all relevant wavelengths (e.g. the bold curve for a = - 0.4). This means that the target for the initial cavity reflectivity that was arrived at in Section 2.5.2 can be met with the

[63] This is the aim for the more demanding space application, as discussed in Section 2.5.2.

chosen cavity geometry – irrespective of the use of Nickel-Phosphorus black or Aeroglaze Z302 as the internal surface coating.

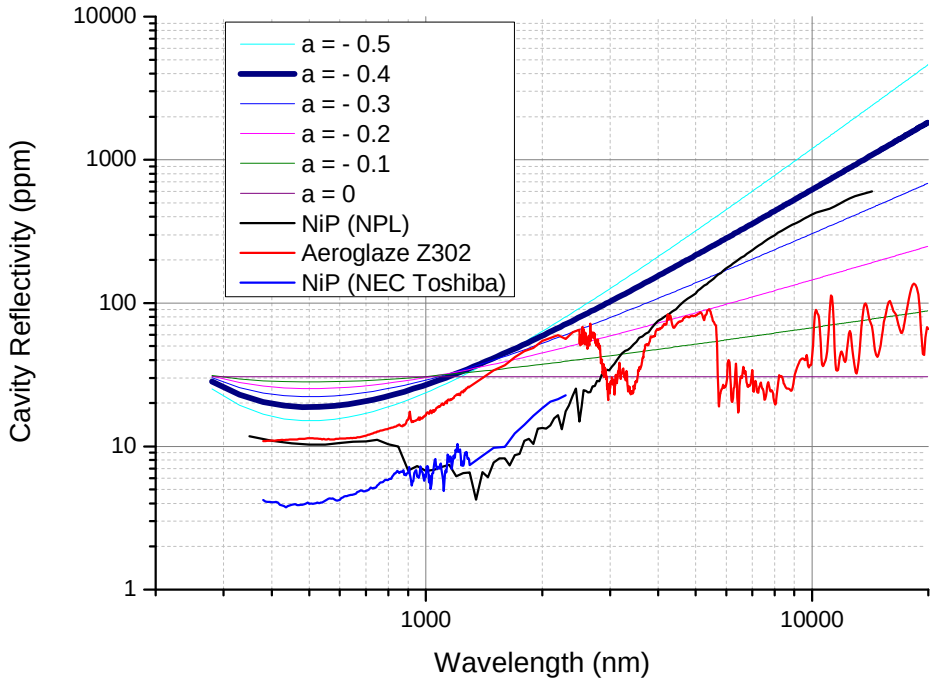


**Figure 101 Spectral cavity reflectivity of CSAR cavity with Nickel-Phosphorus or Aeroglaze Z302 coating in the context of theoretically derived reflectivity distributions**

#### *3.5.3.4 Sensitivity of the cavity absorptivity with respect to changes in the surface reflectivity and end-of-life uncertainty*

While the previous section was concerned with the initial cavity absorptivity at the beginning of the instrument's lifetime, this section focuses on the deterioration of the CSAR cavity over the lifetime of the instrument.

As already discussed in Section 2.5.2, the sensitivity of the overall cavity absorptivity with respect to changes in the surface reflectivity of the interior cavity wall is exclusively dependent on the cavity geometry[64]. In slightly simplified terms, it can be said that (1)

[64] See Equation (2.29).

the larger the cavity, the smaller the sensitivity of cavity absorptivity, but at the same time (2) the larger the cavity, the greater the mass and the greater the natural time constant of the detector system.

The approach taken in the design of the CSAR cavity was to make the cavity as large as possible while not exceeding the limit for the acceptable natural time constant of the detector. This ensures that the sensitivity of the cavity absorptivity is as small as possible. In the case of the CSAR cavity this sensitivity is

$$\left.\frac{\partial\left(\alpha_{cavity}(\lambda)\right)}{\partial\left(\rho_{surface}(\lambda)\right)}\right|_{CSAR} = -0.175\,\% \qquad (3.26)$$

The actual deterioration of the cavity absorptivity does, however, also depend on the deterioration of the black surface coating. In section 2.5.2 it was found that the black coatings deteriorate much more in space than on the ground. The data from the VIRGO space experiment suggest that Aeroglaze Z302 deteriorates by approximately 2.2% in the first year, and the TIM results indicate that Nickel-Phosphor deteriorates by 1.1% in the first year of the satellite operation. If the conservative assumption is made that the black coatings continue to deteriorate in a linear fashion over the lifetime of the instrument, the sensitivity of –0.175% leads to a deterioration of the overall cavity absorptivity of 0.0038% per year in the case of Aeroglaze Z302, and to 0.0019% per year for Nickel-Phosphor. Since the maximum annual deterioration in space was identified as 0.0034%[65] (assuming a lifetime of five years), this limit would be exceeded marginally with an Aeroglaze Z302 coating, but would be fully met in the case of Nickel-Phosphor. After five years, a CSAR

[65] See Section 2.5.2.

cavity with Nickel Phosphor coating is expected to have deteriorated by a total of 0.0095%, which is equivalent to a standard uncertainty of 0.0027% (see Section 2.4.3). For Aeroglaze Z302, the standard uncertainty is 0.0054%.

On the ground, the upper limit for the deterioration of the cavity absorptivity was identified as 0.0043% per year (assuming a 10-year instrument lifetime). With Aeroglaze Z302 deteriorating by approximately 0.5% in the first year, the sensitivity given in Equation (3.26) leads to a deterioration in the cavity absorptivity of 0.0009% in the first year, which is already much lower than the acceptable limit. If it is further assumed that Aeroglaze does not deteriorate any further after the first year of the instrument's lifetime, as suggested by Brusa et al. (Brusa and Fröhlich, 1986), the average annual deterioration becomes a negligible 0.00009% (after a 10-year lifetime). A total deterioration of the cavity absorptivity of 0.0009% is equivalent to a standard uncertainty of 0.00026% (see Section 2.4.3).

For Nickel-Phosphor there is currently no long-term degradation data available for the exposure to solar radiation on the ground. But given the reasonable assumption that the deterioration on the ground will be less than in space, it can be concluded that Nickel-Phosphor would probably be even more adequate on the ground than Aeroglaze Z302.

#### *3.5.3.5 Choice of Aeroglaze Z302 as the black surface coating for the CSAR cavity*

In Sections 3.5.3.3 and 3.5.3.4, it was shown that Aeroglaze Z302, as well as Nickel-Phosphor black very comfortably fulfil the requirements regarding the cavity reflectivity for the measurement

from the ground. However, for satellite measurements, Nickel-Phosphor would in principle be preferable.[66]

Nevertheless, Aeroglaze Z302 was chosen for coating the CSAR cavity which was used for this PhD project. This choice was due to practical reasons of process complexity, availability, and time constraints.

Firstly, the application of Nickel-Phosphor black requires highly specialised expert knowledge. This is underlined by the fact that the Nickel-Phosphor black produced at NPL is reflecting[67] more than twice as much light in the visible part of the spectrum as the black produced by NEC Toshiba Satellite Systems (see Figure 101), and the reflectivity of the NEC Toshiba NiP black is itself about twice as high as the values reported by the Japanese team which originally perfected the process (Kodama et al., 1990). In addition to this inherent difficulty, it is much more challenging to apply NiP black to the internal surfaces of a cavity than to a flat plate; this is explored in more depth in Appendix G. Furthermore, due to the complexity and uncertainty of the process, it was not viable for NEC Toshiba (or for NPL) to promise the delivery of the required outcome within the timescales available for the CSAR project.

The application of the Aeroglaze Z302, on the other hand, was very straightforward, especially since our collaborators at the World Radiation Center have considerable expertise in the application of the paint.

[66] It is also worth noting that the performance of the CSAR cavity would be far superior to the current state-of-the-art, no matter which of the two coatings is chosen.
[67] This refers to the hemispherical diffuse reflectivity only.

#### 3.5.3.6 *Experimental verification of the cavity reflectivity*

The discussion in the previous sections is based on the assumption that the theoretical calculation of the cavity reflectivity (see Equation (2.26) in Section 2.5.2) is correct. In this section, an experimental verification of the calculated cavity reflectivity will be given. These reflectivity measurements were carried out as described by Fox et al. (Fox et al., 1996).

Figure 103 gives an impression of the overall measurement setup for the reflectivity measurements, whereas Figure 104 gives insight into the laser stabilisation setup and Figure 105 shows how the cavity is mounted directly behind the rear port of the integrating sphere. The stabilised laser beam passes the 6 mm diameter entrance port and the 10 mm diameter exit port of an integrating sphere, before entering the cavity under test. The cavity is placed right up against the exit port. The reflected light causes the signal originating from a silicon detector - mounted on a side port of the sphere – to increase by a certain amount – as compared to a "dark signal", where nothing is placed up against the rear port of the integrating sphere.

In a second step, the same measurement setup and procedure is used, with only one difference: this time, the cavity is replaced by a reference sample of known reflectivity. In this case, a sample painted with a diffuse black ("3M Nextel black") was used. Its diffuse reflectivity was determined by NPL to be 2.92% at 647 nm.

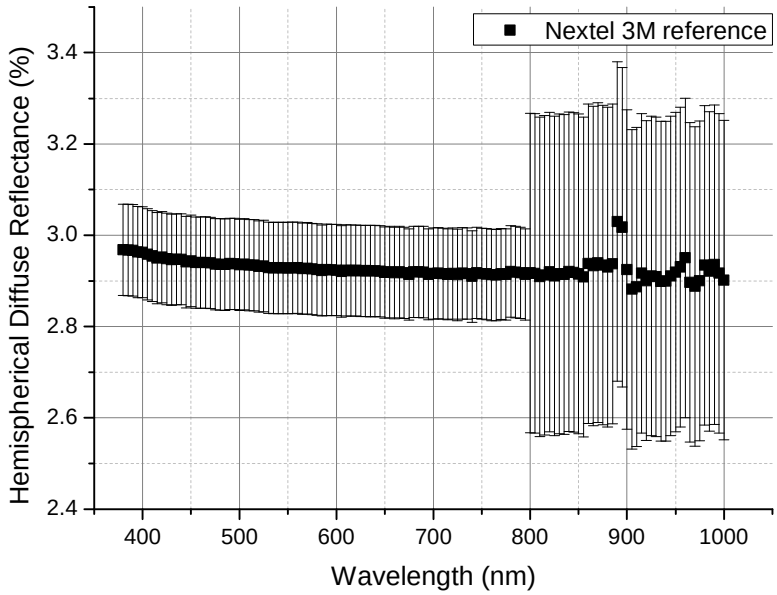


**Figure 102 Diffuse spectral reflectivity of reference sample (Nextel Black 3M). The error bars indicate the standard uncertainties.**

From the ratio of the two signal levels (corrected for the dark signal), and the absolute value for the reflectivity of the reference sample, the diffuse reflectivity of the cavity under test can be determined.

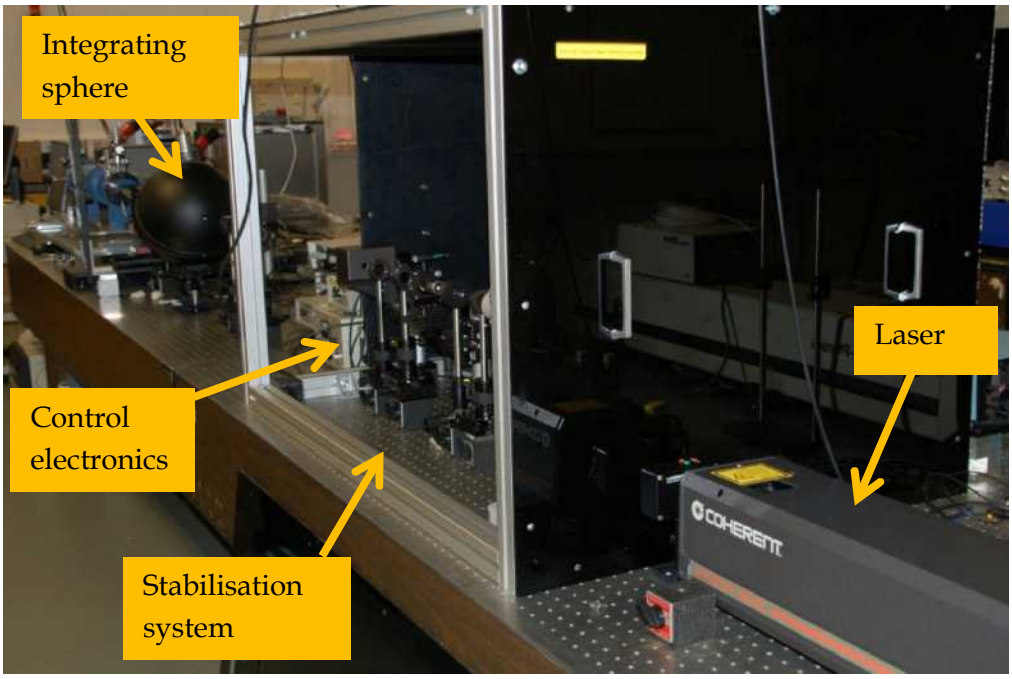


**Figure 103 Experimental set-up for the cavity reflectivity measurement**

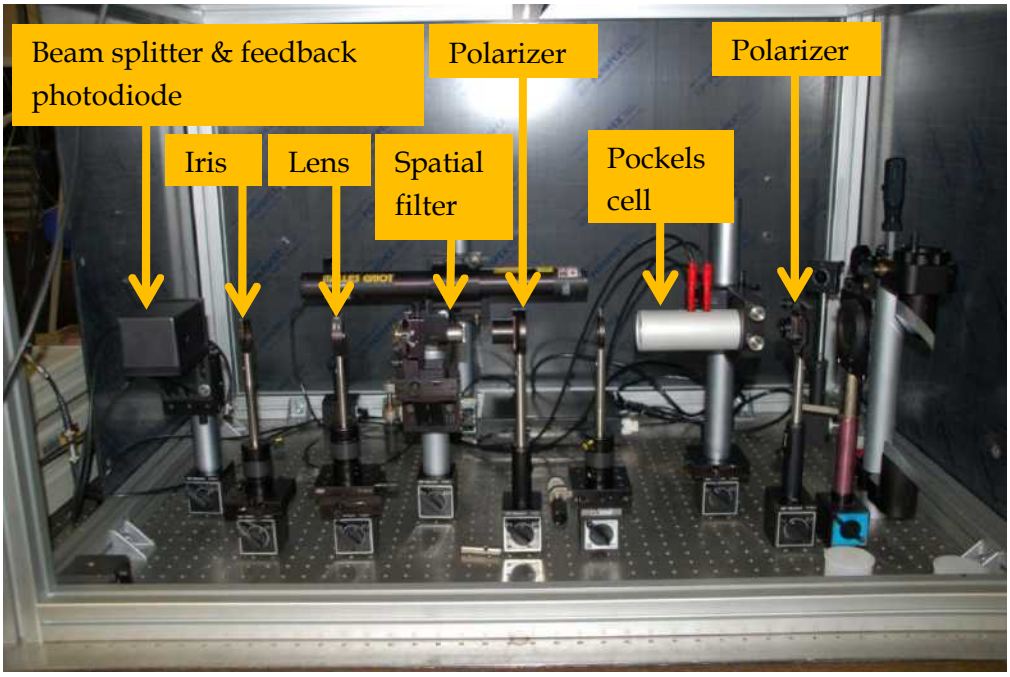


**Figure 104 Laser stabilisation system**

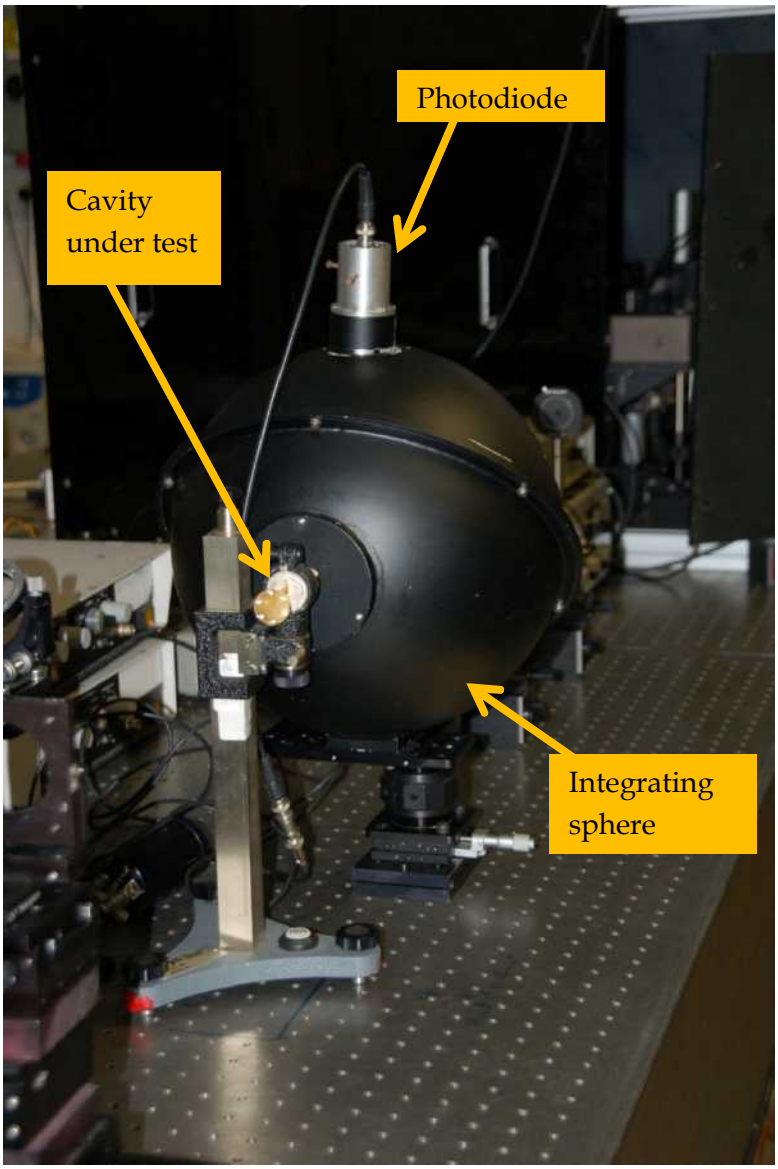


**Figure 105 Cavity reflectivity measurement - cavity at the rear port of the integrating sphere[68]**

As already shown in Figure 101, the theoretical cavity reflectivity is 10 ppm (or 0.001%) at 647 nm. This is also the result of the experimental evaluation; the standard uncertainty of this experimental evaluation is 0.0005%. This experimental verification of the calculated reflectivity value at one particular wavelength (at

[68] Please note: the cavity shown here is not identical with the cavity used for the CSAR measurements, but the measurement principle was the same.

647 nm) significantly increases confidence in the theoretical calculations – also for the other wavelengths which have not undergone experimental verification. The theoretical solar-weighted reflectivity of the CSAR cavity (including the complete solar spectrum) is 20 ppm (or 0.002%). Therefore, the cavity reflectivity of the CSAR cavity is approximately an order of magnitude lower than the values reported for the so-far highest-absorbing TSI cavities (Kopp et al., 2005). The four TIM cavities have solar-weighted reflectivities of 169 ppm, 139 ppm, 307 ppm, and 360 ppm.

#### *3.5.3.7 Cavity absorptivity and spectral distribution of Solar Irradiance*

In the context of the Solar Irradiance measurement, the cavity reflectivity is not only dependent on the properties of the detector cavity, but also on the spectral distribution of the incoming solar radiation. This is illustrated by the equation that was derived for the integrated cavity absorptivity $\alpha$ (see Section 2.4.5):

$$\alpha = \frac{\int_0^\infty \alpha(\lambda) I_{SSI}(\lambda) d\lambda}{\int_0^\infty I_{SSI}(\lambda) d\lambda} \qquad (3.27)$$

In theory, Equation (3.27) implies that a detailed knowledge about the spectral dependence of the various parameters is not necessary. $\alpha$ could conceptually be determined experimentally by making a ratio measurement of two different radiometers that are both exposed to the same Solar Irradiance as CSAR; however, since the cavity absorptivity is already factually unity (with respect to the allowable uncertainties), and since the experimental evaluation in front of the Sun would be very difficult, $\alpha$ is determined using theoretical calculations of the spectral distribution of Solar Irradiance. The uncertainty due to these

calculations is estimated by trying to establish the most extreme cases of these calculations and to assume the resulting values for $\alpha$ as minimum and maximum values.

The extreme cases of the Spectral Solar Irradiance in Davos have already been presented in Section 3.4.6 (see Figure 89). Table 16 shows the integrated cavity absorptivity $\alpha$ for the Solar Spectral Irradiances corresponding to the extreme Solar Zenith Angles. The values were obtained using Equation (3.27); the calculation was using absorptivity values for the CSAR cavity corresponding to the reflectivity values shown in Figure 100 (Aeroglaze Z302) in Section 3.5.3.3.

**Table 16 Integrated cavity absorptivity of the CSAR detector for various spectral distributions of Solar Irradiance.**

| | $\alpha$ | $\rho = 1 - \alpha$ |
|---|---|---|
| **Solar Zenith Angle = 0°** | 0.999982 | 0.000018 |
| **Solar Zenith Angle = 80°** | 0.999978 | 0.000022 |
| **Black Body Radiation ($T_{Sun}$ = 5777 K)** | 0.999981 | 0.000019 |

Table 16 shows that the maximum relative difference in the integrated cavity absorptivity is 0.000004 (or 0.0004%, or 4 ppm). Using Equation (2.6) in Section 2.4.3, the standard uncertainty due to the spectral dependence of the cavity absorptivity can be estimated as 0.0001% (or 1 ppm), and it is therefore negligible in the context of the required uncertainties.

### *3.5.3.8 Uncertainty of the cavity absorptivity*

This section gives a summary of the uncertainty components in relation to the CSAR cavity absorptivity. Table 17 shows that the combined uncertainty due to the cavity absorptivity is a negligible 0.00057% for the ground application.

Table 18 shows the uncertainty budget for the space application, assuming the use of Aeroglaze Z302 as a black surface coating. The combined uncertainty is estimated to be 0.0054%, which only slightly exceeds the target value of 0.005% given in Section 2.4.6. This uncertainty could be reduced to 0.0027% by using a Nickel-Phosphor coating, because the dominating uncertainty component in the uncertainty budget – the uncertainty due to the long-term deterioration – is much smaller for Nickel-Phosphor (see Section 3.5.3.4).

**Table 17 Uncertainty budget for CSAR cavity absorptivity. Ground application with Aeroglaze Z302.**

| Uncertainty component | Standard Uncertainty | Discussed in Section |
|---|---|---|
| Long-term deterioration | 0.00026% | 3.5.3.4 |
| Cavity absorptivity determination | 0.0005% | 3.5.3.6 |
| Absorptivity and Solar Spectral Irradiance distribution | 0.0001% | 3.5.3.7 |
| | | |
| Combined Uncertainty | **0.00057%** | |

**Table 18 Uncertainty budget for CSAR cavity absorptivity. Space application, with Aeroglaze Z302.**

| Uncertainty component | Standard Uncertainty | Discussed in Section |
|---|---|---|
| Long-term deterioration | 0.0054% | 3.5.3.4 |
| Cavity absorptivity determination | 0.0005% | 3.5.3.6 |
| Absorptivity and Solar Spectral Irradiance distribution | 0.0001% | 3.5.3.7 |
| | | |
| Combined Uncertainty | **0.0054%** | |

### 3.5.4 Instrument noise

The detector noise of CSAR is dominated by the fluctuation of the reference block temperature. As a result of this fluctuation, the measured temperature difference between cavity and the reference block varies with a standard deviation of 0.015%, if measurements are acquired at a frequency of 0.1 Hz. This noise level remains approximately constant irrespective of whether the instrument is operating in a highly controlled lab environment at NPL or on the solar tracker at the World Radiation Center in Davos, and irrespective of whether the optical shutter is closed or whether the detector is exposed to stabilised laser light or solar radiation (on a day with clear sky conditions). Averaging the signal over a time period of 160 seconds reduces the contribution of the measurement noise to the uncertainty budget to an insignificant level with respect to the overall uncertainty budget for ground-based measurements (<0.004%).

### 3.5.5 Natural time constant of the detector system

In section 2.5.4 it was found that a time constant of < 10 sec would be highly desirable. This aim has been achieved, as evidenced by Figure 106. Despite of the high absorptivity and large entrance aperture, and consequential size, the detector cavity has a step response time of ~9

seconds, which is comparable to current room-temperature radiometers.

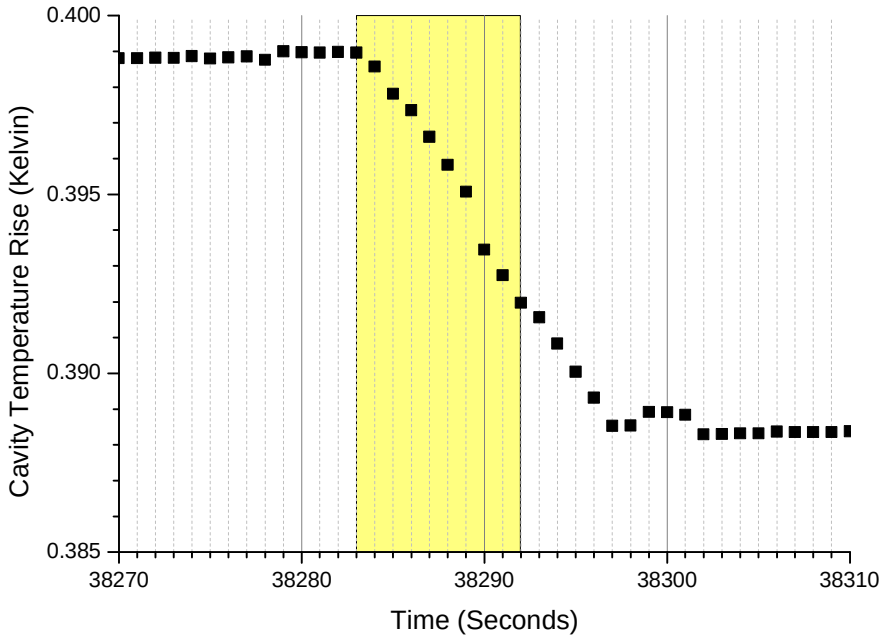


**Figure 106 Step response of the detector cavity. The signal reaches 1/e in approximately nine seconds.**

In Section 3.6.5.1 it will be shown that the method employed for the window transmittance measurement limits the time frame within which useful measurements can be taken with CSAR to the time interval from 0.475 day fraction to 0.575 day fraction. Figure 120 (in section 3.6.5.1) shows that the rate of change of the Solar Irradiance is within ± 0.05% for this time interval. According to the analysis presented in section 2.5.4 (Table 4), this rate of change leads to a relative measurement error of approximately ± 0.01% due to the time lag of a detector cavity with a time constant of 10 seconds; CSAR has a time constant of slightly less than 10 seconds. And if the total range of possible measurement errors due to the time lag effect is ± 0.01%, then the relative standard uncertainty associated with this effect can be

estimated as 0.006%, or 0.01% divided by the square root of three (see Section 2.4.3).

### 3.5.6 Electrical power – measurement principle

Figure 107 illustrates the measurement of electrical power that is dissipated in the cavity heater. The measurement setup consists of a constant-voltage source with an output voltage $U_s$, a standard resistor with dc resistance $R_{ref}$, and the cavity heater with resistance $R_h$. These three electrical components are connected in series. The electrical power $P_h$ dissipated in the cavity heater can be determined by making four-wire measurements of the respective voltages across the two resistors:

$$P_h = U_h I = U_h \frac{U_{ref}}{R_{ref}} \tag{3.28}$$

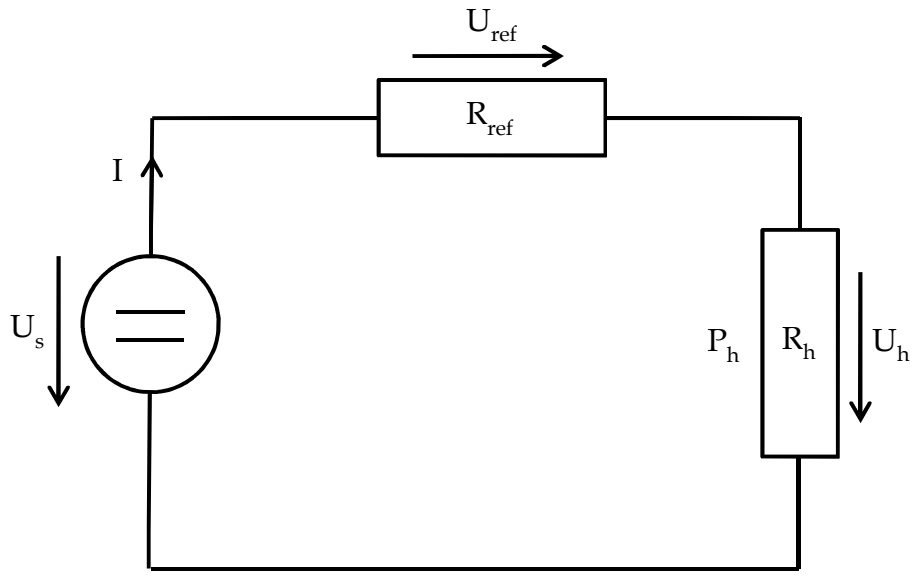


**Figure 107 Measurement of electrical power – schematic**

The standard resistor that is used for the CSAR measurements is a Tinsley 5685B AC/DC Standard Resistor with a nominal resistance

of 1000 Ω. This type of resistor was developed in collaboration between Tinsley and NPL, and is currently used by many National Measurement Institutes worldwide. The actual resistance value of the standard resistor was determined by the NPL Electrical Measurement Team to be 1000.00861 Ω, with a relative standard uncertainty of 0.025 ppm (or 0.0000025%). Table 1 lists some of the most important features of the standard resistor. From this table, it becomes clear that the uncertainty contribution due to the uncertainty in the resistance value of the standard resistor is negligible. Since the CSAR measurements reported in Chapter 4 were carried out less than six months after the calibration of the standard resistor, the value is expected to be within ± 1 ppm of the calibration value. The temperature of the environment in which the CSAR measurement electronics was operated was within ± 5 K of the calibration temperature (293.15 K); with a temperature coefficient of 2 ppm / K, this uncertainty in the environmental temperature is equivalent to a relative standard uncertainty of 5.8 ppm. And finally, the resistance offset due to the heat dissipation of ~ 20 mW is ~ 0.1 ppm. All these uncertainties add up to a combined relative standard uncertainty of the standard resistance value of 6 ppm.

**Table 19 Important features of the Tinsley Standard Resistor**

| Quantity | Value |
|---|---|
| Calibration uncertainty | 0.025 ppm |
| Stability | 2 ppm / year |
| Temperature Coefficient of Resistance | 2 ppm / K |
| Maximum Dissipation | 1 W |
| Approximate Load Coefficient | 6 ppm / W |

The resistor that is used as a cavity heater is a Vishay SMR1D High Precision Metal Foil Resistor with a nominal room-temperature resistance value of 1000 Ω and a temperature coefficient of ± 2 ppm / K. Such a low temperature coefficient is not of any direct relevance for the overall measurement uncertainty, since the absolute resistance value of the cavity heater is not required to be known for the determination of the electrical power dissipated in the heater (see Equation (3.28)). However, a temperature-invariant heater resistance will not introduce non-linearity of the detector response, which makes the detector response more predictable. Besides the small temperature coefficient, the Vishay resistor is also suitable for space-applications. The resistor occupies a rectangular surface area of 5.99 mm × 3.20 mm. This surface area is quite similar to the elliptically irradiated detector area of extension 5.9 mm × 5 mm in the case of the optical heating.

A Time Electronics 5018 Programmable DC/AC V/I Calibrator is used to energise the measurement circuit. On good measurement days (i.e. cloudless sky, with Aerosol Optical Depth < 0.4), the incoming solar power is approximately 18 mW, which means that the voltage source needs to supply a voltage of approximately 8 V. The output of the source is stable to 10 μV in the 22 V – range; therefore, the relative fluctuation of the output voltage is of the order of less than 10 μV / 8 V = 1.3 ppm (0.00013%).

The voltmeters used for measuring the voltage drops across the two resistors are Datron / Wavetek 1281 Digital Voltmeters (8.5 digit). The voltmeters were calibrated directly against the NPL Josephson Array, with the result that the readings deviated by less than 13 μV at the 10 V level, which is equivalent to a relative deviation of less than 1.3 ppm (0.00013%).

In total, the standard uncertainty due to the electrical measurement of the cavity heater power is estimated to be 6.4 ppm (0.00064%).

### 3.5.7 Equivalence of optical and electrical heating

The measurement principle of CSAR is electrical substitution radiometry, like in all other current TSI instrument designs. However, the non-equivalence of optical and electrical heating can be reduced to negligible levels if operating at low temperatures.

A surrounding cold-shield which is maintained at a similar temperature to the gold-coated cavity prevents any significant radiative heat transfer between the detector cavity and its immediate environment. In addition, the operation in vacuum implies that there is no significant heat exchange by convection or conduction through air.

Another important source of non-equivalence in ambient-temperature radiometers are the current-carrying heater wires, which may heat up during electrical heating. In cryogenic radiometers, this effect can be completely avoided through the use of super-conducting leads. Because the detector temperature of CSAR is at ~ 20 K slightly too high to allow the use of conventional superconductors, 50 µm diameter steel-sheathed $MgB_2$-wires were used to exclude this effect. These wires were chosen because they were specifically developed for space flight (Schlachter et al., 2006).

In Figure 108, the $MgB_2$-wire can be seen sheathed in heat shrink tubing. The heat shrink tubing was added for further stability, since the $MgB_2$-wires were found to be very difficult to handle and rather fragile. For the future, it is therefore recommendable to consider the use of thicker $MgB_2$-wires.

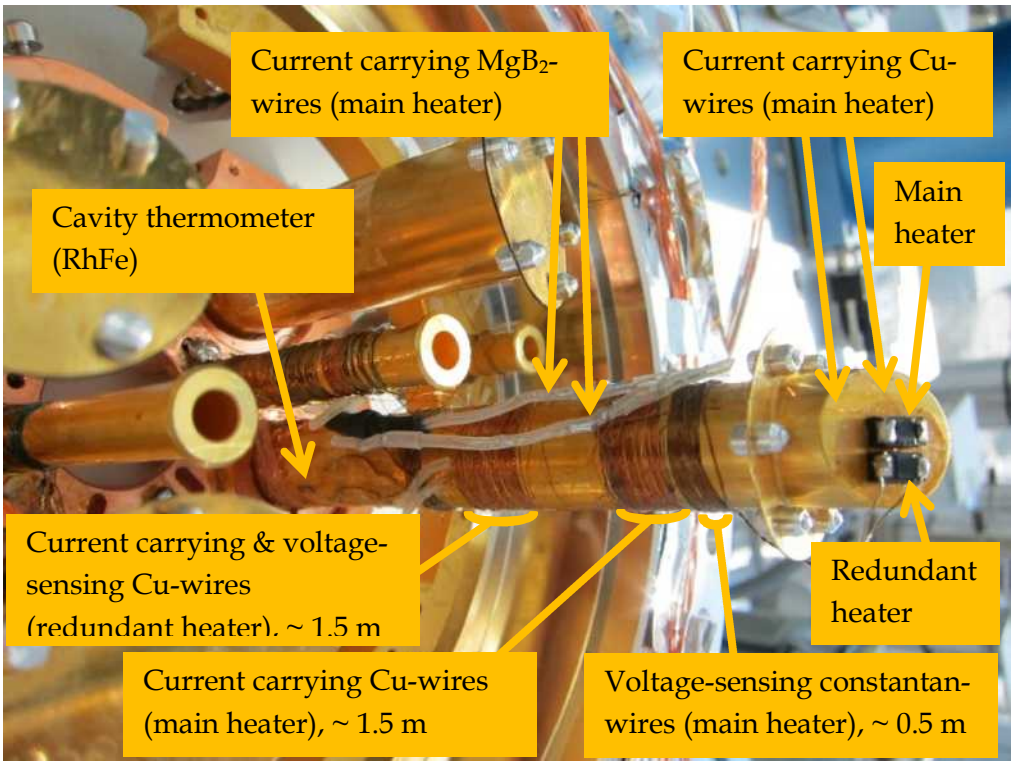


**Figure 108 Wiring of the main cavity–heater and position of thermometer**

### 3.5.8 Dynamic Range and Linearity of the detector system

An indicator for the quality of a detector is its linearity. Good linearity of the detector and large dynamic range are – to a certain extent – competing requirements, since the use of certain heat link materials with non-linear temperature dependence of the thermal conductivity can increase the dynamic range significantly without increasing the time constant (this is discussed, e.g., in (Quinn and Martin, 1985)). In the CSAR design, the preference was given to detector linearity, so that the interpolation of the temperature difference over power – relationship is as straightforward as possible. This is why copper was chosen as a heat link material, whose thermal conductivity does not change significantly in the relevant temperature range and this is also one reason for choosing the highly linear RhFe-sensors over other sensors with greater sensitivity.

The cavity temperature rise of the cavity was found to depend very linearly on the input power (see Figure 109). The range of electrical input powers shown in Figure 109 correspond to Irradiance levels of 650 W/m^2 – 1100 W/m^2 (for a sapphire window) and 600 W/m^2 – 1020 W/m^2 (for a fused silica window). This covers the range of irradiance values that can be reasonably expected in Davos.

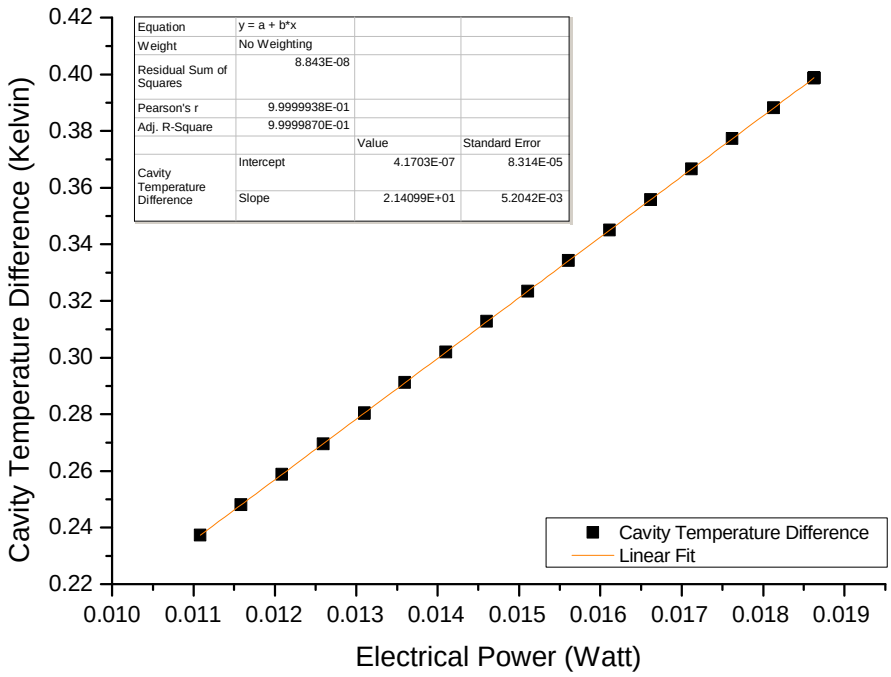


**Figure 109 Temperature dependence of cavity with respect to electrical input power**

The slope of the curve shown in Figure 109 is a measure of the sensitivity of the detector cavity $\sigma_{\text{det}}$; its value is 21.4099 K/W, with an associated standard uncertainty $u(\sigma_{\text{det}})$ of 0.0052 K/W.

When making optical measurements, the electrical power $P_{el}$ during the dark measurement (optical shutter closed) is chosen such

that the cavity temperature $T_{el}$ in this regime is as close as possible to the cavity temperature $T_{light}$ when the optical shutter is open and the cavity is heated by the incoming light energy. The experimentally evaluated detector sensitivity $\sigma_{\mathrm{det}}$ and the temperature difference is then used to extrapolate from the dark measurement value of electrical power[69] $P_{el}$ to the optical power[70] $P_{light}$:

$$P_{light} = P_{el} + \frac{1}{\sigma_{\mathrm{det}}}\left(T_{light} - T_{el}\right) \tag{3.29}$$

Equation (3.29) implies that the size of the temperature difference between the shutter-closed and shutter-open states determines to what extent the uncertainty in the detector sensitivity is translated into an uncertainty in the optical power measurement. The uncertainty in the determination of $P_{light}$ due to the uncertainty in the detector sensitivity $\sigma_{\mathrm{det}}$ is:

$$u^2_{\sigma_{\mathrm{det}}}\left(P_{light}\right) = \left(\frac{\partial P_{light}}{\partial \sigma_{\mathrm{det}}}\right)^2 u^2\left(\sigma_{\mathrm{det}}\right) \tag{3.30}$$

which is equivalent to

$$u_{\sigma_{\mathrm{det}}}\left(P_{light}\right) = \left[\frac{1}{\sigma^2_{\mathrm{det}}}\left|T_{light} - T_{el}\right|\right] u\left(\sigma_{\mathrm{det}}\right) \tag{3.31}$$

During all CSAR measurements reported in this thesis, the temperature difference $\left|T_{light} - T_{el}\right|$ is smaller than 20 mK. This means that the uncertainty $u_{\sigma_{\mathrm{det}}}\left(P_{light}\right)$ is smaller than 227 nW. On a good measurement day in Davos (i.e., assuming an incoming optical power

[69] $P_{el}$ in the current section is identical with $P_h$ in Section 3.5.6.
[70] $P_{light}$ in the current section is identical with $P_{measured}$ in Section 2.4.5.

of 0.017 W), this is equivalent to a relative uncertainty of approximately 0.0013%. In the case of the space application, the 227 nW uncertainty is equivalent to a relative uncertainty of less than 0.0009%.

## 3.6 Window Transmittance

In order to create a vacuum, but also to allow the solar radiation to reach the detector at the same time, a window is used. Two different window materials – fused silica and sapphire – were used to confirm the robustness of the correction for the window transmittance.

### 3.6.1 Choice of window material

The requirements regarding the window material were discussed in Section 2.7. One of the most important requirements is that the window should have a high transmittance in the solar spectrum (see Section 2.5.3). Figure 110 shows the spectral transmittance characteristics of some potentially useful materials.

However, as already mentioned in section 2.7, the spectral characteristic of the window is not the only selection criterion. The window needs to be mechanically strong in order to withstand the atmospheric pressure, it needs to be of high optical quality (in order to reduce stray light) and it should be able to withstand frequent wet cleaning and exposure to humid air. These considerations led us to choose two types of window: uncoated high purity synthetic fused silica and uncoated high purity sapphire.

For these initial tests of CSAR, we wanted to prevent a possible deterioration of the window as much as possible, even at the expense of slightly increased uncertainties due to a relatively narrow transmittance band. As long as the detector performance was

unknown, we did not want a potential further complication of the experimental set-up caused by deteriorating windows. For subsequent evaluations, we plan to use other materials with a broader transmittance spectrum, such as highly polished calcium fluoride (the downside of most other materials such as calcium fluoride is that they are either water soluble or relatively fragile, or both). If any alternative material with a broader transmittance spectrum proves to be useful, then the uncertainties due to the window transmittance may be reduced further.

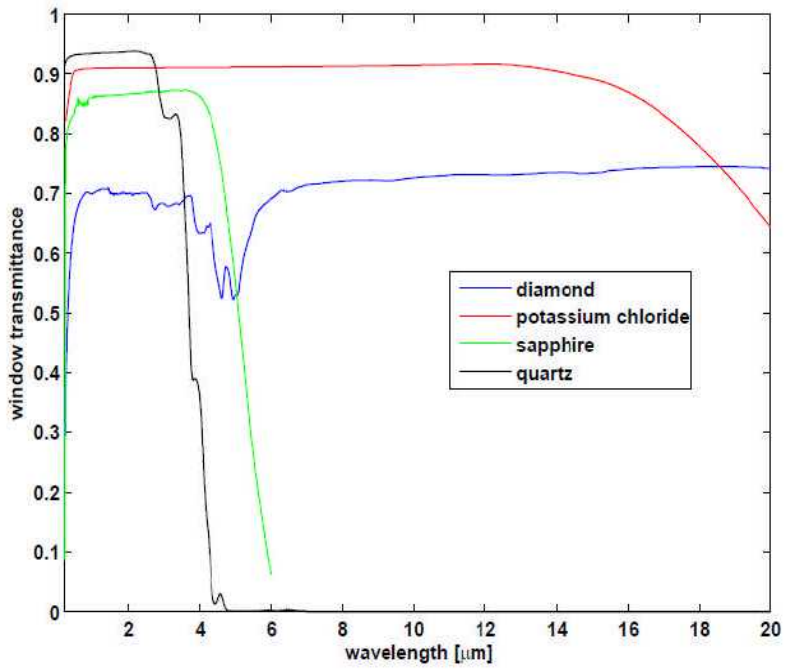


**Figure 110 Spectral transmittance profiles of potential window materials[71]**

### 3.6.2 Spectral characteristics of the windows

The Fresnel losses of the windows were calculated by André Fehlmann and the results presented in his PhD thesis (Fehlmann, 2011); the theoretical transmittance values agree with the measured transmittance values within the stated measurement uncertainties over

[71] Figure courtesy of André Fehlmann, PMOD/WRC

a wide spectral range. However, the measurement uncertainties of the spectral measurements are much larger than the absolute uncertainties we would like to achieve in the CSAR measurements; for the most relevant part of the solar spectrum, the uncertainties in the spectral transmittance measurements are around 0.25% (one standard uncertainty). The solar integrated transmittance value that is calculated from these spectral window transmittance data and from the spectral composition of the Sun light reaching the detector (calculated with the help of atmospheric transmittance models) is therefore not sufficiently accurate. This is not only due to the uncertainties in the spectral transmittance measurements, but also due to the uncertainties in the atmospheric model.

### 3.6.3 Window transmittance – measurement principle

Since the solar integrated transmittance of the window cannot be calculated with sufficient accuracy based on spectrally resolved measurements (as discussed in section 3.6.2), it must be directly measured while CSAR is measuring Solar Irradiance at the same time. The aim of the window transmittance measurement is to monitor the integrated transmittance $\tau$ of the CSAR window in real time, i.e. simultaneous to the CSAR measurements of Solar Irradiance. It has already been shown in Section 2.4.5 that the measurement equation can be presented in such a way that, given an adequate measurement procedure, knowledge of the spectral distribution of the window is not required[72]. It was shown that the integrated window transmittance can be expressed as:

[72] see Equation (2.14) and Equation (2.16)

$$\tau = \frac{\int_0^\infty \tau(\lambda) F_{diff}(\lambda) \alpha(\lambda) I_{SSI}(\lambda) d\lambda}{\int_0^\infty F_{diff}(\lambda) \alpha(\lambda) I_{SSI}(\lambda) d\lambda} \qquad (3.32)$$

Expansion of Equation (3.32) by the aperture area $A$ yields:

$$\tau = \frac{A\int_0^\infty \tau(\lambda) F_{diff}(\lambda) \alpha(\lambda) I_{SSI}(\lambda) d\lambda}{A\int_0^\infty F_{diff}(\lambda) \alpha(\lambda) I_{SSI}(\lambda) d\lambda} \qquad (3.33)$$

Comparison with Equation (2.11) shows that the numerator of the right-hand side of Equation (3.33) is equal to the power measured by CSAR, $P_{measured}$, when exposed to solar radiation. The denominator is the same except for a perfect window transmittance for all wavelengths (which indicates the absence of a window). Therefore, the integrated window transmittance can in principle be determined by a power ratio measurement, without the need for knowledge about the spectral distribution of the window transmittance or of the solar radiation. Ideally, a ratio measurement would be performed of CSAR measuring Solar Irradiance (1) with a window and (2) without a window. However, it is not possible to make CSAR measurements without a window. These measurements must therefore be substituted by measurements performed with a radiometer that does not require operation in vacuum. This radiometer is henceforth referred to as "Transmittance Monitor".

For the ratio measurement performed by the Transmittance Monitor to be a valid substitute for the ideal window transmittance measurement, the following relation needs to hold within the required uncertainties:

$$\tau = \frac{A_{CSAR}\int_0^\infty \tau_{CSAR}(\lambda) F_{diff\ CSAR}(\lambda) \alpha_{CSAR}(\lambda) I_{SSI}(\lambda) d\lambda}{A_{CSAR}\int_0^\infty F_{diff\ CSAR}(\lambda) \alpha_{CSAR}(\lambda) I_{SSI}(\lambda) d\lambda} = \frac{A_{TM}\int_0^\infty \tau_{CSAR}(\lambda) F_{diff\ TM}(\lambda) \alpha_{TM}(\lambda) I_{SSI}(\lambda) d\lambda}{A_{TM}\int_0^\infty F_{diff\ TM}(\lambda) \alpha_{TM}(\lambda) I_{SSI}(\lambda) d\lambda}$$

(3.34)

In terms of the practical measurement, Equation (3.34) means that the transmittance measurement of the CSAR window needs to yield the same result when using the Transmittance Monitor as it would when using CSAR for the transmittance measurement (if CSAR could be operated without window).

This relation holds in general if the following two relations hold for all wavelengths $\lambda$:

$$\alpha_{TM}(\lambda) = C_1 \cdot \alpha_{CSAR}(\lambda) \tag{3.35}$$

$$F_{diff\ TM}(\lambda) = C_2 \cdot F_{diff\ CSAR}(\lambda) \tag{3.36}$$

where $C_1, C_2$ are constants.

The condition given by Equation (3.35) can be considered to be met since the detector cavity of the Transmittance Monitor is coated with the same black coating as CSAR (Aeroglaze Z302); the two radiometers have therefore a similar spectral shape of the cavity absorptivity. The condition given by Equation (3.36) is met since the aperture geometry of the Transmittance Monitor is very similar to the aperture geometry of CSAR.

While the transmission measurement with the help of the Transmittance Monitor (as represented by Equation (3.34)) is one step closer to a practical experimental realisation, the experiment cannot be carried out exactly in the way Equation (3.34) describes it because the CSAR window cannot be put in front of the Transmittance Monitor;

otherwise, the window would need to be removed from CSAR and the vacuum would be lost. This problem can be solved by substituting the CSAR window with another window of the same type and make, and to monitor its transmittance with the Transmittance Monitor instead of the CSAR window. In order that the monitoring of the second window can meaningfully represent the monitoring of the CSAR window, another ratio measurement is required; at some point, the transmittances of both windows need to be compared directly. This measurement procedure is represented by the following relation, which results from multiplying Equation (3.34) with a nominal factor of 1:

$$\tau = \frac{A_{TM}\int_0^\infty \tau_{CSAR}(\lambda)F_{diff\ TM}(\lambda)\alpha_{TM}(\lambda)I_{SSI}(\lambda)d\lambda}{A_{TM}\int_0^\infty \tau_{TM}(\lambda)F_{diff\ TM}(\lambda)\alpha_{TM}(\lambda)I_{SSI}(\lambda)d\lambda} \cdot \frac{A_{TM}\int_0^\infty \tau_{TM}(\lambda)F_{diff\ TM}(\lambda)\alpha_{TM}(\lambda)I_{SSI}(\lambda)d\lambda}{A_{TM}\int_0^\infty F_{diff\ TM}(\lambda)\alpha_{TM}(\lambda)I_{SSI}(\lambda)d\lambda} \tag{3.37}$$

None of the two fractions in Equation (3.37) is directly realisable; the problem with the first fraction is that the two windows cannot be in front of the Transmittance Monitor at the same time. Similarly, the issue with the second fraction is that it is not possible to have a window and no window in front of the Transmittance Monitor at the same time. This problem can be overcome by using a third radiometer to monitor the Solar Irradiance during both ratio measurements. The PMO2 was chosen as this third radiometer. Equation (3.37) is expanded by nominal factors of 1 in order to reflect the function of the PMO2 measurements:

$$\tau = \frac{A_{TM}\int_0^\infty \tau_{CSAR}(\lambda)F_{diff\ TM}(\lambda)\alpha_{TM}(\lambda)I_{SSI}(\lambda)d\lambda}{A_{PMO2}\int_0^\infty F_{PMO2}(\lambda)\alpha_{PMO2}(\lambda)I_{SSI}(\lambda)d\lambda} \cdot \frac{A_{PMO2}\int_0^\infty F_{PMO2}(\lambda)\alpha_{PMO2}(\lambda)I_{SSI}(\lambda)d\lambda}{A_{TM}\int_0^\infty \tau_{TM}(\lambda)F_{diff\ TM}(\lambda)\alpha_{TM}(\lambda)I_{SSI}(\lambda)d\lambda} \cdot$$
$$\cdot \frac{A_{TM}\int_0^\infty \tau_{TM}(\lambda)F_{diff\ TM}(\lambda)\alpha_{TM}(\lambda)I_{SSI}(\lambda)d\lambda}{A_{PMO2}\int_0^\infty F_{PMO2}(\lambda)\alpha_{PMO2}(\lambda)I_{SSI}(\lambda)d\lambda} \cdot \frac{A_{PMO2}\int_0^\infty F_{PMO2}(\lambda)\alpha_{PMO2}(\lambda)I_{SSI}(\lambda)d\lambda}{A_{TM}\int_0^\infty F_{diff\ TM}(\lambda)\alpha_{TM}(\lambda)I_{SSI}(\lambda)d\lambda}$$

(3.38)

The following is an experimental evaluation of the limitations of this procedure as well as the associated uncertainties.

### 3.6.4 Transmittance monitor

For reasons explained in the previous section, a Transmittance Monitor is needed. For this purpose, a PMO6 radiometer was modified (Figure 111) to have a sufficiently similar optical geometry[73] to CSAR and to be able to mount a window in front. The ratio of the modified PMO6 to the PMO2 was established and when CSAR was measuring, the modified PMO6 was operated with a window that is nominally the same as the one mounted in front of CSAR, and the PMO2 radiometer was measuring as well. These measurements allow a real-time determination of the solar-integrated window transmittance.

[73] The optical geometry of the Transmittance monitor is:
1. Diameter of entrance aperture = 5 mm
2. Diameter of cavity aperture = 7 mm
3. Distance between entrance aperture and cavity aperture = 57.3 mm

These parameters result in a slope angle of 1.00˚, a half opening angle of 3.50˚, and a limit angle of 5.98˚.

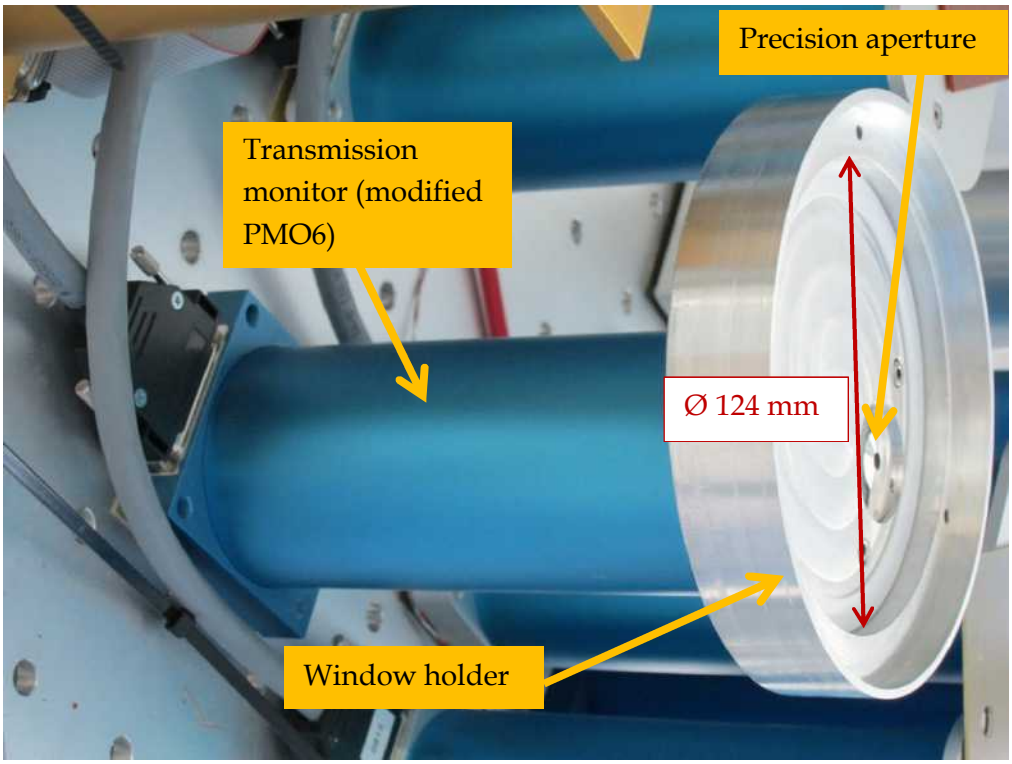


**Figure 111 Transmittance Monitor - Modified PMO6 with CSAR-precision-aperture and window-adapter for fused-silica window.**

Figure 112 shows the transmittance monitor with a fused silica window (Ø 123 mm) mounted in front. This photo serves the purpose of illustration only; when fully assembled, an aperture plate (see Figure 113) is added between the Nylon distance ring and the clamping ring. The idea of inserting this front aperture plate is to reduce stray light and to prevent the window from warming up significantly.

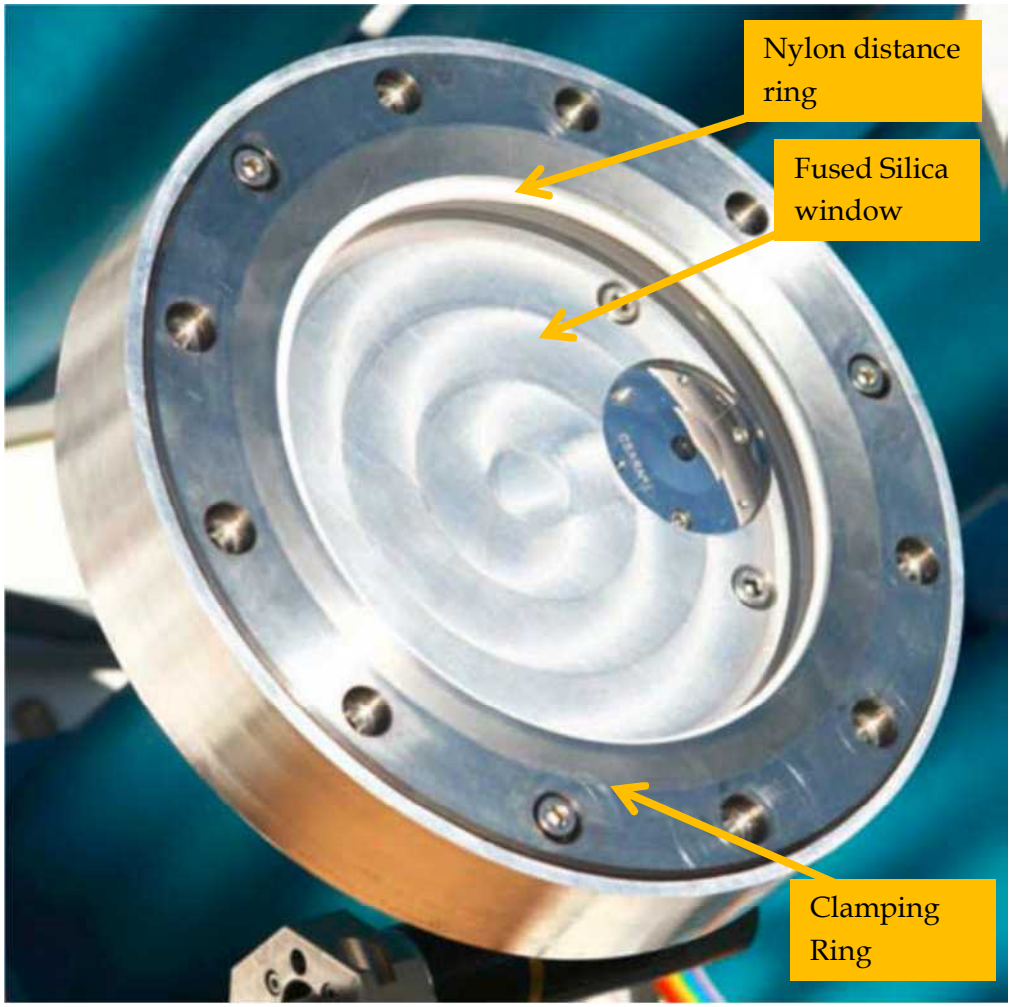


**Figure 112 Transmittance Monitor - Modified PMO6 with fused silica window**

**Figure 113 Front aperture plate**

For the Ø 1 inch sapphire windows, an adapter plate was manufactured, which has the same outer diameter as the fused silica windows. Also, the optical geometry of the fused silica window was replicated. Figure 114 shows the adapter plate, and Figure 115 shows the modified PMO6 with the adapter plate.

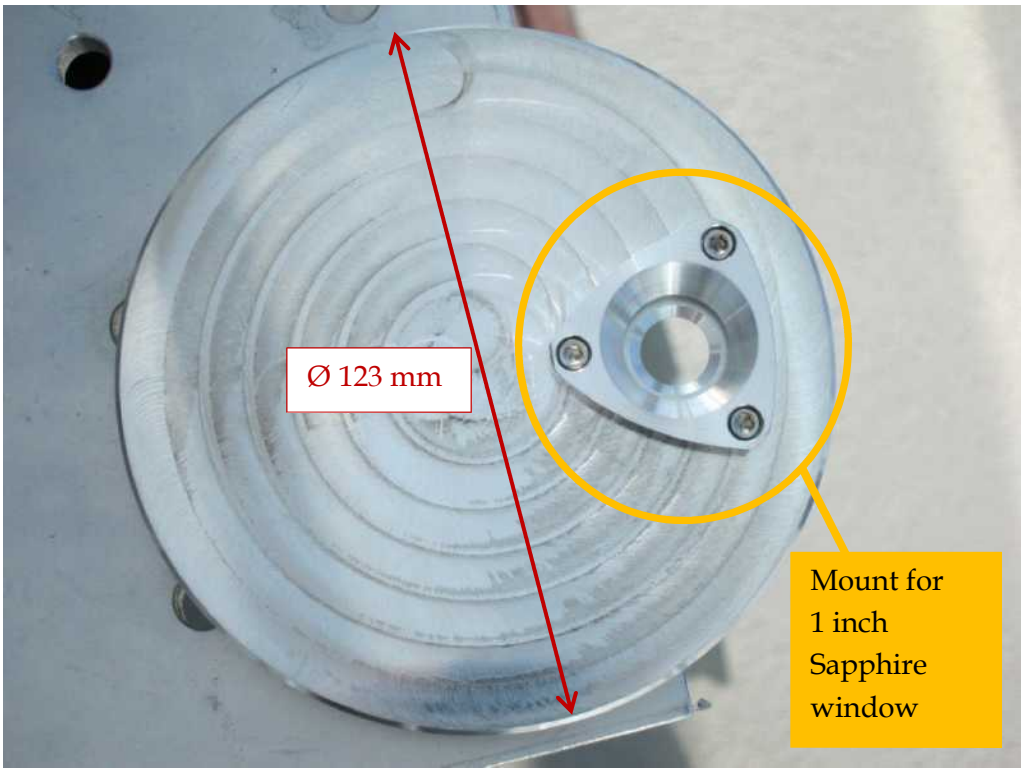


**Figure 114 Adapter plate for 1 inch sapphire window (the window is not mounted in the adapter)**

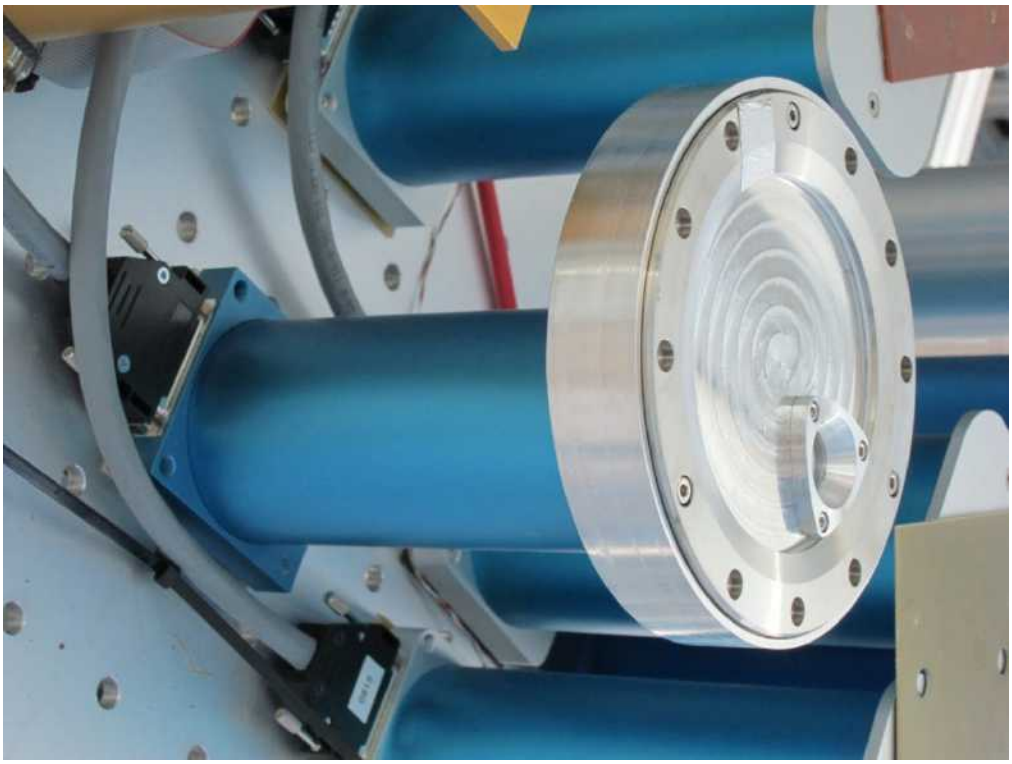

**Figure 115 Transmittance Monitor - Modified PMO6 with window-adaptor for sapphire window.**

### 3.6.5 Validation of the window transmittance measurement

This section deals with the validation of the measurement procedure for the transmittance measurement. If the following list of points can be validated, then the transmittance measurement can be seen as justified:

1. Stability of the window transmittance measurement over the course of a measurement day.
2. Stability of the ratio of the transmittance monitor to PMO2, which means that the window does not need to be removed from the Transmittance Monitor, and PMO2 can be used to estimate the signal that the transmittance monitor would measure without the window.

3. Validity of measuring the transmittance of one window while using the other one in CSAR (this is about the interchangeability of the different windows of the same make).
4. Validity of window transmittance correction after deterioration due to dust.

#### *3.6.5.1 Stability of the transmittance monitor with respect to the WRR*

The PMO2 – one of the World Standard Group instruments – is used as the 'third radiometer' which measures the Solar Irradiance without a window in front. If it can be shown that the ratio of the transmittance monitor to PMO2 (WRR) is long-term stable, then PMO2 could be used to estimate the signal that the transmittance monitor would measure without the window. This implies that the window would not need to be removed from the transmittance monitor.

Figure 116 shows that the ratio of the transmittance monitor to the WRR (as represented by PMO2) is stable over the course of more than a month – at an uncertainty level of 0.01%. Therefore, it is justified to use the PMO2 in order to estimate the measurement of the transmittance monitor without window. It is not necessary to take the window off of the transmittance monitor; rather, the transmittance monitor can be used to take measurements for the whole useful measurement period around mid-day.

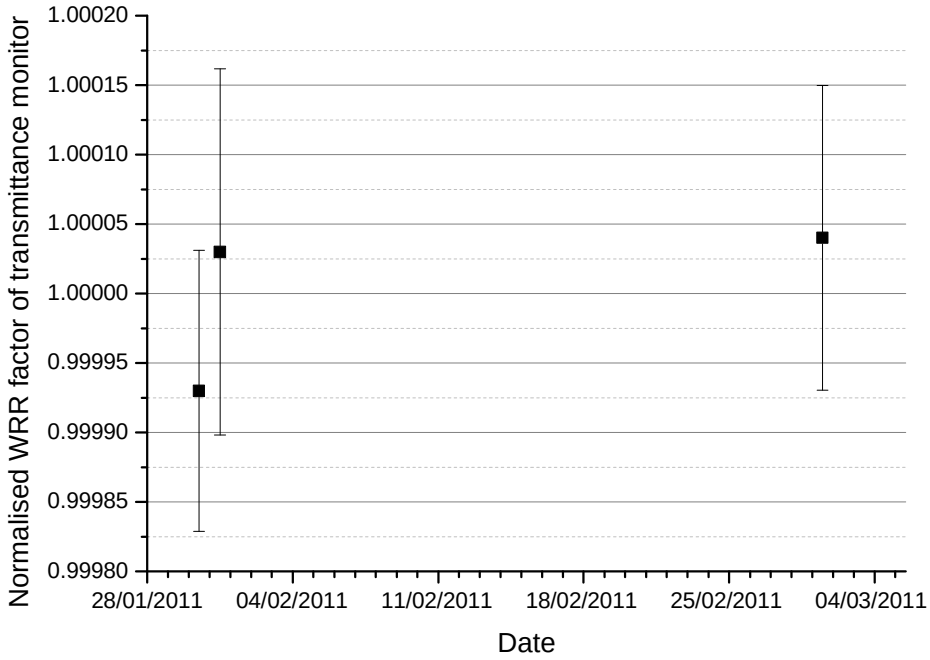


**Figure 116 The normalised ratio of the transmittance monitor to the WRR (as represented by PMO2). Error bars show standard error of the mean. (the original data were divided by a factor of 1.00012, so that 1 is the average of the three measurements.**

### *3.6.5.2 Stability of the window transmittance measurements over the course of a measurement day*

Ideally, the window transmittance measurements are stable over a long time period of a measurement day; this would allow integration of the measurement values over this extended time period and consequently to reduce the standard error of the mean. If, on the other hand, the measurements showed great variation, then it would not be immediately clear whether the variation is due to the experimental method or whether it is due to a variation of the transmittance (i.e. the measurand) itself.

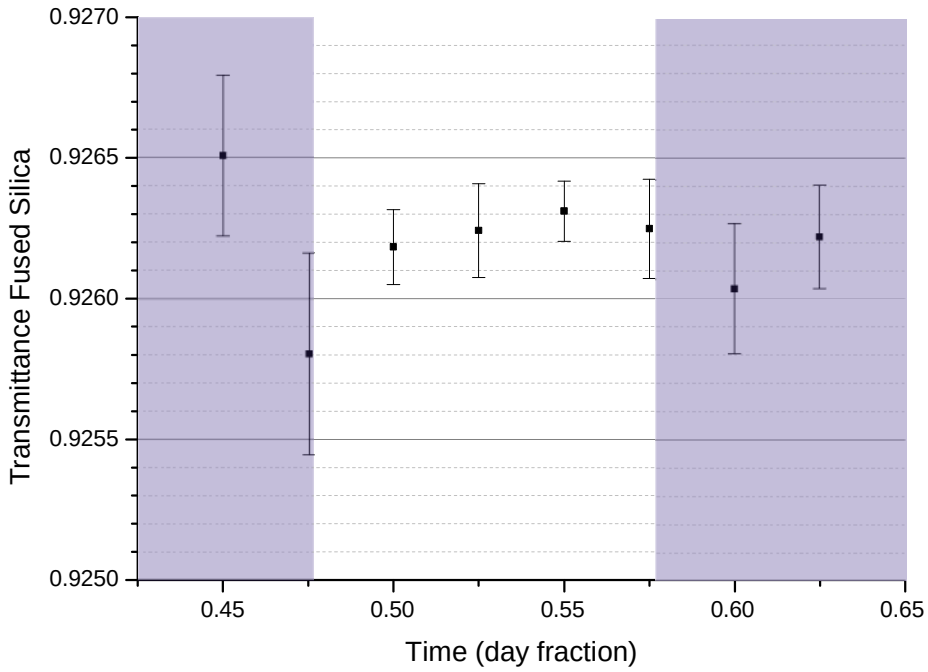


**Figure 117 Transmittance measurements of fused silica window (integration time 0.025 days, 27 Jan 2011), error bars show the standard error of the mean**

Figure 117 shows that the transmittance measurement of a sapphire window over the course of a good measurement day remains very stable within 72 minutes on either side of the solar maximum (0.525 days) – the 31-minute (0.025 day fraction) averages are within a range of less than 0.015%. Outside the central time window, the results are less stable and are associated with larger measurement noise. Figure 118 shows a similar result for the sapphire window.

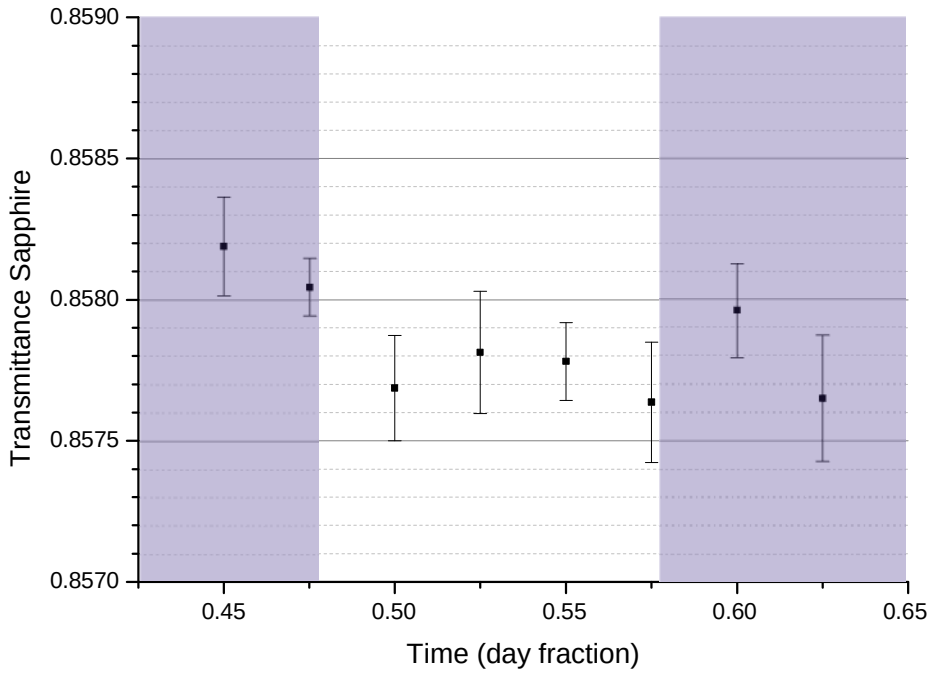


**Figure 118 Transmittance measurements of sapphire window (integration time 0.025 days, 7 Mar 2011), error bars show the standard error of the mean**

The greater variation in the measurements outside the central time window can be attributed to the significantly greater rate of change of the Solar Irradiance outside of this time window combined with the fact that the measurement cycles of the transmittance monitor and the 'third radiometer' are not synchronised.

Figure 119 shows the Solar Irradiance in Davos over the course of a very good measurement day, with an illustration of the time window where the window transmittance measurements are stable. It also shows that at the time of the tests, the solar signal reaches its maximum at a day fraction of about 0.525 (12:36) and that the signal is quite stable for a day fraction of ~ 0.05 (~ 72 min) on either side of the maximum; the relative change in Solar Irradiance is < 1.5%.

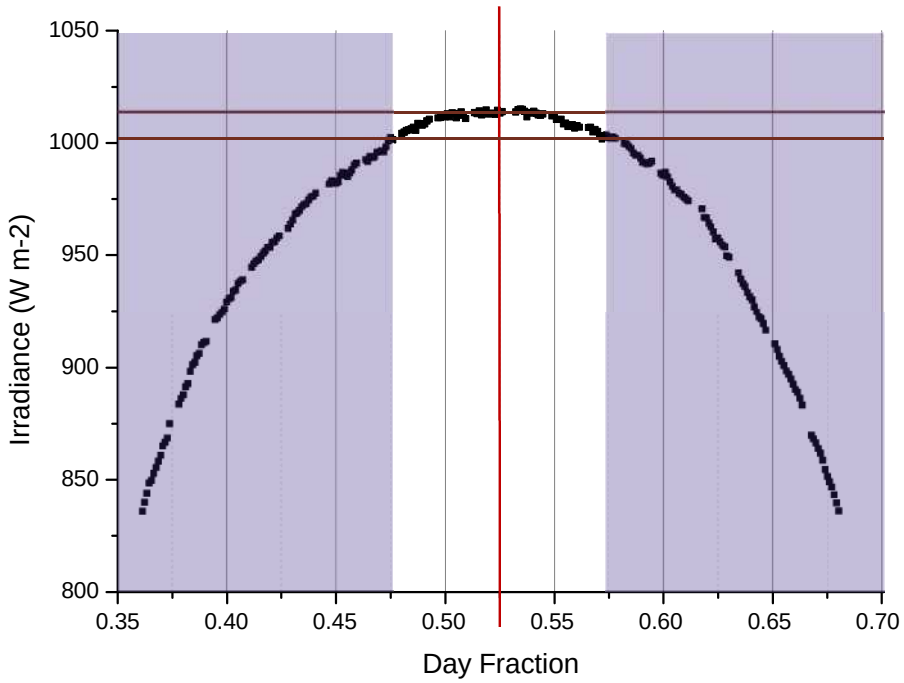


**Figure 119 Solar Irradiance measurements in Davos over the course of a good measurement day (PMO2, 8 Mar 2011)**

Figure 120 shows that the relative rate of change of the Solar Irradiance varies significantly over the course of a measurement day. While the solar signal changes by approximately 0.2% per minute in the morning and in the evening, it changes by less than ± 0.05% in a time window of ± 72 min (± 0.05 day fraction) around the time when the Solar Irradiance is at a maximum (~ 0.525 day fraction).[74]

[74] Please note: Figure 119 and Figure 120 are almost identical with Figure 18 and Figure 19 (see Section 2.5.4).

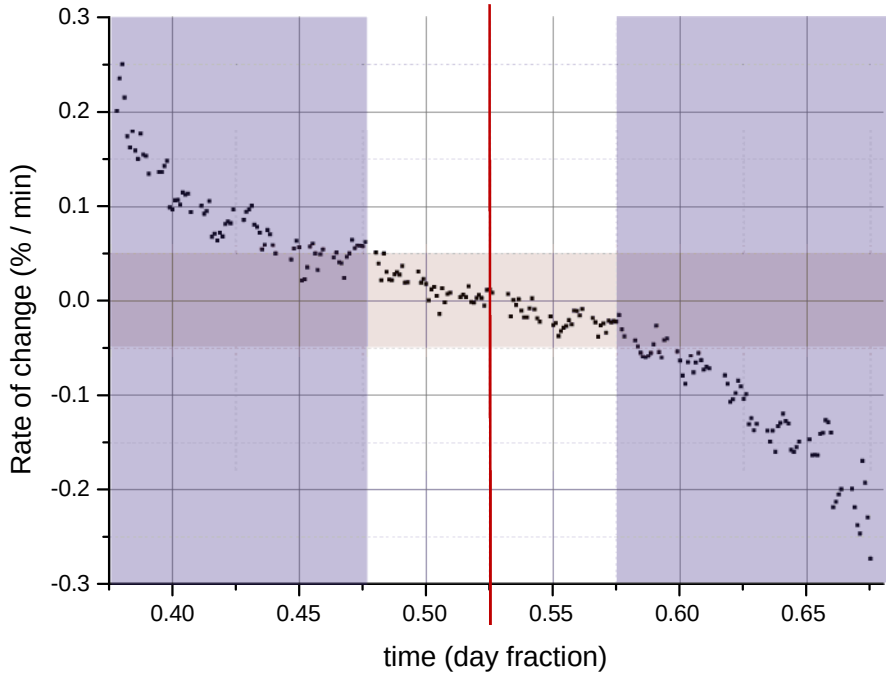


**Figure 120 Rate of change of Direct Solar Irradiance.**

### *3.6.5.3 Validity of measuring the transmittance of one window while using the other one in CSAR*

The measurements taken with the transmittance monitor can only be applied to the CSAR window if the window on the transmittance monitor and the CSAR window are either transmitting the same amount of solar radiation, or the difference is small and known. Measurements were performed to compare the window pairs directly.

Figure 121 shows a series of six comparisons of the two sapphire windows, all taken in one measurement day. The windows were cleaned before each measurement. The individual data points in the graph show the ratio of the transmittances of the window that was used in front of CSAR ("Sapphire 1") and the transmittance of the window that was used in front of the transmittance monitor ("Sapphire 2"). The error bars are indicative of the standard

uncertainty of the individual measurement. The "overall" result shows a weighted mean of the six individual measurement results, together with a standard uncertainty calculated from the individual standard uncertainties[75] (see Appendix H). As a result, the Sapphire windows were found to have the same transmittance within the standard uncertainty of the measurement (the ratio between the transmittance of Sapphire 1 over Sapphire 2 was found to be 1.00004, with a standard uncertainty of 0.016%). The results were found to be consistent using a chi-square test, with $\Pr\left\{\chi^2(\nu) > \chi^2_{obs}\right\} = 0.13 > 0.05$.

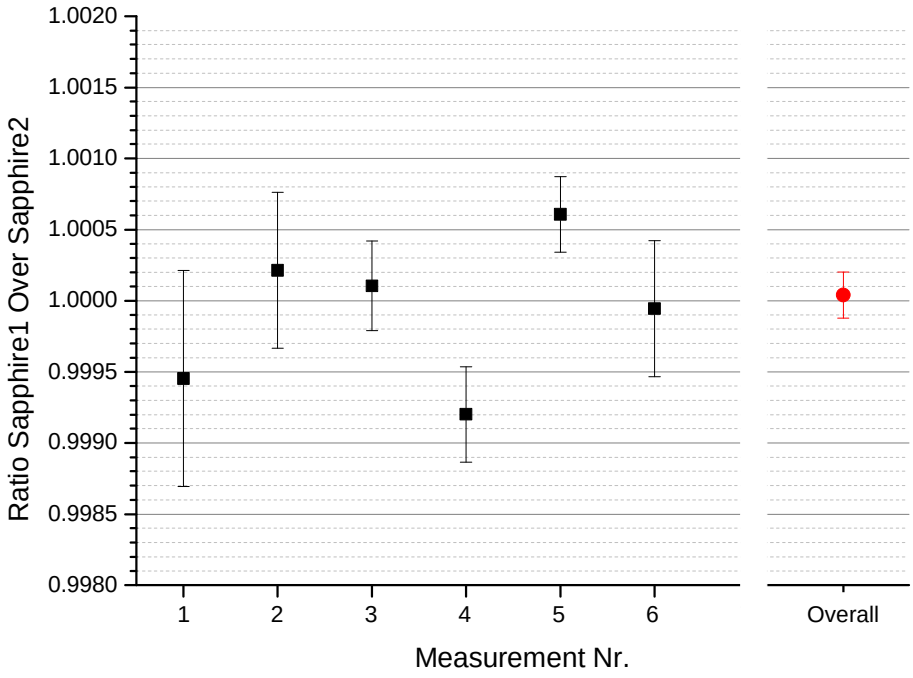


**Figure 121 Comparison of Sapphire windows. Error bars show estimated standard uncertainties**

The fused silica windows were also compared directly after cleaning and the ratio of their transmittances is also close to unity; here, the transmittance of the window that was used in front of CSAR

[75] Peter Harris (Principal Research Scientist, NPL) advised me to use a weighted mean and associated uncertainties in this case.

("AX") was found to be 0.06% higher than the transmittance of the window used in front of the transmittance monitor ("AY"), with an associated standard uncertainty of 0.028%. The measurement result is shown in Figure 122, and they were also analysed using the formalism presented in Appendix H. The results were found to be consistent using a chi-square test, with $\Pr\left\{\chi^2(\nu) > \chi^2_{obs}\right\} = 0.40 > 0.05$.

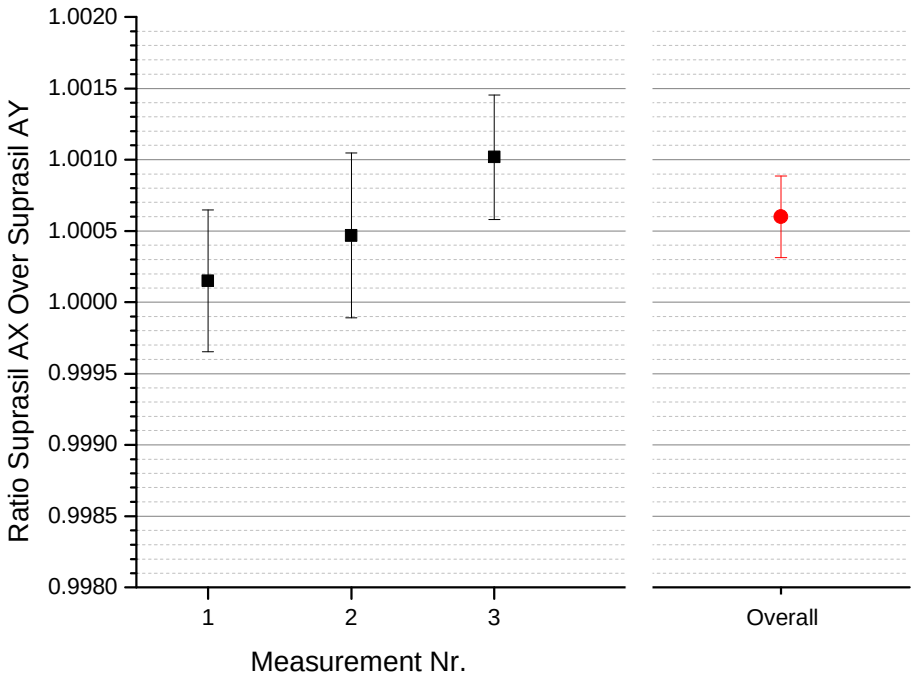


**Figure 122 Transmittance of the two fused silica (Suprasil 3001 from Heraeus) windows**

The cleaning method applied to the windows is a time-tested and highly repeatable process; it is sometimes referred to as the "drop and drag method". An approximately 10 cm long, and a few centimetres wide strip of lens cleaning tissue is placed on top of the window - with most of the strip hanging off of the edge of the window. Then, two or three drops of cleaning fluid are administered to the part of the tissue that is close to the edge of the window. The

tissue is then slowly pulled across the window surface, making sure that the tissue neither 'runs dry' nor that there is excess fluid on the optical surface after dragging the tissue across. The cleaning is done using two different cleaning fluids. First, Acetone is used for degreasing, and then Ethanol 96% is used to remove any residue left from the Acetone. The drop and drag method is repeated until visual inspection yields a satisfactory result. Finally, remaining dust particles that may originate from the tissue are blown off using compressed air.

#### *3.6.5.4 Deterioration of the window transmittance due to dust*

In Section 3.6.5.3, the windows were compared directly after wet cleaning. However, it is not possible to clean the CSAR window every day, because cleaning requires the window to be removed from CSAR, and it would be impractical to go warm and cool the detector down to operating temperatures again before every measurement day. It may be convenient to leave the window on CSAR for at least one week and up to several weeks before it can be cleaned. It is therefore necessary to know how the transmittance of the windows deteriorates when left uncleaned for this time period. It would be ideal if the deterioration was small; however, it would also be acceptable if the two windows (one on CSAR and the other on the transmittance monitor) deteriorated in exactly the same way.

Figure 123 shows a comparison of the two sapphire windows, before cleaning (measurements 1 & 2) and after cleaning (measurements 3 & 4). The windows had not undergone any "wet" cleaning for approximately three weeks. After three weeks of exposure to a relatively dusty environment (building works were ongoing at the PMOD/WRC), the window transmittances had deteriorated by approximately 0.13%. However, the ratio of these windows'

transmittances is very close to one and the ratio stays very close to constant. The transmittance of the window that was used in front of CSAR ("Sapphire 1") was measured to be higher by 175 ppm (before cleaning) and 117 ppm (after cleaning) than the transmittance of the window used in front of the transmittance monitor ("Sapphire 2"). These measurements indicate that the windows tend to deteriorate in the same way.

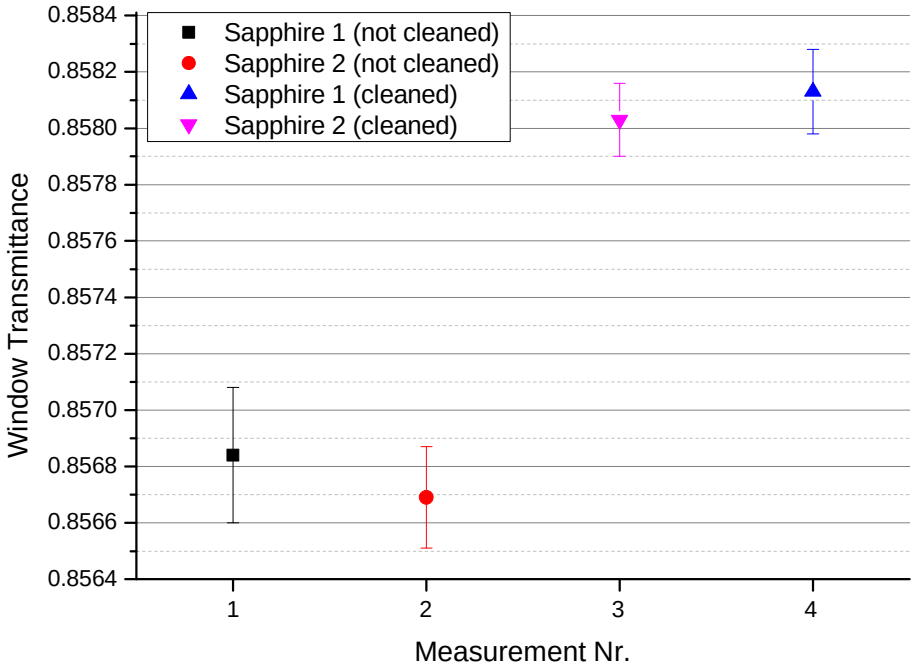


**Figure 123 Comparison of Sapphire windows before and after cleaning**

The data presented in Figure 123 can be used to calculate the ratios of the window transmittances of Sapphire 1 and Sapphire 2 in the cleaned and in the uncleaned state. The result is shown in Figure 124. It shows that there is no statistically relevant difference between the transmittance ratios for the two different states. The uncertainty

due to the assumption that the ratios for the two states is one is estimated to be 0.016%[76].

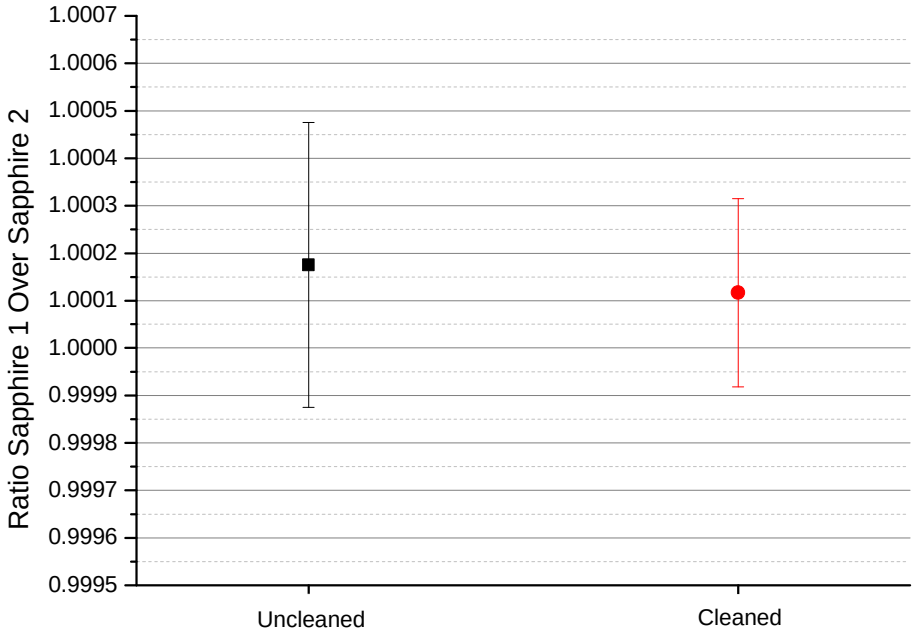


**Figure 124 Ratio of the window transmittance of Sapphire 1 over Sapphire 2, in the cleaned and uncleaned state.**

While the results presented in Figure 124 show that after three weeks the deterioration due to dust deposition on the surface is the same for two windows, it does not show at what rate the windows are deteriorating during the test period. In order to answer this question, the transmittance of one of the fused silica windows was measured on all good measurement days within a three-week period. The window was cleaned on the first day and then left uncleaned; the results are shown in Figure 125. The relative deterioration of the fused silica window was approximately 0.23% over the three weeks. From these measurements, it seems that the main deterioration takes place within

[76] This uncertainty component was calculated using Equation (A.30) in Appendix H.

the first eight days, and that the window transmittance stays constant over the following two weeks.

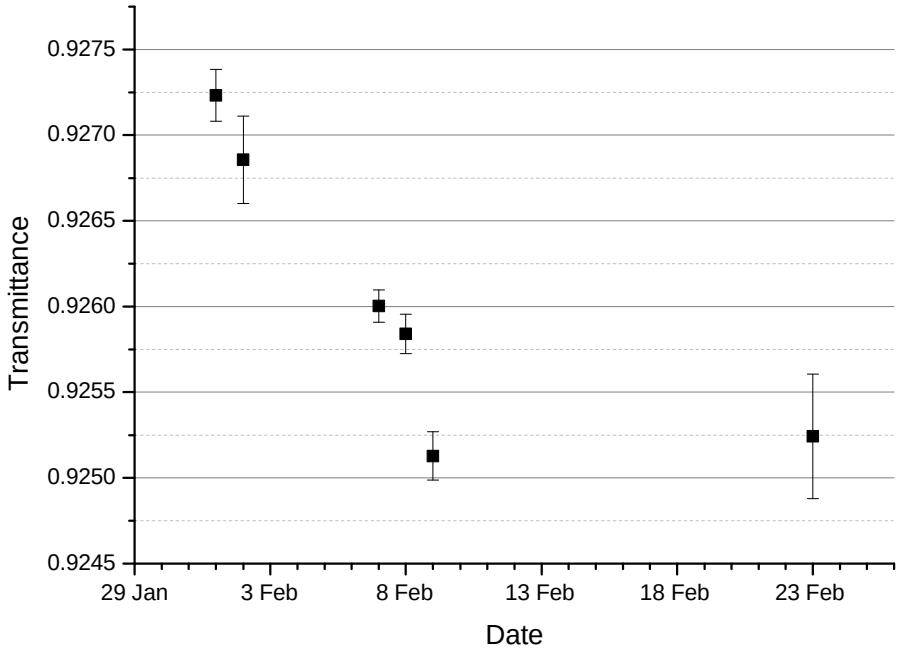


**Figure 125 Deterioration of window transmittance over time if not cleaned (fused silica).**

### 3.6.6 Combined uncertainty due to window transmittance

In the previous sections, various effects are discussed that contribute towards the uncertainty in the determination of the transmittance of the Sapphire and Fused Silica windows. These results are summarised in two tables, one detailing the uncertainty components for the Sapphire window (Table 20), and the other for the Fused Silica window (Table 21).

In addition to uncertainties identified in this thesis, the uncertainty budgets also take account of two effects that were pointed out by André Fehlmann. Fehlmann developed a model for the

window transmittance, and based on manufacturer data, he estimated the standard uncertainty due to temperature-induced changes in the refractive index to be 0.0087% for both types of windows. Apart from this, Fehlmann also identified an uncertainty due to the inter-reflection between the transmittance monitor detector cavity and the window; the standard uncertainty due to this effect is estimated to be 0.0013%. Other effects such as birefringence due to mechanical stress in the window material and lensing due to bending of the window have been shown to be negligible (Fehlmann, 2011).

**Table 20 Uncertainty budget for Sapphire window transmittance**

| Uncertainty component | Standard Uncertainty | Discussed in Section |
|---|---|---|
| **Transmittance monitor stability** | 0.01% | 3.6.5.1 |
| **Transmittance ratio of different windows** | 0.016% | 3.6.5.3 |
| **Deterioration of window transmittance due to dust** | 0.016% | 3.6.5.4 |
| **Temperature dependence of refractive index** | 0.0087% | André Fehlmann (Fehlmann, 2011) |
| **Inter-reflection between Transmission Monitor and window** | 0.0013% | André Fehlmann (Fehlmann, 2011) |
| **Overall uncertainty** | **0.026%** | |

**Table 21 Uncertainty budget for Fused Silica window transmittance**

| Uncertainty component | Standard Uncertainty | Discussed in Section |
|---|---|---|
| Transmittance monitor stability | 0.01% | 3.6.5.1 |
| Transmittance ratio of different windows | 0.028% | 3.6.5.3 |
| Deterioration of window transmittance due to dust | 0.016% | 3.6.5.4 |
| Temperature dependence of refractive index | 0.0087% | André Fehlmann (Fehlmann, 2011) |
| Inter-reflection between Transmission Monitor and window | 0.0013% | André Fehlmann (Fehlmann, 2011) |
| Overall uncertainty | **0.035%** | |

## 3.7 Size and Mass

Table 22 shows that the requirements regarding size and mass of the CSAR radiometer head and the vacuum assembly, as formulated in Section 2.9, are met by the CSAR design.

**Table 22 Size and Mass of CSAR**

| Quantity | Required specification | CSAR design |
|---|---|---|
| Radiometer head - mass | < 10 kg | 8.8 kg |
| Radiometer head - volume | L×H×W < 250 mm × 300 mm × 300 mm | L×H×W = 243 mm × 274 mm × 274 mm |
| CSAR – overall mass of vacuum assembly | < 100 kg | 86 kg |

Another requirement is that the centre of mass of the vacuum assembly should be as close as possible to the tracker table. Figure 126 and Figure 127 show the position of centre of mass relative to the central geometrical axis (distance: ~ 5 mm), and relative to the mounting surface (distance: ~ 158 mm). While it is not ideal that the centre of mass is 158 mm in front of the mounting surface of the solar tracker, the resulting imbalance could be removed by a counterweight on the back of the solar tracker. As a result, the solar tracker moved smoothly and without any problems when CSAR was mounted.

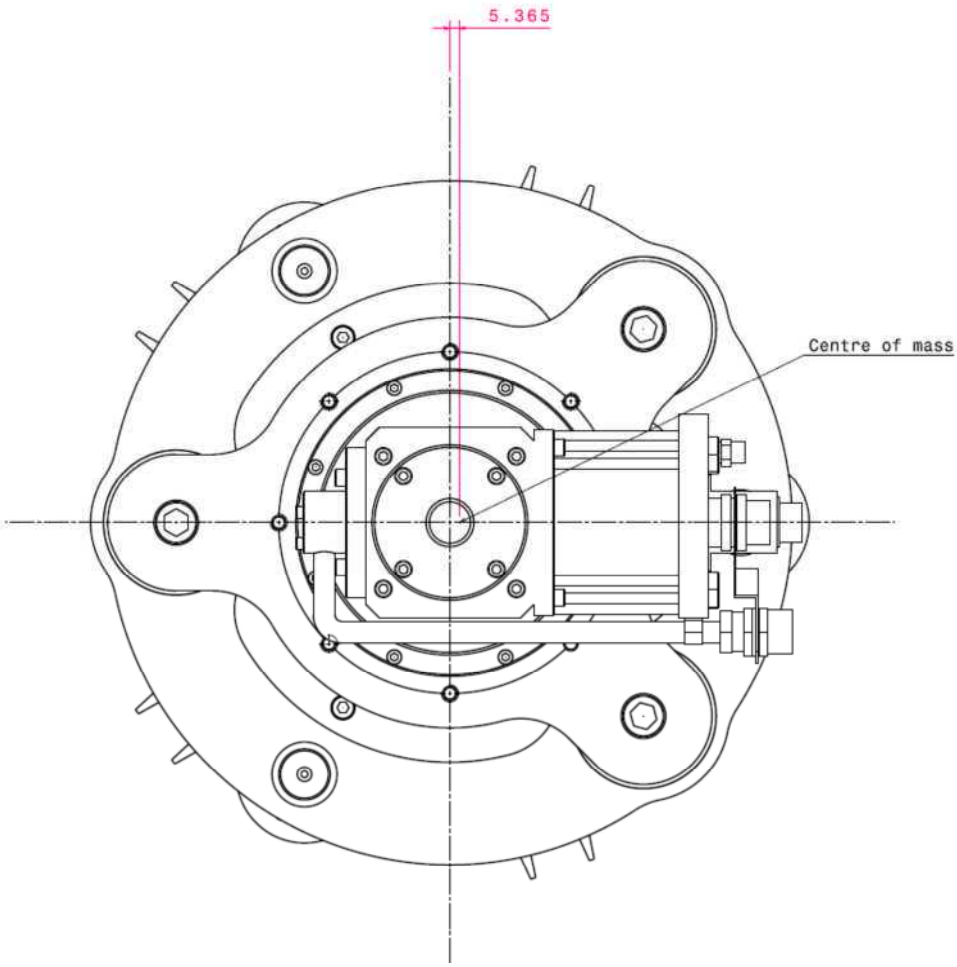


**Figure 126 Centre of mass - distance from central vacuum chamber axis**

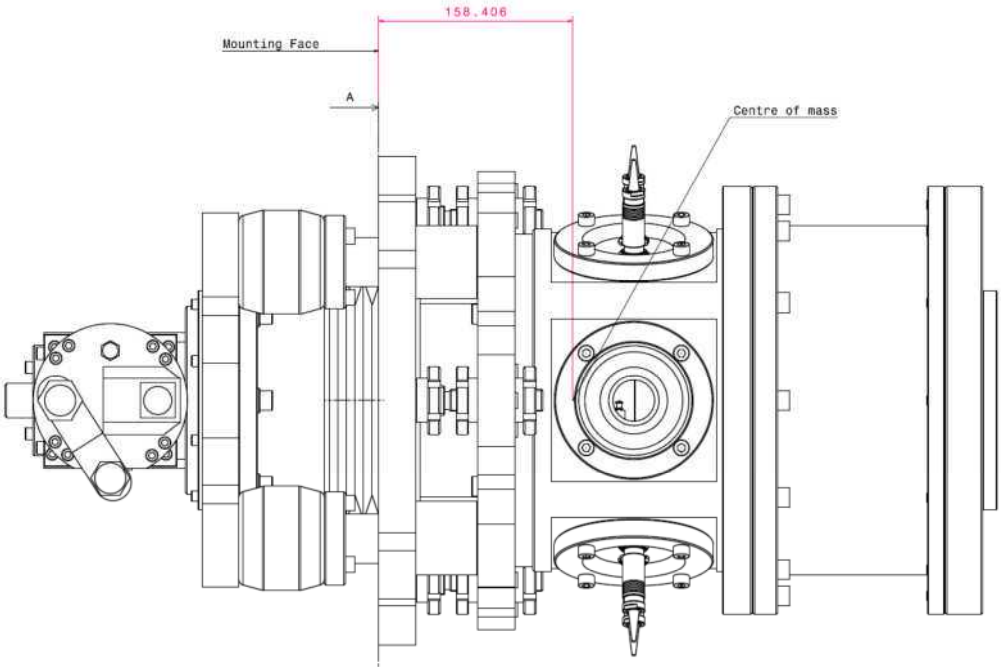


**Figure 127 Centre of mass - distance from mounting surface**

## 3.8 Uncertainty budget for CSAR

Table 23 and Table 24 show the uncertainty budget for CSAR. The individual uncertainty components lead to three different overall instrument uncertainties, depending on the mode of operation. If operated in space, where the need for the window is removed, the overall instrument uncertainty is 0.011% (see Table 23). With respect to the terrestrial application, the overall uncertainty for a CSAR measurement for the time period of one measurement day adds up to 0.032% for the operation with the sapphire windows, and 0.039% for the operation with the fused silica windows (see Table 24).

**Table 23 Uncertainty budget for operation of CSAR on board a satellite.**

| Uncertainty component | Standard Uncertainty | Discussed in Section |
|---|---|---|
| Size of precision aperture | 0.0059% | 3.4.1.8 |
| Alignment of CSAR to the Sun | 0.001% | 3.4.5.3 |
| Diffraction and spectral distribution of the solar irradiance | 0.0057% | 3.4.6 |
| Cavity absorptivity | 0.0054% | 3.5.3.8 |
| Instrument noise | 0.004% | 3.5.4 |
| Electrical power measurement[77] | 0.00064% | 3.5.6 |
| Detector linearity | 0.0009% | 3.5.8 |
| | | |
| Overall uncertainty | **0.011%** | |

[77] This is the same value as the value estimated for the ground application. The real value depends on the specific electronics used; however, the uncertainty due to the electrical measurement equipment is not usually a dominating element of the overall uncertainty budget.

**Table 24 Uncertainty budget for operation of CSAR in Davos with Sapphire window and Fused Silica Window**

| Uncertainty component | Standard Unc. | Discussed in Section |
|---|---|---|
| Size of precision aperture | 0.0152% | 3.4.1.8 |
| Stray light | 0.003% | 3.4.2 |
| Alignment of CSAR to the Sun | 0.001% | 3.4.5.3 |
| Diffraction and spectral distribution of the solar irradiance | 0.0057% | 3.4.6 |
| Cavity absorptivity | 0.00026% | 3.5.3.8 |
| Instrument noise | 0.004% | 3.5.4 |
| Detector time lag effect | 0.006% | 3.5.5 |
| Electrical power measurement | 0.00064% | 3.5.6 |
| Detector linearity | 0.0013% | 3.5.8 |
| | | |
| Window transmittance (Sapphire) | 0.026% | 3.6.6 |
| Window transmittance (Fused Silica) | 0.035% | 3.6.6 |
| | | |
| Overall Uncertainty (CSAR + Sapphire window) | **0.032%** | |
| Overall Uncertainty (CSAR + Fused Silica window) | **0.039%** | |

# Chapter 4 Test Results

The previous chapter presented various design choices and test results on a component level. The aim of this chapter is to present tests of the instrument performance on a system level.

Section 4.1 chapter presents the comparisons of CSAR with NPL's SI standard for radiant power. It shows that CSAR agrees well with the SI Radiometric Scale within the uncertainties associated with the comparison.

Section 4.2 gives details of the comparison of CSAR with the World Radiometric Reference (WRR). CSAR measures 0.309% lower than the WRR.

## 4.1 Comparisons of CSAR with SI Radiometric Scale

NPL has a fairly long-standing history of comparing pyrheliometers with the SI Radiometric Scale (Romero et al., 1991, Romero et al., 1996, Finsterle et al., 2008, Fehlmann et al., 2012). The knowledge acquired during these earlier comparisons was used for the comparison of CSAR with the SI radiometric scale.

### 4.1.1 Trap detectors as transfer standards

CSAR was not compared directly with the primary standard of the SI radiometric scale (the Cryogenic Radiometer), but was rather compared indirectly to the SI scale via a transfer standard. This transfer standard is a so-called "trap detector". Figure 128 and Figure 129 show the rear and the front of a trap detector, respectively.

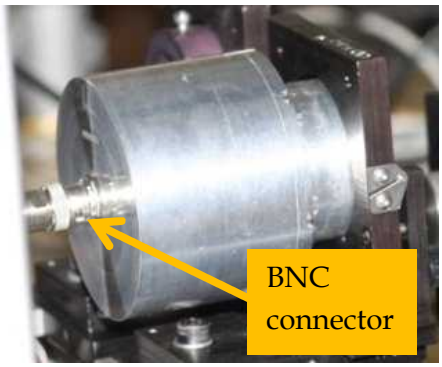


**Figure 128 Trap detector – rear view**

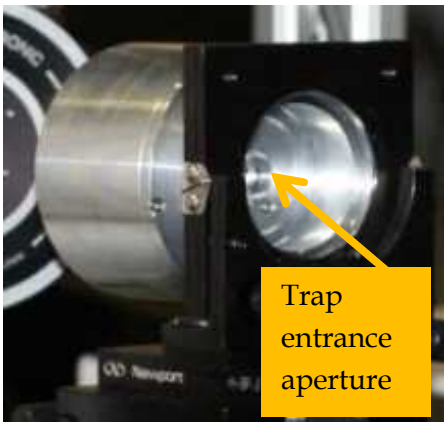


**Figure 129 Trap detector – front view**

Trap detectors are secondary standards that are employed to transfer the SI scale from the primary standard (Cryogenic Radiometer) to other radiometric devises. A trap detector is essentially an assembly of three Silicon photodiodes that are spatially placed in such a way that the incoming laser beam undergoes five reflections at the surfaces of the photodiodes before the last reflection leaves the detector. With a specular surface reflectivity of approximately 30% of a single photodiode, five reflections lead to an overall absorptivity of the trap of > 99.7%; this means that the trap behaves almost like an ideal photodiode, which makes it ideal for its use as a transfer standard. Further details on trap detectors can be found in (Fox, 1991).

### 4.1.2 Measurement principle for comparison of CSAR with SI

The comparison of CSAR with the SI scale at NPL was carried out using a similar experimental set-up to the one used in earlier comparisons of the World Radiometric Reference with the SI radiometric scale; see, for example, (Romero et al., 1991) . Figure 130 shows a schematic of the experimental set-up. A laser beam is power-stabilised with the help of a Pockels cell, polarisers, and an electronic control system. The beam also passes a spatial filter in order to reduce the stray light around the main beam. The power stabilisation system and spatial filter are the same as in the setup for the cavity reflectivity measurements (for photographs see Figure 103 and Figure 104 in Section 3.5.3.6).

In addition, the beam is vertically polarised in order to make full use of the Brewster effect, which means that the window transmittance is very close to unity if the window is placed at the Brewster angle. A beam splitter is used such that the main beam enters the "Reference trap", and the reflected beam enters the "Monitor trap". Figure 131 shows the relative position of the two traps (please note that the Brewster window shown in this photograph is only present during window transmittance measurements and not during the main measurements).

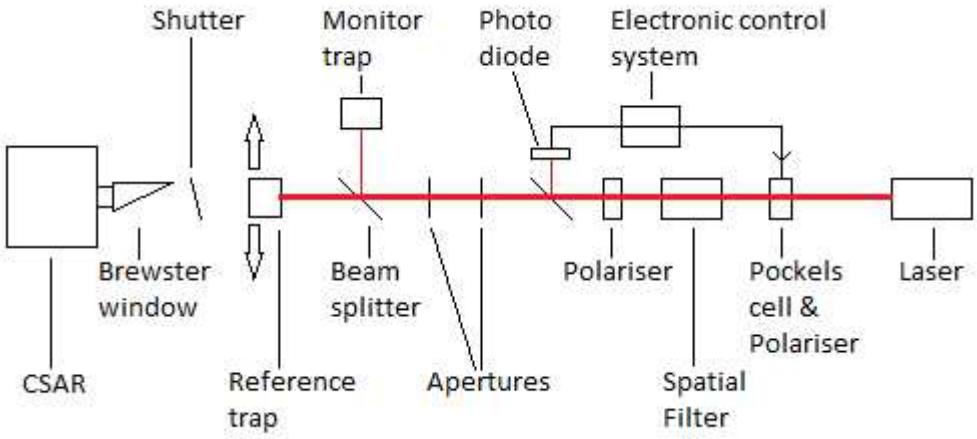


**Figure 130 Schematic of the measurement set-up for comparison of CSAR with SI Radiometric Scale**

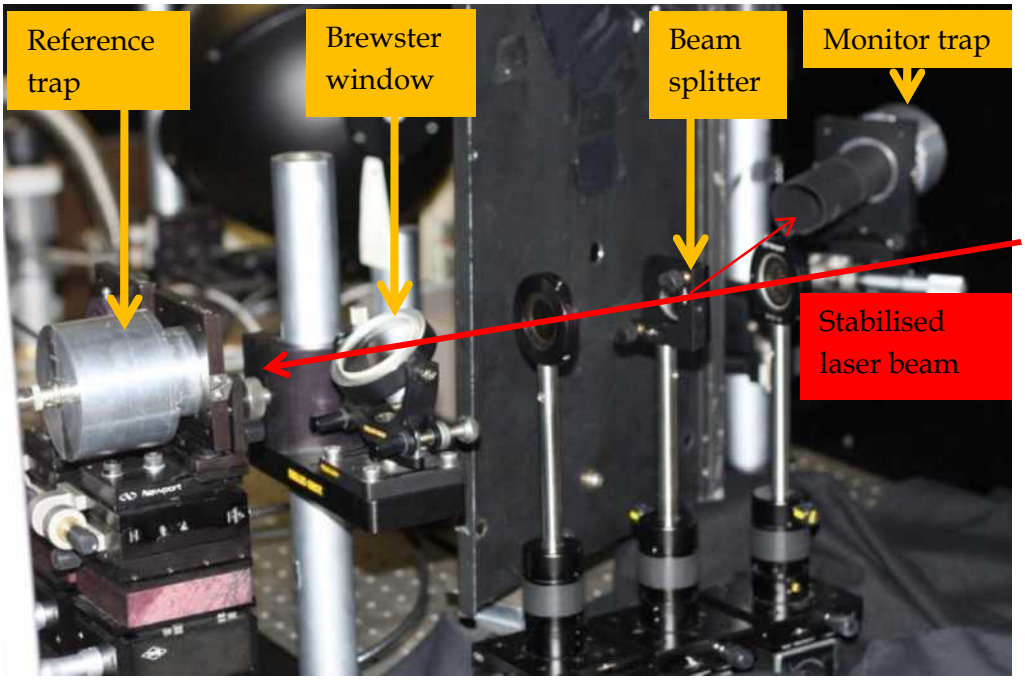


**Figure 131 Arrangement of reference trap, monitor trap, and beam splitter. This picture also shows the Brewster window, which is only present for the window transmittance measurement. For the SI-CSAR comparison, the Brewster window is mounted directly in front of CSAR.**

The Reference trap sits on an optical rail (see Figure 132), so that it can be moved in and out of the laser beam. When the Reference trap is exposed to the laser beam, the "Beam splitter ratio" is determined, i.e. the ratio between the signal measured by the Monitor trap and the Reference trap. The Beam splitter ratio is of the order of 1 : 20, and it is measured with a power level of 0.6 mW at the Reference trap, which is the same power level at which the Reference trap was calibrated against the primary standard of the SI Radiometric Scale. Once the Beam splitter ratio has been measured, the signal the Reference trap would measure can be deduced from the signal measured by the Monitor trap – even if the Reference trap is not exposed to the laser beam.

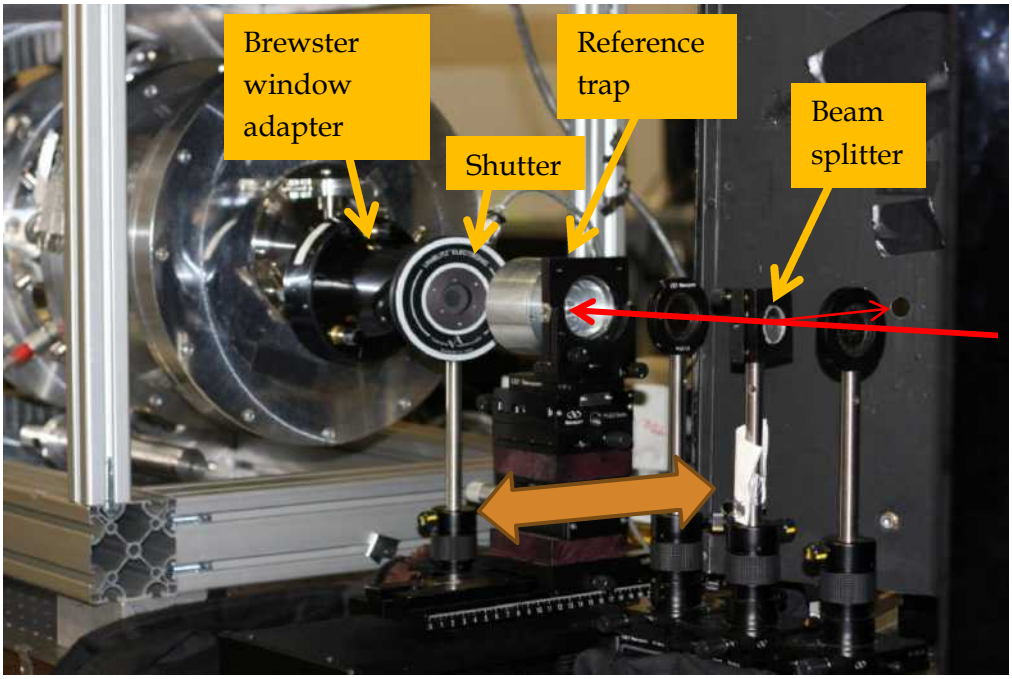


**Figure 132 CSAR fitted with Brewster window, shutter and reference trap on optical rail in front of CSAR**

After determining the Beam splitter ratio, the Reference trap is moved to the side, in order to admit the laser beam into the CSAR detector cavity. Since CSAR is not designed to have sufficient

resolution in the range of power levels where the traps are linear, the power in the laser beam needs to be increased for the CSAR measurements (for these measurements, an optical power level of 6.6 mW was chosen).

The front of the CSAR vacuum can is fitted with a Brewster window (see Figure 133) to minimise reflection-losses at the window surfaces and to avoid interference-effects due to the parallel window surfaces.

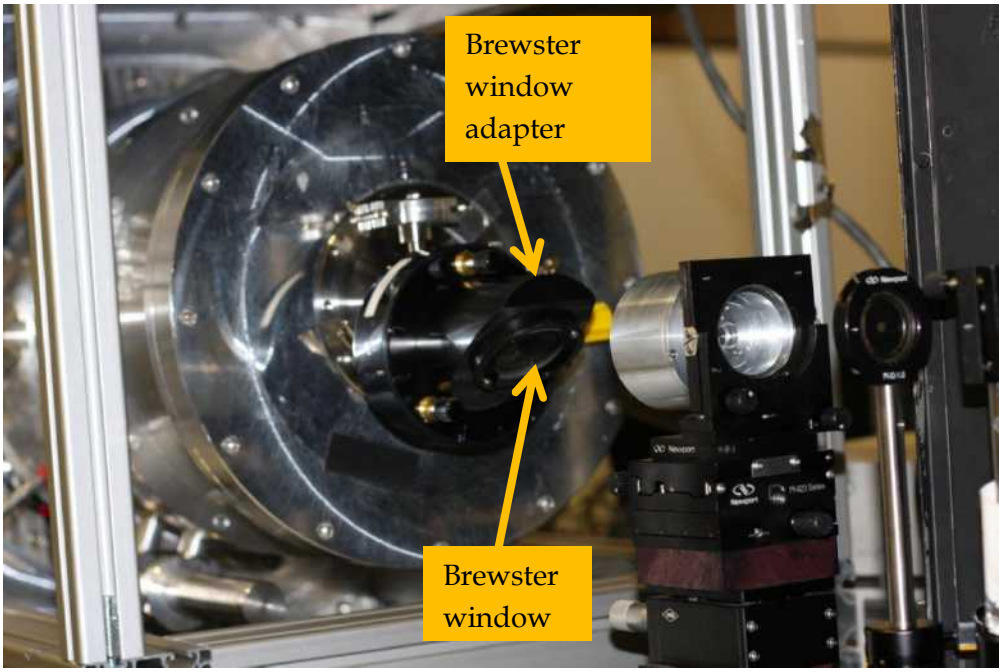


**Figure 133 CSAR fitted with Brewster window and Reference trap in front.**

### 4.1.3 Determination of the Beam splitter ratio

Ideally, for the Reference trap, the conditions during the determination of the beam splitter ratio should be as similar as possible to the conditions during the calibration of the Reference trap against the primary standard. This was achieved (1) by aligning the Reference trap in the same way as during calibration (the trap was aligned centrally with the help of an alignment target), (2) by choosing the same laser wavelength as during calibration (647.1 nm), (3) by creating the same

laser beam diameter (4 mm), and (4) by selecting the same power level (0.6 mW) as during calibration.

Apart from the Reference trap being used in the same way as during calibration, another condition must be fulfilled for a good measurement: the response of the Monitor trap needs to remain linear when the power level in the main beam is increased for the CSAR measurements (from 0.6 mW to 6.6 mW). The power increase in the main beam is equivalent to an increase for the Monitor trap from 0.03 mW to 0.33 mW.

The trap linearity was measured by monitoring the Beam splitter ratio with increasing power levels. The deviation from a constant Beam splitter ratio is shown in Figure 134. For power levels below 0.33 mW, the non-linearity of the traps is < 0.001%, which is negligible in the context of an uncertainty target of 0.01%.

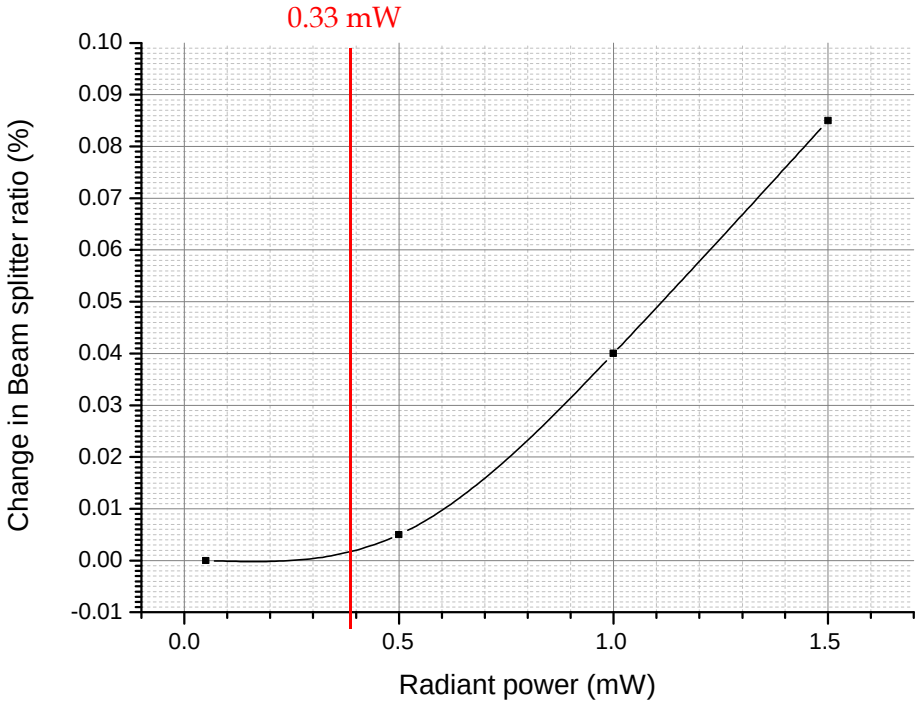


**Figure 134 Change in Beam splitter ratio due to trap non-linearity**

### 4.1.4 Optical and Electrical measurements

For the purpose of this comparison, an optical power level of 6.6 mW is chosen for the CSAR measurements. The cavity is also electrically heated with a base load of 11.6 mW, so that the total power input is 18.2 mW, which is equivalent to a Solar Irradiance of ~ 1000 W $m^{-2}$ (with a fused silica window).

The laser light has a wavelength of 647.1 nm, and the laser beam under-fills the cavity aperture (Figure 135), i.e. the laser beam diameter (approx. 4 mm) is significantly smaller than the cavity aperture diameter (10 mm). The 5 mm diameter precision aperture is not installed; therefore, the cavity aperture is the smallest aperture in the optical system of CSAR.

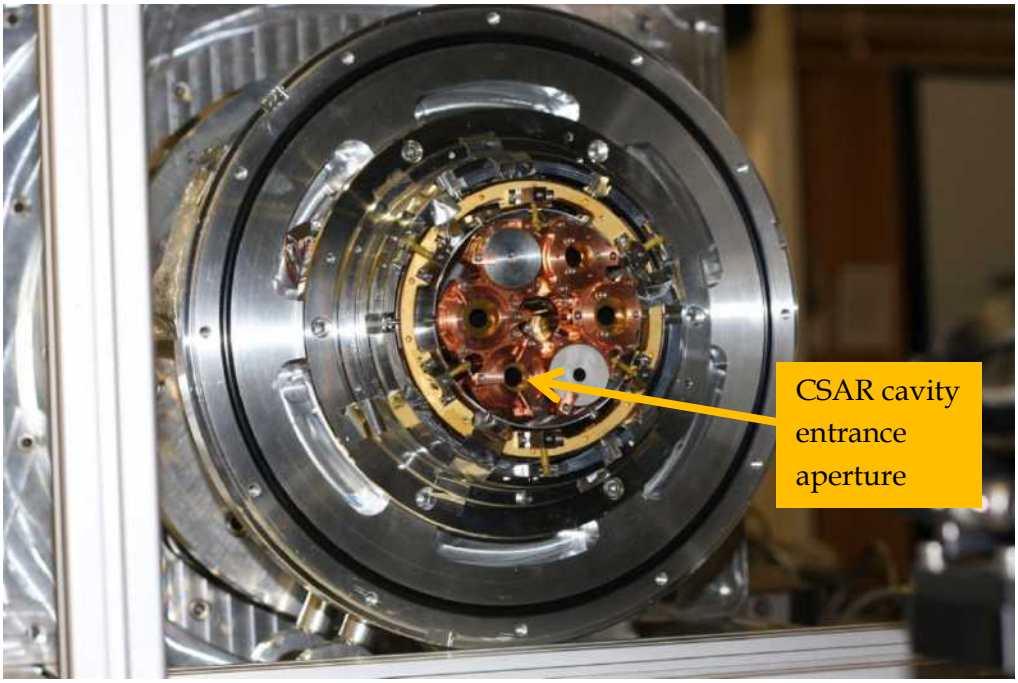


**Figure 135 Before the cold shields and the vacuum can are attached, the cavity is aligned to the laser beam (taking into account the vertical offset due to the Brewster window).**

The transmittance of the Brewster window was determined using the setup shown in Figure 131. The Reference trap signal was measured (1) with the Brewster window in front of the Reference trap

and (2) without the window in front of the Reference trap, and the ratio of these two measurement results is used to estimate the Brewster window transmittance. The Brewster window transmittance was found to be equal to 0.99967 (with a standard error of the mean of the measurements of approximately 0.001%).

Figure 136 shows the temperature rise of the CSAR cavity with respect to the reference block during "light" and "dark" measurements. This graph shows that the light and dark measurements are highly repeatable (Please note that the small difference of ~ 2 mK between light and dark measurements is a deliberate offset, so that the two different measurement modes are clearly discernible during the data analysis).

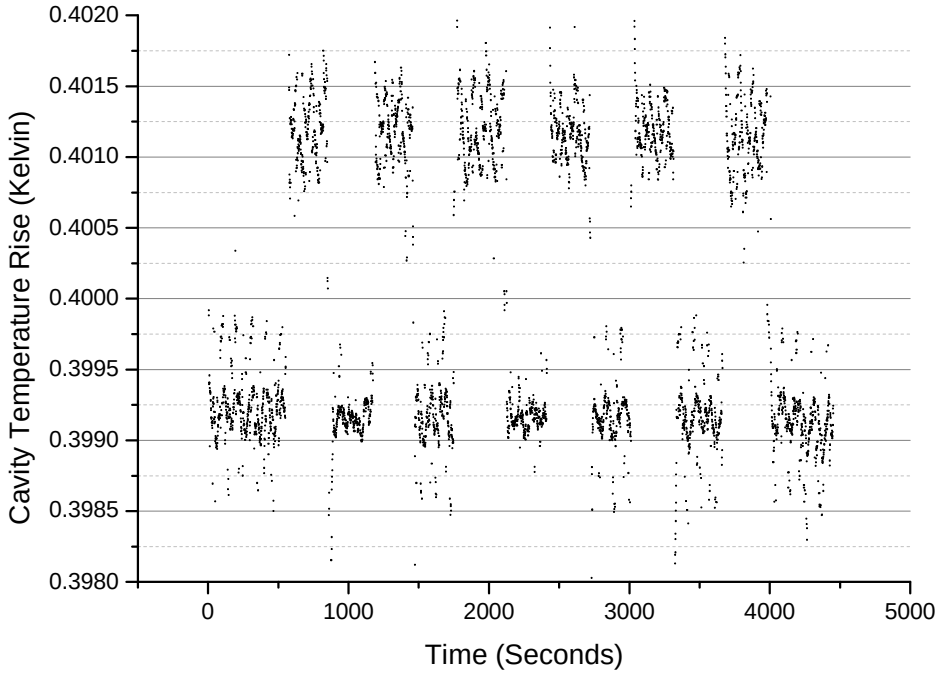


**Figure 136 Cavity Temperature Rise during the comparison of CSAR against the SI (trap detector). The lower values were measured during electrical heating (shutter closed) and the higher values were measured during optical and electrical heating of the cavity (shutter open). This graph shows measurements number 3 to 8 (see Figure 137). Measurement numbers 1 and 2 were taken on the previous day.**

### 4.1.5 Comparison of CSAR with SI – test results

The temperature rise values can be converted into power values based on the measurement of the cavity temperature rise while the shutter is closed and the cavity is only heated electrically, and the measurement of the electrical power being dissipated into the cavity, and the relation between incoming power and temperature rise established in Section 3.5.8 (see Figure 109) CSAR dark measurements (shutter closed, electrical heating only).

One measurement cycle consists of (1) a determination of the beam splitter ratio, (2) a CSAR measurement with the shutter open, and (3) a CSAR measurement with the shutter closed. A total of eight of these measurement cycles were performed for the purpose of

comparing CSAR with the SI Radiometric Scale. The result is shown in Figure 137. CSAR and the SI agree within the stated uncertainties.

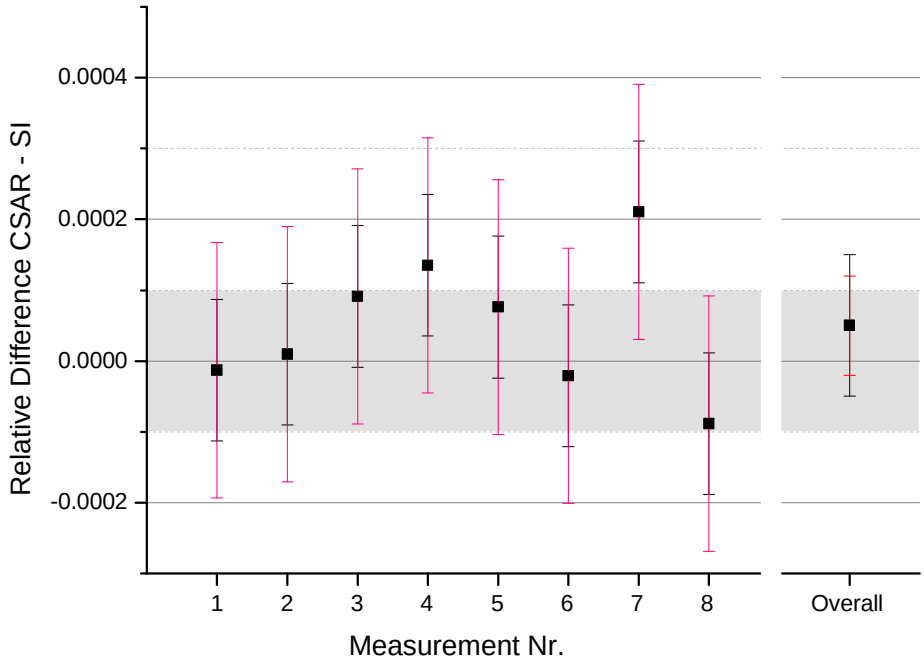


**Figure 137 Comparison of CSAR against SI. The red error bars represent the measurement noise and the black error bars represent the uncertainty in the trap calibration. The error bars indicate the uncertainty in the measurement at the one standard uncertainty level. The shaded area represents the absolute uncertainty in the CSAR measurements (one standard uncertainty).**

## 4.2 Comparison of CSAR with the World Radiometric Reference

Arguably the most important measurement that can be performed with CSAR is the comparison with the World Radiometric Reference. For this purpose, CSAR was mounted on the same solar tracker as the instruments of the World Standard Group. Figure 138 shows the author with Swiss colleagues during the installation of CSAR, and Figure 139 shows CSAR on the tracker, together with instruments of the World Standard Group and other radiometers.

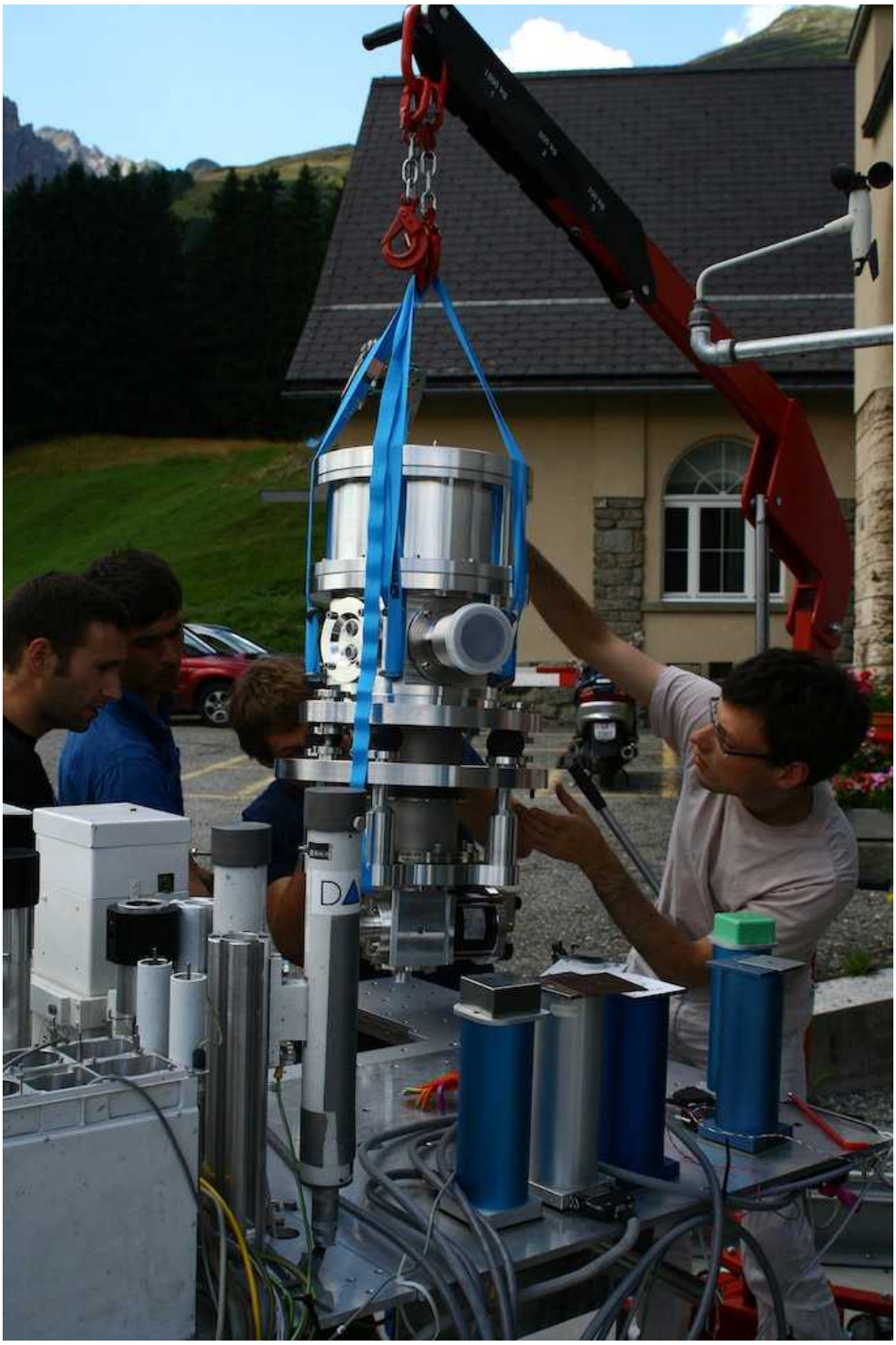

**Figure 138 Installation of CSAR on the solar tracker at the World Radiation Center in Davos. Although the picture shows a vertical installation, in the end, it was found more practical to install the instrument horizontally.**

**Figure 139 CSAR on the solar tracker with World Standard Group instruments.**

In total, measurements were made on seven separate days in the time period from 27 Jan 2011 – 8 Mar 2011. In order to verify the validity of the measurement, three different measurement setups were used:

1. The first three measurements were made using fused silica windows, and using superconducting $MgB_2$-wires connecting the cavity heater.
2. Measurement on measurement days 4 and 5 were made using fused silica windows and copper wires connecting the cavity heater.
3. Measurement on measurement days 6 and 7 were made using sapphire windows and copper wires connecting the cavity heater.

All measurements were performed under very good measurement conditions. The Aerosol Optical Density was in all cases < 0.3.

Figure 140 shows the individual measurement results, together with an overall measurement result. All individual measurements are consistent with each other. The overall measurement result is that the World Radiometric Reference (WRR) - as represented by the World Standard Group (WSG) - is measuring 0.309% higher than CSAR[78]; the standard uncertainty associated with this result is 0.028%[79].

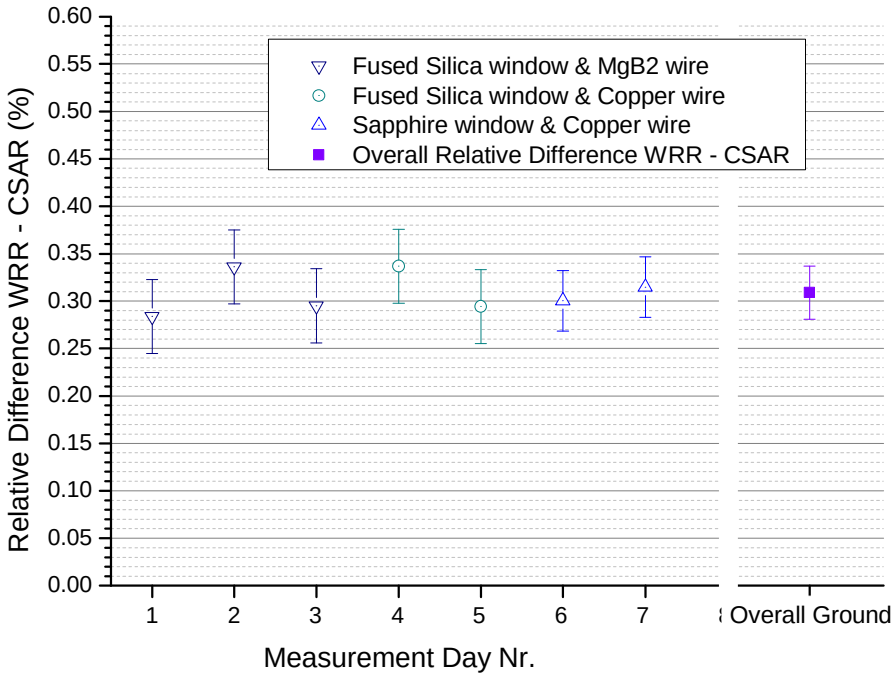


**Figure 140 Relative Difference between CSAR and the World Radiometric Reference. The error bars are indicative of the standard uncertainties of the measurements.**

[78] This is a weighted mean calculated according to the procedure outlined in Appendix H.
[79] Most measurements taken on the seven different days are highly correlated. The only change in the measurement setup that can potentially have a significant impact on the uncertainty estimate is the use of the two different windows. Therefore, a weighted window transmittance uncertainty was calculated according to Equation (A.31) in Appendix H: 1/[1/(0.026%)^2+1/(0.035%)^2]^0.5=0.021%. Combining this uncertainty with the rest of the uncertainties in the uncertainty budget (see Table 24 in Section 3.8), which is equivalent to 0.018%, the resulting standard uncertainty is [(0.021%)^2+(0.018%)^2]^0.5=0.028%.

Figure 141 shows the results presented according to the three measurement setups described above. It shows that neither the use of Fused Silica vs. Sapphire as window materials, nor the use of superconducting $MgB_2$ vs. Copper as current-carrying cavity heater wires makes a statistically relevant difference. This indicates that the effects are well understood and that they have either been made insignificant by design (as in the case of the heater wires) or that they have been adequately corrected for (as in the case of the window transmittance).

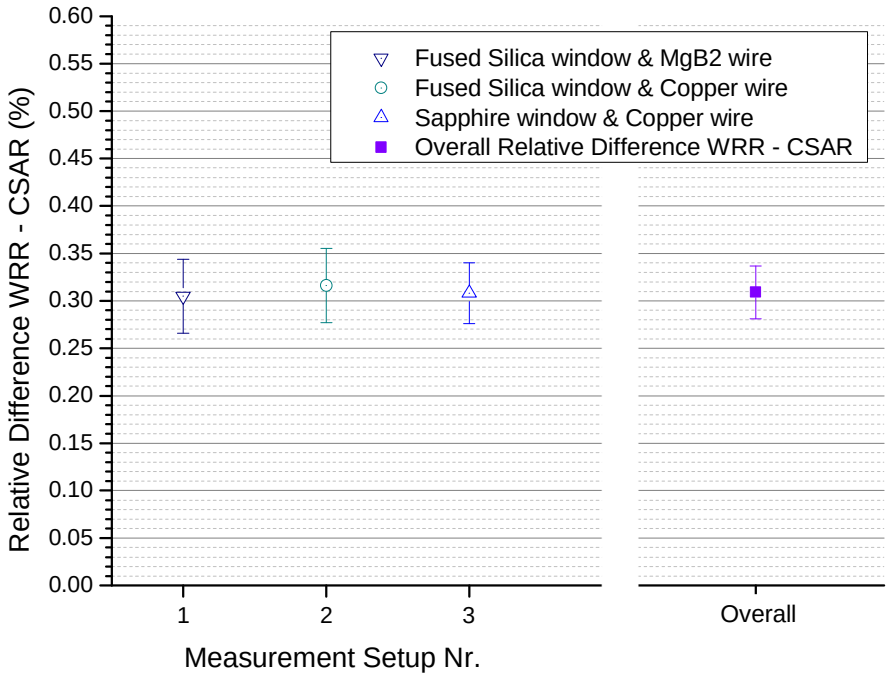


**Figure 141 Comparison Results according to different types of measurement setup.**

# Chapter 5 Discussion and Conclusions

During the five years of this PhD project, various science teams have made significant efforts towards improving the understanding of Solar Irradiance measurements. Section 5.1 attempts to place the CSAR results in the context of the most relevant recent developments in the field, with a particular focus on the space-based measurement of Total Solar Irradiance.

Section 5.2 points out the future steps that are required in order to establish CSAR as the new Solar Irradiance standard.

## 5.1 Resolving the offsets in the Total Solar Irradiance record

The historic satellite-based record of Total Solar Irradiance measurements revealed significant offsets between different radiometers, and therefore indicated a possible lack of understanding of the underlying physics. Figure 142 shows the Total Solar Irradiance record of the various space experiments as it was at the beginning of this PhD project – this figure was already discussed in the introductory chapter.

**Figure 142 Satellite-based TSI record of the last three decades. Plot reproduced from (Kopp and Lean, 2011).**

Figure 143 shows annual averages of the relative difference between the space experiments VIRGO and TIM; the difference is in the interval ranging from 0.300% to 0.306% over the last nine years[80].

[80] As far as the historic situation in 2003 is concerned, the ACRIM data are not included in this discussion about absolute measurement uncertainties. This is because the ACRIM data were, until very recently, not even corrected for the diffraction effect; this effect has been commonly known to be relevant for applied radiometry at least since the 1970s. Reading their webpage also gives the impression that the ACRIM team seemed - at least in the past - much more concerned with relative changes of Solar Irradiance than with absolute accuracy. This is evidenced by the following quote: "A TSI monitoring strategy that relies on 'absolute uncertainty' for its long term traceability cannot provide the long term traceability required by a TSI database for climate change on centennial time scales." (www.acrim.com, website accessed 30 September 2012).
However, in the very recent past, the ACRIM team have made an effort to link their measurements to the SI system. This fact will be considered in the following discussion.

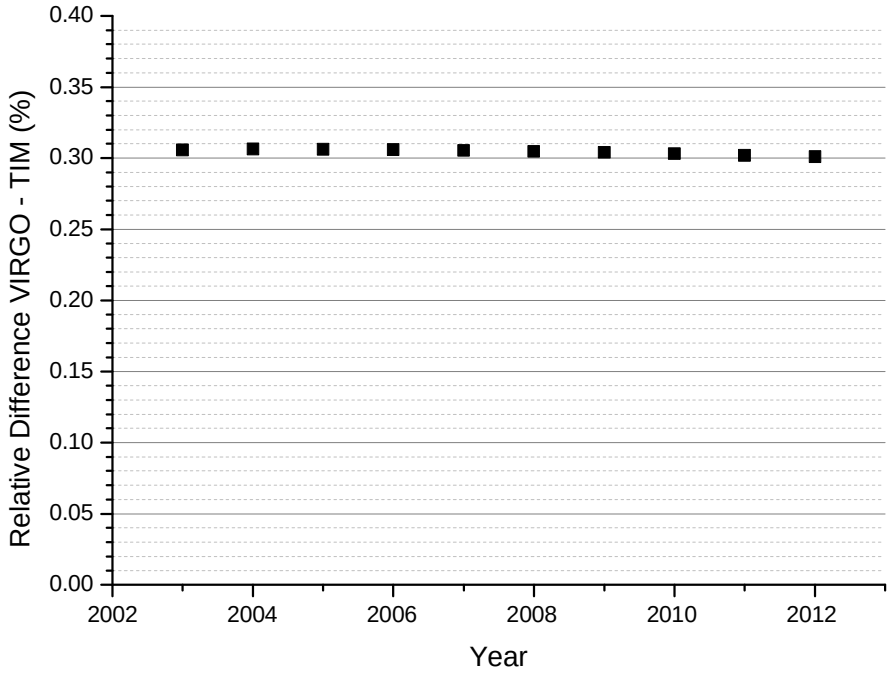


**Figure 143 Relative Difference VIRGO/SOHO – TIM/SORCE**

In 2003, the year of the TIM/SORCE launch, TIM was arguably the Total Solar Irradiance radiometer associated with the best characterisation at the component level. The TIM flight instrument was calibrated traceably to the SI scale, and it was found to agree with the SI scale within the quoted uncertainties (Kopp and Lean, 2011). VIRGO on SOHO, on the other hand, derives its absolute calibration from the WRR[81].

It needs to be stated clearly that this is in contrast to the publications associated with VIRGO, which do not make this link of VIRGO to the WRR obvious; in the publications, it is rather suggested that VIRGO is traceable to the SI [see (Fröhlich et al., 1995) and (Fröhlich et al., 1997)]. This is understandable in the historical context,

[81] Personal communication with André Fehlmann, PMOD/WRC, 26 Jun 2012.

since the comparisons of WRR and the SI-system based on radiant power measurements (i.e. measurements with a beam that is under-filling the defining aperture) yielded no statistically significant difference; however, since it is now evident that there is a significant difference between WRR and SI, it needs to be pointed out very clearly that VIRGO derives its calibration from the WRR. Otherwise, future researchers may be confused by the published literature.

As long as no significant difference could be found between the SI-system and the WRR when measuring radiant power (i.e. underfilling the defining aperture), it was assumed without any further testing that the measurement of irradiance with the WRR was also consistent with the SI-system. Hence, the 0.3% difference between TIM and VIRGO could not be explained. One very reasonable conclusion was that the calibration of the radiometers may be lost during launch.

However, in the meantime, it has – independently from the CSAR results – been shown that there is a difference between SI and WRR when measuring irradiance (i.e. when the optical beam overfills the defining aperture). Fehlmann et al. have made an irradiance comparison of the PREMOS-3 radiometer with the SI-system by using the newly developed "TSI Radiometer Facility (TRF)" (Kopp et al., 2007). The TSI Radiometer Facility allows the irradiance-mode[82] comparison of solar radiometers with an SI-traceable cryogenic radiometer; the comparison is performed under vacuum, and using monochromatic laser light. This comparison revealed a significant stray light component that had previously not been accounted for. The same PREMOS-3 radiometer was then also compared with the WRR

[82] "Irradiance mode" means that the entrance aperture of the radiometers are overfilled with the optical beam.

on the solar tracker in Davos; together with the result of the comparison of PREMOS-3 with the SI, these tests allow a determination of the relative difference between WRR and SI under irradiance conditions. This difference was found to be 0.3358%, where the WRR measures higher than the SI; the associated standard uncertainty of this result is 0.0923%.

Figure 144 summarises the various comparisons between WRR-scale-based and SI-scale-based measurements. This figure shows the result of the comparison of the WRR to the SI via CSAR, alongside with the comparison of WRR to the SI via the TSI Radiometer Facility (TRF), and the relative difference between VIRGO and TIM[83]. It can be concluded that the CSAR result is in agreement with the TRF result within the stated uncertainties. Furthermore, as much as TIM can be seen as representative of the SI scale in space, and as much as VIRGO can be seen as a representation of the WRR scale in space, their difference is also in agreement with the difference between the WRR and the SI on the ground. In summary, it can therefore be said that (1) the WRR-CSAR comparison result has been verified independently (albeit by a measurement with a larger associated uncertainty), and that (2) the WRR-CSAR comparison offers a plausible explanation for the observed difference between VIRGO/SOHO and TIM/SORCE.

[83] While the TIM flight instrument was not originally calibrated to the SI on a system level, it was very well characterised on a component level. In addition, the fact that the flight-spare instrument agrees with the SI on a system-level within the stated uncertainties indicates that the TIM flight radiometer is also likely to be in agreement with the SI. In summary, the TIM data are the best substitute for SI-based TSI measurements – since the TIM/GLORY experiment was launched unsuccessfully and since the PREMOS data have not been officially released as yet.

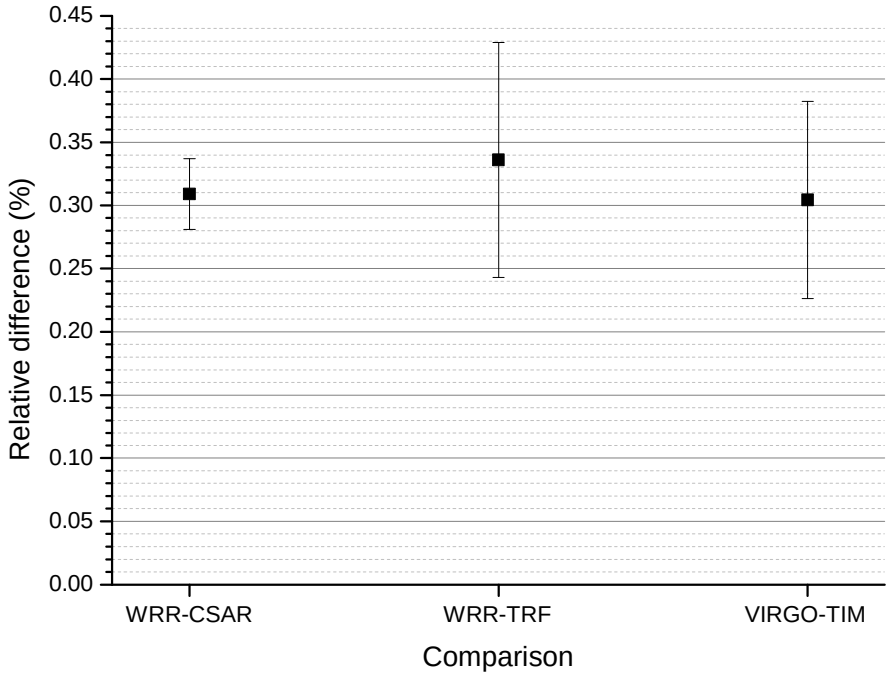


**Figure 144 Relative differences between (a) WRR & CSAR, (b) WRR & TRF, and (c) VIRGO/SOHO & TIM/SORCE.**

In the following, the impact of correcting the VIRGO data for the observed difference between the WRR and the SI is discussed.

Figure 145 shows the VIRGO measurements corrected by the offset found as a result of the WRR-CSAR comparison[84]; also shown are the TIM[85] results. Please note that the y-axis of this figure is the same as that of Figure 142. Especially in the first few years of the TIM mission, the two curves agree extremely well; in the latter years they are drifting apart very slightly, but well within the respective uncertainties. Figure 145 also shows the corrected ACRIM3[86] results (the ACRIM team have added a diffraction correction, as well as corrections following a comparison with the TRF, in addition to other scale adjustments).

[84] The VIRGO data-set used here are the VIRGO level 2.0 data from virgo_tsi_d_v6_002_1204[1].dat, kindly made available by the VIRGO team, PMOD/WRC, Davos, Switzerland.
[85] The TIM data-set used here are the TSI@1AU level 3 TIM data from sorce_tsi_L3_c24h_latest.txt, kindly made available by the TIM team, LASP, Colorado, USA.
[86] The ACRIM3 data-set used here is taken from the "ACRIM3 Results (Time Series of Daily Means – Table), Last Update:11/11, Version 11/11, kindly made available by the ACRIM Science Team, Coronado, USA

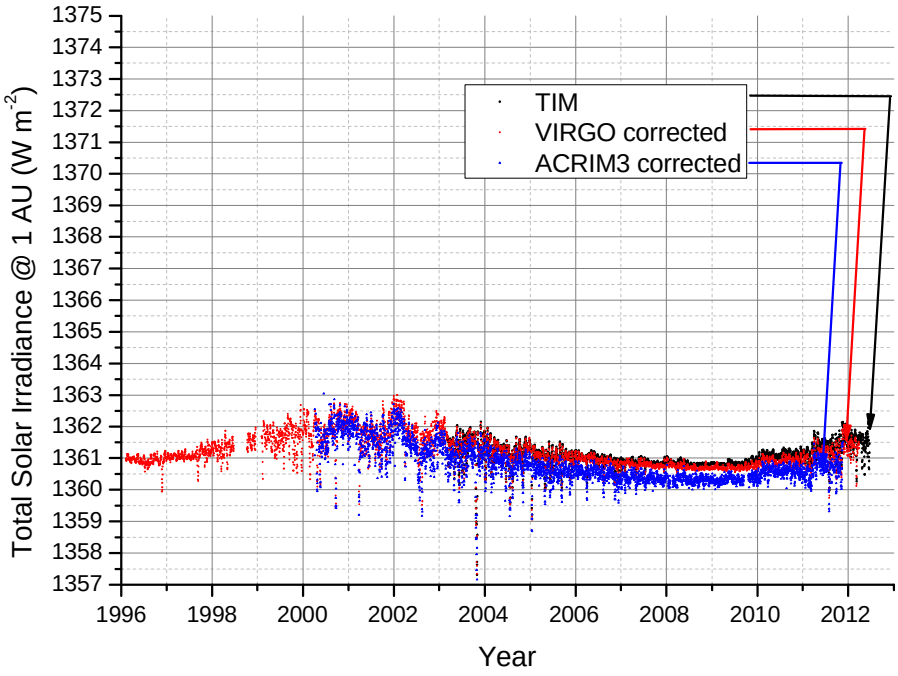


**Figure 145 Adjusted Total Solar Irradiance data from space experiments[87].**

Figure 146 shows the relative difference of the TIM and the ACRIM3 data with respect to the corrected VIRGO data. Figure 147 is based on the same data as Figure 146, but this time the data is shown as a moving average of 365 days. Figure 147 shows that the ACRIM3 instrument was reading approximately 0.01% lower than the corrected VIRGO at the beginning of the mission in 2000 and that this offset increases to approximately 0.035% by the end of 2002. Since 2003, ACRIM3 reads consistently lower than the corrected VIRGO; the offset is within a range between 0.025% and 0.035%.

Figure 147 also shows the relative difference between TIM and the corrected VIRGO readings. In the first three years of the mission,

[87] In a more general context, this graph clearly shows the well-known 11-year cycle that is due to the periodically varying solar activity, and it shows furthermore the well-known fact that the Total Solar Irradiance measurements are much less noisy during solar minima than during solar maxima.

i.e. from 2003 to 2006, TIM was reading consistently very slightly higher than VIRGO (by less than 0.005% on average). In the time period from 2005 to 2012, the readings of TIM and VIRGO progressively drifted further apart, with TIM reading higher by approximately 0.002% in 2005 and TIM reading higher by 0.017% at the beginning of 2012. This is equivalent to a linear drift of approximately 0.025% per decade.

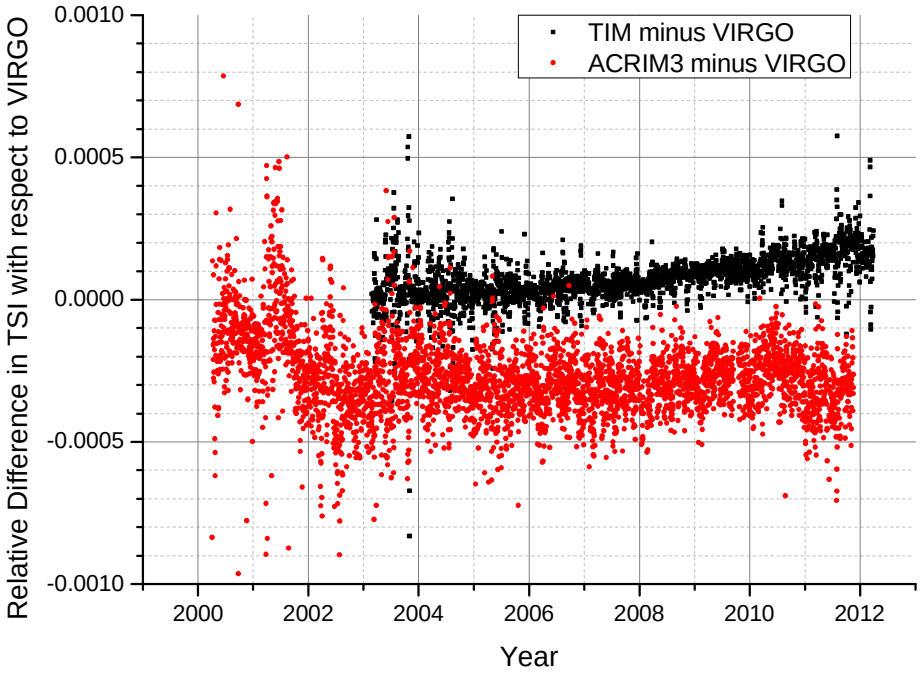


**Figure 146 Relative difference of TIM and ACRIM3 with respect to the corrected VIRGO data. Daily values.**

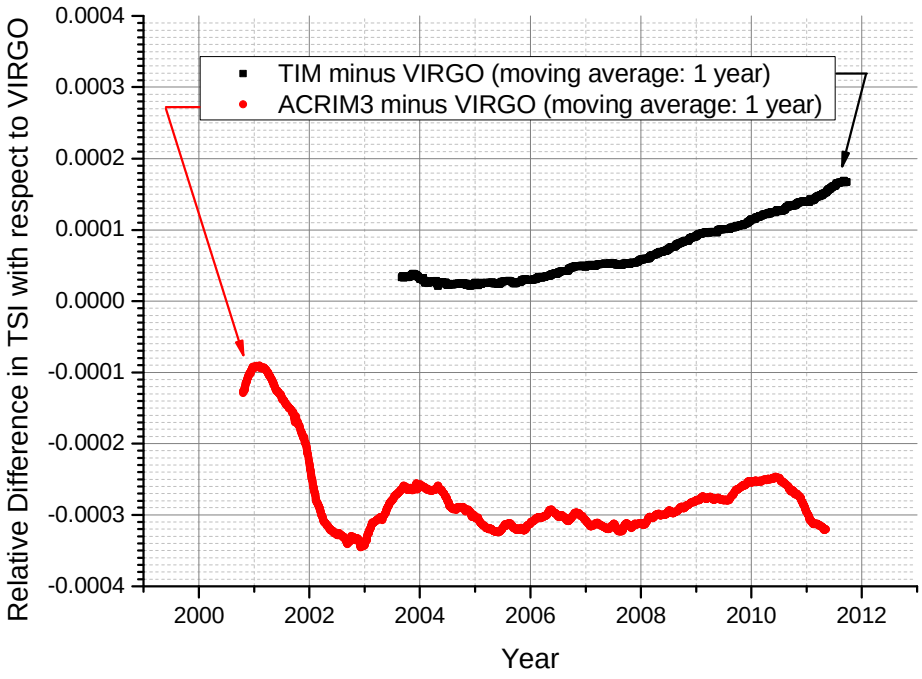


**Figure 147 Relative difference of TIM and ACRIM3 with respect to the corrected VIRGO data. Moving average: 365 days.**

Figure 147 is very interesting. Maybe its most striking feature is that at the beginning of the respective measurement recordings, both ACRIM3 and TIM agree very well with the VIRGO data which were corrected for the difference between CSAR and the WRR; only in subsequent years, the ACRIM3 and TIM records start drifting away from VIRGO. However, at no point during the record do the instruments differ significantly based on the respective stated uncertainties and a confidence level of 95%.

It is worth noting that the three datasets used in Figure 147 rely on three different calibration chains for their absolute accuracy; TIM relies on the calibration of subcomponents and the instrument design, the corrected ACRIM3 data rely on the correction applied on the basis of the TSI Radiometer Facility which – for the first time – allows an

evaluation of the stray light effect caused by overfilling the entrance aperture, and the corrected VIRGO data rely on the correction of the World Radiometric Reference for its offset with respect to CSAR and on degradation models of the TSI radiometers. The fact that all three radiometers agree within their stated uncertainties indicates that the applied calibrations are valid and that the radiometers are capable of transferring their ground-calibration to space.

It is encouraging that the newly developed end-to-end ground-calibration techniques have now reached a level of sophistication which leads to the space radiometers agreeing within their stated uncertainties. However, these stated uncertainties significantly exceed the desired absolute uncertainty of 0.01% in the case of all currently operating space radiometers, especially because the corrections have been applied in retrospect. In the case of ACRIM, the current correction is based on the calibration of a flight-spare instrument. And the VIRGO correction by the CSAR-WRR difference relies on the long-term stability of the WRR (which has been demonstrated, but only at the 0.1% uncertainty level). It can be expected that future space experiments will benefit to a larger extent from the new end-to-end calibration techniques than existing experiments. Direct comparison of the Solar Irradiance radiometers in a vacuum environment against CSAR on the solar tracker or comparison against the Total Solar Irradiance Radiometer Facility can both potentially lead to end-to-end calibrations approaching uncertainty levels of 0.01%.

TIM on SORCE is the only currently operating space instrument which does not rely on an end-to-end calibration, but a calibration at component level. While the uncertainty of the current TIM is 0.035%, the technology has been improved in the meantime, allowing this

uncertainty to be reduced to 0.01%; these improvements would have taken effect with a new TIM on the GLORY mission which unfortunately did not reach orbit. The next TIM will fly on NPOESS-C2, scheduled for launch in 2013.

Apart from absolute uncertainty, the other requirement that space radiometers should ideally fulfil is that of long-term stability of approximately 0.01% per decade. Not all of the currently operating space radiometers fulfil this requirement. Figure 147 does not provide conclusive evidence as to the cause for the relative drifts, i.e. which one of the three radiometers is drifting. However, the conclusion that can be drawn at this stage is that at least two of the three radiometers are drifting significantly. More specifically it can be said that either TIM is drifting in the time period from 2006 to 2012, or VIRGO and ACRIM3 are both drifting in a similar way during this time period, or all three radiometers are drifting. It can be argued that TIM is less likely to be drifting than VIRGO and ACRIM3 due to TIM's lower cavity reflectivity, but it would be interesting to compare TIM to a radiometer of a similar or better quality.

In conclusion it can be said that none of the currently operating radiometers fully meets the requirements of climate science. Only the improved version of TIM (which was on the failed GLORY payload and which will be part of NPOESS-C2) is likely to fulfil all requirements in terms of absolute accuracy and long-term stability. The improved end-to-end calibration techniques will bring the absolute uncertainty of the other space radiometers (of the type currently used on VIRGO and of the ACRIM-type) much closer to the required 0.01% level, but the long-term stability requirement will still

not be met if no significant improvements are made to the radiometers.

A space version of CSAR is likely to perform at a similar level as - or better than - the improved TIM. It would be interesting to have two different instrument types in space that fulfil all the requirements of climate science; if they agreed with each other, it would be convincing evidence that the issues around Total Solar Irradiance measurements have been solved satisfactorily.

## 5.2 Future Work

In this thesis I have presented the first evidence for the suitability of CSAR as a potential future replacement of the World Radiometric Reference. I also hope to have given some evidence – although not conclusive evidence – for the feasibility of using the instrument in space, and thereby making a valid contribution to meeting the needs of climate science with respect to Total Solar Irradiance measurements.

The estimated uncertainties of CSAR are only slightly larger than the uncertainty goals of 0.01% for Total Solar Irradiance and 0.03%[88] for Direct Solar Radiation. In the case of the Direct Solar Radiation, the uncertainty can relatively easily be made lower by controlling the temperature of the apertures, and thereby reducing the aperture area uncertainty significantly. This was originally planned, but the temperature control was not implemented due to time restrictions. Furthermore, window materials with a broader range of spectral transmittance may also yield lower uncertainties. And finally, the development of a dedicated transmission monitor (rather than a

[88] This is the uncertainty aim for the measurement results of a single day.

modified PMO6 as used for the work here) may further reduce the overall uncertainty.

In an effort to further improve the instrument, the development of a custom-made measurement and control electronics is currently underway; it should make CSAR a much more user-friendly instrument than it is currently. This new electronics is also expected to read the temperature values much quicker than the Tinsley bridges used for the purpose of this thesis, and therefore, the control of the reference block should be improved, and it should allow the operation of the TSI cavities as 'active' cavities (i.e. held stable at one temperature level). With the new electronics, CSAR could also be operated in phase-sensitive mode, which would significantly decrease the measurement time.

CSAR needs to go through a validation process over the next 5-10 years before it can be formally introduced as the primary SI standard for Solar Irradiance.

In the near future, CSAR will be fitted with high sensitivity cavities, with the intent of making it a suitable reference standard for calibrating earth-observing systems as outlined in (Fox et al., 2011). And as a next step regarding the demonstration of space-worthiness, the intermediate stage could be operated at 120 K, and the results compared to the results obtained with the intermediate stage operating at 50 K. However, in order to conclusively prove the space-worthiness of CSAR, the instrument would need to undergo qualification testing for space; for example, vibration testing and exposure to thermal vacuum.

# Appendix A Solar Spectral Irradiance at the top of the atmosphere

The idealised Solar Spectral Irradiance $I_{SI}(\lambda,T)$ at the top of the atmosphere is given by the relation

$$I_{SI}\left(\lambda,T_{Sun}\right)=\Omega\times L_{BB}\left(\lambda,T_{Sun}\right) \qquad \text{(A.1)}$$

where

$\Omega$ is the solid angle between the Sun and the Earth,

$L_{BB}$ is the radiance of an ideal blackbody,

$T_{Sun}$ is the effective temperature of the Sun, and

$\lambda$ is the wavelength of the electromagnetic radiation emitted by the Sun.

## A.1 Solid angle / Radiative transfer between Sun and Earth

When a light emitting source of radius $r_s$ is at a distance $d$ from a detector of radius $r_d$, and source and detector are normal to and centred around the same optical axis, the solid angle $\Omega$ between them is given by the following relation:

$$\Omega=\frac{2\pi r_s^2}{r_s^2+r_d^2+d^2+\sqrt{\left(r_s^2+r_d^2+d^2\right)^2-4r_s^2r_d^2}} \qquad \text{(A.2)}$$

Substituting the observational values of the solar radius, the radius of the Earth, and the mean distance between Sun and Earth for $r_s$, $r_d$, and d respectively, yields a solid angle of $6.79\times10^{-5}$ sr for the radiative transfer from the Sun to the Earth.

## A.2 Blackbody radiation

The radiance of an ideal blackbody $L_{BB}$ is a function of wavelength $\lambda$ of the electromagnetic radiation and temperature $T$ and is given by

$$L_{BB}(\lambda, T) = \frac{2hc^2}{\lambda^5} \frac{1}{e^{\left(\frac{hc}{\lambda kT}\right)} - 1} \qquad \text{(A.3)}$$

where

$h$ is the Planck constant,

$c$ is the speed of light, and

$k$ is the Boltzmann constant.

## A.3 Effective temperature of the Sun

This appendix gives further information about how some numbers given in Section 2.5.3 were derived.

The effective temperature of the Sun is the temperature of an ideal blackbody with the same emissive power as the Sun. The Stefan-Boltzmann law states that

$$\frac{P_{Sun}}{A_{Sun}} = \sigma T_{Sun}^4 \qquad \text{(A.4)}$$

where

$P_{Sun}$ is the total power emitted by the Sun,

$A_{Sun}$ is the surface area of the Sun,

$T_{Sun}$ is the effective temperature of the Sun, and

$\sigma$ is the Stefan-Boltzmann constant.

The Total Solar Irradiance ($I_{TSI}$) measured at the top of the atmosphere is can be expressed as

$$I_{TSI} = \frac{P_{Sun}}{4\pi r^2_{Sun-Earth}} = \frac{A_{Sun}\sigma T^4_{Sun}}{4\pi r^2_{Sun-Earth}} = \frac{r^2_{Sun}}{r^2_{Sun-Earth}}\sigma T^4_{Sun} \qquad \text{(A.5)}$$

where

$r_{Sun\text{-}Earth}$ is the mean distance between the Sun and the Earth,

$r_{Sun}$ is the radius of the Sun.

Therefore, the effective blackbody temperature of the Sun is

$$T_{Sun} = \sqrt[4]{\frac{1}{\sigma}\frac{r^2_{Sun-Earth}}{r^2_{Sun}} I_{TSI}} \qquad \text{(A.6)}$$

# Appendix B Theoretical distribution of spectral cavity reflectivity

In this appendix, the derivation of Equation (2.30) in section 2.5.3 is given.

The spectral cavity reflectivity $\rho(\lambda)$ can be expressed as

$$\rho(\lambda) = 1 \cdot \rho(\lambda) \tag{A.7}$$

or,

$$\rho(\lambda) = \frac{\int_0^\infty J(\lambda)d\lambda}{\int_0^\infty \rho(\lambda)\cdot J(\lambda)d\lambda} \cdot \frac{\int_0^\infty \rho(\lambda)\cdot J(\lambda)d\lambda}{\int_0^\infty J(\lambda)d\lambda} \cdot \rho(\lambda) \tag{A.8}$$

Using Equation (2.24), Equation (A.8) can be expressed as

$$\rho(\lambda) = \frac{\int_0^\infty J(\lambda)d\lambda}{\int_0^\infty \rho(\lambda)\cdot J(\lambda)d\lambda} \cdot \rho \cdot \rho(\lambda) \tag{A.9}$$

or,

$$\rho(\lambda) = \frac{\int_0^\infty J(\lambda)d\lambda}{\int_0^\infty \rho(\lambda)\cdot J(\lambda)d\lambda} \cdot \rho(\lambda) \cdot \rho \tag{A.10}$$

If $\rho(\lambda)$ is directly proportional to $[J(\lambda)]^a$, then

$$\rho(\lambda) = \frac{\int_0^\infty J(\lambda)\,d\lambda}{\int_0^\infty C \cdot \left[J(\lambda)\right]^a \cdot J(\lambda)\,d\lambda} \cdot C \cdot \left[J(\lambda)\right]^a \cdot \rho \quad \text{(A.11)}$$

where C is a constant.

Equation (A.11) is equivalent to

$$\rho(\lambda) = \frac{\int_0^\infty J(\lambda)\,d\lambda}{C \cdot \int_0^\infty \left[J(\lambda)\right]^a \cdot J(\lambda)\,d\lambda} \cdot C \cdot \left[J(\lambda)\right]^a \cdot \rho \quad \text{(A.12)}$$

which leads to the relation that was to be proven:

$$\rho(\lambda) = \frac{\int_0^\infty J(\lambda)\,d\lambda}{\int_0^\infty \left[J(\lambda)\right]^a \cdot J(\lambda)\,d\lambda} \cdot \left[J(\lambda)\right]^a \cdot \rho \quad \text{(A.13)}$$

# Appendix C Solar Spectral Irradiance in Davos

Figure A - 1 shows a MODTRAN-generated solar spectrum for Davos, Switzerland. Davos is where the World Radiation Center / Physikalisch-Meteorologisches Observatorium Davos (WRC/PMOD) is located. There is no significant radiation at wavelengths below 300 nm (of the order of 5 ppm, see Table A - 1) and there is no significant radiation above 15 µm (see Table A - 2). The greatest part – or 99.64% - of the sunlight is in the wavelength range from 300 nm to 4 µm.

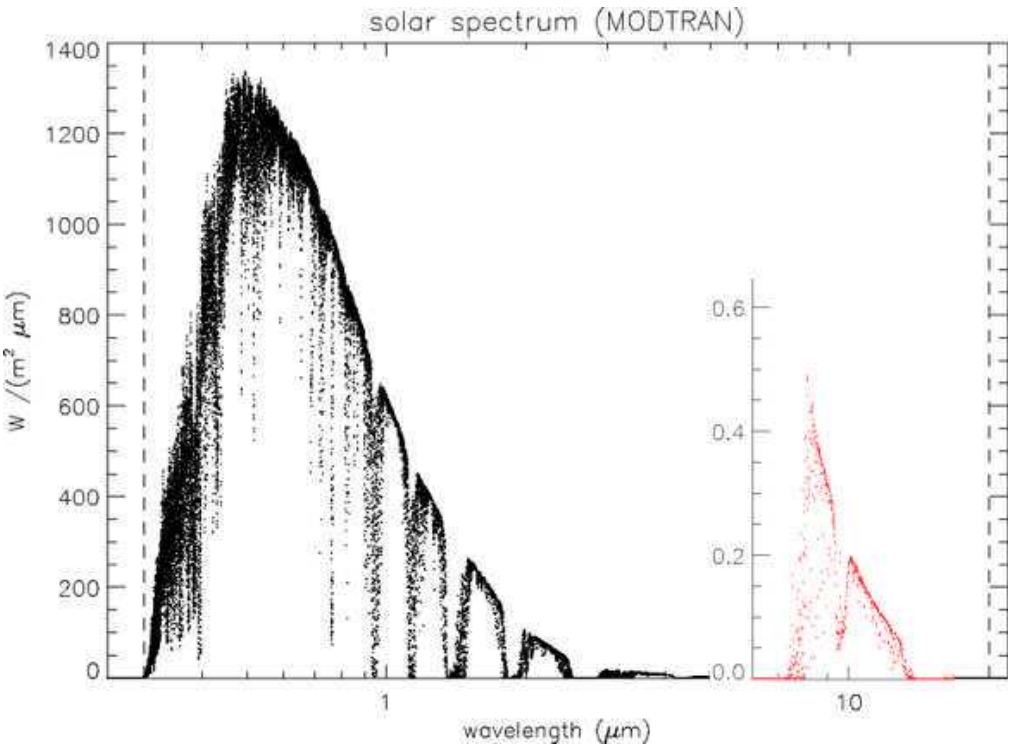


**Figure A - 1 Solar Spectrum on the ground (Davos)[89]**

[89] Figure courtesy of André Fehlmann, PMOD/WRC

**Table A - 1 Calculated fraction of the Solar Irradiance being irradiated below certain cut-on wavelengths. Table courtesy of PMOD/WRC.[90]**

| Cut-on wavelength in µm | Fraction of TSI below cut on in ppm |
|---|---|
| 0.29 | $6.7 \cdot 10^{-5}$ |
| 0.3 | 5 |
| 0.31 | 260 |
| 0.32 | $1.5 \cdot 10^{3}$ |
| 0.33 | $4.0 \cdot 10^{3}$ |

**Table A - 2 Calculated fraction of the Solar Irradiance being irradiated above certain cut-off wavelengths[91]**

| Cut-off wavelength in µm | Fraction of TSI above cut off in ppm |
|---|---|
| 4 | $3.6 \cdot 10^{3}$ |
| 5 | $1.3 \cdot 10^{3}$ |
| 6 | $1.1 \cdot 10^{3}$ |
| 7 | $1.1 \cdot 10^{3}$ |
| 8 | $1.0 \cdot 10^{3}$ |
| 9 | 640 |
| 10 | 450 |
| 15 | 6 |
| 20 | 0.3 |

[90] Table courtesy of André Fehlmann, PMOD/WRC
[91] Table courtesy of André Fehlmann, PMOD/WRC

# Appendix D Theoretical spectral hemispherical emissivity

In order to estimate the spectral hemispherical emissivities of the cold shield surfaces, the model presented by Tsujimoto et al. [(Tsujimoto et al., 1982), Equations(1)-(4)] is used to calculate the wavelength- and temperature-dependent complex refractive index of the surface. The temperature dependence of the complex refractive index is estimated using measured values of the temperature dependence of the electrical resistivity of the material. The complex refractive index is then used to determine the temperature-dependent spectral hemispherical emissivity. Further detail regarding these calculations can be found in this appendix.

## D.1 The complex refractive index as a function of wavelength and temperature

Tsujimoto et al. use the Roberts equation (Roberts, 1959) in order to determine the complex refractive index $n-ik$:

$$\left(n-ik\right)^2 = 1+\sum_j^n \frac{K_{bj}\lambda^2}{\lambda^2-\lambda_{bj}^2+i\delta_{bj}\lambda_{bj}\lambda} - \frac{\lambda^2\sigma_0}{2\pi c\varepsilon_0\left(\lambda_{\tau 0}-i\lambda\right)} \quad \text{(A.14)}$$

where

$K_{bj}$ is the oscillation intensity of the j[th] bound electron,

$\lambda_{bj}$ is the resonance wavelength of the j[th] bound electron,

$\delta_{bj}$ is the parameter for oscillation damping for the j[th] bound electron,

$\sigma_0$ is the optical dc conductivity,

$\lambda_{\tau 0}$ is the relaxation wavelength of the conduction electrons,

$\varepsilon_0$ is the dielectric constant of vacuum,

$c$ is the velocity of light in vacuum, and

$\lambda$ is the wavelength of light in vacuum.

The optical dc conductivity $\sigma_0$ can also be expressed as:

$$\sigma_0 = \frac{Ne^2\tau_0}{m^*} \tag{A.15}$$

where

$\tau_0$ is the optical relaxation time,

$N$ is the number density of conduction electrons,

$e$ is the electric charge of an electron, and

$m^*$ is the effective mass of a conduction electron.

The relaxation wavelength $\lambda_{\tau 0}$ can be expressed as:

$$\lambda_{\tau 0} = 2\pi c\tau_0 \tag{A.16}$$

Furthermore the following equation holds:

$$\frac{1}{\tau_0} = \frac{1}{\tau_{dc}} + \frac{1}{\tau_s} \tag{A.17}$$

which gives the relationship between the optical relaxation time $\tau_0$, the relaxation time due to additional scattering at the surface layer $\tau_s$,

and the collision frequency $1/\tau_s$. $\tau_{dc}$ can be determined through the following relationship:

$$\tau_{dc} = \sigma_{dc} \frac{m^*}{Ne^2} \tag{A.18}$$

where $\sigma_{dc}$ is the electrical dc conductivity.

In the Tsujimoto model, $K_{bj}$, $\lambda_{bj}$, $\delta_{bj}$, and $N/m^*$ are assumed to be independent of temperature. However, the electrical conductivity $\sigma_{dc}$ does change with temperature, which means according to Equation (A.18) that $\tau_{dc}$ also changes with temperature. This in turn implies a temperature dependence of $\tau_0$ via Equation (A.17) and this leads to a temperature dependence of $\lambda_{\tau 0}$ (see Equation (A.16)) and $\sigma_0$ (see Equation (A.15)). The temperature dependence of $\lambda_{\tau 0}$ and $\sigma_0$, finally, lead to temperature dependence of the complex refractive index $n - ik$.

The CSAR cold shields are manufactured from the aluminium alloy Al6082. The temperature dependence of the electrical dc conductivity for this specific aluminium alloy was deduced from the published literature and manufacturer data, since no direct measurement of its behaviour at cryogenic temperatures seems to be publicly available.

Clark et al. report measurement values for the electrical resistivity of various aluminium alloys in the temperature range from 4 K to 273 K (Clark et al., 1970). The results can be seen in Figure A - 2. It may be observed that all the graphs for the various different alloys have approximately the same shape, regardless of composition or heat

treatment. This has also been noted by Clark et al. and they draw the conclusion that "from a simple room temperature measurement, one could quite reliably extrapolate the rest of the low temperature curve for similar or new aluminium alloys." In order to do that, the room temperature value of the electrical resistivity of Al6082 ($3.8\times10^{-8}$ Ω m, see (Azom.com, 2012)) was compared to the room temperature value of the electrical resistivity of Al6061(T6)[92], and the offset between the two was used to calculate the cryogenic temperature values for Al6082 from the measured values of Al6061(T6). And finally, the electrical conductivity is calculated as the inverse of the electrical resistivity.

[92] $4.175\times10^{-8}$ Ω m. This value was obtained by linear extrapolation of the data reported by Clark et al.

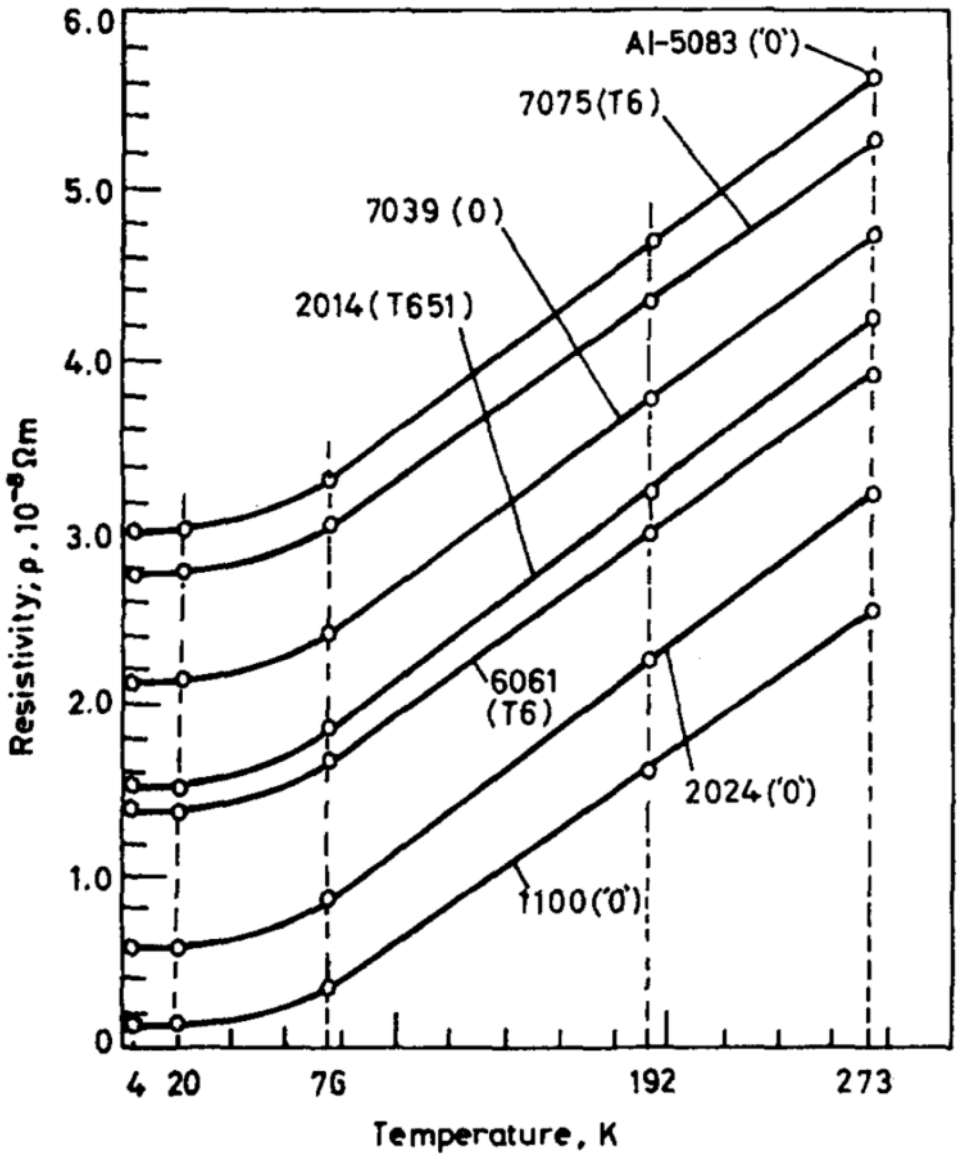


**Figure A - 2 Electrical resistivity of Aluminium alloys**

## D.2 Calculating the hemispherical emissivity from the complex refractive index

The temperature- and wavelength- dependent complex refractive index (that is derived as described in the previous section), can be used to calculate the hemispherical emissivity of the cold shield surfaces[93].

For a metal (with large extinction coefficient $k$) with an optically smooth surface and assuming the emission from the metal to be unpolarized, the emissivity $\varepsilon(\theta)$ in the direction of angle $\theta$ is given by Howell et al. (see (Howell et al., 2010), p.96):

$$\varepsilon(\theta) = \frac{\varepsilon_{\parallel}(\theta) + \varepsilon_{\perp}(\theta)}{2} \qquad \text{(A.19)}$$

with

$$\varepsilon_{\parallel}(\theta) = \frac{4n\cos\theta}{\left(n^2 + k^2\right)\cos^2\theta + 2n\cos\theta + 1} \qquad \text{(A.20)}$$

and

$$\varepsilon_{\perp}(\theta) = \frac{4n\cos\theta}{\cos^2\theta + 2n\cos\theta + n^2 + k^2} \qquad \text{(A.21)}$$

The hemispherical emissivity $\varepsilon_H$ is obtained by integrating $\varepsilon(\theta)$ over the hemisphere (Howell et al., 2010):

$$\varepsilon_H = \int_0^1 \varepsilon(\theta)\, d\left(\sin^2\theta\right) \qquad \text{(A.22)}$$

[93] The hemispherical emissivity is also a function of wavelength and temperature. Henceforth, this fact is taken as understood for the rest of this section, even though the equations might not explicitly state this relationship. Otherwise the clarity of the presentation of the equations would suffer.

With the help of Mathematica, it is straightforward to solve this integral[94].

[94] The integral can be solved numerically, but Wolfram Mathematica 7 also finds the (rather lengthy) analytical solution.

# Appendix E Radiative heat transfer through clearances

Consider the case, where radiation exchange takes place between a room temperature blackbody and two infinitely extended parallel surfaces – one of the surfaces is at the temperature of the outer surface of the detector stage cold shield, and the second surface is at the temperature of the inner surface of the intermediate temperature stage cold shield.

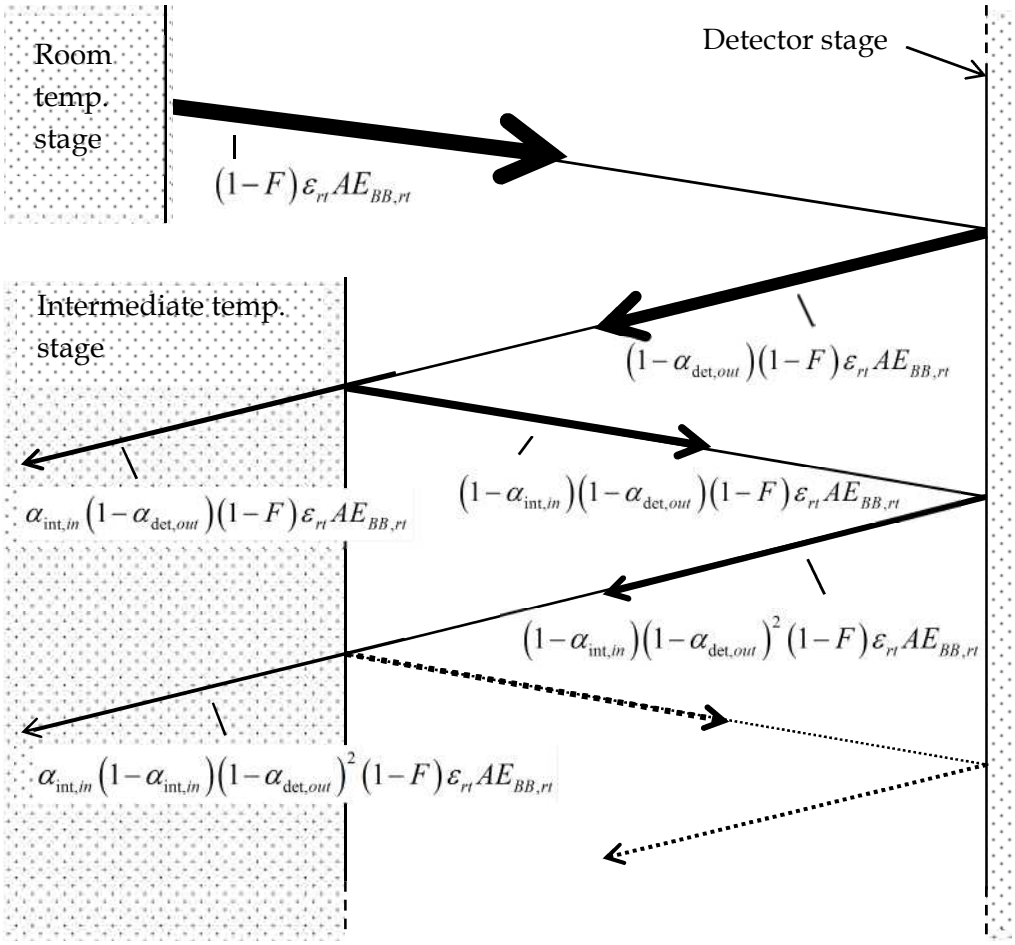


**Figure A - 3 Illustration of the radiative heat transfer from surface 1 to surface 2** [95]

The spectral radiative heat transfer $\dot{Q}_{1(rt->\mathrm{int},in),\lambda}(\lambda)$ from the room-temperature blackbody with entrance area $A$ to the inside of the intermediate cold shield can be expressed as[96]:

[95] The radiation emitted by surface 2 is not shown here.
[96] This is the radiation that originates from the room temperature blackbody, not the net radiation. The net radiation, which also takes into account the radiation of the intermediate cold shield, is considered below.

$$\dot{Q}_{1(rt->\mathrm{int},in)}(\lambda) = (1-F)\,\varepsilon_{rt,\lambda} A E_{BB,rt,\lambda} \sum_{n=1}^{\infty} \alpha_{\mathrm{int},in,\lambda} \left(1-\alpha_{\mathrm{int},in,\lambda}\right)^{n-1} \left(1-\alpha_{\mathrm{det},out,\lambda}\right)^{n}$$

(A.23)

The derivation of Equation (A.23) is illustrated in Appendix E. After evaluating the infinite sum[97], Equation (A.23) can be expressed as

$$\dot{Q}_{1(rt->\mathrm{int},in)}(\lambda) = (1-F)\,\varepsilon_{rt,\lambda} A E_{BB,rt,\lambda} \left(1-\frac{\alpha_{\mathrm{det},out,\lambda}}{\alpha_{\mathrm{int},in,\lambda}+\alpha_{\mathrm{det},out,\lambda}-\alpha_{\mathrm{int},in,\lambda}\alpha_{\mathrm{det},out,\lambda}}\right)$$

(A.24)

where

$(1-F)$ is the view factor that describes the fraction of the hemispherically emitted blackbody radiation that is "seen" by the cold shields,

$\varepsilon_{rt,\lambda}$ is the hemispherical emissivity of the room temperature stage at wavelength $\lambda$,

$\alpha_{\mathrm{int},in,\lambda}$ is the hemispherical absorptivity of the inner surface of the intermediate stage cold shield at wavelength $\lambda$,

$\alpha_{\mathrm{det},out,\lambda}$ is the hemispherical absorptivity of the outer surface of the detector stage cold shield at wavelength $\lambda$, and

$E_{BB,rt,\lambda}$ is the hemispherical emissive power of the room temperature blackbody.

So far, only radiation emitted by the room temperature blackbody was considered. The situation is equivalent for radiation originally emitted by the inner surface of the intermediate stage cold shield. For the

[97] The evaluation was carried out with 'Wolfram Mathematica 7.0 for Students'

purpose of this derivation, consider the case where the room temperature blackbody is at the same temperature as the intermediate cold shield. The radiative heat flow from the "room temperature blackbody" to the intermediate cold shield must in this case be equal to the radiative heat flow from the intermediate cold shield to the "room temperature blackbody". The spectral radiative heat flow from the intermediate cold stage to the room temperature blackbody is therefore:

$$\dot{Q}_{2(\text{int},in->rt)}(\lambda) = (1-F)\,\varepsilon_{rt,\lambda} A E_{BB,\text{int},\lambda}\left(1-\frac{\alpha_{\text{det},out,\lambda}}{\alpha_{\text{int},in,\lambda}+\alpha_{\text{det},out,\lambda}-\alpha_{\text{int},in,\lambda}\alpha_{\text{det},out,\lambda}}\right) \quad \text{(A.25)}$$

The net radiative transfer $\dot{Q}_{rt->\text{int},in}$ is given by:

$$\dot{Q}_{rt->\text{int},in} = \int_0^\infty \left[\dot{Q}_{1(rt->\text{int},in)}(\lambda) - \dot{Q}_{2(\text{int},in->rt)}(\lambda)\right] d\lambda \quad \text{(A.26)}$$

With all hemispherical surface emissivities equal to the respective hemispherical absorptivities, and using Equation (A.24) and Equation (A.25), Equation (A.26) leads to:

$$\dot{Q}_{rt->\text{int},in} = \int_0^\infty \left[(1-F)\,\varepsilon_{rt,\lambda} A\left(1-\frac{\varepsilon_{\text{det},out,\lambda}}{\varepsilon_{\text{int},in,\lambda}+\varepsilon_{\text{det},out,\lambda}-\varepsilon_{\text{int},in,\lambda}\varepsilon_{\text{det},out,\lambda}}\right)\left[E_{BB,rt,\lambda}-E_{BB,\text{int},\lambda}\right]\right] d\lambda \quad \text{(A.27)}$$

Note that the term $\left(1-\frac{\varepsilon_{\text{det},out,\lambda}}{\varepsilon_{\text{int},in,\lambda}+\varepsilon_{\text{det},out,\lambda}-\varepsilon_{\text{int},in,\lambda}\varepsilon_{\text{det},out,\lambda}}\right)$ in Equation (A.27) can be seen as the fraction of spectral radiation transferred to the inner surface of the intermediate temperature cold shield, due to the interreflection of the radiation between the two cold

shields. Since the remainder of the radiated energy must be transferred to the outside of the detector cold shield, the equivalent fraction for the cold shield is $1-\left(1-\frac{\varepsilon_{\text{det},out,\lambda}}{\varepsilon_{\text{int},in,\lambda}+\varepsilon_{\text{det},out,\lambda}-\varepsilon_{\text{int},in,\lambda}\varepsilon_{\text{det},out,\lambda}}\right)$, or $\frac{\varepsilon_{\text{det},out,\lambda}}{\varepsilon_{\text{int},in,\lambda}+\varepsilon_{\text{det},out,\lambda}-\varepsilon_{\text{int},in,\lambda}\varepsilon_{\text{det},out,\lambda}}$. The net radiative heat transfer from the room temperature stage to the outer surface of the detector stage cold shield is therefore:

$$\dot{Q}_{rt->\text{int},in} = \int_0^\infty \left[ (1-F)\varepsilon_{rt,\lambda} A \left( \frac{\varepsilon_{\text{det},out,\lambda}}{\varepsilon_{\text{int},in,\lambda}+\varepsilon_{\text{det},out,\lambda}-\varepsilon_{\text{int},in,\lambda}\varepsilon_{\text{det},out,\lambda}} \right) \left[ E_{BB,rt,\lambda} - E_{BB,\text{int},\lambda} \right] \right] d\lambda \quad \text{(A.28)}$$

# Appendix F View factor: Two rectangles in parallel planes

Consider the two rectangular areas $A_1$ and $A_2$, which lie in parallel planes at a distance $z$ (see Figure A - 4).

**Figure A - 4 Illustration of two areas in two parallel planes. Reproduced from (Howell, 2010).**

The view factor $F_{1-2}$ for radiative transfer from area $A_1$ to area $A_2$ is governed by the equations of configuration C13 in Howell's online catalogue of view factors (Howell, 2010):

$$F_{1-2} = \frac{1}{(x_2 - x_1)(y_2 - y_1)} \sum_{l=1}^{2} \sum_{k=1}^{2} \sum_{j=1}^{2} \sum_{i=1}^{2} (-1)^{(i+j+k+l)} G(x_i, y_j, \eta_k, \xi_l)$$

$$G = \frac{1}{2\pi} \left( \begin{array}{l} (y-\eta)\left[(x-\xi)^2 + z^2\right]^{1/2} \tan^{-1}\left\{ \dfrac{y-\eta}{\left[(x-\xi)^2 + z^2\right]^{1/2}} \right\} \\ +(x-\xi)\left[(y-\eta)^2 + z^2\right]^{1/2} \tan^{-1}\left\{ \dfrac{x-\xi}{\left[(y-\eta)^2 + z^2\right]^{1/2}} \right\} \\ -\dfrac{z^2}{2} \ln\left[(x-\xi)^2 + (y-\eta)^2 + z^2\right] \end{array} \right)$$

(A.29)

# Appendix G Evaluation of NiP - coatings

It has been a long-known phenomenon that etching NiP with acid produces a black surface coating. The phenomenon received serious attention of the scientific community when a Japanese research team published the lowest-ever reported reflectivity values for their NiP-coating (Kodama et al., 1990).

The main reasons for using NiP coating are:

- its low reflectivity in the VIS and NIR (Brown et al., 2002, Dury, 2005, Dury et al., 2006, Kodama et al., 1990)
- its resistance to solar and thermal ageing. NiP is a metallic coating and is much more long-term stable than organic blacks (Dury et al., 2006, Gibbs et al., 1995, Dury, 2005).
- its proven long term stability in cryogenic radiometers (NPL primary standard for radiant power)
- its proven performance in space-qualification tests (Saxena et al., 2006).

## G.1 Description of samples

The NiP-coating process is an example of "wet chemistry", where the skill and know-how of the technicians plays an important role. This is probably why no other science team could reproduce the excellent results achieved by the Japanese team. The original know-how of Kodama et al. has most recently been handed over to a team at NEC Toshiba.

Various electroformed copper samples were sent to NEC Toshiba in the autumn of 2008. These included two identical cavities that consist of two pieces each: one cylindrical nose cone with a flange

at the back (outer diameter at the front: 10 mm, outer diameter of the flange: 20 mm, see Figure A - 5) and a circular back plate (outer diameter: 20 mm, length: 45 mm, 6 small holes along the rim, see Figure A - 7). The wall thickness is 100 µm.

**Figure A - 5 Nose cone after coating – side view**[98]

**Figure A - 6 Nose cone after coating - top view**[99]

[98] Photo courtesy of NEC Toshiba Satellite Systems
[99] Photo courtesy of NEC Toshiba Satellite Systems

Figure A - 7 Back plates after coating[100]

### G.1.1 Coating process

We pursued two aims when we sent the cavities to Japan. Firstly, we wanted to know how well the coating could be done when the two parts of the cavity were coated separately (from now on called "Cavity A" in this document). Secondly, we wanted to know how well the coating could be applied to the inside of a top-hat shaped cavity. For the benefit of this latter aim, the other one of the cavities was coated while the back plate was bolted onto the nose cone (this assembly is henceforth referred to as "Cavity B" in this document).

### G.1.2 Surface morphology of NiP samples

SEM images were taken of the inside surfaces of both cavity back plates in order to compare their surface morphology. In addition, the features on the back plate of Cavity B were inspected more closely.

Upon visual inspection, Cavity A appears to have a homogeneous and faultless coating on the entire surface area. However, the appearance of Cavity B is not as good. The inside of the cone does not look as black as that of Cavity A. Furthermore, the back plate of Cavity B is not coated homogeneously, i.e. there appear to be

[100] Photo courtesy of NEC Toshiba Satellite Systems

small uncoated spots (this was the impression during visual inspection, but Scanning Electron Microscope (SEM) images revealed that this initial assessment was not correct.

Before going into the detail of the anomalies, the homogeneously coated areas of the two cavities are explored in greater depth. Figure A - 8 shows an SEM image[101] of the Cavity A backplate surface, and Figure A - 9 shows a view from a 30˚ - angle. These images show well-formed craters of diameters around a few µm. These craters act as microcavities that are trapping light in the spectral range where the wavelengths are smaller than these microcavities.

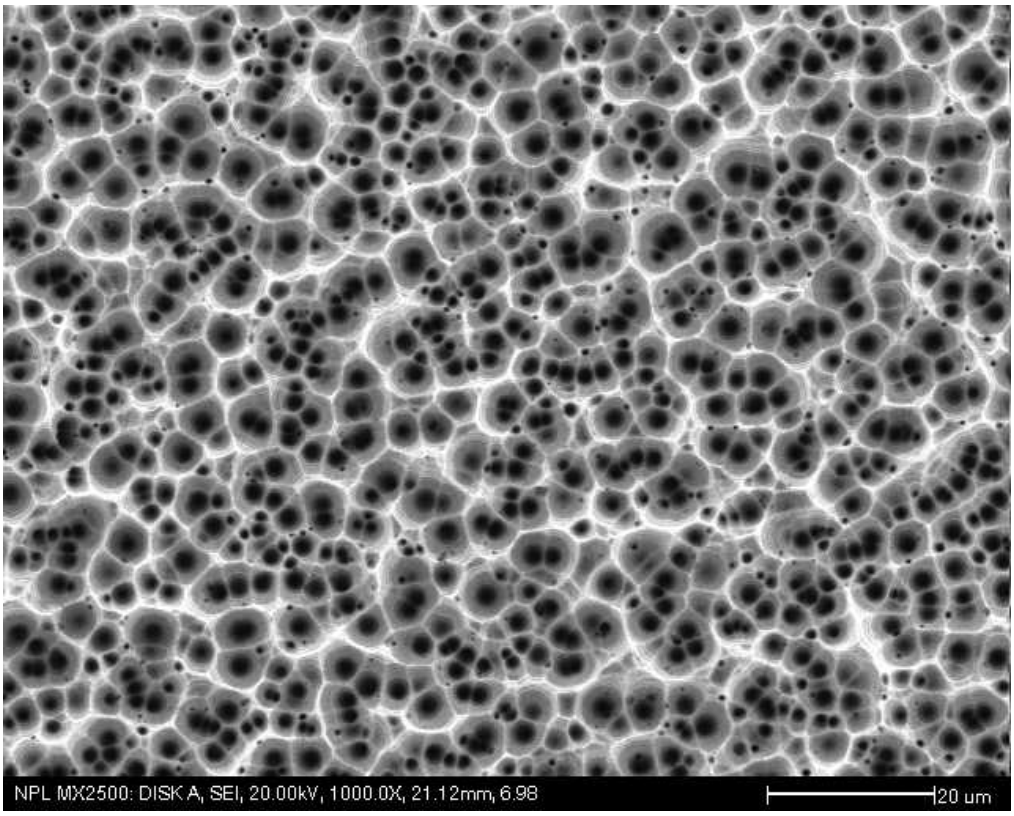


**Figure A - 8 Cavity A: back plate viewed from the top**

[101] All SEM images in this Appendix were taken with the help of Dipak Gohil (NPL)

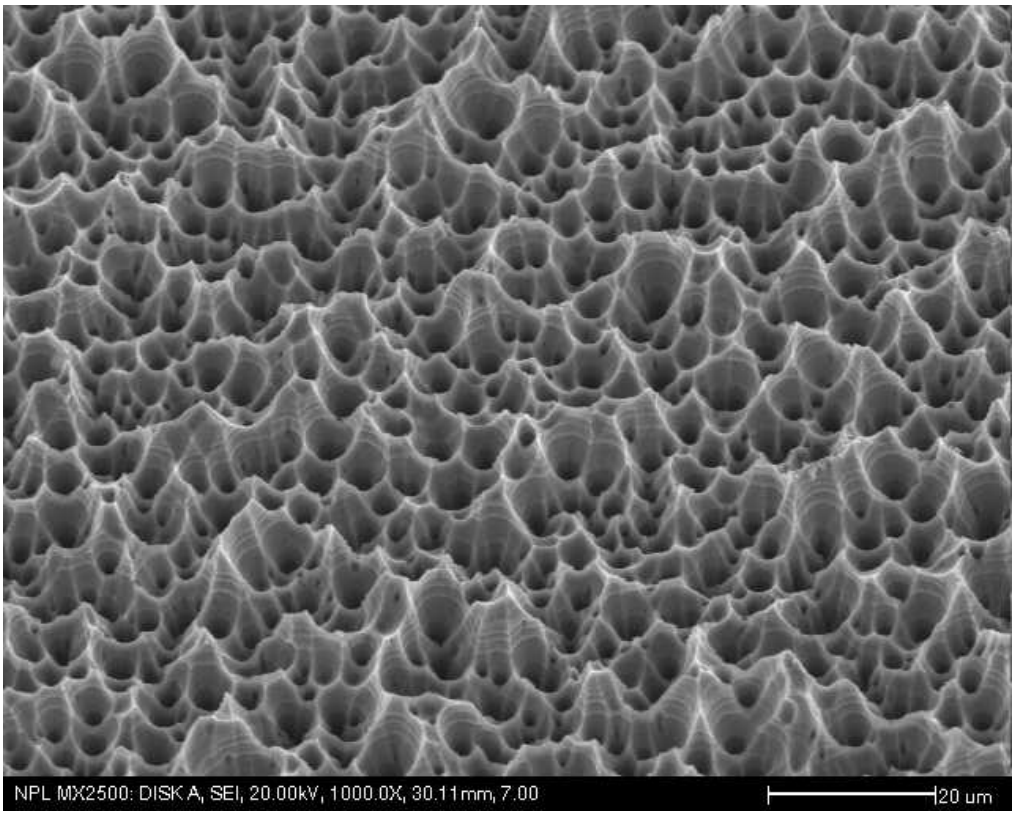


**Figure A - 9 Cavity A: back plate viewed under a 30° - angle**

The SEM images of Cavity B confirm the results of the visual inspection with regard to the regular areas of coating. When compared to Cavity A, the surface craters on Cavity B are less deep, and there are also larger plateau-areas, where there are no significant craters to be found (see Figure A - 10 and Figure A - 11).

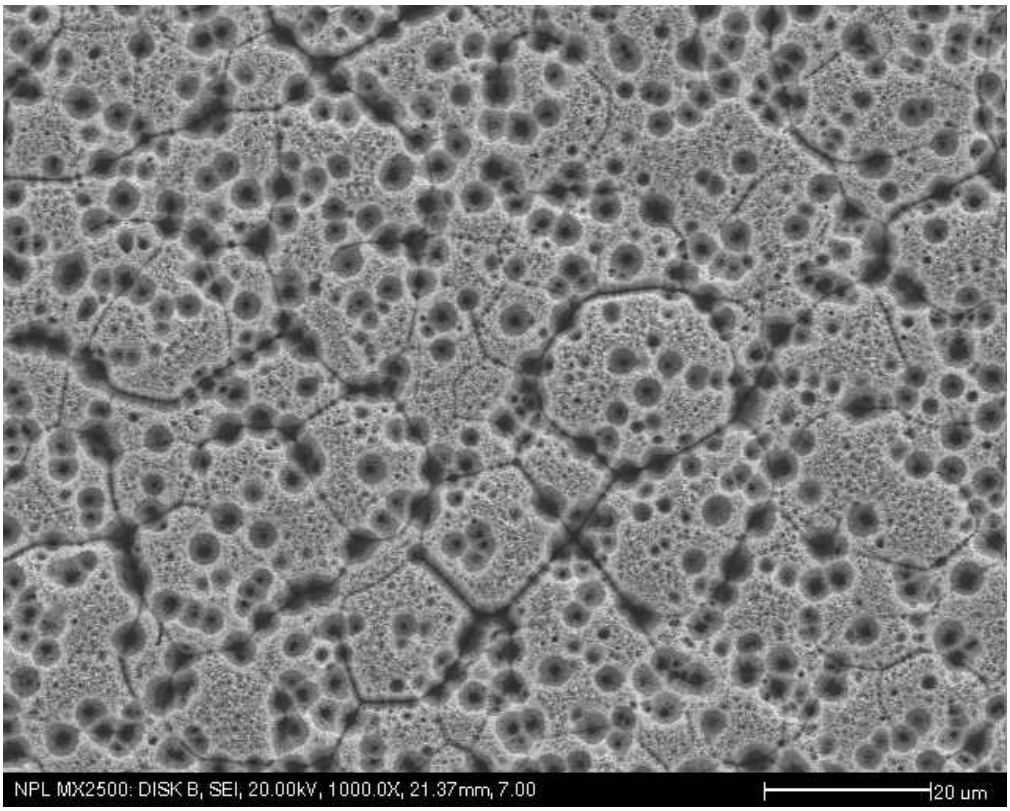


**Figure A - 10 Cavity B: back plate viewed from the top**

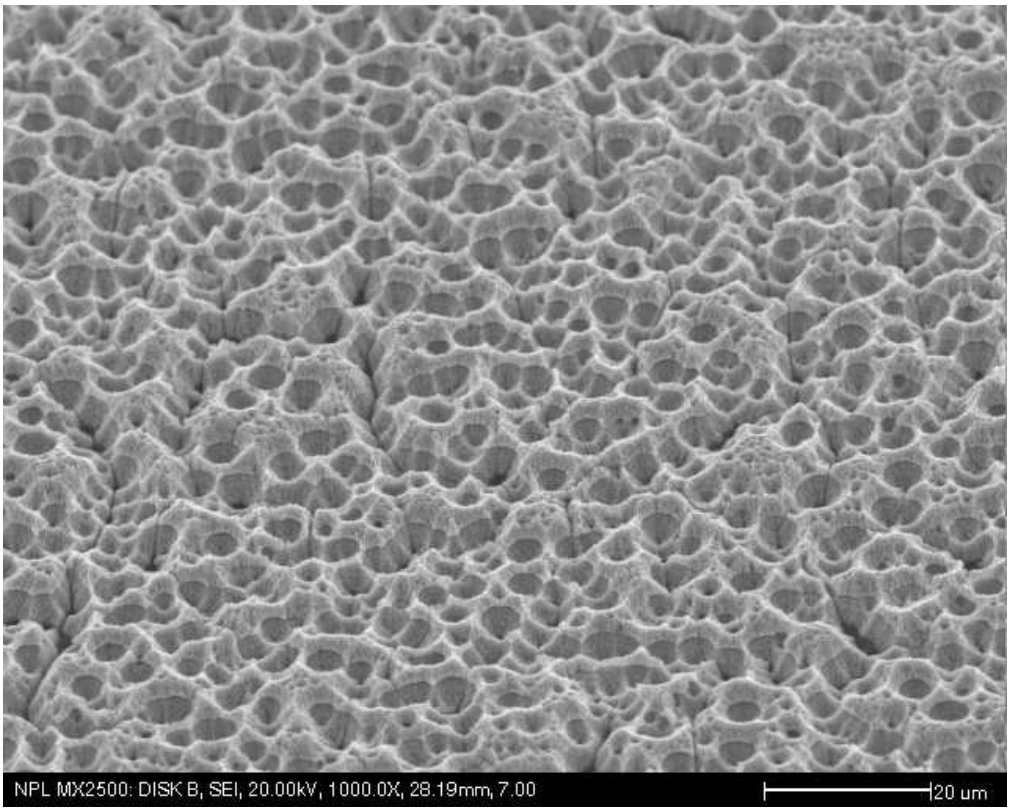


**Figure A - 11 Cavity B: back plate viewed under a 30° - angle**

### G.1.3 Anomalous features

On visual inspection, the backplate of Cavity A appears almost faultless, whereas the backplate of Cavity B clearly shows 'bright spots'. However, the SEM images reveal anomalies in the surface morphology in both Cavity A (see Figure A - 12) and Cavity B (see Figure A - 13), although the ones in Cavity B are much more pronounced – as expected from visual inspection. The largest of the unusual features on the back plate of Cavity B (Figure A - 13) was selected for further investigation. Initially its high reflectivity (visual inspection) was assigned to a lack of NiP coating; the initial working hypothesis was that the 'spot' was uncoated copper. However, the SEM images show that this assessment is not valid; rather, the specular reflectivity is due to an elevated area which is approximately 220 µm long, 80 µm wide and 20 µm high.

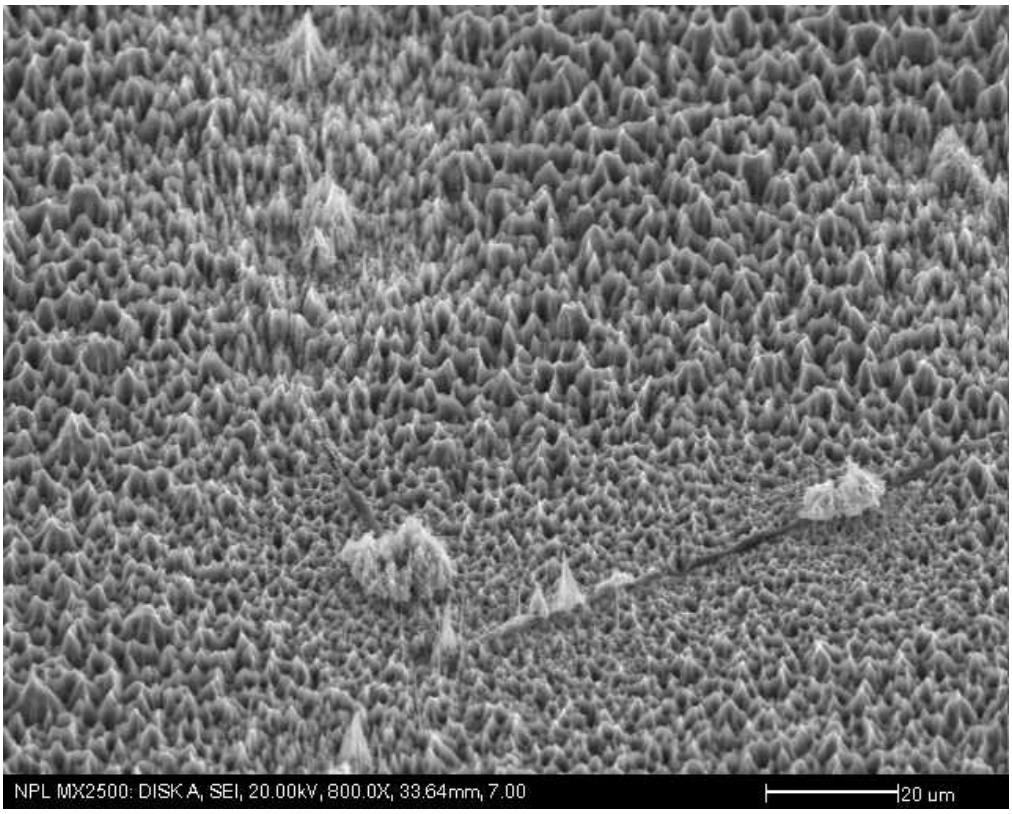


**Figure A - 12: Anomalous features on the Cavity A surface**

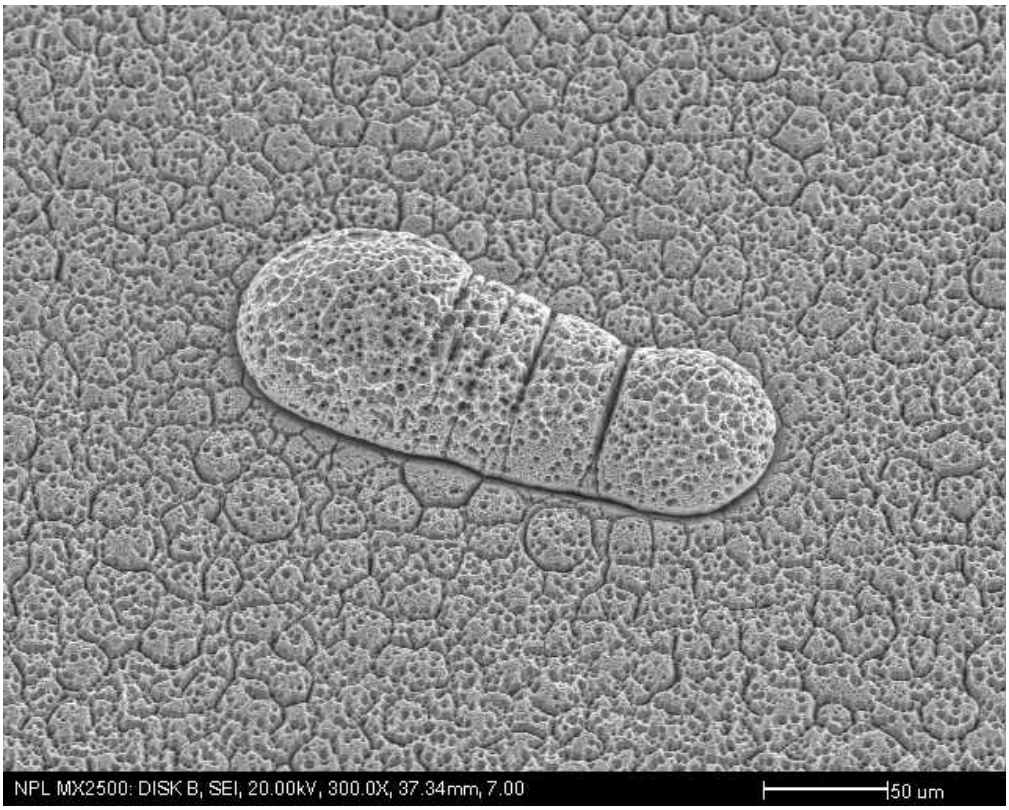


**Figure A - 13 Largest anomalous feature on the Cavity B surface**

### G.1.4 Chemical analysis

Brown et al. investigated the relationship between reflectivity and phosphorus content (Brown et al., 2002); Figure A - 14 is a reproduction of their results with respect to this investigation. It shows that the optimum phosphorus content is 5-7% (weight percent); outside of this percentage range, the reflectivity of the coating increases with decreasing as well as increasing phosphor content.

**Figure A - 14 The average reflectivity at 633 nm of Ni-P blacks with varying nominal pre-etch phosphorus compositions. Reproduced from (Brown et al., 2002).**

Figure A - 15 shows the chemical analysis of the Cavity A backplate surface coating; with 6.58%, the phosphor content is within the range that was identified as optimal by Brown et al. In the same way, Figure A - 16 shows the chemical analysis of the Cavity B backplate surface coating. The phosphor content of the Cavity B Ni-P coating is 9.41.

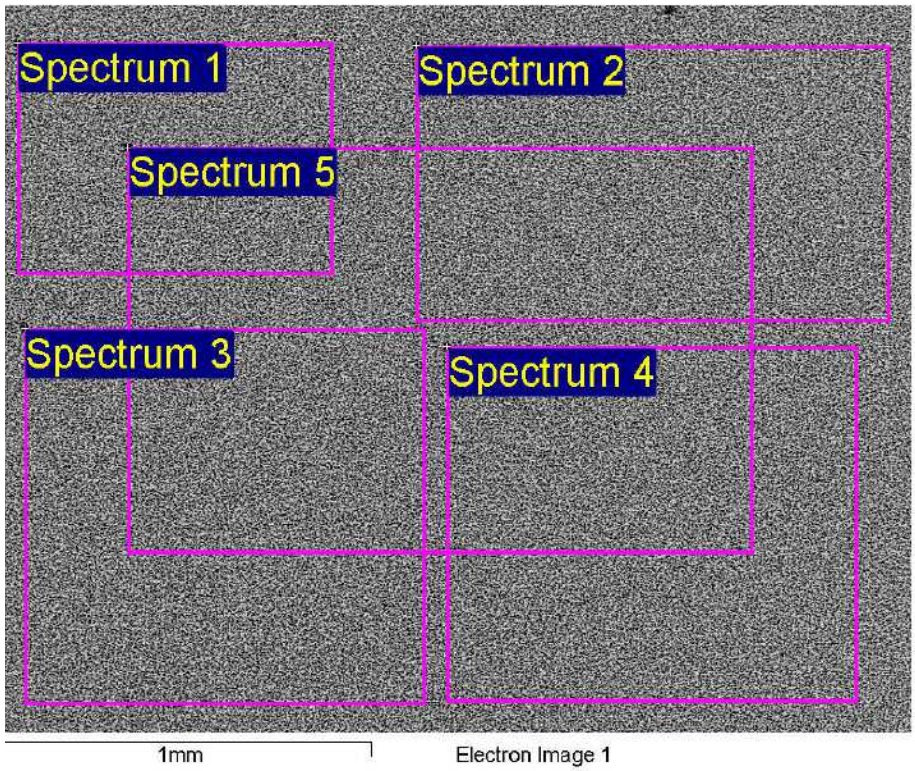


Processing option : All elements analyzed (Normalised)

| Spectrum | O | P | Co | Ni | Total |
|---|---|---|---|---|---|
| Spectrum 1 | 3.78 | 6.52 | 0.30 | 89.41 | 100.00 |
| Spectrum 2 | 3.76 | 6.73 | 0.00 | 89.50 | 100.00 |
| Spectrum 3 | 3.65 | 6.43 | 0.22 | 89.70 | 100.00 |
| Spectrum 4 | 3.52 | 6.41 | 0.20 | 89.87 | 100.00 |
| Spectrum 5 | 3.78 | 6.79 | 0.00 | 89.43 | 100.00 |
| Mean | 3.70 | 6.58 | 0.14 | 89.58 | 100.00 |
| Std. deviation | 0.12 | 0.17 | 0.14 | 0.20 | |
| Max. | 3.78 | 6.79 | 0.30 | 89.87 | |
| in. | 3.52 | 6.41 | 0.00 | 89.41 | |

**Figure A - 15 Chemical analysis of Cavity A coating (back plate)**

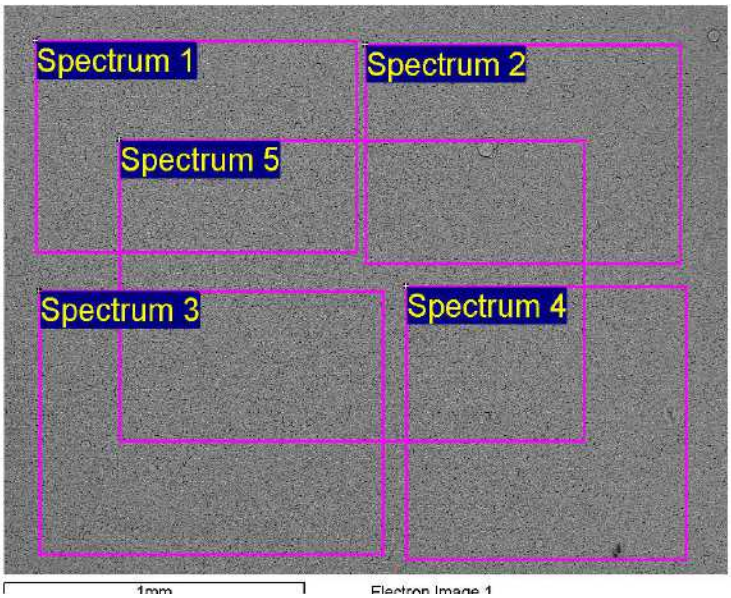


Processing option : All elements analyzed (Normalised)

| Spectrum | O | P | Co | Ni | Total |
|---|---|---|---|---|---|
| Spectrum 1 | 2.05 | 9.40 | 0.59 | 87.96 | 100.00 |
| Spectrum 2 | 1.98 | 9.47 | 0.60 | 87.95 | 100.00 |
| Spectrum 3 | 1.74 | 9.25 | 0.52 | 88.49 | 100.00 |
| Spectrum 4 | 1.91 | 9.36 | 0.69 | 88.04 | 100.00 |
| Spectrum 5 | 1.78 | 9.54 | 0.46 | 88.22 | 100.00 |
| Mean | 1.89 | 9.41 | 0.57 | 88.13 | 100.00 |
| Std. deviation | 0.13 | 0.11 | 0.09 | 0.23 | |
| Max. | 2.05 | 9.54 | 0.69 | 88.49 | |
| Min. | 1.74 | 9.25 | 0.46 | 87.95 | |

All results in Weight Percent

**Figure A - 16 Chemical analysis of Cavity B coating (back plate)**

The chemical analysis of the largest anomalous feature on the Cavity B backplate (see Figure A - 17) shows an increased phosphorus content (11%) when compared to the surrounding area (8.95%). However, it is hard to quantify the exact phosphorus content of this feature because the feature is relatively thin and the chemical analysis may include some of the material beneath the feature.

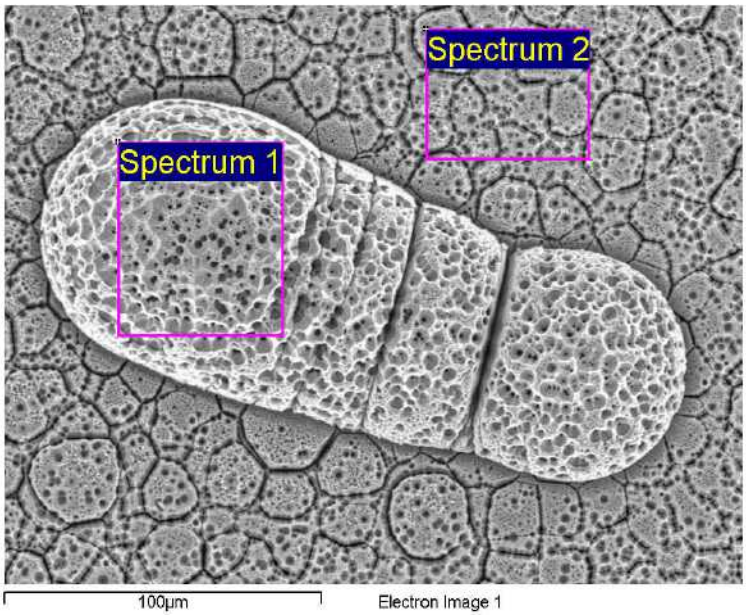


Processing option : All elements analyzed (Normalised)

| Spectrum | O | P | Co | Ni | Total |
|---|---|---|---|---|---|
| Spectrum 1 | 2.10 | 11.00 | 0.43 | 86.46 | 100.00 |
| Spectrum 2 | 1.24 | 8.95 | 0.35 | 89.46 | 100.00 |
| Mean | 1.67 | 9.98 | 0.39 | 87.96 | 100.00 |
| Std. deviation | 0.61 | 1.45 | 0.05 | 2.12 | |
| Max. | 2.10 | 11.00 | 0.43 | 89.46 | |
| Min. | 1.24 | 8.95 | 0.35 | 86.46 | |

All results in Weight Percent

**Figure A - 17 Chemical analysis of the largest feature on the Cavity B (back plate) surface**

### *G.1.4.1 Cavity Absorptivity*

The absorptivity of both cavities was measured. To that end, the parts of Cavity A were bolted together. The measurement setup was as described in (Fox et al., 1996).

These measurements show that the absorptivity of the cavities at wavelength 647 nm is 0.99994 (Cavity A) and 0.99966 (Cavity B). If the reflectivity at the back plate is assumed to be perfectly diffuse, the corresponding values for the total hemispherical reflectivity are 0.5 %

(surface coating of Cavity A) and 2.8 % (surface coating of Cavity B). However, the assumption that the reflection is diffuse seems not to be completely valid (as discussed below).

### *G.1.4.2 Spectral measurements of diffuse hemispherical reflectivity*

After the Cavity absorptivity measurements, the nose cone was removed from Cavity A and the total reflectivity of the back plate was measured for wavelengths between 400 nm and 2300 nm. As shown in Figure A - 18, the diffuse reflectivity was found to be less than 0.35 % in the visible region, and less than 1.3 % for wavelengths below 2300 nm.

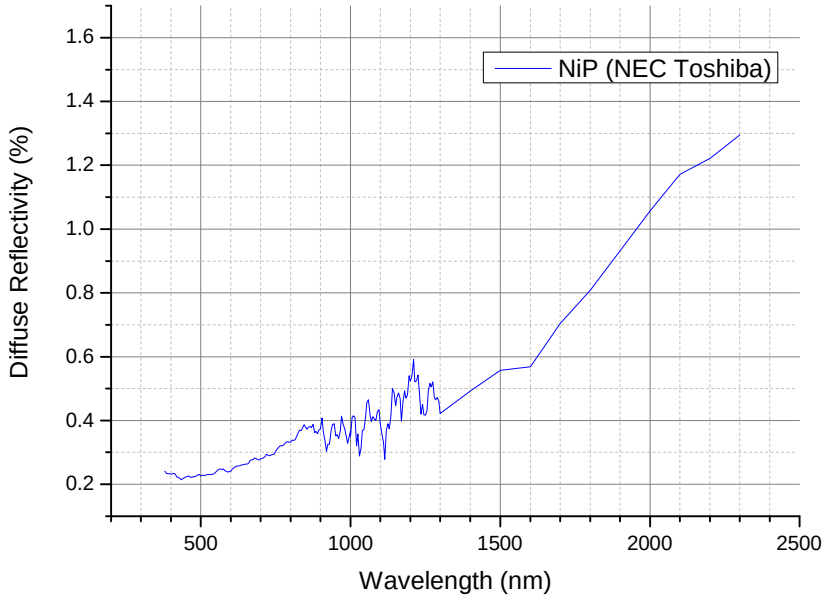


**Figure A - 18 Diffuse reflectivity of the NiP-coating on the back plate of Cavity A[102]**

### *G.1.4.3 Discussion of measurement results*

The coating of Cavity A has a phosphorus content of approx. 6.6% (weight percent) and Cavity B 9.4%. According to Brown et al.'s

[102] Measurement performed by Andrew Deadman (NPL)

analysis (Figure A - 14), one would expect a difference in reflectivity between the two samples of approximately a factor of 1.8, if all other conditions remained the same. However, the difference in reflectivity at 647 nm is approximately a factor of 5, which cannot be explained by the difference in phosphorus content. The remaining difference is very likely due to other changes in the process due to the reduced accessibility of the surface, resulting in a less optimal flow of acid in the closed cavity (during the etching process).

In addition, the measured cavity absorptivity of Cavity A is lower than expected based on the results of the spectral measurements and based on the assumption that the diffuse component is dominating. These considerations would lead to a theoretical cavity absorptivity of 0.99998 (at 647 nm) when using the measured value for diffuse hemispherical reflectivity as shown in Figure A - 18, rather than the measured 0.99994. This discrepancy indicates that the specular reflectivity is higher than expected. This is especially significant regarding the measurement result of the overall cavity absorptivity since the back plate was perpendicular to the incident beam. This increased specular reflectivity is however not surprising given the observed imperfections in the coating that were revealed by SEM imaging.

# Appendix H Weighted mean and associated uncertainty

Ordinarily, the value of a measurand is estimated by a simple arithmetic mean (see Equation (2.3)) of a series of observation values, and the associated standard uncertainty is estimated according to Equation (2.5). However, sometimes every observation value $x_i$ itself is already the arithmetic mean of a measurement series and is associated with a specific standard uncertainty $u(x_i)$

In this case, a weighted mean $y$ can be calculated for the overall result, which takes the quality of the $N$ independent observations into account (the following equations are taken from (Cox, 2002)):

$$y = \frac{\sum_{i=1}^{N} \frac{x_i}{u^2(x_i)}}{\sum_{i=1}^{N} \frac{1}{u^2(x_i)}} \tag{A.30}$$

The standard deviation $u(y)$ associated with y can be determined from

$$\frac{1}{u^2(y)} = \sum_{i=1}^{N} \frac{1}{u^2(x_i)} \tag{A.31}$$

The overall consistency of the results can be checked via a statistical Chi-square test:

(a) Calculate the observed chi-squared value:

$$\chi^2_{obs} = \sum_{i=1}^{N} \frac{(x_i - y)^2}{u^2(x_i)} \tag{A.32}$$

(b) Determine the degrees of freedom:

$$\nu = N - 1 \tag{A.33}$$

(c) Regard the consistency check as failing if $\Pr\left\{\chi^2(\nu) > \chi^2_{obs}\right\} < 0.05$ , where Pr denotes "probability of", and it should be noted that this test assumes normality (Gaussian distribution of the individual measurements).

# Bibliography


AZOM.COM. 2012. Available: www.azom.com [Accessed 10 Aug 2012].

BARUCCI, M., OLIVIERI, E., PASCA, E., RISEGARI, L. & VENTURA, G. 2005. Thermal conductivity of Torlon between 4.2 and 300 K. *Cryogenics,* 45**,** 295-299.

BEDFORD, R. E., BONNIER, G., MAAS, H. & PAVESE, F. 1997. Rhodium-Iron Resistance Thermometers. *Techniques for approximating the international temperature scale 1990.* Sevres: Bureau International des Poids et Mesures.

BROWN, R. J. C., BREWER, P. J. & MILTON, M. J. T. 2002. The physical and chemical properties of electroless nickel-phosphorus alloys and low reflectance nickel-phosphorus black surfaces. *Journal of Materials Chemistry,* 12**,** 2749 - 2754.

BRUSA, R. W. & FRÖHLICH, C. 1986. Absolute radiometers (PM06) and their experimental characterization. *Applied Optics,* 25**,** 4173-4180.

BUTLER, J. J., JOHNSON, B. C., RICE, J. P., SHIRLEY, E. L. & BARNES, R. A. 2008. Sources of Differences in On-Orbital Total Solar Irradiance Measurements and Description of a Proposed Laboratory Intercomparison. *Journal of Research of the National Institute of Standards and Technology,* 113**,** 187-203.

BUYANOV, Y. L., FRADKOV, A. B. & SHEBALIN, I. Y. 1975. REVIEW OF CURRENT LEADS FOR CRYOGENIC DEVICES. *Cryogenics,* 15**,** 193-200.

CGPM. 1999. *Resolution 4 of the 21st meeting of the CGPM* [Online]. Available: http://www.bipm.org/en/CGPM/db/21/4/ [Accessed 5 October 2012].

CGPM. 2007. *Resolution 11 of the 23rd CGPM* [Online]. Available: http://www.bipm.org/en/CGPM/db/23/11/ [Accessed 5 October 2012].

CLARK, A. F., CHILDS, G. E. & WALLACE, G. H. 1970. ELECTRICAL RESISTIVITY OF SOME ENGINEERING ALLOYS AT LOW TEMPERATURES. *Cryogenics,* 10**,** 295-&.

COHEN, E. R. & TAYLOR, B. N. 1973. The 1973 Least-Squares Adjustment of the Fundamental Constants *J. Phys. Chem. Ref. Data* 2**,** 663 - 734.

COX, M. G. 2002. The evaluation of key comparison data. *Metrologia,* 39**,** 589-595.

DATLA, R. U., STOCK, K., PARR, A. C., HOYT, C. C., MILLER, P. J. & FOUKAL, P. V. 1992. Characterization of an Absolute Cryogenic Radiometer as a Standard Detector for Radiant-Power Measurements. *Applied Optics,* 31**,** 7219-7225.

DETOMA, G. & WHITE, O. R. 2006. Empirical Modeling of TSI: A Critical View. *Solar Physics,* 236**,** 1-24.

DEWITTE, S., CROMMELYNCK, D., MEKAOUI, S. & JOUKOFF, A. 2004. Measurement and Uncertainty of the Long-Term Total Solar Irradiance Trend. *Solar Physics,* 224**,** 209-216.

DURY, M. R. 2005. *Development of the NPL wide-area MIR calibration source.* PhD, University of Reading.
DURY, M. R., THEOCHAROUS, T., HARRISON, N., FOX, N. & HILTON, M. 2006. Common black coatings – reflectance and ageing characteristics in the 0.32–14.3 μm wavelength range. *Optics Communications,* 270**,** 262-272.
EDWARDS, P. J. 2004. *Diffraction Theory and Radiometry.* PhD, Imperial College.
FEHLMANN, A. 2011. *Metrology of Solar Irradiance.* Dr. sc. nat., University of Zuerich.
FEHLMANN, A., KOPP, G., SCHMUTZ, W., WINKLER, R., FINSTERLE, W. & FOX, N. 2012. Fourth World Radiometric Reference to SI radiometric scale comparison and implications for on-orbit measurements of the total solar irradiance. *Metrologia,* 49**,** S34-S38.
FINSTERLE, W. 2011. *WMO International Pyrheliometer Comparison IPC-X Final Report* [Online]. Davos: PMOD / WRC. Available: http://www.wmo.int/pages/prog/www/IMOP/publications/IOM-108_IPC-XI_Davos.pdf [Accessed 5 October 2012].
FINSTERLE, W., BLATTNER, P., MOEBUS, S., RÜEDI, I., WEHRLI, C., WHITE, M. & SCHMUTZ, W. 2008. Third comparison of the World Radiometric Reference and the SI radiometric scale. *Metrologia***,** 377–381.
FOUKAL, P. V., HOYT, C., KOCHLING, H. & MILLER, P. 1990. Cryogenic Absolute Radiometers as Laboratory Irradiance Standards, Remote Sensing Detectors, and Pyroheliometers. *Applied Optics,* 29**,** 988-993.
FOX, N., KAISER-WEISS, A., SCHMUTZ, W., THOME, K., YOUNG, D., WIELICKI, B., WINKLER, R. & WOOLLIAMS, E. 2011. Accurate radiometry from space: an essential tool for climate studies. *Philosophical Transactions of the Royal Society a-Mathematical Physical and Engineering Sciences,* 369**,** 4028-4063.
FOX, N. P. 1991. Trap Detectors and their Properties. *Metrologia,* 28**,** 197-202.
FOX, N. P., HAYCOCKS, P. R., MARTIN, J. E. & UL-HAQ, I. 1996. A Mechanically Cooled Portable Cryogenic Radiometer. *Metrologia,* 32**,** 581-584.
FOX, N. P. & RICE, J. P. 2005. Absolute Radiometers. *In:* PARR, A. C., DATLA, R. U. & GARDNER, J. L. (eds.) *Optical Radiometry.* Elsevier.
FRÖHLICH, C. 1977. World Radiometric Reference. *Commission for Instruments and Methods of Observation - Abridged Final Report of the Seventh Session (CIMO-VII, WMO-No. 490).* Hamburg: Secretariat of the World Meteorological Organisation.
FRÖHLICH, C. 1991. History of Solar Radiometry and the World Radiometric Reference. *Metrologia,* 28**,** 111-115.
FRÖHLICH, C. 2000. Observations of Irradiance Variations. *Space Science Reviews,* 94**,** 15-24.
FRÖHLICH, C. 2003. Long-term behaviour of space radiometers. *Metrologia,* 40**,** S60-S65.

FRÖHLICH, C. 2006. Solar Irradiance Variability since 1978. *Space Science Reviews,* 125**,** 53-65.

FRÖHLICH, C., CROMMELYNCK, D. A., WEHRLI, C., ANKLIN, M., DEWITTE, S., FICHOT, A., FINSTERLE, W., JIMÉNEZ, A., CHEVALIER, A. & ROTH, H. 1997. In-flight performance of the VIRGO Solar Irradiance Instruments on SOHO. *Solar Physics,* 175**,** 267-286.

FRÖHLICH, C. & LEAN, J. 1998. The Sun's Total Irradiance: Cycles, Trends and Related Climate Change Uncertainties since 1976. *Geophysical Research Letters,* 25**,** 4377-4380.

FRÖHLICH, C., ROMERO, J., ROTH, H., WEHRLI, C., ANDERSEN, B. N., APPOURCHAUX, T., DOMINGO, V., TELLJOHANN, U., BERTHOMIEU, G., DELACHE, P., PROVOST, J., TOUTAIN, T., CROMMELYNCK, D. A., CHEVALIER, A., FICHOT, A., DÄPPEN, W., GOUGH, D., HOEKSEMA, T., JIMÉNEZ, A., GÓMEZ, M. F., HERREROS, J. M., CORTÉS, T. R., JONES, A. R., PAP, J. M. & WILLSON, R. C. 1995. VIRGO: Experiment for helioseismology and solar irradiance monitoring *Solar Physics,* 162**,** 101-128.

GIBBS, D. R., DUNCAN, F. J., LAMBE, R. P. & GOODMAN, T. M. 1995. Ageing of materials under intense ultraviolet radiation. *Metrologia,* 32**,** 601-607.

GINNINGS, D. & REILLY, M. 1972. Calorimetric Measurement of Thermodynamic Temperatures Above 0 °C using Total Blackbody Radiation. *Temperature: its Measurement and Control in Science and Industry.* Pittsburgh: Instrument Society of America.

GROBNER, J. 2008. Operation and investigation of a tilted bottom cavity for pyrgeometer characterizations. *APPLIED OPTICS,* 47**,** 4441-4447.

HARTMANN, J. 2007. *High-temperature measurement techniques for the application in Photometry, Radiometry, and Thermometry*. Habilitation, Technische Universität Berlin.

HOWELL, J. R. 2010. *A Catalog of Radiation Heat Transfer Configuration Factors* [Online]. Available: http://www.engr.uky.edu/rtl/Catalog/ [Accessed 20 July 2012].

HOWELL, J. R., SIEGEL, R. & MENGUC, M. P. 2010. *Thermal Radiation Heat Transfer*, CRC Press.

ICEOXFORD. Available: http://www.iceoxford.com/Cryogenic-spares/Wiring.htm [Accessed 04 Aug 2011].

IPCC. 2007. *IPCC Fourth Assessment Report: Climate Change 2007, Glossary P-Z* [Online]. Available: http://www.ipcc.ch/publications_and_data/ar4/wg1/en/annex1sglossary-p-z.html [Accessed 16 Nov 2010].

JCGM. 2008. *Evaluation of measurement data — Guide to the expression of uncertainty in measurement* [Online]. Available: http://www.bipm.org/utils/common/documents/jcgm/JCGM_100_2008_E.pdf [Accessed 5 October 2012].

KODAMA, S., HORIUCHI, M., KUNII, T. & KURODA, K. 1990. Ultra-Black Nickel-Phosphorus Alloy Optical Absorber. *IEEE Transactions on Instrumentation and Measurement,* 39**,** 230-232.
KOPP, G., HEUERMAN, K. & LAWRENCE, G. 2005. The Total Irradiance Monitor (TIM): Instrument calibration. *Solar Physics,* 230**,** 111-127.
KOPP, G., HEUERMANN, K., HARBER, D. & DRAKE, G. 2007. The TSI Radiometer Facility - absolute calibrations for total solar irradiance instruments. *Proceedings of SPIE,* 6677**,** 67709-67709.
KOPP, G. & LEAN, J. L. 2011. A new, lower value of total solar irradiance: Evidence and climate significance. *Geophysical Research Letters,* 38.
LOCKWOOD, M. & FRÖHLICH, C. 2007. Recent oppositely directed trends in solar climate forcings and the global mean surface air temperature. *Proceedings of the Royal Society A,* 463**,** 2447-2460.
LOCKWOOD, M. & FRÖHLICH, C. 2008. Recent oppositely directed trends in solar climate forcings and the global mean surface air temperature. II. Different reconstructions of the total solar irradiance variation and dependence on response time scale. *Proceedings of the Royal Society A,* 464**,** 1367-1385.
MARQUARDT, E. D., LE, J. P. & RADEBAUGH, R. 2000. Cryogenic Material Properties Database.
MARTIN, J. E. & FOX, N. P. 1994 Cryogenic Solar Absolute Radiometer CSAR. *Solar Physics,* 152**,** 1-8.
MARTIN, J. E., FOX, N. P. & KEY, P. J. 1985. A Cryogenic Radiometer for Absolute Radiometric Measurements. *Metrologia,* 21**,** 147-155.
MELCHERT, F. 1978. Monitoring a Group of Standard Cells in a New Enclosure by Means of Ac Josephson Effect. *Metrologia,* 14**,** 167-170.
MILTON, M. J. T., WILLIAMS, J. M. & BENNETT, S. J. 2007. Modernizing the SI: towards an improved, accessible and enduring system. *Metrologia,* 44**,** 356-364.
NIST. 2000. *Cryogenic Materials Database* [Online]. Available: http://cryogenics.nist.gov/MPropsMAY/material%20properties.htm [Accessed 5 October 2012].
OHRING, G. 2007. *Achieving Satellite Instrument Calibration for Climate Change (ASIC3)* [Online]. Available: http://www.star.nesdis.noaa.gov/star/documents/ASIC3-071218-webversfinal.pdf [Accessed 5 October 2012].
QUINN, T. J. 1983. *Temperature,* London, Academic Press.
QUINN, T. J. & FRÖHLICH, C. 1999. Accurate radiometers should measure the output of the Sun. *Nature,* 401**,** 841.
QUINN, T. J. & MARTIN, J. E. 1985. A radiometric determination of the Stefan-Boltzmann constant and thermodynamic temperatures between -40 °C and +100 °C. *Philosophical Transactions of the Royal Society of London A,* 316**,** 85-189.
ROBERTS, S. 1959. OPTICAL PROPERTIES OF NICKEL AND TUNGSTEN AND THEIR INTERPRETATION ACCORDING TO DRUDES FORMULA. *Physical Review,* 114**,** 104-115.

ROMERO, J., FOX, N. P. & FROHLICH, C. 1991. FIRST COMPARISON OF THE SOLAR AND AN SI RADIOMETRIC SCALE. *Metrologia,* 28**,** 125-128.

ROMERO, J., FOX, N. P. & FROHLICH, C. 1996. Improved comparison of the World Radiometric Reference and the SI radiometric scale. *Metrologia,* 32**,** 523-524.

SAXENA, V., RANI, R. U. & SHARMA, A. K. 2006. Studies on ultra high solar absorber black electroless nickel coatings on aluminum alloys for space application. *Surface & Coatings Technology,* 201**,** 855-862.

SCHLACHTER, S. I., GOLDACKER, W., FRANK, A., RINGSDORF, B. & ORSCHULKO, H. 2006. Properties of MgB2 superconductors with regard to space applications. *Cryogenics,* 46**,** 201-207.

SCHMUTZ, W., FEHLMANN, A., HULSEN, G., MEINDL, P., WINKLER, R., THUILLIER, G., BLATTNER, P., BUISSON, F., EGOROVA, T., FINSTERLE, W., FOX, N., GROBNER, J., HOCHEDEZ, J. F., KOLLER, S., MEFTAH, M., MEISONNIER, M., NYEKI, S., PFIFFNER, D., ROTH, H., ROZANOV, E., SPESCHA, M., WEHRLI, C., WERNER, L. & WYSS, J. U. 2009. The PREMOS/PICARD instrument calibration. *Metrologia,* 46**,** S202-S206.

SMITH, R. A., JONES, F. E. & CHASMAR, R. P. 1968. *The detection and measurement of infra-red radiation,* London, Clarendon Press.

TSUJIMOTO, S., KANDA, M. & KUNITOMO, T. 1982. THERMAL RADIATIVE PROPERTIES OF SOME CRYOGENIC MATERIALS. *Cryogenics,* 22**,** 591-597.

VENKANNA, B. K. 2010. *Fundamentals of Heat and Mass Transfer,* New Delhi, PHI Learning Pvt. Ltd.

WHITE, G. K. & MEESON, P. J. 2002. *Experimental Techniques in Low-Temperature Physics,* New York, Oxford University Press.

WILLSON, R. C. 1997. Total solar irradiance trend during solar cycles 21 and 22. *Science,* 277**,** 1963-1965.

WILLSON, R. C. & MORDVINOV, A. V. 2003. Secular total solar irradiance trend during solar cycles 21–23. *Geophysical Research Letters,* 30.

WMO 2006. WMO Guide to Meteorological Instruments and Methods of Observation (CIMO Guide, WMO-8). 7 ed.

WMO. 2008. *WMO Guide to Meteorological Instruments and Methods of Observation (CIMO Guide, WMO-8)* [Online]. Geneva. Available: http://www.wmo.int/pages/prog/gcos/documents/gruanmanuals/CIMO/CIMO_Guide-7th_Edition-2008.pdf [Accessed 5 October 2012].

WMO. 2010. *Report on the WMO-BIPM workshop on Measurement Challenges for Global Observation Systems for Climate Change Monitoring: Traceability, Stability and Uncertainty* [Online]. Geneva: World Meteorological Organisation. Available: http://www.bipm.org/utils/common/pdf/rapportBIPM/2010/08.pdf [Accessed 5 October 2012].